Critical Evaluation of Slip Synchronous Wind Generator Technology

by

Dillan K. Ockhuis

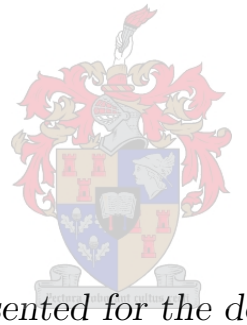

Dissertation presented for the degree of Doctor of Philosophy in Electrical Engineering in the Faculty of Engineering at Stellenbosch University

Supervisor: Prof M.J Kamper

December 2022

Declaration

By submitting this dissertation electronically, I declare that the entirety of the work contained therein is my own, original work, that I am the sole author thereof (save to the extent explicitly otherwise stated), that reproduction and publication thereof by Stellenbosch University will not infringe any third party rights and that I have not previously in its entirety or in part submitted it for obtaining any qualification.

Date: December 2022 .....

Abstract

Critical Evaluation of Slip Synchronous Wind Generator Technology

D.K. Ockhuis

Dissertation: PhD (Elec)

December 2022

Historically, the strength and stability of an electrical power grid depended on the number of synchronous generators (SGs) connected to that grid. However, as traditional SG-based electrical power sources are replaced with converter-tied renewable energy sources (RESs), electrical power grids may become unstable following a grid disturbance. In this dissertation, it is proposed that slip synchronous wind turbine systems (SS-WTSs) be used to assist with grid stability by providing grid strength, inertia and reactive power compensation in areas with a high concentration of converter-tied RESs.

An SS-WTS drivetrain fundamentally consists of a slip-permanent magnetic coupler (S-PMC) and a directly grid-tied SG, i.e., without a power converter. However, the literature regarding the design and modelling of the SG and S-PMC units in SS-WTSs for grid-tied applications is not sufficient. Firstly, the designed SGs typically have low synchronous reactance values, thus their performance is highly susceptible to grid voltage variations. Secondly, the generators designed for SS-WTSs are not grid code compliant and are thus ineligible for large-scale grid connected applications. Thirdly, the methods used to model and analyse the S-PMC unit can yield inaccurate results when predicting the maximum torque of the S-PMC, which can jeopardise the stability of the SS-WTS. Finally, there are concerns regarding the added mass and cost of the S-PMC unit.

In this dissertation, optimal impedance matching for grid-tied SGs is investigated. It is found that a synchronous reactance of 0.5 per unit yields the best grid-connected performance. Furthermore, a rotor hybrid-excited design methodology for grid-tied synchronous generators is proposed and evaluated. Accurate finite-element (FE) analysis shows that the proposed hybrid-excitation method ensures that the grid-tied generator has variable-flux and hence variable reactive power compensation capabilities to comply with modern grid codes. Measured results from a novel 15 kW hybrid-excited SG verify the FE results and the grid code compliance of the generator. Additionally, in this dissertation, the FE-based, frozen permeability method is used to accurately determine the modelling parameters and performance characteristics of the S-PMC over its entire operating range. Measured results from an S-PMC prototype validate the FE analysis results. A study that compares medium- and low-speed S-PMCs at a 3 MW power rating indicates that the medium-speed S-PMC has a significantly lower cost-per-kW and active mass compared to the low-speed S-PMC. Thus, S-PMCs in high-speed SS-WTSs should be considered to reduce the overall mass and cost of the SS-WTSs.

Acknowledgements

I would like to express my sincere gratitude to the following people and organisations:

- **Katherine Ann Nel**, for her endless support, unwavering encouragement and understanding from the very beginning.
- **My promoter and study supervisor Prof. Maarten Kamper**, for his guidance, supervision and support throughout my research.
- **The Electrical Machines Laboratory staff**: Petro Petzer, Andre Swart, Howard Koopman, Kenan Cloete and Keenan Fillies for their assistance, perseverance and insights during the design, construction and testing of the various experiments throughout my research.
- To **Dr Hannes (Casper) Labuschagne**, **Dr Christoff Botha**, and **Dr Ore Olubamiwa** for all the much-needed coffee breaks, philosophical debates, countless jokes, endless discussions and contributions that helped me persevere during the difficult days and that made this journey invaluable.
- A special thank you to **Andrew Loubser** for all his help and insights during the various experiments and tests conducted throughout my research.
- **My parents**, for all their support and encouragement.

List of Conferences and Publications

Local Conferences

D. Ockhuis, M. J. Kamper and A. T. Loubser, "Impedance Matching of Direct Grid-Connected Renewable Energy Synchronous Generators," 2020 International SAUPEC/RobMech/PRASA Conference, 2020, pp. 1-6.

Awards: This paper won The SAIEE Rotating Machines Section Award for the best student paper at SAUPEC 2020.

International Conferences

D. K. Ockhuis, M. J. Kamper and A. T. Loubser, "Hybrid Excitation Method for Higher Pole Number Grid-Tie Synchronous Generators," 2020 IEEE Energy Conversion Congress and Exposition (ECCE), 2020, pp. 1439-1446.

D. K. Ockhuis and M. J. Kamper, "Static-FE Harmonic Analysis of PM Slip Couplers," 2021 International Aegean Conference on Electrical Machines and Power Electronics (ACEMP) & 2021 International Conference on Optimization of Electrical and Electronic Equipment (OPTIM), 2021, pp. 398-40.

Noteworthy Achievement: This paper was included in the list of selection of ACEMP-OPTIM 2021 presented papers for direct consideration by IEEE Transactions on Industry Applications in view of eventual publication after further reviewing. Papers are selected on their quality (as assessed by reviewers) and their performance in their track.

D. K. Ockhuis and M. J. Kamper, 3 MW Design of Geared Slip-Synchronous Wind Turbine Systems, in 2022 IEEE Energy Conversion Congress and Exposition (ECCE), 2022.

Journal Publications

Ockhuis, D.K.; Kamper, M. Potential of Slip Synchronous Wind Turbine Systems: Grid Support and Mechanical Load Mitigation. Energies 2021, 14, 4995.

D. K. Ockhuis and M. J. Kamper, Static-FE Harmonic Analysis of PM Slip Couplers for Wind Turbine Applications, in IEEE Transactions on Industry Applications, 2022, doi: 10.1109/TIA.2022.3217748.

Dedications

To my parents,
Anita and David Ockhuis

Contents

List of Figures

List of Tables

Nomenclature

Abbreviations

2D	Two dimensional
3D	Three dimensional
AC	Alternating current
AEP	Annual energy production
AF	Axial flux
BDC	Brushless-DC
CapEx	Capital expenditure
CPU	Central processing unit
DC	Direct current
DD-PMSG	Direct drive permanent magnet synchronous generator
DFIG	Doubly-fed induction generator
DL	Double layer
DL-NO	Double layer non-overlap
ECC	Eddy-current coupler
EESG	Electrically-excited synchronous generator
FE	Finite element
FRC	Full-rated converter
GHz	Gigahertz
GW	Gigawatt
GCC	Grid connection controller
HESG	Hybrid-excited synchronous generator
IG	Induction generator
IM	Induction motor
kW	kilowatt
kWh	kilowatt hours
LCOE	Levelised cost of energy
LVRT	Low-voltage ride through
MAVr	Megavolt ampere of reactive power
MMF	Magneto-motive force
MW	Megawatt
MWh	Megawatt hours
MMFD	Modified method of feasible directions

NREL	National Renewable Energy Laboratory
NSGA-II	Non-Dominated Sorting Genetic Algorithm-II
O&M	Operational and maintenance
pu	per unit
PM	Permanent magnet
PMIG	Permanent magnet induction generator
PMSG	Permanent magnet synchronous generator
PV	Photovoltaic
PEC	Power electronic converter
RAM	Random access memory
ReCapEx	Replacement capital expenditure
RES	Renewable energy sources
RF	Radial flux
RoCoF	Rate of change of frequency
ROI	Return on investment
SLR	Series line reactance
SCC	Short-circuit capacity
SL	Single layer
SL-NO	Single layer non-overlap
S-PMC	Slip-permanent magnetic coupler
SSG	Slip synchronous generator
SS-PMG	Slip synchronous permanent magnet generator
SS-WTS	Slip synchronous wind turbine system
S-FE	Static finite element
SCIG	Squirrel cage induction generator
SC	Synchronous condenser
SG	Synchronous generator
SM	Synchronous machine
T-FE	Transient finite element
US	United States
VRT	Variable ratio transmission
VSD	Variable-speed drive
WT	Wind turbine
WTS	Wind turbine system

Variables

a_{max}	Maximum number of possible parallel circuits	
AEP	Annual energy production	[kWh]
A_f	SS-WTS attenuation factor	[dB]
A_k	Amplitude of the k^{th} harmonic component	
C_{kwh}	Cost of electricity	[$/kWh]

$CapEX$	WT drivetrain capital expenditure	[\$/kW]
d	Refers to d-axis in $dq0$-reference frame	
D_g	Generator airgap diameter	[m]
E_{df}	HESG induced back-emf voltage due to d-axis field-flux component	[V]
E_{dm}	HESG induced back-emf voltage due to d-axis PM-flux component	[V]
E_{dmf}	HESG d-axis induced back-emf voltage due to magnet- and field-flux components	[V]
E_f	PMSG induced back-emf voltage	[V]
E_{loss}	Energy losses incurred by WT drivetrain components	[kWh]
E_{qf}	HESG induced back-emf voltage due to q-axis field-flux component	[V]
E_{qm}	HESG induced back-emf voltage due to q-axis PM-flux component	[V]
E_{qmf}	HESG q-axis induced back-emf voltage due to magnet- and field-flux components	[V]
f_c	Low-pass filter cut-off frequency	[Hz]
f_{cu}	Slot copper fill factor	
f_s	Grid electrical frequency	[Hz]
g_m	SG or S-PMC mechanical airgap clearance	[mm]
G_c	S-PMC gain	
H	Grid inertia constant	[s]
i_d	Transient d-axis current	[A]
i_{dss}	Transient d-axis current under short-circuit conditions	[A]
i_o	Transient zero-sequence current	[A]
i_{on}	Transient $n^{th}phase$zero-sequence S-PMC coil current	[A]
i_q	Transient q-axis current	[A]
i_{qss}	Transient q-axis current under short-circuit conditions	[A]
I_d	Steady-state d-axis current	[A]
I_{df}	Steady-state d-axis field current component	[A]
I_{dn}	n^{th} phase steady-state S-PMC d-axis coil current	[A]
I_f	Field-winding current	[A]
I_o	Steady-state zero-sequence S-PMC coil current	[A]
I_q	Steady-state q-axis current	[A]
I_{qf}	Steady-state q-axis field current component	[A]
I_{qn}	n^{th} phase steady-state S-PMC q-axis coil current	[A]
I_s	PMSG stator current	[A]
j	Complex operator	
J_m	PMSG inertia	[kg.m^2]
J_r	HESG rotor current density	[A/mm^2]
J_s	HESG stator current density	[A/mm^2]

J_{ss}	S-PMC coil current density	[A/mm^2]
J_t	Turbine inertia	[kg.m^2]
J_t'	Reflected turbine inertia	[kg.m^2]
k	Harmonic component indicator	
k_{w1}	Fundamental winding factor	
$\mathbf{K_p}$	Park transformation	
$\mathbf{K_p}^{-1}$	Inverse park transformation	
L_d	d-axis inductance	[H]
L_{df}	d-axis inductance due to the field winding	[H]
L_{ext}	Externally added inductance	[H]
L_o	Zero-sequence inductance	[H]
L_q	q-axis inductance	[H]
L_{qf}	q-axis inductance due to the field winding	[H]
L_s	Per phase inductance	[H]
L_{st}	Generator axial length	[m]
M_{act}	Total mass of SG or S-PMC active material	[kg]
M_{dq}	dq-axis mutual inductance	[H]
M_{PM}	Mass of SG or S-PMC magnet material	[kg]
N_m	Number of PM poles	
N_{ph}	Turns per phase	
o	Refers to zero-sequence component (o-axis) in $dq0$-reference frame	
p	Total number of magnetic poles	
p_f	Number of field-winding poles	
p_m	Number of permanent magnet poles	
P	Real power component	[W]
P^*	Desired real power component	[W (pu)]
P_c	Per unit PMSG core losses	[W (pu)]
P_{core}	Hybrid-excited generator total core losses	[W]
P_{cu}	Total S-PMC coil copper losses	[W]
P_{cuf}	Hybrid-excited generator field winding copper losses	[W]
P_{cus}	Hybrid-excited generator stator winding copper losses	[W]
P_d	Per unit PMSG developed power	[pu]
P_{out}	Power output from turbine blades	[W]
P_{RE}	Input mechanical power from a renewable energy source	[pu]
P_s	Per unit PMSG supplied power	[pu]
q	Refers to the q-axis in $dq0$-reference frame	
Q	Reactive power component	[VAr]
Q^*	Desired reactive power component	[VAr (pu)]
Q_s	Per unit PMSG reactive power	[pu]
r	Ratio of wound-field to magnet pole sections	
R	Turbine-governor controller regulating constant	

$ReCapEx$	WT drivetrain capital replacement cost	[$/kW]
ROI	Return on investment	[$]
R_s	Per phase PMSG resistance	[Ω]
R_{sn}	n^{th} phase S-PMC resistance	[Ω]
R_{ext}	Externally added resistance	[Ω]
s	Laplace operator in the frequency domain	
T_a	Armature transient time constant	[s]
T_b	Steady-state S-PMC breakdown torque	[Nm]
T_{coil}	Steady-state S-PMC coil temperature	[°C]
T_{pm}	Steady-state S-PMC PM-flux torque component	[Nm]
T_m	Steady-state S-PMC cross-magnetisation torque component	[Nm]
T_{mag}	Steady-state S-PMC magnet temperature	[°C]
T_{net}	Steady-state S-PMC net developed torque	[Nm]
T_o	Steady-state S-PMC zero-sequence torque component	[Nm]
T_r	Steady-state S-PMC torque	[Nm]
T_{rl}	Steady-state S-PMC reluctance torque component	[Nm]
T_s	Steady-state SG developed torque	[Nm]
T_{ss}	SG developed torque under short-circuit conditions	[Nm]
T_t	Steady-state mechanical turbine input torque	[Nm]
T'_t	Steady-state reflected mechanical turbine input torque	[Nm]
V	Hybrid-excited generator open-circuit voltage	[pu]
V_d	Steady-state d-axis terminal voltage	[V]
V_L	Grid line voltage	[V]
V_q	Steady-state q-axis terminal voltage	[V]
V_s	Per phase grid or PMSG terminal voltage	[V]
W_f	Number of field-winding sections	
W_m	Number of magnet-pole sections	
W_s	Number of winding-pole sections	
x_{ds}	Per phase d-axis synchronous reactance	[Ω]
x'_d	Per phase transient d-axis reactance	[Ω]
x''_d	Per phase subtransient d-axis reactance	[Ω]
x_{qs}	Per phase d-axis synchronous reactance	[Ω]
x''_q	Per phase subtransient q-axis reactance	[Ω]
X_d	Per phase d-axis reactance	[Ω]
X_{dq}	Per phase dq-axis reactance	[Ω]
$X_{o(3)}$	Per phase 3^{rd} order zero-sequence reactance	[Ω]
X_q	Per phase d-axis reactance	[Ω]
X_s	Per phase PMSG reactance	[Ω]
Z_s	Per phase SG impedance	[Ω]
α	Coil current angle	[°]
γ	Electrical conductivity	[S/m]

δ	PMSG electrical load angle	[°]
δ_m	Mechanical load angle	[°]
Δ	Power angle between the q-axis and the grid voltage phasor	[°]
$\Delta\tau$	Percentage torque ripple	[%]
ΔV	Hybrid-excited generator open-circuit voltage variation	[%]
η	Efficiency	[%]
θ	Power factor angle	[°]
θ_o	Zero-sequence power factor angle	[°]
λ_d	d-axis flux linkage	[wb.t]
λ_{dm}	Permanent magnet d-axis flux linkage component	[wb.t]
λ_{dn}	n^{th} phase d-axis S-PMC flux linkage	[wb.t]
λ_o	Zero-sequence flux linkage	[wb.t]
λ_{om}	Permanent magnet zero-sequence flux linkage component	[wb.t]
λ_{on}	n^{th} phase zero-sequence S-PMC flux linkage	[wb.t]
λ_q	q-axis flux linkage	[wb.t]
λ_{qm}	Permanent magnet q-axis flux linkage component	[wb.t]
λ_{qn}	n^{th} phase d-axis S-PMC flux linkage component	[wb.t]
Λ_L	Slot magnetic permeance factor	
μ_o	Permeability of free space	[H/m]
ξ	Relative skin depth of a conductor	
ρ	Steel density	[kg.m^{-3}]
σ_m	Magnetic sheer stress	[kN/m^2]
ς	Slip	
τ	Hybrid-excited generator developed torque	[Nm]
τ_d	Harmonic leakage coefficient	
$\tau_{o(3)}$	S-PMC alternating zero-sequence (3^{rd}) torque component	[Nm]
ϕ_k	k^{th} order S-PMC signal phase shift angle	[°]
ϕ_p	Generator flux per pole	[wb]
χ	Generator aspect ratio	
ω	Angular speed	[rad/s]
ω_m	Generator rotor mechanical angular speed	[rad/s]
ω_e	S-PMC electrical angular speed	[rad/s]
ω_s	Electrical grid angular speed	[rad/s]
ω_{sl}	Angular slip speed	[rad/s]
ω_{sm}	Mechanical synchronous angular speed	[rad/s]
ω_{syn}	Synchronous angular speed	[rad/s]
ω_t	Turbine mechanical angular speed	[rad/s]
ω_t'	Reflected Turbine mechanical angular speed	[rad/s]

Chapter 1

Introduction

In the 2015 Paris Agreement [1], 192 countries pledged to substantially reduce their greenhouse gas emissions in an attempt to limit the rise in the average global temperature to below 2 degrees Celsius in this century [2]. To reach this target, countries across the world have agreed that the world's reliance on traditional fossil fuel-based electrical power generation needs to be reduced or phased out and replaced or supplemented with renewable energy sources (RESs) [3, 4].

Fig. 1.1 shows the annual additional renewable power installation capacity per year by technology. From Fig. 1.1, it is evident that solar photovoltaic (PV) and wind power are the preferred RESs as they represent the overwhelming majority of yearly added capacity. In 2020, 139 GW of solar PV capacity and 93 GW of wind power capacity was added [5], which amounted to over 85% of the total yearly added installed capacity. Moreover, [6] expects the annual yearly capacity of wind and solar to increase by 1123 GW between 2020 and 2025. If this growth is achieved, wind and solar power's installed capacity is forecast to surpass that of natural gas in 2023 and coal in 2024 [6]. In contrast to the year-on-year growth in the proliferation of solar PV and wind power systems, hydroelectric power has seen a year-on-year decline in added installed capacity from 2014 to the present day. Despite the decline in installed capacity, hydropower is still expected to be the dominant source (almost half) of global renewable electricity in 2025, followed by wind and solar PV [6]. Furthermore, the cumulative yearly installed capacity

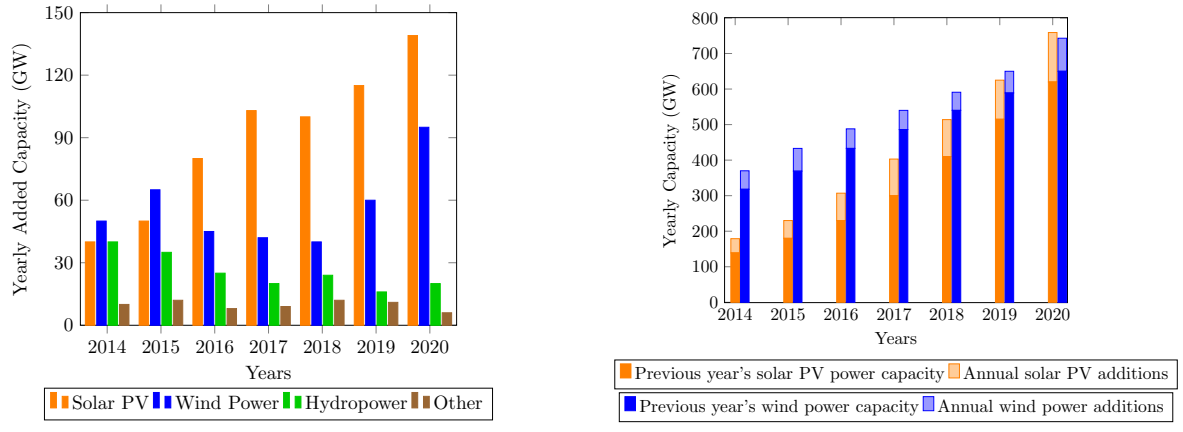

Figure 1.1: Annual renewable capacity additions by technology per year from 2014 to 2020 [5]. Other cumulatively refers to biofuels, geothermal, ocean power and concentrated-solar power.

of biofuels, ocean power, and concentrated-solar power has remained relatively constant during the time period between 2014 and 2020.

The European Union, China and the United States (US) are among many countries that have pledged to reach net-zero emissions by as early as 2050 or 2060 [3]. China continues to lead the world in yearly added installed RES capacity (140 GW in 2020) followed by the US (36 GW in 2020) [5, 6]. Moreover, in Europe and in some parts of Asia, many countries have pledged to decommission or phase out their coal-fired power plants. It is reported that Austria and Sweden closed their last coal-fired power plants in 2020 [3]. The German government has implemented the "Coal Phase-Out Act", which outlines Germany's strategy to reduce its use of coal-powered generation by 2038. Furthermore, Japan has committed to close approximately 66% of its older coal-fired power fleet by 2030, and Pakistan has announced it will no longer construct new coal-fired power plants [5].

It is clear from Fig. 1.1 and from [4, 5, 6] that the proliferation of renewable energy systems into power networks (grids) is increasing year-on-year, worldwide. In conjunction with this, many countries plan to phase out or decommission most if not all of their fossil fuel-based power plants to meet their respective net-zero emission targets. However, replacing traditional coal-fired power plants that generate electricity using grid-tied synchronous generators with converter-based renewable energy sources can adversely impact existing power grids by reducing the grid's strength, inertia and stability. So-called "weak" grids are more prone to loadshedding events or local blackouts following even a minor disturbance within the grid. Hence, care must be taken to ensure that there is sufficient grid strength within key areas within a particular grid to ensure continued and stable operations [7].

The following section describes how grid-tied synchronous machines provide grid stability to electrical power grids. Moreover, converter-tied renewable energy sources' influence on existing grid protection schemes and grid stability is also described. Furthermore, the advantages and disadvantages of existing, directly grid-connected RES technologies, such as hydroelectric power, concentrated solar and wind turbine systems, are discussed. This chapter concludes by proposing further investigation and research into using directly grid-connected synchronous-generator-based wind turbine systems as an alternative or supplementary source of grid strength and stability.

1.1 Background: Grid Strength and Inertia

The stability of a power network or power grid depends on many facets, of which grid strength and grid inertia are vitally important. Grid strength and inertia can broadly be described as the ability of a grid to resist respective changes in grid voltage and frequency following a disturbance in the power network[1]. This section compares and contrasts how traditional grid-tied synchronous generators and converter-tied RESs contribute to grid strength and inertia.

[1]The terms "network" and "grid" are used interchangeably within this Chapter.

1.1.1 Grid Strength and Inertia from Synchronous Machines

An electrical grid's strength has historically been governed by the number of nearby synchronous generators (SGs) connected to that grid, as shown in Fig. 1.2, and by the number of transmission or distribution lines connecting those SGs to the rest of the grid [7]. A commonly used measure of a power network's strength is its short-circuit capacity (SCC), which indicates the fault current availability at a given location within the grid. SGs increase the fault current levels and hence the strength of a network by supplying large amounts of short-circuit current to the grid in the event of a fault, typically between 3-5 per-unit (pu) rated current [8, 9]. Areas with high fault current levels are termed "strong", whereas areas with low fault current levels are termed "weak". The voltage in strong areas within a grid changes very little following a disturbance in the grid (changes in loading or generation). In contrast, weak areas are more susceptible to significant variations in grid voltage magnitude following a fault. Large deviations in grid voltage can cause grid protection schemes to trigger the protection schemes of nearby SGs, resulting in the SGs disconnecting from the grid resulting in local loadshedding events [7, 10, 11].

Grid inertia is defined as the ability of an electrical grid to resist changes in grid frequency following a shift in demand or supply within the network [12]. Small deviations in grid frequency occur spontaneously and usually pose no immediate threat to the grid. However, significant variations in grid frequency within a network can trigger loadshedding events [13]. Much like grid strength, SGs have historically been responsible for dictating the frequency dynamics within power networks. Moreover, the frequency dynamics of electrical grids have traditionally been linked to the sum of the kinetic energy stored in the rotors of the online synchronous machines (SMs) connected to the grid. The kinetic energy stored in the rotors of the SMs is commonly indicated by an inertia constant H. The inertia constant indicates how long the stored kinetic energy can maintain rated power output. Large SMs have an H value in the range of 3-5 seconds, and the inertia constant of an electrical grid is thus the sum of the H-values of all the grid-connected SMs.

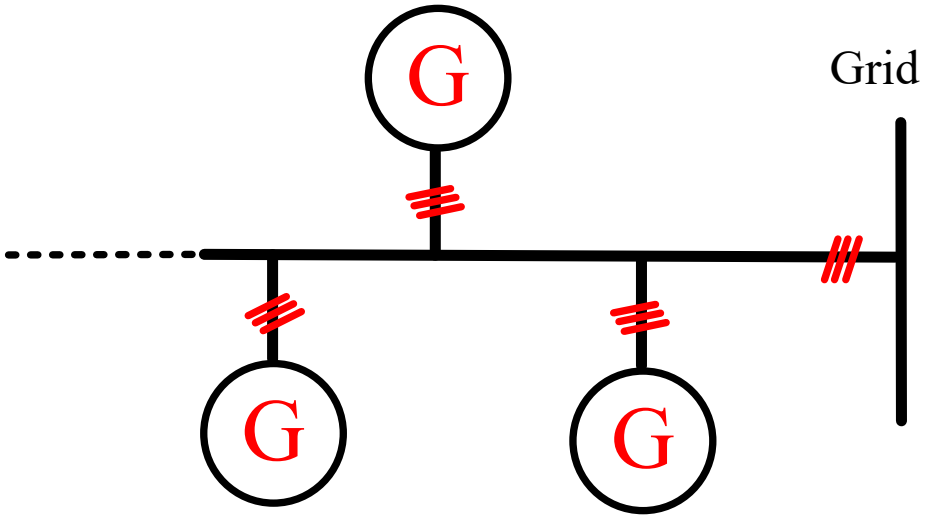

Figure 1.2: Representation of grid-tied generators connected to an electrical grid.

1.1.2 Grid Strength and Inertia from Converter-Tied Resources

Modern-day wind and solar PV farms interface with the grid using a power electronic converter (PEC), as shown in Fig. 1.3. The PEC effectively decouples the renewable energy source (RES) from the grid, which protects the RES from grid faults and disturbances while allowing complete control of the power being supplied to the grid. However, to reduce capital costs, PECs are typically rated to withstand fault currents in the range of 1.05 to 1.5 pu, significantly lower than the fault currents supplied by direct grid-tied SGs [8, 9]. The low levels of short-circuit current provided by RESs can threaten the stability of already weak power grids. This threat is increased as the ratio of converter-tied RESs to grid-tied SG-based power systems increases [8, 9].

Converter-tied RESs don't inherently provide an inertial response following a change in grid frequency because the converter effectively decouples the RES from the grid. Instead, converter-tied RESs provide inertia in the form of so-called "virtual" or "synthetic" inertia [14]. Synthetic inertia is supplied to the grid by using the stored energy in the DC-link, as shown in Fig. 1.3, or from storage elements placed on the DC-link bus. The DC-link

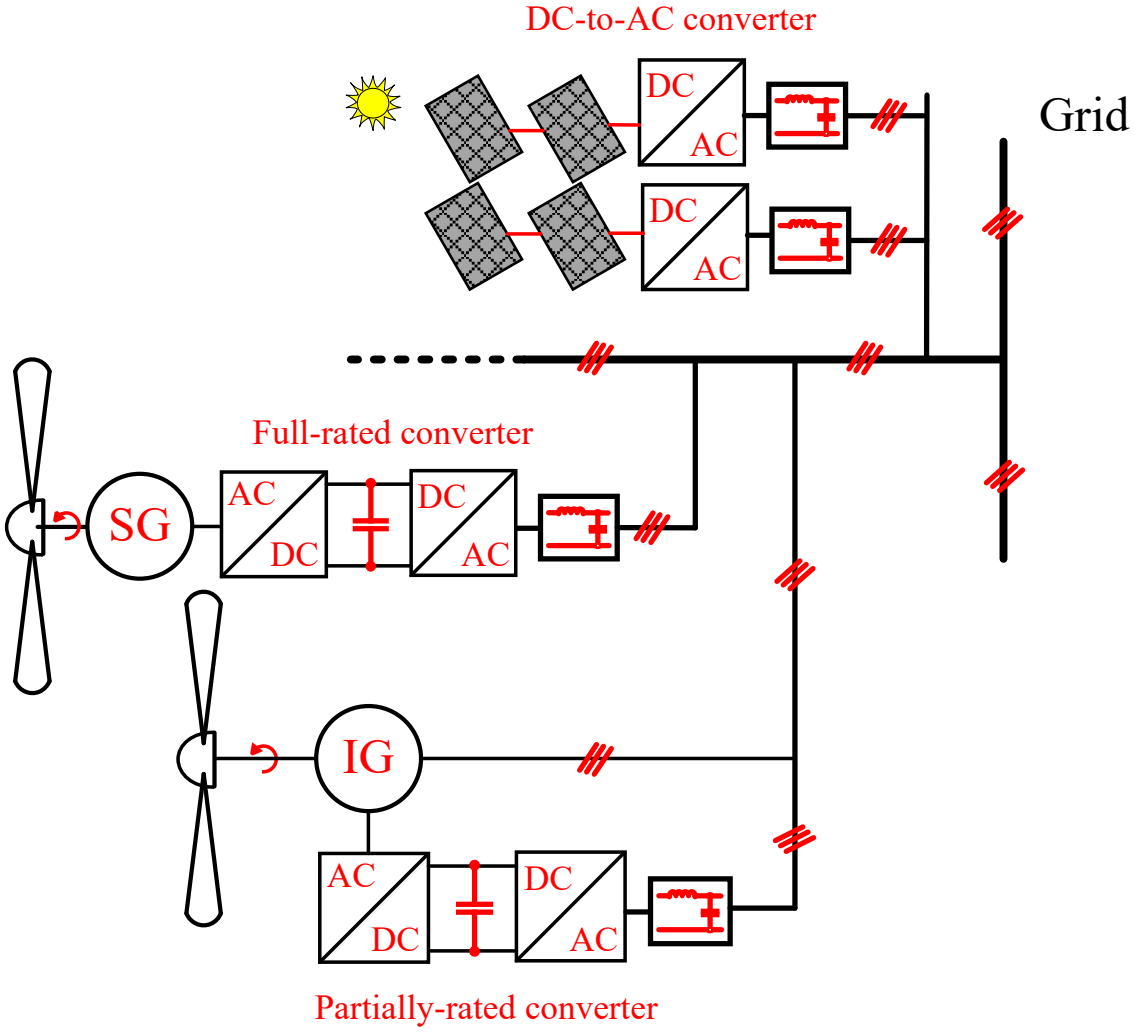

Figure 1.3: Representation of converter-tied renewable energy sources connected to an electrical grid.

typically have H-values in the order of milliseconds, which again is significantly lower than the H-values of SMs [14]. Converter-tied wind turbine systems can, however, provide an additional synthetic inertia response by varying the speed of the wind turbine generator. Doing so releases the kinetic energy of the rotor, which is converted into electrical power and injected into the grid [15, 16, 17, 18]. This form of synthetic inertia is limited by the wind turbine drivetrain's speed range and the rating of the power converter.

1.2 Converter-Tied Resources in Existing Grids

This section examines converter-tied RESs' impact on existing power grid protection schemes and grid stability. The proper functioning of an electrical grid depends on the coordination and synchronisation of various protection schemes within the grid. In the past, these protection schemes and systems were tuned to respond to fault-current signatures of grid-connected synchronous generators. The rapid rise in the penetration levels of RESs into existing grids can thus present problems for these existing protection schemes.

1.2.1 Influence of Converter-Tied Resources on Existing Grid Protection Schemes

Existing grid protection schemes are tuned and synchronised to respond to the short-circuit signatures arising from SGs within an SG-dominated power network [19]. The short-circuit response of an SG is high in amplitude, and essentially inductive [19]. In contrast, the short-circuit response of converter-tied RESs is low in amplitude, which may be insufficient and thus impact the performance of over-current distance relays in power systems [19]. Moreover, many protection schemes trigger upon detecting the presence of a significant magnitude of zero-sequence or negative-sequence current components [14, 19]. However, converter-tied RESs are typically controlled to suppress any negative-sequence and zero-sequence currents [20, 21]. The suppression of these currents can cause exiting protection schemes to malfunction, which could jeopardise the stability of the power network [22, 23].

1.2.2 Influence of Converter-Tied Resources on Power System Stability

Due to socio-political requirements and generally greater energy yields, converter-tied RESs are typically installed in remote areas of the power grid with limited transmission lines [24], away from most load centres and grid-forming synchronous generators. This poses a significant problem to these areas, primarily if converter-tied RESs provide large proportions of power generation to these areas. This is because many converter-tied RESs are equipped with so-called grid-following converters that require a stable and consistent grid voltage to maintain regular operations and to ride through grid disturbances effectively [10, 25, 26, 27]. An unstable grid voltage would increase the likelihood of converter-tied RESs activating their fault protection schemes and disconnecting from the grid. Real-world examples of converter-tied RESs erroneously disconnecting from the grid following a disturbance can be found in [14, 28, 29]. These examples depict instances where the unwarranted loss of a large proportion of power infeed from converter-tied renewable energy sources resulted in a cascade of events that ultimately led to loadshedding events [29] and local blackouts [28].

1.3 Industry Solutions to Grid Strength Shortages

In the past, grid strength shortages weren't seen as a problem as power grids were predominately comprised of grid-forming SGs. Consequently, there were no economic incentives to invest in or develop technologies to provide grid strength. However, this is likely to change in the future [30]. In the United States and the United Kingdom, market mechanisms are already emerging that are aimed at compensating and monetising the provision of grid strength and inertia [5].

1.3.1 Hydroelectric and Pumped Storage

In the United Kingdom, the first tender for "grid stability" was held, and in 2020 a contract was awarded to the 440 MW Cruachan pumped storage station to supply synchronous compensation [5, 31]. The inertia provided by the Cruachan facility is estimated to save British customers up to £128 million over six years [5]. The Indian government has promoted hydroelectric power as a source of grid strength. In 2020, India added 473 MW of hydroelectric power capacity and plans to have 70 GW of installed hydroelectric power capacity by 2030 [5, 32]. Furthermore, Australia has highlighted pumped storage as an essential component in its plans to ingrate RESs [5]. In Australia, the Dungowan (500 MW) and Big-T (400 MW) pumped storage projects are being developed with the specific aim of providing grid strength to support the integration of converter-tied RESs into existing electrical grids [5, 33].

1.3.2 Synchronous Condensers

Synchronous condensers (SCs) are large synchronous machines equipped with a conventional AC stator winding and a freely-rotating (unloaded) DC-excited salient-pole rotor. Like traditional SGs, SCs are fitted with a large rotating mass that provides inertia to the power system. Moreover, the DC-field winding equipped to the rotor allows for continuous reactive power compensation. In the past, SC technology was used to regulate the reactive power, stabilise the voltage and reduce the rate-of-change-of-frequency within power networks since the early 1900s [34]; however, the advent of power electronic converters all but ended the need for SCs.

The rapid increase in the penetration levels of converter-tied renewable energy sources into power networks has sparked a revival in the market for synchronous condenser (SC) technology both in literature [35, 36] and in industry. In industry, ABB plans to add two 67 MVAr synchronous condensers, each equipped with 40-tonne flywheels, to the power network in Liverpool [37]. In 2016, a project known as *Project Phoenix* was approved that plans on connecting a hybrid-SC to address the significant issues on Great Britain's transmission network due to the gradual retirement of its synchronous generation plants [38]. In New Zealand, a fleet of 8 SCs (installed between 1955 and 1965) has been deemed essential to ensure the continued stability and operation of New Zealand's transmission system [38]. The fleet of SCs are expected to remain in service until 2035.

1.4 Grid-Tied Wind Turbine Synchronous Generators

From the preceding section, it is evident that the industry has identified the need to reintroduce grid-tied SG-based technologies back into electrical grids. Table 1.1

Table 1.1: Advantages and Disadvantages of Synchronous Machine-Based Grid-Connected Technology

Grid Strength Technology	Advantages	Disadvantages
Concentrated Solar Power	• Thermal energy can be stored. • Scalable power ratings • No external fuel source is required	• Requires consistent direct sunlight for efficient operation. • High construction and installation costs.** • Installations are extremely location dependent**.
Nuclear Power	• Nuclear energy source is reliable.** • Reliable and mature technology.**	• Disposal of nuclear waste is costly. • High capital, legislation and regulation costs.** • High operating costs.**
Synchronous Condensers	• Grid support functionality. • No high-frequency harmonics.** • Electromechanically robust	• Expensive cooling systems may be required.** • High maintenance costs.** • Capital costs tend to be higher than alternatives. • Lack of starting torque necessitates auxiliary equipment.
Hydropower	• Safe, mature and reliable technology. • Power output can be adjusted to match demand.	• Installations can irreversibly damage existing ecosystems. • Installations are extremely location dependent. • Large initial investment costs.**

* Compared to non-renewable energy sources
** Compared to converter-tied wind and/or solar power

provides some well-known advantages and disadvantages of some of the existing grid-tied technologies that can provide grid strength and inertia. From Table 1.1, it is clear that many of the grid-tied technologies that can provide grid strength require high installation, capital, and operating costs. The high costs deter further investment in these grid-tied technologies when compared to the relatively low costs associated with converter-tied wind and solar PV technologies.

As an alternative to the grid-tied RESs of Table 1.1, Fig. 1.4 shows four examples of wind turbine systems equipped with directly grid-connected synchronous generators. These grid-tied, SG-based wind turbine systems can provide grid strength while potentially having comparable installation costs compared to converter-tied wind power systems. The following subsections briefly discuss some of the advantages and disadvantages of these grid-tied WTSs.

1.4.1 Variable Gear-Ratio Transmission Wind Turbine Systems

Fig. 1.4a shows an example of a so-called Type-5 wind turbine system that consists of a gearbox, a torque-speed converter and a synchronous generator that is directly connected to the grid. The torque-speed converter, also known as a variable gear-ratio transmission (VRT), converts the variable speed of the wind to a constant output speed that is used to rotate the shaft of a grid-tied synchronous generator. It is reported that a significant reduction in the weight of the nacelle can be achieved as there is no need for a bulky power electronic converter or a voltage transformer. Furthermore, the omission of the PEC significantly increases the overall reliability of the WTS [39]. Utility-scale examples Type-5 WTSs include: the 2.2 MW D8.2 from De Wind and the 2.0 MW W2000 from Wikov [39]. However, concerns regarding torque and speed oscillations that stem from gear shifts, increased drivetrain control complexity, and the durability of the VRT under severe loading conditions have limited the utility-scale application of the Type-5 WTS [39, 40].

1.4.2 Hydrostatic Transmission Wind Turbine Systems

Fig. 1.4b shows an example of a hydrostatic WTS. The operating principle of a hydrostatic WTS involves converting the aerodynamic torque of the wind turbine rotor into a

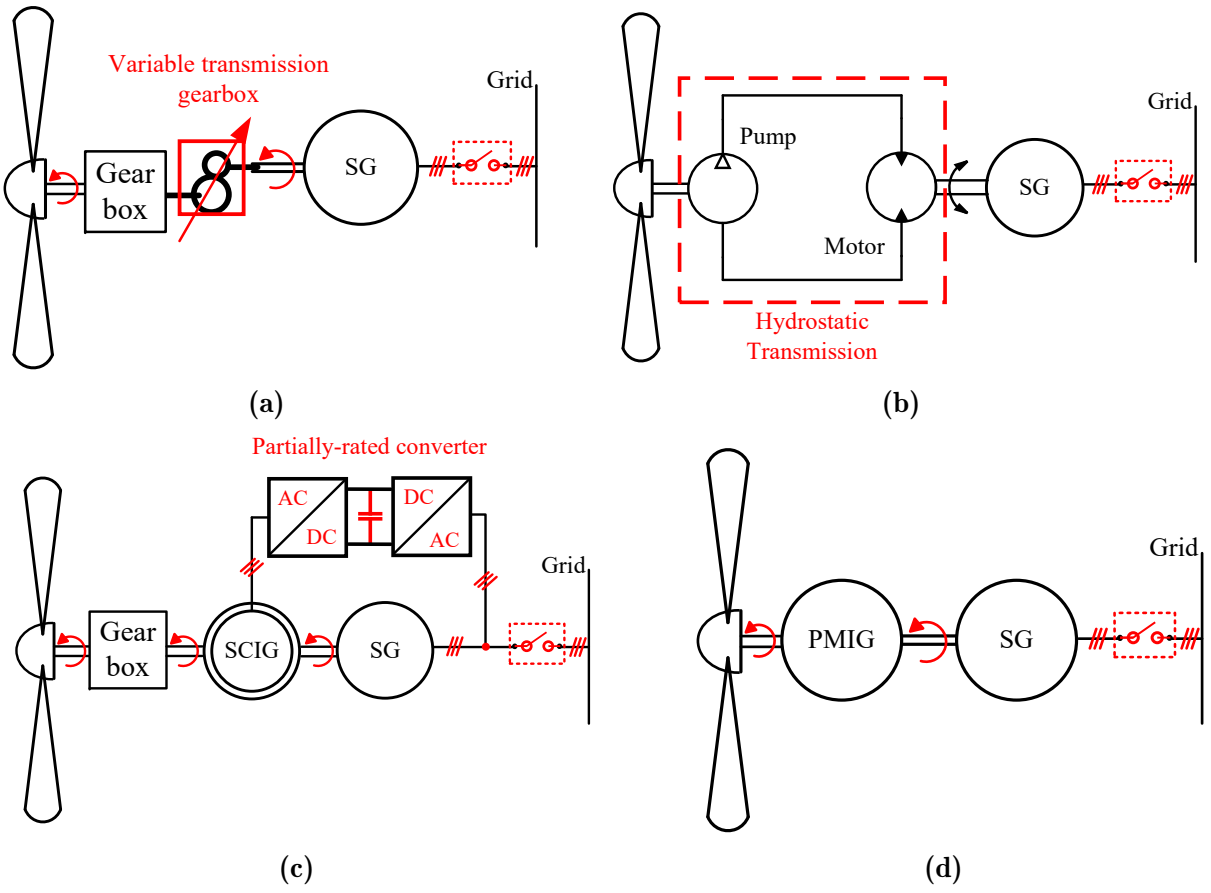

Figure 1.4: Line diagram representations of grid-connected synchronous generator-based wind turbine systems equipped with: (a) A variable gear-ratio transmission (VRT) drivetrain, (b) a hydrostatic transmission drivetrain, (c) a converter speed-controlled, squirrel cage induction generator (SCIG) drivetrain transmission, and (c) a permanent magnet induction generator (PMIG) and synchronous generator drivetrain.

pressurised fluid using a hydraulic pump motor. The hydraulic motor converts the pressurised fluid back into mechanical power that is then used to drive a grid-tied synchronous generator [41]. As with the Type-5 WTS, the hydrostatic WTS does not require a power electronic converter and can be connected to high-voltage transmission lines without a step-up transformer [41, 42]. Moreover, the semi-compressible hydraulic fluid provides a form of damping against torque pulsations induced by the wind [41, 42]. This damping reduces some of the mechanical loading imparted onto the drivetrain components, thus potentially increasing their life cycle. Additionally, it is also possible to have the pump and motor system in the nacelle and have the SG on the ground, which would reduce the top-tower mass and reduce the installation and maintenance costs [42]. Utility-scale examples of hydrostatic WTS include: the 2.3 MW and the 7 MW hydrostatic wind turbines from Mitsubishi heavy industries and Artemis, as noted in [43]. However, there are concerns regarding the drivetrain's efficiency at partial loads. The hydrostatic units' efficiency reduces considerably when operated at partial loads [42], which is a concern as WTS operate at partial loads for a considerable period of time [42].

1.4.3 Converter-Tied Magnetic Induction Transmission Wind Turbine

Fig. 1.4c shows a geared wind turbine system, proposed in [44], that uses a converter-controlled squirrel-cage induction generator (SCIG) that is on the same shaft as a directly grid-connected synchronous generator. In [44], a 1.5 MW experimental platform is built to verify the performance of the proposed drivetrain. It is reported that this WTS has superior transient overload, fault ride-through and grid frequency support capabilities than converter-tied WTSs [44]. The disadvantages this WTS stem from there being two generating units and a power electronic converter in the drivetrain, which inherently increases the complexity of the drivetrain. Moreover, the increased cost and weight, in conjunction with the reduced reliability and efficiency of this WTS, will be a concern compared to conventional converter-tied WTSs.

1.4.4 Slip Synchronous Wind Turbine Systems

In [45], a so-called slip-synchronous wind turbine system (SS-WTS) is extensively studied. The SS-WTS, shown in Fig. 1.4d, consists of a permanent magnet induction generator (PMIG) and a conventional permanent magnet synchronous generator (PMSG) that is directly connected to the grid. Unlike the grid-tied WTSs mentioned above, the SS-WTS does not require a gearbox with variable gear ratios, hydraulic pumps and motors, or partially-rated converters for direct grid-connected operation. Instead, the wind turbine is connected to a short-circuited, eddy-current rotor of a PMIG, which operates at a slip speed with respect to the PM-rotor. This slip speed provides the necessary damping and stability that allows the PMSG to be connected to the grid without a power electronic converter or damper windings, which significantly simplifying the WT drivetrain and increasing the SS-WTS's overall reliability [45]. Moreover, the capital, installation and operation and maintenance costs of the grid-tied SS-WTS are expected to be comparable to those of exiting converter-tied WTS, which is a notable economic advantage compared to the traditional grid-tied RESs given in Table 1.1. However, there are concerns regarding the added weight and costs associated with having two generating in the drivetrain. Additionally, at least one if not both of the generating units require expensive permanent magnet materials, which will inevitably increase the cost of the SS-WTS compared to a conventional converter-tied generator.

1.5 Motivation for this Study

As the world continues to decommission and phase out traditional fossil fuel-based grid-connected synchronous generators (SGs) in favour of converter-based renewable energy sources (RESs), existing electrical power grids may become more susceptible to instability during grid fault conditions. SGs have historically been responsible for providing grid stability in the form of grid strength and grid inertia. Although converter-tied RESs can provide grid inertia, they are inherently and necessarily limited in their ability to provide grid strength.

Nations and the industry have already recognised the risks associated with grid strength shortages. The industry has responded by increasing the capacity of grid-tied hydroelectric storage systems and synchronous condensers to supplement the transition from a fossil fuel-based grid toward a more renewable energy-oriented solution. However, hydroelectric systems require large amounts of capital and installation costs as their

construction is heavily dependent on a given location. Moreover, although synchronous condensers can provide grid strength, they cannot generate power.

The slip synchronous wind turbine system (SS-WTS) is a renewable energy source (RES) with a grid-tied SG. Thus, the SS-WTS has the ability to assist grid stability by being capable of providing valuable grid services in the form of grid strength, inertia and reactive power compensation. Moreover, the SS-WTS's simple and robust drivetrain make it an attractive solution from an operational-and-maintenance cost point of view.

However, despite these advantages, the literature regarding the design of the grid-tied SG unit used in SS-WTSs has neglected to consider the on-grid performance of these generating units. This has resulted in SGs that aren't grid-code compliant and whose performances are extremely susceptible to even minor grid voltage variations. Moreover, the literature has focused on SS-WTSs in the sub-MW power range. There is thus significant uncertainty regarding the design, performance and techno-economic feasibility of SS-WTSs for utility-scale, multi-MW applications.

Nevertheless, the potential economic advantages of SS-WTSs, coupled with its ability to provide grid strength, inertia and supplementary grid services, justify further research and investigation into designing and developing slip synchronous generators that are grid code compliant and that can support the grid.

1.6 Aims and Objectives of this Study

In this study, the fundamental aim is to design and to develop a grid-tied and grid compliant slip synchronous generator (SSGs) with the purpose of providing grid strength, inertia and other grid supporting services. To fulfil these aims, the objectives of this study include but are not limited to the following:

1) Reviewing the relevant literature on SS-WTSs to assess its advantages and disadvantages with respect to providing grid services.

2) Developing modelling and analysis frameworks for designing grid code compliant slip synchronous generators. This includes integrating fast but accurate analytical and finite element analysis processes to evaluate the electromagnetic performance of grid code compliant SSGs.

3) Verify (to the degree possible) the developed modelling and analysis frameworks using measured results from built 15 kW S-PMC and SG prototypes.

4) Investigating and comparing geared SS-WTSs with medium- and low-speed S-PMCs at a utility-scale power rating on a drivetrain cost-per-kW basis.

5) Develop and investigate the dynamic stability of geared SS-WTSs during grid fault conditions.

1.7 Scope

The scope of this dissertation is limited to the electromagnetic design, evaluation and comparison of electrical machines for specific use in slip-synchronous wind turbine systems. The following is excluded from this study:

- The design of mechanical and structural support mechanisms required by slip synchronous wind turbine systems for a given drivetrain topology at a specific power rating.
- The specific electrical apparatus (transformers, switchgear, etc.) required to connect the slip-synchronous wind turbine systems to power grids.
- A thorough levelised cost of energy analysis. Techno-economic comparisons are performed on a drivetrain capital cost basis, and operational and maintenance costs values are inferred from recent literature and commercial documentation.
- Any form of thermal analysis. However, care is taken within the design processes to ensure that the designed machines are restricted in their maximum air-gap shear stress, current and torque densities, respectively, such that ambient air cooling would be sufficient.
- The optimal placement of slip synchronous wind turbine systems within existing power grids.

1.8 Dissertation Layout

The rest of this dissertation consists of six Chapters, each contributing to the objectives stated above, followed by a conclusion chapter. Fig. 1.5 shows a visual representation of the dissertation outline, which includes a summary of the approach taken in each Chapter.

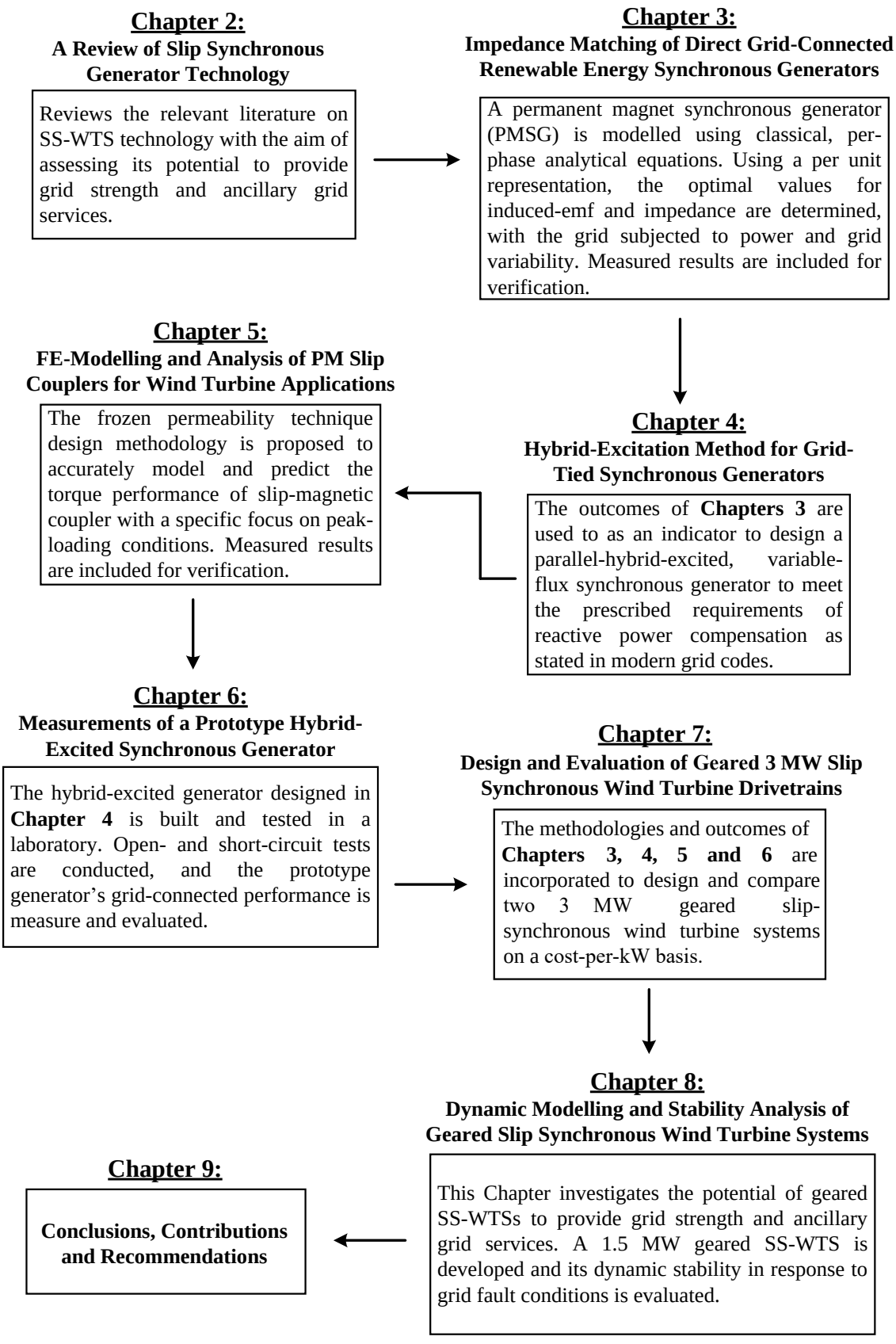

Figure 1.5: Visual representation of the Chapters within the dissertation.

Chapter 2

A Review of Slip Synchronous Generator Technology

In this Chapter, the literature regarding the design of slip synchronous generator technology is reviewed and summarised. The aim of this Chapter is to asses the advantages and disadvantages of slip synchronous generator technology as it pertains to providing services to the grid.

2.1 Slip-Synchronous Wind Turbine Systems

Fig. 2.1 shows a line diagram representation of a so-called slip synchronous wind turbine system (SS-WTS) first proposed by [46, 47] circa 2010. The SS-WTS is a fixed-speed system equipped with two magnetically separated generating units mechanically linked by a common, freely rotating permanent magnet (PM) rotor. One of the generating units consists of a permanent magnet induction generator, referred to as a slip-permanent magnet coupler (S-PMC), or "slip coupler". The other generating unit is a conventional permanent magnet synchronous generator (PMSG) whose stator windings are directly connected to the grid. The SS-WTS was initially designed as an electro-mechanically robust and reliable alternative to the fixed-speed, directly grid-connected induction generator (IG) WTS. Compared to the fixed-speed IG-WTS, the SS-WTS has an improved power factor, superior low-voltage ride-through capabilities, and no need for soft-starting devices. Moreover, as in the case of Fig. 2.1, a direct-drive SS-WTS does not require a gearbox, which inherently increases its overall reliability as there are fewer points of

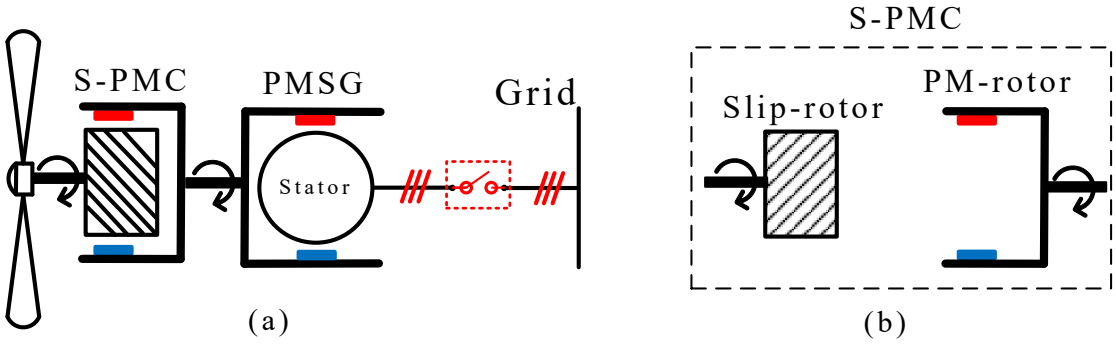

Figure 2.1: Line diagram of (a) a direct-drive slip-synchronous wind turbine drivetrain and (b) a separated view of a slip-permanent magnetic coupling (S-PMC).

potential failure within the drivetrain.

2.1.1 Slip-Synchronous Operating Principle

The S-PMC unit within an SS-drivetrain consists of two rotating sections, as illustrated in Fig. 2.1b. One of the rotating sections is a slip-rotor composed either of a conductive plate or an iron-cored, short-circuited rotor. The slip-rotor is mechanically connected to the wind turbine and operates at slip-speed with respect to a common PM-rotor. The PM-rotor of the S-PMC is mechanically linked with the PM-rotor of the SG unit. Both PM-rotors rotate at synchronous speed, as determined by the grid frequency. The rotation of the mechanically linked PM-rotors induces a voltage in the stator windings of the SG at grid frequency. Similarly, a voltage is induced in the slip-rotor at slip frequencies, typically in the range of 1-3% that of the grid frequency. Electromagnetic torque is induced in the slip-rotor due to the relative difference in speed between the slip-rotor and the PM-rotor. A counter torque is induced in the PMSG, and the subsequent electrical power is transferred to the grid.

2.1.2 Grid Connection Controller

An SS-WTS is connected to the grid using a so-called grid connection controller (GCC) [48, 49]. The GCC is a power electronic device used to arrest the acceleration and control the speed of an SS-WTS before grid connection. In [48], a thyristor-based GCC is implemented, whereas in [49], a diode rectifier and dc-dc chopper system is used. Fig. 2.2 shows a simplified line diagram representation of the SS-WTS and the GCC implemented in [49].

A typical grid connection procedure involves allowing the wind turbine to be accelerated by the wind until the drivetrain approaches synchronous speed. At this point, the GCC activates a DC-DC chopper circuit to arrest the WT-drivetrain's acceleration and regulate

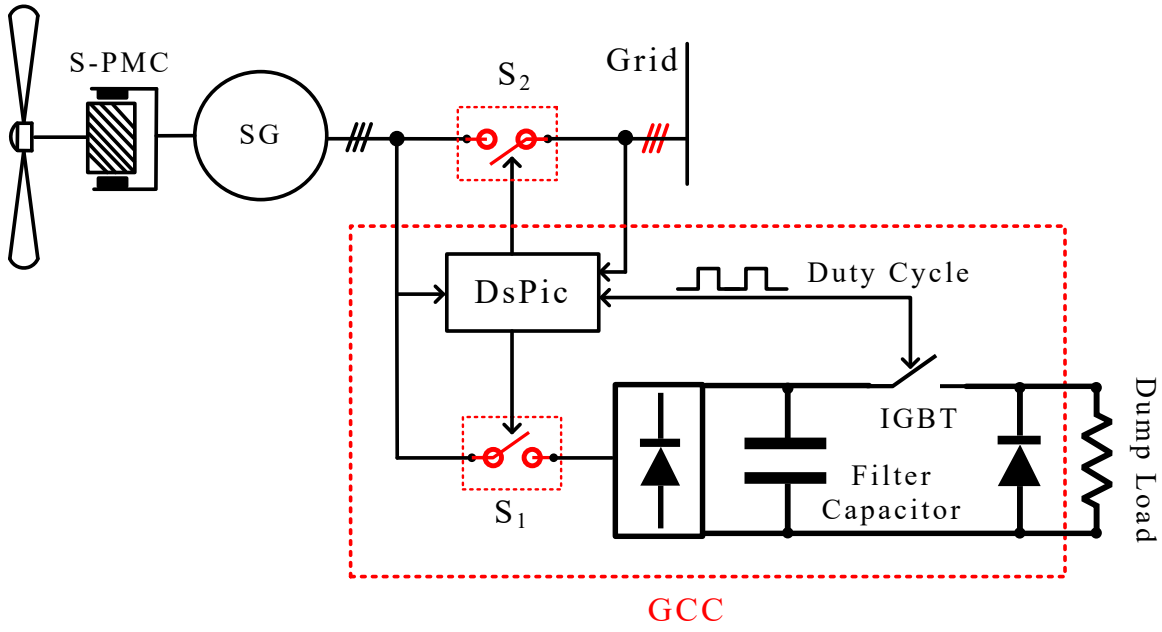

Figure 2.2: Simplified line-diagram representation of the SS-WTS and the grid-connection controller (GCC).

its speed at synchronous speed. During this time, the GCC monitors both the generator's and the grid's respective frequency, voltage magnitude and voltage phase angle. Once the relevant grid connection criteria have been met, the GCC deactivates the chopper circuit and connects the wind turbine generator to the grid. It is worth noting that the GCC is connected in parallel with the PMSG and the grid. Consequently, the GCC is only active during the grid connection and grid disconnection process. Once the generator is connected to the grid, the chopper circuit is deactivated, and power flows directly from the PMSG to the grid. However, while grid-connected, the microcontroller (DsPIC) monitors the voltages and currents at the point of coupling with the grid. It will disconnect the SS-WTS from the grid if the grid's voltage and frequency exceed the boundary limits set out in the grid code requirements. A brief summary of the grid code requirements as stated in [50] is given in Appendix A.

2.2 Fixed-Flux Synchronous Generators Considered in the Literature

Four 15 kW PMSGs with different winding topologies are designed and optimised in [51]. The modified method of feasible direction (MMFD) algorithm is used. The design objectives are set to minimise the active mass and PM material mass of the respective PMSGs, subject to a set of design specifications and constraints. Additionally, each topology is evaluated based on its respective torque quality, active mass, manufacturability and grid-connected performance. Table 2.1 provides a comparison of the four considered design-optimised PMSG topologies, which includes:

- a single-layer (SL) non-overlap winding topology,
- a double-layer (DL) non-overlap winding topology,
- a conventional three-phase overlap winding topology and,
- a novel double-rotor, toothed-toroidal winding topology.

Table 2.1: Comparison of the Considered Design-Optimised PMSGs [51].

	SL-non-overlap	DL-non-overlap	Three-phase-overlap	Toroidal
Breakdown torque (pu)	2.22	2.16	3.11	4.40
No-load torque ripple (%)	1.90	2.34	13.37	2.35
Load torque ripple (%)	4.55	3.42	31.52	4.93
Outer diameter (mm)	655	655	655	655
Active length (mm)	129.0	125.0	114.5	80.00
Line voltage, V_L (V)	400	400	400	400
Synchronous reactance, X_s (pu)	0.247	0.208	0.082	0.068
Power factor	0.964	0.974	0.996	0.997
PM mass, M_{PM} (kg)	7.62	7.00	7.82	6.49
Copper winding mass, M_{Cu} (kg)	16.69	20.16	25.22	21.04
Lamination iron mass, M_{Fe} (kg)	66.37	62.44	60.77	45.22
Total active mass, M_{Tot} (kg)	90.68	89.61	93.91	71.43
Manufacturability (relative)	Very easy	Easy	Moderate/difficult	Moderate/difficult

2.2.1 Generator Performance Comparison

From Table 2.1, it is apparent that the toroidal winding topology possesses significant advantages that include this topology requiring the least amount of active and PM material. This winding topology also has the highest torque density and specific torque values of the considered winding topologies. However, its relatively small synchronous reactance (X_s) value means that the toroidal winding topology will be extremely sensitive to grid voltage variations and grid faults; the same is true for the overlap winding topology. The toroidal and overlap winding topologies are also reported to be the most challenging to manufacture. The excessively high torque ripple of the overlap winding topology excludes it from consideration for grid-tied wind turbine applications as it exceeds the constraints outlined in [51] for no-load torque ripple ($\Delta\tau_{NL} \leq 2.5\%$) and for load torque ripple ($\Delta\tau_{FL} \leq 4\%$).

From Table 2.1, it is evident that the SL and DL non-overlap winding topologies are comparable to each other in terms of performance, active material mass and manufacturability. Nonetheless, in [52], it is reported that the voltage quality of the SL non-overlap winding is significantly worse than the DL non-overlap winding topology. It is ultimately concluded that the DL non-overlap winding topology should be the preferred winding when torque quality, active mass, manufacturability and grid-connected performance are considered as a collective [53].

2.2.2 On-Grid Performance Comparison

Grid-connected renewable power producing systems with a power rating of sub-100 kW are required to operate at unity power factor, as stated in the grid codes of South Africa [50]. In [51], it is found that all four winding topologies will require additional power factor correcting circuit elements, tap-changing transformers or partially-rated static var compensating devices to achieve unity power factor over the generators' load range. Measured results indicate that the SL and DL non-overlap winding machines act as passive, reactive power compensating devices. Both generators supply reactive power to the grid during periods of low grid voltage. Both generators also absorb reactive power during elevated grid voltage periods.

2.3 Slip-Magnetic Coupler Topologies Considered in the Literature

One of the main functions of the S-PMC unit within an SS-WTS is to dampen torque pulsations resulting from turbulent winds to improve the torque quality transferred to the generator. Moreover, the S-PMC is a second generating unit that requires its own set of permanent magnets. Hence, minimising the required active mass and the PM material in the design process is critical for the economic viability of SS-WTSs. A final and essential requirement of an S-PMC is that it always is capable of generating more torque than that developed within the drivetrain to ensure that the tight electromagnetic coupling between the turbine and the rest of the drivetrain is maintained [54].

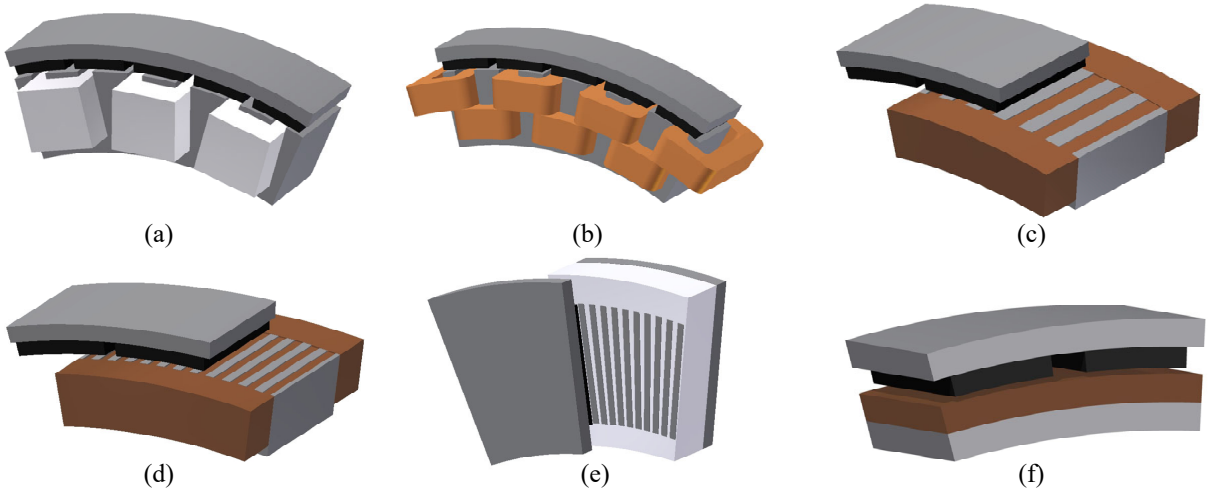

Figure 2.3: Six slip-coupler topologies designed and evaluated by [55] and [56]: (a) Single-layer non-overlap (SL-NO), (b) double-layer non-overlap (DL-NO), (c) overlap cage, (d) radial-flux brushless-DC (RF-BDC), (e) axial-flux brushless-dc (AF-BDC), and (f) eddy-current coupling [56].

Table 2.2: Overview of the Optimisation Results for the considered S-PMCs of Fig. 2.3 [55].

	SL-NO	DL-NO	Overlap cage	RF-BDC	AF-BDC	Eddy current*
Breakdown torque (pu)	2.00	2.01	2.02	2.03	2.10	8.00
Cogging torque (%)	2.54	1.65	5.56	1.64	1.33	0.00
Torque ripple (%)	3.12	1.18	10.78	0.44	2.28	0.00
Torque density (kNm/m^3)	22.52	27.71	36.2	47.48	53.47	23.97
Active mass	60.7	56.3	40.70	33.0	28.76	65.3
PM mass	5.57	5.62	3.53	3.53	3.62	24.0
Relative manufacturability	Easy	Easy	Moderate/Difficult	Very Difficult	Moderate/Easy	Very Easy

* Only results for a slip-rotor with a copper conduction disk is presented.

In [55], six direct-drive, 15 kW S-PMC topologies are evaluated based on their respective torque quality, manufacturability, and design complexity. The considered topologies are shown in Fig. 2.3. In [55], the considered S-PMC topologies are optimised using the gradient-based, modified method of feasible direction (MMFD) optimisation algorithm. The design objectives are set to minimise the active mass and the PM mass of the respective S-PMC topologies, subject to a set of design constraints. The design optimisation process considers windings made of aluminium (Al) and copper (Cu) respectively. It is concluded that aluminium short-circuited coils (or cage bars) can be used as a replacement for copper coils/bars to reduce the cost of the S-PMC without incurring a significant reduction in performance [55]. Table 2.2 provides a summary of the results of the optimised S-PMCs that are equipped with aluminium coils. From Table 2.2, the following is apparent:

The single-layer (SL) and double-layer (DL) non-overlap topologies have the highest PM mass content of the considered iron-cored S-PMCs. Moreover, both non-overlap topologies have the lowest torque density compared to the overlap cage winding and both brushless-dc (BDC) topologies. The DL-NO topology is superior to the SL-NO topology in terms of torque quality. Furthermore, the DL-NO topology is easier to manufacture compared to the rest of the iron-cored topologies.

The overlap cage winding topology has the second-lowest active mass (after the two BDC topologies) while requiring comparably small quantities of PM material. However, the optimum overlap cage winding has the highest values for cogging torque and full-load torque ripple, both of which exceeds the design constraints outlined for cogging torque ($\Delta\tau_{NL} \leq 2.5\%$) and for torque ripple ($\Delta\tau_{NL} \leq 4\%$), as outlined in [55].

The radial-flux (RF) and axial-flux (AF) brushless-DC (BDC) slip couplers have the lowest torque ripple and cogging torque values for the considered slotted iron-cored S-PMCs. Furthermore, the AF-BDC, followed by the RF-BDC, has the lowest active mass and requires comparatively little PM material than the other topologies. However, both RF- and AF-BDC slip couplers are challenging to manufacture. For the RF-BDC topology, it is reported that the small slot openings make it difficult to fix the rotor bars to the end rings, which increases the overall contact resistance and degrades the machine's torque performance. The AF-BDC topology is reported to have significantly large attraction forces, which considerably increases the manufacturing difficulty [55].

The eddy-current coupler (ECC) developed by [56] performs the best with regards to torque quality as it produces zero no-load and full-road torque ripple, something which is very important in slip-synchronous drivetrains [57]. Moreover, it is very easy to manufacture. However, the ECC requires 5 to 8 times more PM material when compared to the other S-PMCs topologies. The considerable amount of PM material required by the S-PMC would drastically increase the overall cost of the SS-WTS and ultimately increase the overall cost-of-energy production of the SS-WTS.

Additional conclusions from [55] are summarised as follows:

- In terms of mass contribution, the S-PMC increases the top-tower mass of a direct-drive SS-WTS by 12% - 20%.
- In terms of demagnetisation, it is found using FE solutions that irreversible demagnetisation only occurs if maximum short-circuit current is flowing in the short-circuited bars/coils at a magnet temperature of 100°C.
- Although no outright conclusion is made regarding which of the considered S-PMC topologies should be preferred; the DL non-overlap topology performs the best when all of the design criteria are considered a collective. However, the AF-BDC topology would be the outright preferred topology if suitable methods are implemented to mitigate the effect of the large attraction forces.

2.4 On-Grid Dynamic Stability

In [57], a block-diagram transfer function representation a direct-drive, grid-connect SS-WTS is developed to evaluate the dynamic stability of the considered SS-WTS during transient wind and grid conditions. From [57], it is concluded that:

- The SS-WTS remains stable when subjected to significant and rapid changes in applied torque, i.e., wind gusts, and during significant and sudden changes in grid voltage, such as during a low voltage ride through (LVRT) event.

- However, the SS-WTS becomes unstable if the PMSG's stator winding inductance is sufficiently small. In [57], it is shown that a PMSG equipped with an SL-NO winding can become unstable if its winding inductance were to decrease by 55%. The instability arises because reducing the stator winding inductance effectively reduces the damping ratio of the drivetrain. An example of such a decrease in winding inductance can occur if, for example, the SL-NO stator winding is replaced by a conventional overlap or toroidal winding (see Table 2.1).
- Moreover, it is found that the damping ratio of the system notably decreases if copper instead of aluminium is used for the short-circuited S-PMC coils. A low damping ratio changes the step-response of the SS-WTS from critically damped to underdamped, which increases the overshoot and settling time of the draintrain in response to step changes in input torque (changes in wind speed).
- The SS-WTS has a very low bandwidth, which means it acts as a filter toward torque pulsations caused by the wind, wind shear, and the tower shadowing effect, which would otherwise cause voltage flickering within parts of the grid.
- The relatively high-frequency torque ripple produced by the PMSG is filtered out by the wind turbine drivetrain and is thus not a problem. Nonetheless, the magnitude of the torque ripple should be minimised in the design process. The low-frequency torque ripple produced by the S-PMC can influence the grid current over the considered load range. However, the torque ripple produced by the S-PMC does not destabilise the SS-WTS but must be minimised in the design optimisation process.

2.5 Hybrid-Excited Direct Grid-Connected Generator Technology

In [59, 60, 58, 61], the design and optimisation of various direct-drive, fixed-speed, hybrid-excited synchronous generator (HESG) topologies are considered. The considered HESGs are proposed as an alternative to the conventional, fixed-flux PMSGs studied in [51]. Fig. 2.4 shows an example of a series-HESG considered in [58], where the generator consists

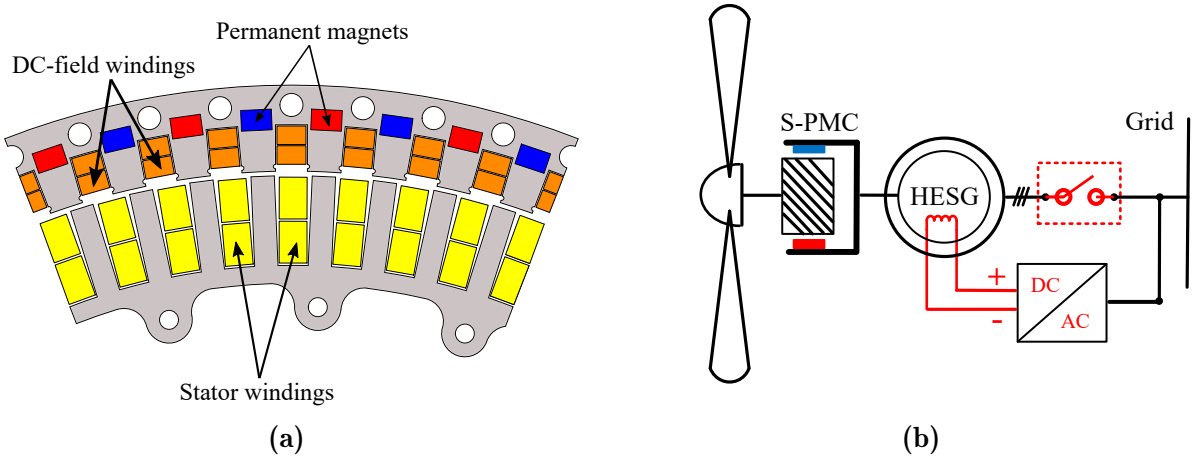

(a) (b)

Figure 2.4: Illustrations of (a) a finite element model of a series hybrid-excited synchronous generator [58] and (b) a line diagram representation of a hybrid-excited slip-synchronous wind turbine system.

of a conventional iron-cored stator that is equipped with conventional double-layer non-overlap stator windings, which are connected directly to the grid. Moreover, the rotor of the series-HESG is equipped with DC-field windings placed in a slotted rotor and embedded PMs buried deep within the rotor core. The DC-field coils allow for variable flux operation, which allows the series-HESG to vary its induced voltage by ± 10% such that it adheres to grid code requirements (see Appendix A). The series-HESG is designed such that the PMs produce the flux required (and hence voltage) for grid synchronisation and normal grid-connection operation. Thus, the rotor-field windings are inactive during normal operating conditions, and the HESG behaves as a conventional PMSG.
In [58], three series-HESGs with respective power ratings of 13 kW, 100 kW and 1000 kW are designed and optimised using the non-sorted genetic algorithm-II (NSGA-II) algorithm. The optimisation objectives are set to minimise the active mass, reduce the amount of PM material required, and minimise the rotor loss ratio of the considered generators, subject to a set of design specifications while remaining grid code complaint. Table 2.3 provides the results for the selected optimised machines.
From Table 2.3 and from [59, 60, 61, 58], the following conclusions are made:

- The series-HESG requires 30-40% less copper material to obtain a ± 10% flux variation when compared to an equivalent wound-rotor, electrically-excited synchronous generator (EESG) [60].
- For a ± 10% flux variation, the considered series-HESG has a reactive power capability of ± 0.22 pu at 1.0 pu grid voltage. The power rating required by the rotor-field supply to achieve this flux variation is 0.03 pu of the HESG's rated power [59, 60, 61].
- Additionally, if the rotor-field windings were to fail, the series-HESG can still operate as a conventional PMSG [60].
- From Table 2.3, it can be seen that significantly high current densities are required for the 100 kW and 1000 kW series-HESGs. Consequently, additional and expensive water-based or oil-based cooling systems are needed at these high-power ratings.
- Series-HESGs are typically more prone to demagnetisation when compared to conventional PMSGs, and parallel-HESGs [62]. From Table 2.3, demagnetisation would be even more of a concern when considering the high current densities required by the 100 kW and 1000 kW generators [63].
- The series-HESG's ability to control its power factor and reactive power flow has yet to be practically verified. Furthermore, simulations regarding the dynamic stability of the series-HESG have yet to be conducted.

Table 2.3: Optimisation results for a 13 kW, 100 kW and 1000 kW series-HESG [63].

Power rating	13 kW	100 kW	1000 kW
Efficiency (%)	95.2	96.6	97.0
Current density (A/mm^2)	4.12	11.2	10.4
Torque density (kNm/m^3)	31.7	43.7	79.3

2.6 Multi-MW Slip-Synchronous Generators

The available literature regarding the design and performance comparison of multi-MW SS-generators is minimal. The only publication which investigates multi-MW SS-generators is found in [64]. In [64] various SS-drivetrain derivatives are proposed, designed and analytically optimised at power ratings of 0.1 MW, 0.5 MW, 1.0 MW, 3.0 MW, and 5.0 MW, respectively. All considered drivetrain derivatives consist of an S-PMC equipped with a squirrel-cage slip-rotor (similar to Fig. 2.3c) and a PMSG with an SL-NO stator winding. The S-PMC and PMSG are collectively referred to as a slip-synchronous permanent magnet generator (SSPMG). It should be noted that the considered generators are fixed-flux PMSGs and hence aren't grid code compliant.

Fig. 2.5 shows a simplified representation of the three best performing SSPMG derivatives. Notable conclusions made by [64] include:

- The specific torque of the considered multi-MW SSPMGs (12 kg/kNm) is notably lower than the specific torque of an equivalent, conventional direct-drive PMSG (25 kg/kNm). However, the specific torque of the SSPMG is comparable to that of an EESG at sub-5MW power ratings.
- For the SSPMG drivetrain derivative shown in Fig. 2.5(a), the S-PMC unit accounts for approximately 45% of the total PM material required by the SSPMG drivetrain. For the drivetrain derivatives of Fig. 2.5(b) and (c), this ratio increases to $\approx$ 59%.
- The total losses incurred by the PMSG unit are dominated by the 50 Hz grid frequency, which are comparable to or exceeds the copper losses at high power ratings. However, the relatively low iron-core losses of the S-PMC open the possibility of replacing the laminated yokes with solid iron yokes for easier manufacturing.
- A minimum pull-out torque of 1.6 pu of the PMSG's rated torque is required by the S-PMC unit for wind turbine rotor power control options [64].

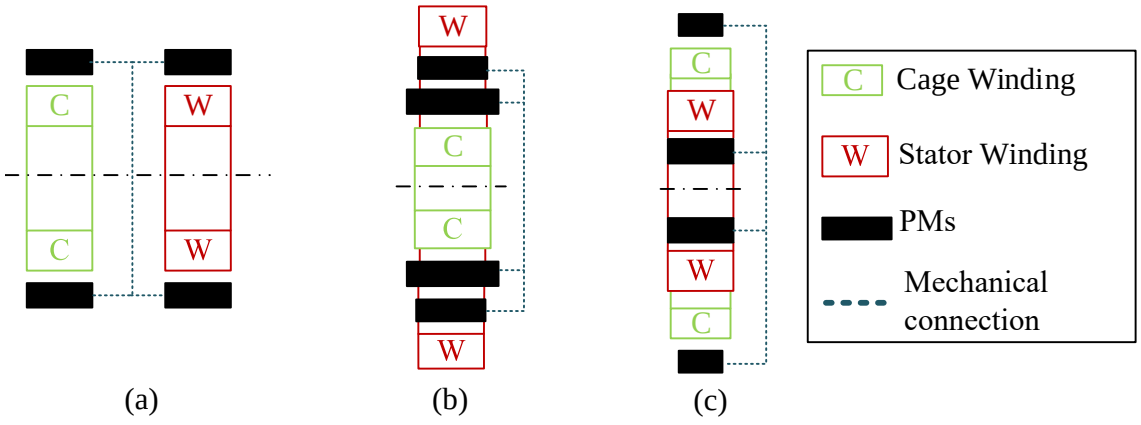

Figure 2.5: Best performing slip-synchronous drivetrain derivatives considered in [64], where the S-PMC and the SG are (a) axially separated, (b) radially separated with the SG on the outside, and (c) radially separated with the SG in the inside.

2.7 Chapter Summary and Discussion

The direct-drive slip synchronous wind turbine system (SS-WTS) was initially proposed and developed as a reliable and robust alternative to the traditional fixed-speed IG-WTS. The SS-WTS consists of two generating units, namely a slip-magnetic coupler (S-PMC) and a directly grid-connected synchronous generator. The windings of the SG are directly connected to the grid without a power converter or damper windings. Of the six generator winding topologies considered in the literature, the preferred winding topology for a grid-connected PMSG is the double-layer non-overlap (DL-NO) winding due to its torque quality and manufacturability. Regarding the S-PMC, the preferred topology is the DL-NO winding topology; however, an axial-flux brushless-DC topology could also be considered if the problem of large attraction forces is addressed.

The design of slip synchronous generators (S-PMC and SGs) presented in the literature focuses on minimising the active mass and the PM material required by the respective generating units to lower the SS-WTS's overall cost and top-tower mass. However, the design methodologies do not consider the on-grid performance of the SGs. The resulting optimum SG designs often yield machines with low synchronous reactances, making these machines extremely sensitive toward even small changes in grid voltages. To rectify this issue, additional series line reactance components are added to the terminals of the SGs.

The research literature on SS-WT technology has primarily focused on the sub-MW power range. The few SS-WT generator designs in the literature that consider higher power ratings conclude that the combined mass of the S-PMC plus the SG is a significant concern, especially for direct-drive topologies. Additional considerations regarding cost, efficiency and the need for advanced cooling methods are also reported in the literature.

Chapter 3

Impedance Matching of Direct Grid-Connected Synchronous Generators

As the ratio of converter-tied renewable energy sources (RESs) to synchronous generators (SGs) increases, future power grids may experience grid strength shortages due to the lack of short-circuit capacity in the grid. In Chapter 1, it is suggested that wind turbines equipped with directly grid-connected synchronous generators be used to provide grid strength to electrical grids with significant quantities of converter-tied RESs. Of the wind turbine systems with grid-tied SGs, it is argued that the slip synchronous wind turbine system (SS-WTS) is ideally suited due to its robust and simplistic drivetrain.

However, from Chapter 2, the current design methodologies used to design slip synchronous generators neglect to consider the on-grid performance of these grid-tied generators. The resulting generators often have low synchronous reactance (X_s) values, which means their performance is very sensitive to even minor changes in grid voltages. To reduce the generator's sensitivity to grid voltage variations, additional series line reactances (SLR) are added to the generator's terminals to increase the generator's synchronous reactance. In this Chapter, we use impedance matching to find the optimal value for the generator's synchronous reactance that will yield the desired generator response and performance for changes in grid-voltage magnitude. It should be noted that the work presented in this Chapter has been presented at a conference by Ockhuis, Kamper and Loubser (2020) [65].

3.1 Synchronous Generator Modelling

The analysis of an SG connected directly to the grid is done on a per-unit basis using the equivalent circuit of Fig. 3.1a and the phasor diagram of Fig. 3.1b. The input mechanical power, P_{RE}, is that of the renewable energy source. As the speed is fixed, we subtract in the analysis a fixed amount of core losses, P_c, from the input power to obtain the developed power, P_d, as

$$P_d = P_{RE} - P_c = E_f I_s \cos(\delta - \theta), \tag{3.1}$$

where E_f is the induced per unit induced-emf due to the permanent magnet (PM) field flux, I_s is the per-unit stator current, and δ and θ are the load and power angles, respectively, as explained in Fig. 3.1b. Subtracting the conduction losses from the developed power, we obtain the output power, P_s, of the generator supplied to the grid as

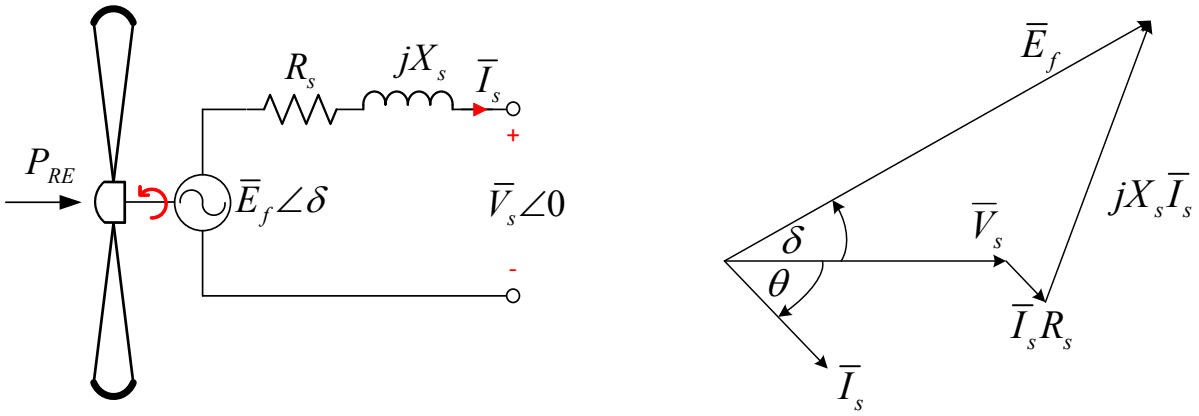

Figure 3.1: Per phase representation of (a) a synchronous generator equivalent circuit and (b) the subsequent phasor diagram.

$$P_s = P_d - I_s^2 R_s = V_s I_s \cos(\theta), \tag{3.2}$$

where V_s is the voltage of the ideal micro-grid voltage source, as shown in Fig. 3.1a. The efficiency of the system is hence determined by

$$\eta = \frac{P_s}{P_s + I_s^2 R_s + P_c} \times 100\%. \tag{3.3}$$

Between the grid and the induced-emf voltages, we have the synchronous generator's impedance as

$$Z_s = R_s + jX_s = Z_s \angle \theta_s. \tag{3.4}$$

The power and reactive power supplied to the grid, P_s and Q_s, can also be expressed as derived in all classical texts by

$$P_s = \frac{V_s E_f}{Z_s} \cos(\theta_s - \delta_s) - \frac{V_s^2}{Z_s} \cos(\theta_s), \text{ per unit watts} \tag{3.5}$$

and

$$Q_s = \frac{V_s E_f}{Z_s} \sin(\theta_s - \delta_s) - \frac{V_s^2}{Z_s} \sin(\theta_s), \text{ per unit VARs} \tag{3.6}$$

3.2 Synchronous Generator Parameter Analysis

In this section, we investigate the effect of the generator's internal impedance, more specifically the synchronous reactance, X_s, and the induced-emf voltage, E_f, on the general performance of the generator under variable input power and grid voltage conditions. To do this, we keep the per unit values of the stator resistance and core losses constant at typical synchronous machine values, namely

$$\mathbf{C} = \begin{bmatrix} R_s \\ P_c \end{bmatrix} = \begin{bmatrix} 0.05 \\ 0.02 \end{bmatrix} \text{ pu}. \tag{3.7}$$

We then determine the generator's performance for a synchronous reactance X_s and an induced-emf voltage E_f described as

$$\mathbf{G} = \begin{bmatrix} X_s \\ E_f \end{bmatrix} = \begin{bmatrix} 0.1 < X_s < 1.0 \\ 0.95 < E_f < 1.05 \end{bmatrix} \text{pu.} \tag{3.8}$$

The parameters that are then varied for a fixed $\mathbf{C}$ and given $\mathbf{G}$ are the grid supply power and voltage as

$$\mathbf{X} = \begin{bmatrix} P_s \\ V_s \end{bmatrix} = \begin{bmatrix} P_s = 0.2 \text{ and } P_s = 1.0 \\ 0.9 < V_s < 1.1 \end{bmatrix} \text{pu.} \tag{3.9}$$

With $\mathbf{C}$, $\mathbf{G}$ and $\mathbf{X}$ of (3.7) - (3.9) known we can determine from (3.5) the load angle δ as

$$\delta = \theta_s - \cos^{-1}\left[\frac{P_s Z_s}{V_s E_f} + \frac{V_s}{E_f}\cos(\theta_s)\right]. \tag{3.10}$$

With δ known we can determine Q_s from (3.6) and the stator current I_s from

$$I_s \angle\theta = \frac{E_f \angle\delta - V_s \angle 0}{Z_s \angle\theta_s}. \tag{3.11}$$

With all this known, we can calculate the generator's efficiency from (3.3). We are particularly interested in how the generator's performance parameters with respect to efficiency η, reactive power Q_s, and the stator current I_s vary versus power loading and grid voltage. Hence we can write an output vector containing these parameters as

$$\mathbf{Y} = f(\mathbf{X}) = \begin{bmatrix} \eta \\ Q_s \\ I_s \end{bmatrix}. \tag{3.12}$$

3.3 Calculated Results

The respective results of $\mathbf{Y}$ of (3.12) are shown in Figs. 3.2a to 3.3c for two values of E_f, namely $E_f = 1.0$ pu and $E_f = 1.05$ pu respectively. From the efficiency results of Figs. 3.2a and 3.3a, it is evident that the efficiency at low power conditions drops sharply for small X_s values for both lowered and elevated grid voltage conditions. However, good overall results are obtained with $X_s = 0.5$ pu for both values of $E_f = 1.0$ pu and $E_f = 1.05$ pu.

Regarding the reactive power of Figs. 3.2b and 3.3b, the best overall result is obtained with $E_f = 1.05$ pu and with X_s being either $X_s = 0.2$ pu or $X_s = 0.5$ pu. The case where $E_f = 1.05$ pu and $X_s = 0.2$ pu is interesting because although the efficiency drops sharply at low voltage and low power, as shown in Fig. 3.3a, the reactive power response of the generator in Fig. 3.3b is ideally suited to compensate for low or high grid voltage conditions, which is precisely what is needed for grid voltage compensation. Finally, regarding the generator current, the best results are for the case where $X_s = 0.5$ pu, as is shown in Figs. 3.2c and 3.3c, where the generator current changes the least as the grid voltage changes.

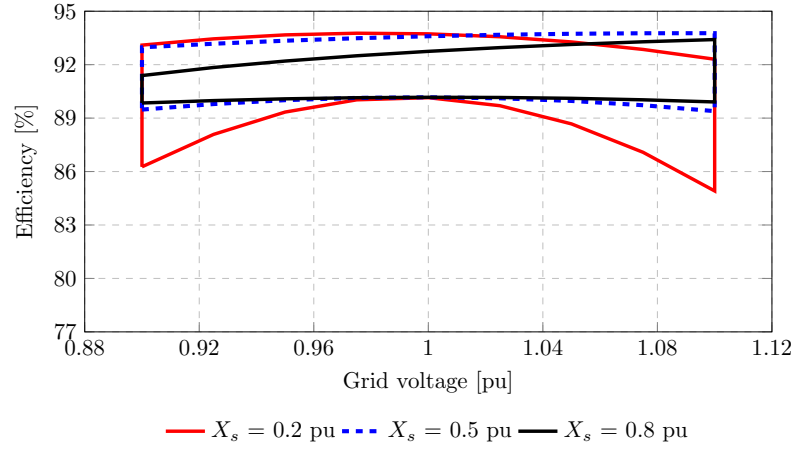

(a)

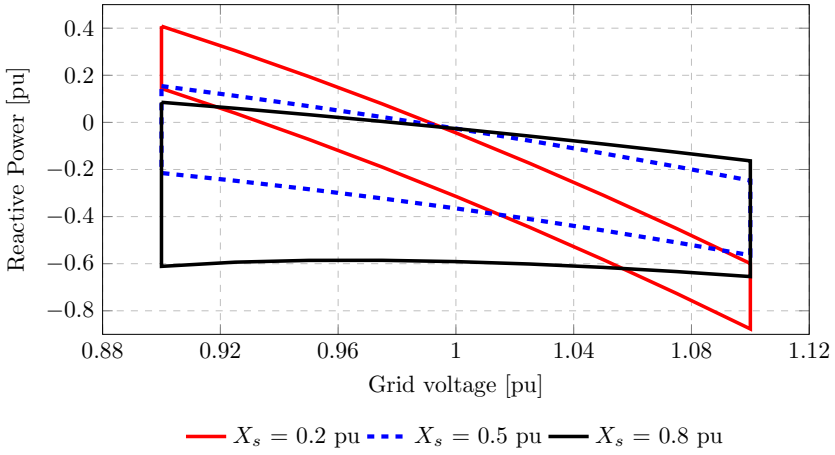

(b)

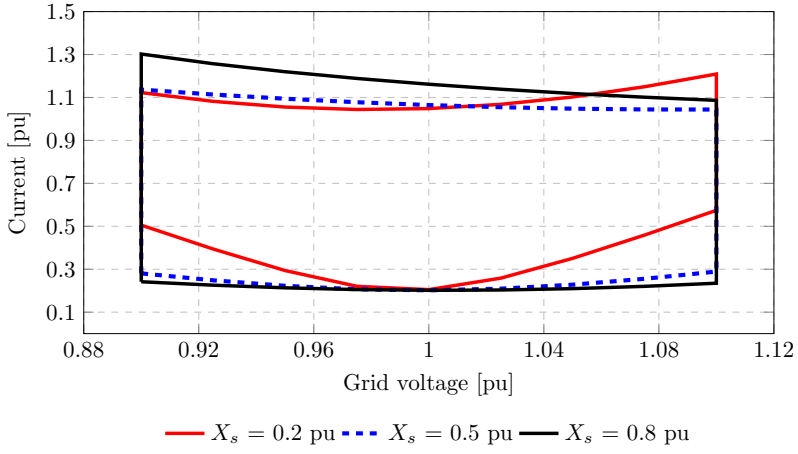

(c)

Figure 3.2: Calculated generator results for: (a) efficiency, (b) reactive power and (c) current versus supply power and grid voltage with generator reactance X_s a parameter, and with E_f = 1.0 pu. Note the upper curves are for P_s = 1.0 pu and the bottom curves for P_s = 0.2 pu for (a) and (c), whereas for (b), the upper curve is for P_s = 0.2 pu and the bottom curve is for P_s = 1.0 pu.

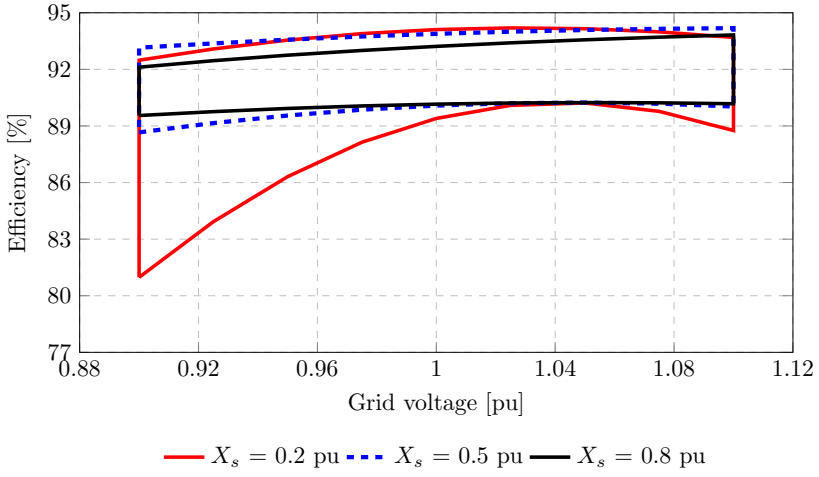

(a)

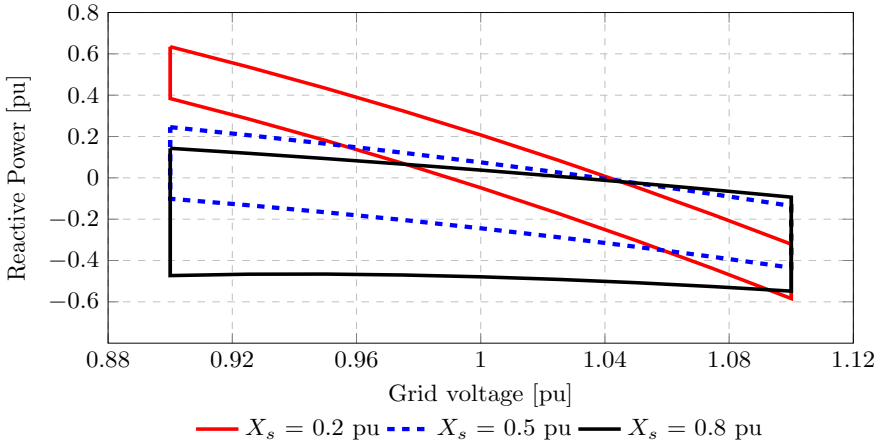

(b)

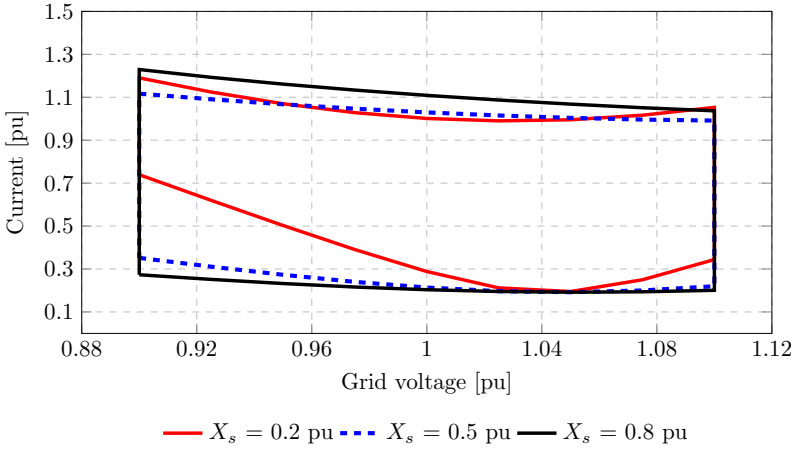

(c)

Figure 3.3: Calculated generator results for: (a) efficiency, (b) reactive power and (c) current versus supply power and grid voltage with generator reactance X_s a parameter, and with E_f = 1.05 pu. Note the upper curves are for P_s = 1.0 pu and the bottom curves for P_s = 0.2 pu for (a) and (c), whereas for (b), the upper curve is for P_s = 0.2 pu and the bottom curve is for P_s = 1.0 pu.

3.4 Synchronous Generator Measured Results

Fig. 3.4 shows the laboratory testbench layout used to measure the performance of a directly grid-connected slip synchronous permanent magnet generator (SS-PMG) under varying grid voltage and changing input power conditions. Fig. 3.5 shows a simplified line diagram representation of the test bench of Fig. 3.4. The SS-PMG is coupled to and driven by an induction motor (IM) that is subjected to speed control using an Allen-Bradly *Powerflex 755* variable-speed drive (VSD). The IM-VSD is used to rotate the SS-PMG at synchronous speed, and a set of synchronisation lights and an oscilloscope are used to connect the generator to the grid once the generator's respective frequency, voltage-magnitude and voltage-phase angle are aligned with that of the grid. Once grid-connected, the voltage at the generator's terminals is adjusted using a variac.

3.4.1 Synchronous Generator Open- and Short-Circuit Tests

Table 3.1 gives some of the specifications of the synchronous generator unit of the SS-PMG of Fig. 3.4. A respective open- and short-circuit test is conducted to determine the synchronous reactance X_s of the SG unit in the SS-PMG. Fig. 3.6 shows the results of an open-circuit test. From Fig. 3.7, the PMSG's induced-emf voltage, E_f, is approximately

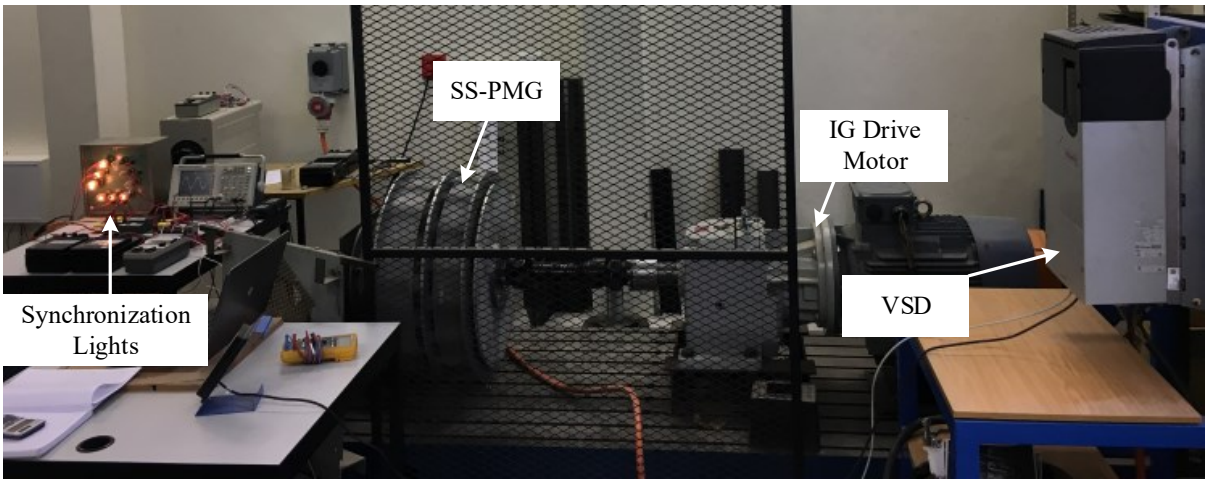

Figure 3.4: Laboratory testbench layout used to obtain measured results of a directly direct-connected 15 kW SS-PMG.

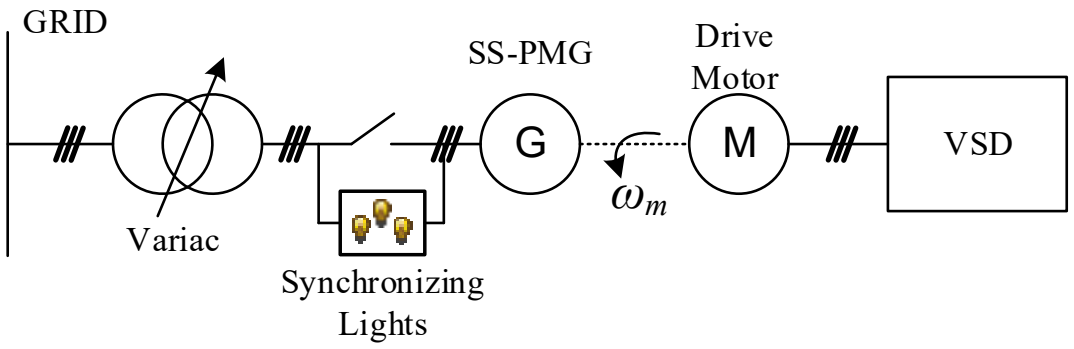

Figure 3.5: Simplified line diagram of the testbench of the grid connected SS-PMG of Fig. 3.4.

Table 3.1: Specifications and Parameters of the Synchronous Generator unit of Fig. 3.4.

Parameter	**Value**	**Parameter**	**Value**
Line voltage	400 V	Rated open-circuit voltage	1.03 pu
Rated current	21.7 A	Rated power	15 kW
Grid frequency	50 Hz	Synchronous speed	150 rpm
Synchronous reactance $X_{s(pu)}$	0.17	Number of poles	40
Per phase winding resistance $R_{s(pu)}$	0.03	Rated torque	1000 Nm

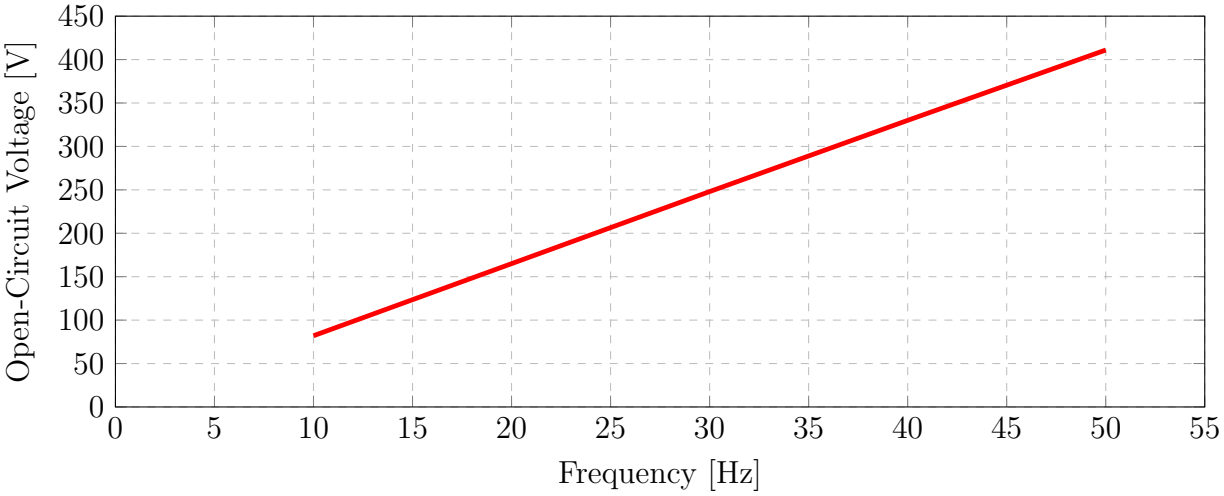

Figure 3.6: Measured results of an open-circuit test conducted on the PMSG of Fig. 3.4.

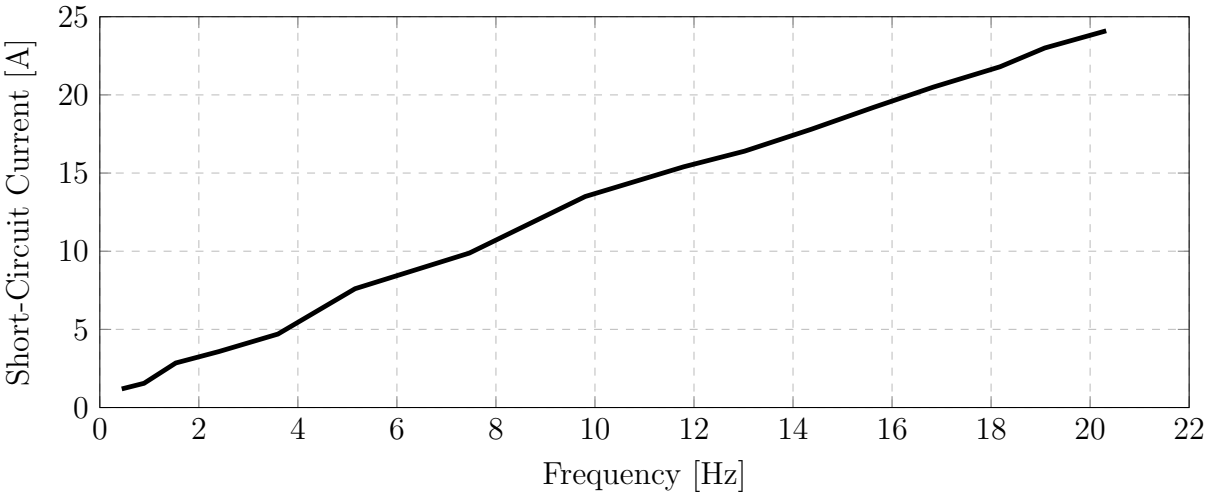

Figure 3.7: Measured results of a short-circuit test conducted on the PMSG of Fig. 3.4 where an external resistance of 3.5 Ω/phase is added to the generator's terminals.

411 V or 1.03 pu at synchronous speed (50 Hz). Fig. 3.7 shows the results of a short-circuit test. In the short-circuit test, an external resistance of $R_{ext} = 3.5$ Ω/phase was added to the generator's terminals to increase the speed at which rated current occurs. From the open- and short-circuit tests, the generator's synchronous reactance is determined to be approximately $X_s = 0.17$ pu.

3.4.2 Grid Current versus Grid Voltage

Fig. 3.8 shows measured results for generator current for the grid-connected PMSG of Fig. 3.4 where the grid voltage is varied between 0.88 pu and 1.12 pu. The generator current is measured for an input power of 0.2 pu and 1.0 pu, respectively. Additionally, Fig. 3.9 shows the results of an experiment where an external inductance of L_{ext} = 16 mH is added between the generator's terminals and the grid. Adding L_{ext} effectively increases the reactance between the generator and the grid to X_s = 0.64 per unit. From Figs. 3.8 and 3.9, a good correlation between the individual analytical results of Figs. 3.2c and 3.3c is achieved, barring a small difference between the analytical and measured results for high-power conditions.

3.4.3 Reactive Power versus Grid Voltage

Figs. 3.10 and 3.11 show the results of two grid-connected tests where the grid voltage is varied, and the resulting reactive power is measured for an input power of 0.2 per unit and 1.0 per unit, respectively. In Fig. 3.11, the same external reactance of L_{ext} = 16 mH is added between the generator's terminals and the grid. Once again, a good agreement between the analytical results of Figs. 3.2b and 3.3b and the measured results is achieved. From Figs. 3.10, it can be seen that with X_s = 0.17 pu, the reactive power response of the PMSG remains within a relatively narrow range of values between Q = 0.15 pu and Q = -0.05 pu for an input power range of P = 0.2 pu and P = 1.0 pu respectively. In contrast, with the added external reactance, the range of reactive power values widens to Q = 0.01 pu and Q = -0.4 pu for an input power range of P = 0.2 pu and P = 1.0 pu respectively. From Figs. 3.10 and 3.11, it is evident that for a given input power, the slope of the generator's reactive power response becomes less steep with an increase in synchronous reactance X_s, which effectively reduces the sensitivity of the PSMG towards

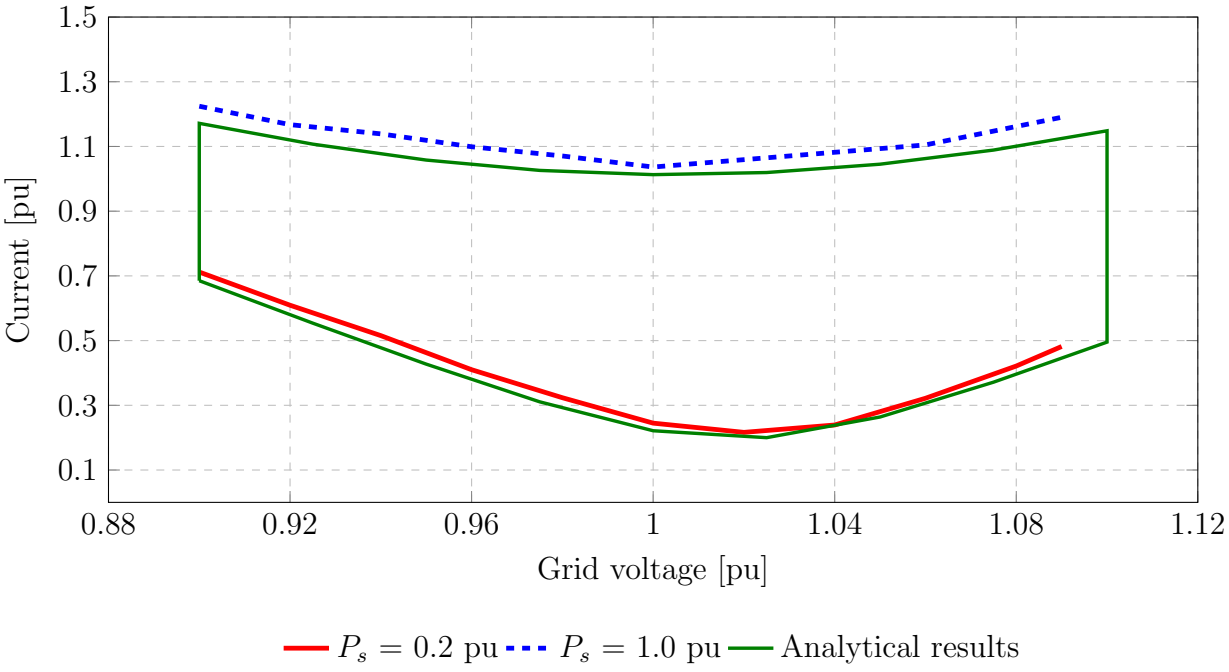

Figure 3.8: Measured generator current versus grid voltage with input power as a parameter for a PMSG where, E_f = 1.03 pu and X_s = 0.17 pu. The analytical results for a PMSG with E_f = 1.03 pu and X_s = 0.17 pu are included for comparison.

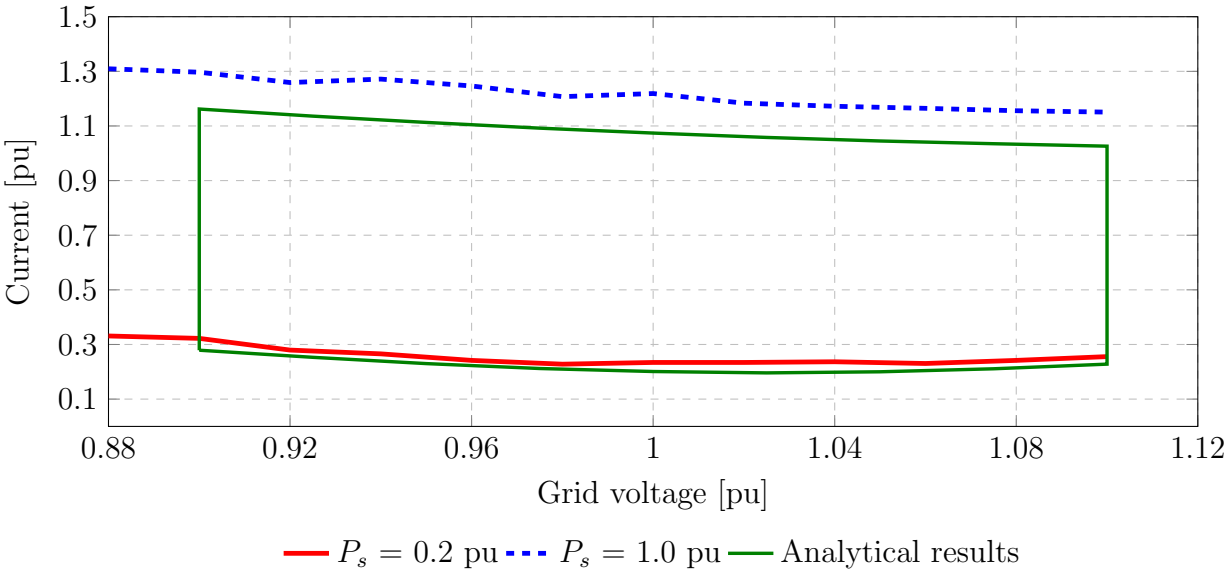

Figure 3.9: Measured grid current versus grid voltage with input power as a parameter for a PMSG where, $E_f = 1.03$ pu and $X_s = 0.64$ pu. The analytical results for a SG with $E_f = 1.03$ pu and $X_s = 0.64$ pu are included for comparison.

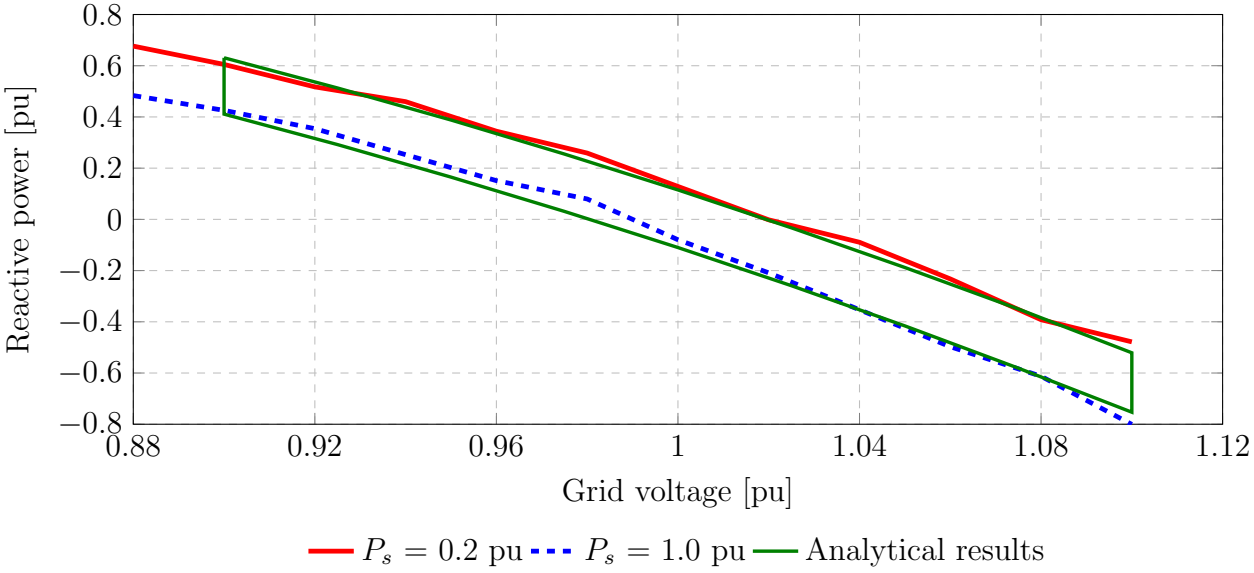

Figure 3.10: Measured reactive power versus grid voltage with input power as a parameter for a PMSG where, $E_f = 1.03$ pu and $X_s = 0.17$ pu. The analytical results for a SG with $E_f = 1.03$ pu and $X_s = 0.17$ pu are included for comparison.

changes in grid voltage.

3.4.4 Discussion

From Figs. 3.10 and 3.11, it can be seen that the directly grid-connected PMSG supplies capacitive reactive power to the grid during periods of low grid voltage and absorbs inductive reactive power during periods of high grid voltage. Although the grid voltage regulation provided by the PMSG is uncontrolled, it stands to reason that a directly grid-connected synchronous generator-based wind turbine system can aid in assisting the grid voltage recovery time in the event of a change in grid voltage following

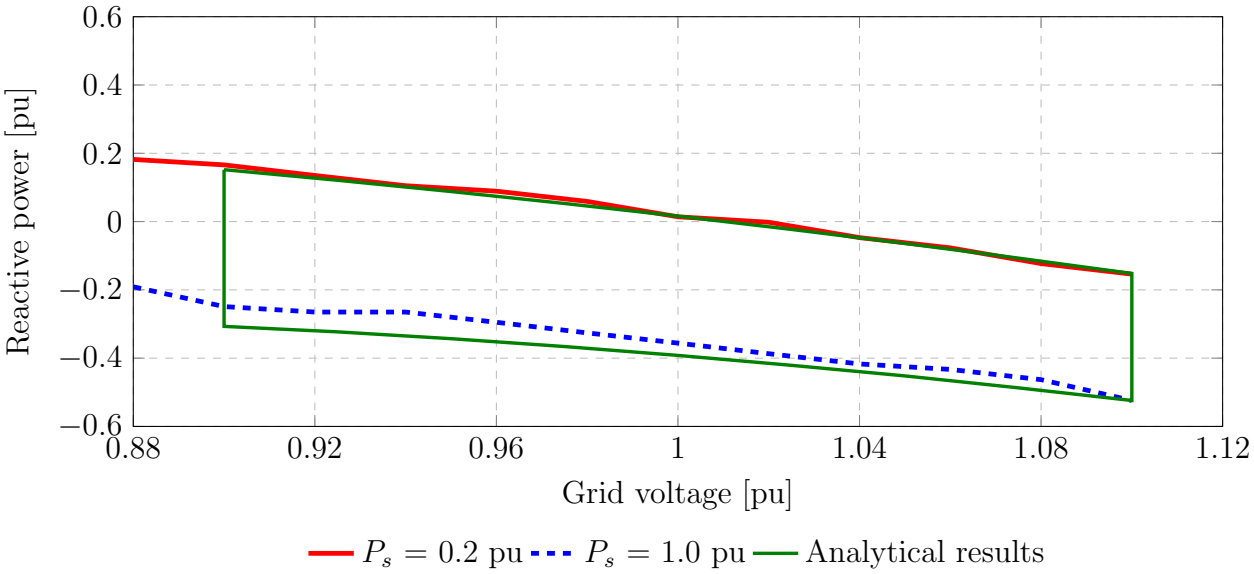

Figure 3.11: Measured reactive power versus grid voltage with input power as a parameter for a PMSG where, $E_f = 1.03$ pu and $X_s = 0.64$ pu. The analytical results for a SG with $E_f = 1.03$ pu and $X_s = 0.64$ pu are included for comparison.

the addition or the loss of a sizeable reactive power source or sink within the grid. Moreover, the classical PMSG can be replaced with a conventional wound-rotor SG or a hybrid-excited PMSG as in [63] to provide more control over its reactive power response.

Nevertheless, there remains a clear trade-off between on-grid performance and short-circuit response. That is to say, designing for a high synchronous reactance yields an SG that is less sensitive to grid voltage variation. However, it would reduce the generators short-circuit current response ($I_{sc} = \frac{E_f}{X_s}$).

3.5 Chapter Summary

This chapter investigates the optimum synchronous reactance (X_s) value for a grid-connected synchronous generator. It is shown that the best overall result in terms of efficiency, reactive power and current is obtained with a synchronous reactance of $X_s = 0.5$ pu and an induced-EMF of $E_f = 1.05$ pu. One may also consider the case with $X_s = 0.2$ pu and $E_f = 1.05$ pu for good reactive power response, which would also yield a higher fault-current response, but at the expense of low generator efficiency at low power and low voltage conditions.

Practical testing of a direct-grid connected SS-PMG is conducted. A good correlation between the measured and analytical results was achieved for low-power conditions; however, a slight error between the measured and practical was observed for high-power conditions. The study's outcome allows electrical machine design engineers to design grid-connected synchronous generators with a per-unit reactance and per unit induced-emf voltage to provide the desired performance at a particular location within a grid. Note that the results exclude the impedance of the transformers and the transmission lines at the point of connection with the grid, which will impact the generator's short-circuit response.

Chapter 4

Hybrid Excitation Method for Grid-Tied Synchronous Generators

In Chapter 3, a design methodology by which the optimum per unit (pu) values for induced-emf and synchronous reactance for fixed-flux grid-tied, conventional permanent magnet synchronous generator (PMSG) is outlined. This Chapter builds on the results of Chapter 3 by proposing a design methodology for grid-tied hybrid-excited synchronous machines. The hybrid-excitation method allows for variable-flux operation and controlled reactive power compensation capability. Variable-flux adjustment capability is essential in directly grid-connected applications where the generator must operate in accordance with a set of grid code requirements (see Appendix A). Methods to achieve variable-flux operation in synchronous machines can be divided into two groups, namely series hybrid-excitation, as in [58], where the PMs and the field-winding work magnetically in series, or parallel hybrid-excitation, where the PMs and the field-winding work magnetically in parallel.

An overview of various hybrid-excitation methodologies is given in [66]. These methodologies can be categorised into three groups where, (i) the hybrid-excitation sources are placed on the rotor of the synchronous machine, (ii) the hybrid-excitation sources are located on the stator of the synchronous machine and (iii) where hybrid-excitation is divided between the stator and the rotor. In this Chapter, the focus is on the first group of hybrid-excitation methodologies where the excitation sources are placed on the rotor of a synchronous generator. Hybrid-rotor excitation allows for a relatively standard and easily manufacturable machine capable of generating good quality sinusoidal voltages. It should be noted that the strategies and parts of this Chapter have been presented at a conference by Ockhuis, Kamper and Loubser (2020) [67].

4.1 Series and Parallel Hybrid-Rotor Excitation

Of the hybrid-rotor excitation synchronous generators considered in the literature, series hybrid-excitation is most commonly used [58, 68, 69, 70, 71]. One of the disadvantages of series hybrid-excitation is the relatively large field winding MMF needed due to the relatively large effective air gap. Consequently, these designs require a relatively thin magnet thickness, which in turn results in low open-circuit, zero-field-current generated voltage [71].

A classic parallel hybrid-rotor excitation method, referred to by many, is found in [72]

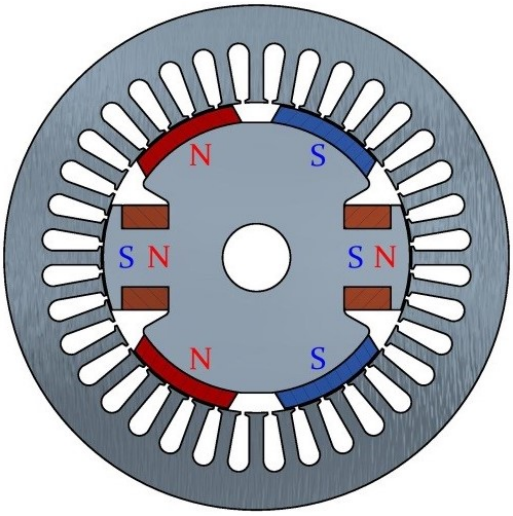

Figure 4.1: Six-pole hybrid-rotor excited synchronous machine [72].

and is shown in Fig. 4.1. The generator in Fig. 4.1 has 36 slots and six poles, of which four poles are magnet-poles, and two are field-winding poles. Alternative parallel hybrid-rotor excitation methods can be found in [71] and [73], where the magnets are tangentially magnetised and placed in the slot openings of the field winding. However, these methods are for PM-assisted synchronous generators, where the magnets are used to enhance the field-flux of an ordinary wound-rotor excited generator (thus not a PM generator). A final parallel hybrid-excitation method is found in [74], where the PM excitation and field-winding excitation are done separately using two separate rotors mounted in tandem on the rotor shaft. This method is probably the best parallel hybrid-excitation method, however to the expense that part of the stator's axial length is not actively used. Moreover, the rotor construction is also somewhat complex, especially in the case of a generator with an externally rotating rotor.

4.2 Proposed Design Criteria for Hybrid-Rotor Excitation

In this section, the parallel hybrid-excitation method of [72] is further investigated and adapted for synchronous machines equipped with double-layer, non-overlapping stator windings. To employ the proposed parallel hybrid-excitation method for machines with double-layer, non-overlap windings, a minimum of two field-winding pole sections (W_f) and two magnet-pole sections (W_m) on opposite sides of the rotor is required to avoid unbalanced magnetic pull in the machine. Furthermore, because we are only considering double-layer non-overlapping windings, we only need to consider winding-pole sections (W_s) instead of an absolute number of poles. Moreover, since the machine is predominantly a permanent magnet machine and thus only requires some variable field flux excitation, we have $W_m \geqslant W_f$ and thus, for a three-phase, double-layer stator winding; we require that.

$$\begin{aligned} &W_s = \gcd(p, N_s) \quad \text{and} \quad W_s = W_f + W_m \geq 4, \\ &W_f \geq 2; \quad W_m \geq 2; \quad W_m \geq W_f; \quad W_m/W_f = \text{integer} \\ &a_{\max} = W_f \\ &p_f = p\frac{W_f}{W_s}; \quad p_m = p\frac{W_m}{W_s}. \end{aligned} \tag{4.1}$$

Where:

- p is the total number of magnetic poles.
- p_f is the number of field poles.
- p_m is the number of magnet poles.
- a_{max} is the maximum number of possible parallel circuits.
- N_s is the number of stator slots.

In Table 4.1, we consider the hybrid-rotor possibilities of two different pole-number synchronous generators with high winding factor, non-overlapping stator windings. From Table 4.1, it is evident that the number of parallel circuits and the number of possible pole-slot combinations for non-overlapping winding machines is limited, which is a disadvantage of the proposed hybrid-excitation method. However, in general, the higher the pole number of the generator, the more the hybrid-rotor winding-pole sections and winding layout possibilities become.

4.3 Variable Voltage Method

From the proposed hybrid-rotor excitation design criteria, it makes great sense to use the availability of the wound field rotor excitation to help generate the machine's rated power and rated voltage. As such, we propose that the generator's open-circuit rated voltage must be induced with half of the rated field current. Consequently, the lowest open-circuit induced voltage is obtained with zero field current, and the highest induced voltage is induced with rated field current. This method of voltage variation with field current variation is explained in Fig. 4.2, and depends on the ratio r of the wound-field pole sections to the magnet pole sections, which can be expressed as

$$r = \frac{p_f}{p_m} = \frac{W_f}{W_m}. \tag{4.2}$$

With this, and assuming a linear voltage variation as in Fig. 4.2, the per unit open-circuit voltage of the generator can be expressed by

$$V = \left(\frac{2r}{2+r}\right) I_{f(\text{pu})} + \frac{2}{2+r} \quad (\text{pu}), \tag{4.3}$$

Table 4.1: Hybrid-Rotor Excitation Possibilities of 40- and 48-Pole Non-Overlapping Winding Synchronous Machines.

$p = 40$								
N_s	W_s	W_f	W_m	p_f	p_m	$a_{\max}$	r	$\pm \triangle V$ (%)
36	4	2	2	20	20	2	1	33.3
48	8	2	6	10	30	2	1/3	14.3
		4	4	20	20	4	1	33.3
$p = 48$								
54	6	2	4	16	32	2	1/2	20
		3	3	24	24	3	1	33.3

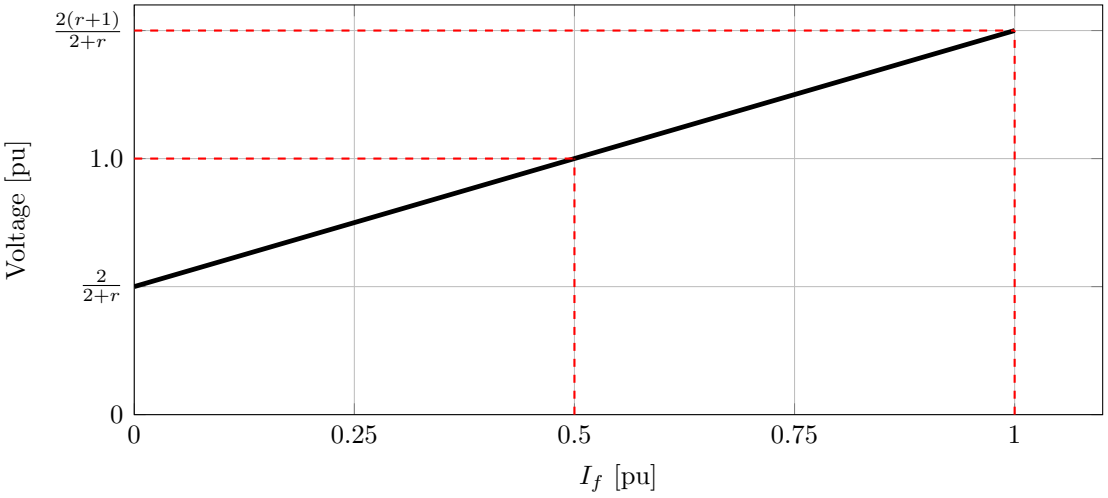

Figure 4.2: Method of per unit voltage variation versus per unit field current variation.

and the percentage voltage variation by

$$\pm\Delta V = \pm\frac{r}{2+r} \times 100\%. \tag{4.4}$$

In general, for grid-connected generators, a minimum of ± 10% voltage variation is required, which requires the ratio r to be $r \geq 0.23$. With the maximum ratio possible of $r = 1$, the maximum voltage variation is theoretically ± 33.3%, which can be considered as relatively large. Hence the ratio between wound-field and magnet poles/sections in this method is always in the range $0.23 \leq r \leq 1$. From Table 4.1, the ratios and percentage voltage variations of the machines under consideration are given. There are examples of small (14.3 %) and large (33.3 %) voltage variations. One can select an option according to the required voltage variation. Finally, it should be noted that the linear voltage variation of Fig. 4.2 depends on the degree of saturation in the machine.

4.4 Finite-Element Analysis of a Hybrid-Rotor Excited Synchronous Generator

This section uses finite element (FE) analysis to investigate a 48-pole, 54-slot, non-overlapping winding machine as highlighted in Table 4.1. The machine has two wound-field-poles and four magnet-pole sections with a theoretical ±20% voltage variation. The cross-section of the FE model of this machine is shown in Fig. 4.3. It has six winding sections where each section has eight poles. The detailed specifications of the generator are given in Table 4.2.

It can be seen from the generator of Fig. 4.3 that large open slots are used for the stator and wound-rotor sections. Large open slots allow for manufactured, pre-wound coils to be inserted into the slots. The large open slots also reduce the stator slot leakage reactance. The rotor field winding has eight side-by-side DC-winding coils. These coils are connected in series to ensure that the net induced field winding voltages caused by the travelling stator-MMF-harmonic-fluxes is zero.

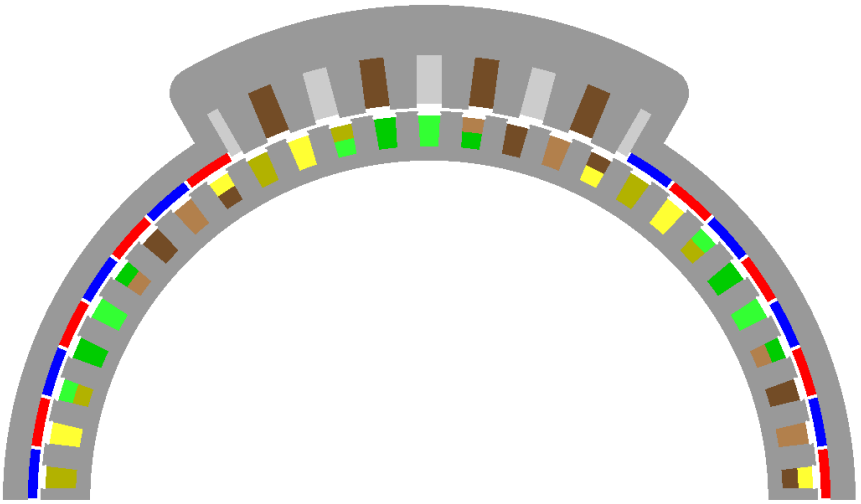

Figure 4.3: Finite element cross-section model of 15 kW, 48-pole hybrid excited generator.

Table 4.2: Specifications and Dimensions of the Hybrid-Excited Generator of Fig. 4.3

Rated power	15 kW	Number of poles	48
Rated voltage	400 V	Number of magnet poles	32
Rated stator current	21 A	Number of stator slots and coils	54
Rated frequency	50 Hz	RMS stator current density	6.0 A/mm^2
Rated speed	125 r/min	Number of parallel stator circuits	2
Rated torque	1145 Nm	Rated field current density	6.0 A/mm^2
Open circuit voltage variation	$\pm$20%	Stator inner diameter	530 mm
Stator fundamental winding factor (k_{w4})	0.945	PM rotor outer diameter	655 mm
Harmonic leakage flux coefficient τ_d	1.175	Wound rotor outer diameter	740 mm
Number of wound-field poles	16	Axial stack length	114 mm
Number of rotor field slots and coils	16	Airgap length	1.8 mm

A stator winding section consists of eight poles and nine slots. The 8-9 pole-slot combination generates the MMF harmonics as shown in Fig. 4.4. The relatively large sub and higher-order harmonics are classical for these non-overlap windings. These MMF harmonics generate a large amount of harmonic leakage flux in the machine, which causes the harmonic leakage coefficient τ_d to be significant, as indicated in Table 4.2. This, in turn, increases the machine's net synchronous reactance, an aspect that is important for grid connection (from Chapter 3) and is considered further in subsequent sections. The magnets are segmented, and the rotor core is laminated to reduce the core losses due to the harmonic generated fluxes. However, the core losses in the wound-rotor section of the rotor of Fig. 4.3 may be severe due to the much larger harmonic fluxes in the rotor due to the small air gap in that part of the machine. The core losses in the wound rotor poles are evaluated in Section 4.6.

The flux density field line plots of this machine without and with wound-field excitation, is shown in Fig. 4.5, and indicates the parallel hybrid-excitation action of hybrid-rotor field excitation. FE analysis is used to determine the d-axis flux linkages to calculate the machine's induced voltage versus field current. This result is shown in Fig. 4.6 where a $\pm$20% voltage variation is obtained for the rated 400 V machine of Fig. 4.3, which verifies the proposed voltage variation method outlined in Section 4.3.

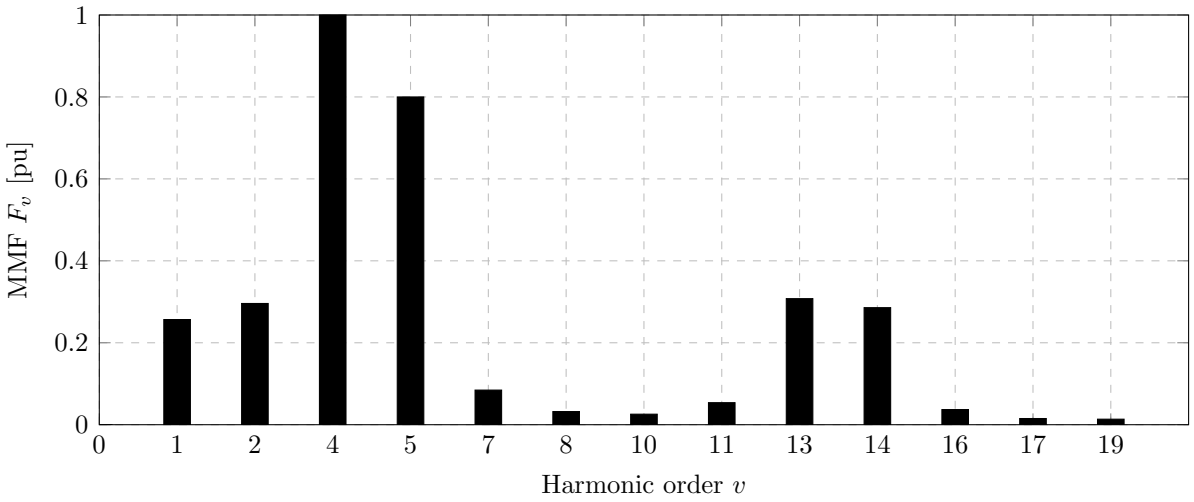

Figure 4.4: Per unit stator MMF harmonics of the generator. The working harmonic is $v = 4$.

Figure 4.5: Flux density field line plots with (a) zero and (b) rated wound-field excitation.

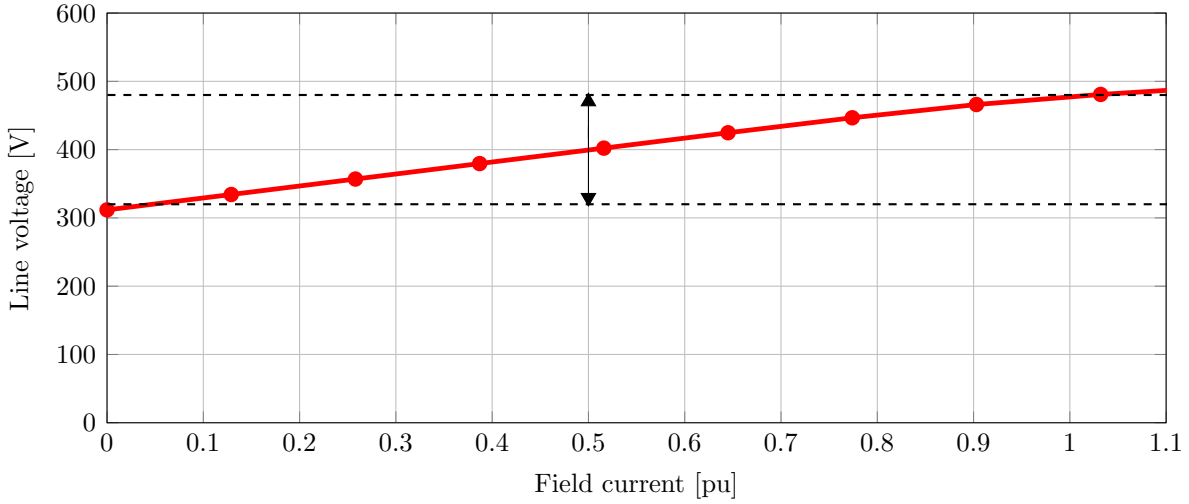

Figure 4.6: Open circuit FE calculated line voltage versus per unit field current of the machine of Fig. 4.3 with 400 V the rated voltage.

4.5 FE Modelling and Performance Calculation

In this section, the FE modelling of the inductances of the generator is considered, and a solution method for performance estimation at specific power and reactive power operating points is provided.

4.5.1 Frozen permeability FE inductance modelling

In the FE modelling, we use the frozen permeability technique to investigate the exact flux contribution of the wound-field poles and magnet poles to the machine's total flux linkage. The latter is significant under load conditions. Furthermore, the frozen permeability method allows one to determine accurate solutions for the hybrid-rotor's effective self- and mutual-inductances. Consequently, the effects of magnetic saturation and cross magnetisation on the machine's performance can be considered. The steady-state the dq flux linkages in the generator reference frame (positive current flowing out of the machine) can thus be expressed as

$$\lambda_d = -L_d I_d - M_{dq} I_q + L_{df} I_f + \lambda_{dm} \tag{4.5}$$

$$\lambda_q = -L_q I_q - M_{qd} I_d + L_{qf} I_f + \lambda_{qm}. \tag{4.6}$$

The inductances of (4.5) and (4.6) are all accurately determined using the FE frozen permeability (FP) technique. Furthermore, the inductance values of (4.5) and (4.6) include the end-winding inductance which is determined using the methods described in [75]. Note from (4.6) that we take the q-axis flux linkages due to the field winding and the magnets into account. In this way, we evaluate the effects of the integrated wound-field poles on the performance of the grid-connected hybrid excited synchronous machine.

4.5.2 Performance calculation

To determine the performance of the generator in the steady-state, we use the dq-voltage equations with generator reference as

$$V_d = \sqrt{\frac{2}{3}} V_L \sin(\Delta) = -R_s I_d - \omega \lambda_q \tag{4.7}$$

$$V_q = \sqrt{\frac{2}{3}} V_L \cos(\Delta) = -R_s I_q + \omega \lambda_d, \tag{4.8}$$

where Δ is the classical power angle between the q-axis and the voltage phasor, which is positive for generator mode. The power and reactive power at the grid is calculated by

$$P = \frac{3}{2}(V_d I_d + V_q I_q) \tag{4.9}$$

$$Q = \frac{3}{2}(V_q I_d - V_d I_q). \tag{4.10}$$

The efficiency is calculated as

$$\eta = \frac{P}{\tau \omega_m + P_{core} + P_{cuf}}, \tag{4.11}$$

and the generated developed torque, τ, is given by

$$\tau = \frac{3}{2} p(\lambda_d I_q - \lambda_q I_d), \tag{4.12}$$

In (4.11), P_{core} is the stator and rotor core losses calculated from rotor-position-stepped FE analysis and P_{cuf} is the rotor field winding losses. In (4.11), we ignore the eddy current losses in the stator conductors and the generator's rotational windage and friction losses.

4.5.3 Performance solution at P^* and Q^* operating points

Since the considered machine is directly connected to the grid, the instantaneous values of the generator's current and hence performance is not known for a desired operating point. For grid-tied applications, the performance of the generator needs to be determined at desired power P^* and reactive power Q^* operating points. From (4.5), (4.6), (4.7) and (4.8), we see that there are four unknown variables for the grid-connected generator, namely I_d, I_q, I_f and Δ. With the FP-technique, the inductances and PM flux linkages of (4.5) and (4.6) can be estimated from an initial set of dq currents. If Δ and I_f are given, then we can solve for new, more accurate I_d and I_q currents using an iterative convergent methodology as expressed by (4.13). With the dq voltages and currents known, P and Q can be solved from (4.9) and (4.10) as shown in (4.13).

$$\text{Given} : \begin{bmatrix} \Delta \\ I_f \\ V_L \end{bmatrix} \rightarrow \begin{bmatrix} \text{Finite Element Analysis} \\ \text{Using Frozen Permeabilty Method} \end{bmatrix} \rightarrow \begin{bmatrix} I_d \\ I_q \end{bmatrix} \rightarrow \begin{bmatrix} P \\ Q \end{bmatrix} \tag{4.13}$$

An estimated value for Δ is first determined to come close to the desired P^* and Q^* power operating points. We approximate the machine model by ignoring saliency and cross-coupling effects and ignoring the stator resistance. From this, it can be shown that Δ can approximately be determined by

$$\Delta \approx \tan^{-1}\left[\frac{P^* X_s}{Q^* X_s + V_L^2}\right]. \tag{4.14}$$

In (4.14) all the parameters are in per unit. We estimate that the per unit value of the synchronous reactance X_s in (4.14) for the machine of Fig. 4.3 is about $X_s = 0.5$ pu (from Chapter 3). Since P and Q are smooth functions of Δ and I_f, (4.13) is used to determine interpolating polynomial functions that are used to quickly calculate analytically the performance of the generator over its entire power operating region. A second-degree interpolating polynomial requires only three data points per curve fitting. Hence, Δ and I_f are varied from minimum to maximum with three data values $\Delta_{i=1,2,3}$ and $I_{fj=1,2,3}$ as

$$\mathbf{\Delta} = \begin{bmatrix} \Delta_1 = \Delta_{\min} \\ \Delta_2 = \frac{1}{2}(\Delta_{\min} + \Delta_{\max}) \\ \Delta_3 = \Delta_{\max} \end{bmatrix} \text{(a)}; \qquad \mathbf{I_f} = \begin{bmatrix} I_{f1} = 0 \quad \text{pu} \\ I_{f2} = 0.5 \text{ pu} \\ I_{f3} = 1.0 \text{ pu} \end{bmatrix} \text{(b)}, \tag{4.15}$$

where $\Delta_{\min}$ and $\Delta_{\max}$ are estimated from (4.14) for the entire power operating region of the generator. Using this as input to (4.13) the power data of the generator can be determined as

$$\mathbf{P_{ij}} = \begin{bmatrix} P_{11} & P_{12} & P_{13} \\ P_{21} & P_{22} & P_{23} \\ P_{31} & P_{32} & P_{33} \end{bmatrix} \text{(a)}; \qquad \mathbf{Q_{ij}} = \begin{bmatrix} Q_{11} & Q_{12} & Q_{13} \\ Q_{21} & Q_{22} & Q_{23} \\ Q_{31} & Q_{32} & Q_{33} \end{bmatrix} \text{(b)}. \tag{4.16}$$

With second-degree interpolating polynomials, analytical functions can be obtained from the data of (4.15) and (4.16) as

$$\Delta_j = f(P, I_f = I_{fj}) \tag{4.17}$$

$$Q_j = f(\Delta, I_f = I_{fj}), \tag{4.18}$$

for $j = 1, 2, 3$. From (4.17) we generate the data for Δ that satisfies $P = P^*$, that is

$$\Delta_{xj} = f(P = P^*, I_f = I_{fj}) \rightarrow \mathbf{\Delta_{xj\{P=P^*\}}} = \begin{bmatrix} \Delta_{x1} \\ \Delta_{x2} \\ \Delta_{x3} \end{bmatrix}. \tag{4.19}$$

Using the Δ_{xj} data of (4.19) as input in (4.18) we generate the data for $\mathbf{Q}$ that satisfies $P = P^*$ as

$$Q_{xj} = f(\Delta = \Delta_{xj}, I_f = I_{fj}) \rightarrow \mathbf{Q_{xj\{P=P^*\}}} = \begin{bmatrix} Q_{x1} \\ Q_{x2} \\ Q_{x3} \end{bmatrix}. \tag{4.20}$$

Again second-degree interpolating polynomial functions can be obtained from the data of (4.19) and (4.20) as well as from the data of (4.15b) and (4.20) as

$$\Delta = f(Q, P = P^*) \tag{4.21}$$

$$I_f = f(Q, P = P^*) \tag{4.22}$$

From above note that (4.15) – (4.18) need only to be done once, hence Δ_x and I_{fx} can then be determined fast for different desired P^* and Q^* power values.

4.6 Performance Evaluation

In this section, the performance of the hybrid-excited generator is evaluated by first comparing its performance to that of a conventional PM-excited generator as shown in Fig. 4.7a. The conventional PM-excited generator has similar specifications to those given in Table 4.2 and similar dimensions to that of the hybrid-excited machine shown in Fig. 4.7b. The machines shown in Figs. 4.7a and 4.7b have the same stator but have different rotors. Secondly, the hybrid-excited generator's performance is assessed according to specific grid code requirements at various operating conditions. The different performance parameters considered are the torque ripple, core losses, efficiency, reactive power and per unit synchronous reactance. Regarding the latter, the following per unit impedance and voltage parameters are considered in the performance evaluation, namely

$$V_{d(\text{pu})} = -R_s I_d + X_q I_q + \{X_{qd}\} I_d - \{E_{qmf}\} \tag{4.23}$$

$$V_{q(\text{pu})} = -R_s I_q + X_d I_d + \{X_{dq}\} I_q - \{E_{dmf}\} \tag{4.24}$$

where

$$\begin{aligned} E_{dmf} &= \omega(L_{df} I_{df} + \lambda_{dm}) \\ E_{qmf} &= \omega(L_{qf} I_{qf} + \lambda_{qm}). \end{aligned} \tag{4.25}$$

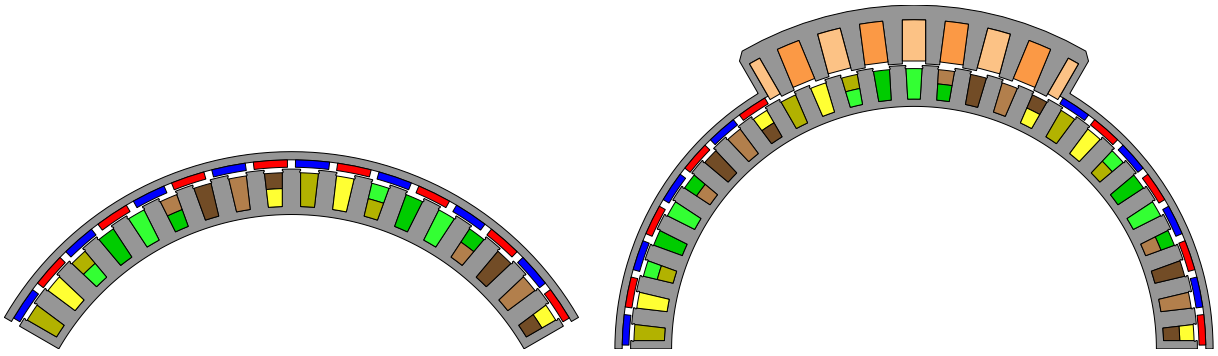

(a) (b)

Figure 4.7: Finite element section models of (a) a conventional fixed-flux permanent magnet synchronous generator and (b) a comparable hybrid-excited synchronous generator.

4.6.1 Comparison between PM- and Hybrid-Excitation Synchronous Machines

In the performance comparison between the PM- and hybrid-excited generators of Fig. 4.7, we focus on two power operating points, namely 0.2 and 1.0 pu active power. At these points, we evaluate the torque ripple, losses, inductance parameters and flux-linkage components for both generators. The performance and parameter results are shown in Table 4.3.

The percentage torque ripple $\Delta\tau$ in Table 4.3 is calculated as the peak-to-peak torque difference as a percentage of the rated torque of the generator. Fig. 4.8 shows the waveforms of the FE-determined torque of the generators versus rotor position. Fig. 4.8 indicates that the hybrid-excited generator has a slightly higher torque ripple. However, the generated torque quality is very much the same as that of the PM generator.

The core losses of the hybrid-excited generator are shown in Table 4.3 to be similar to those of the PM generator. This indicates that the wound rotor part of the hybrid-excited generator does not significantly increase the core losses. This agrees with the findings of [76] and [77] for non-overlapping stator windings with wound-pole rotors, where core losses are shown not to be a particular problem.

Table 4.3: Performance Results of PM- and Hybrid-Excited Generators of Fig. 4.7

Type →	PM		Hybrid	
P(pu)	0.2	1.0	0.2	1.0
Q(pu)	0.08	-0.17	0.08	-0.17
Torque (pu)	0.2	1.0	0.2	1.0
$\Delta\tau$ (%)	3.4	3.5	3.6	4.4
P_{core} (W)	315	327	300	362.5
P_{cus} (W)	26.1	566	51.02	1182
P_{cuf} (W)	0	0	315.5	863
X_d (pu)	0.278	0.278	0.55	0.54
X_q (pu)	0.279	0.279	0.50	0.49
X_{dq} (pu)	0.0002	0.0007	0.0004	0.0014
λ_{df} (mWb-t)	0	0	188.4	301.9
λ_{qf} (mWb-t)	0	0	0.0357	-4.3
λ_{dm} (mWb-t)	1073	1071	916.7	901.1
λ_{qm} (mWb-t)	0.85	0.849	-1.65	-10.99
Efficiency (%)	88.4	94.78	82.5	86.27

Type →	PM	Hybrid
PM height [mm]	7.35	8.1
PM pitch [mm]	33	33
PM-rotor yoke thickness [mm]	8.00	8.00
Number of magnet poles	48	32
Number of stator slots and coils	54	54
Stator slot depth [mm]	33.4	33.4
Stator slot width [mm]	17.5	17.5
Number of parallel circuits	8	1
Total iron mass [kg]	57.34	75.6
Rotor iron mass	14.3	33.2
Stator iron mass	43.0	43.0
Total Copper mass [kg]	14.44	19.2
Rotor copper mass	0.0	4.74
Stator copper mass	14.44	14.44
Magnet mass [kg]	10.0	6.57
Total Active mass [kg]	81.78	101.37

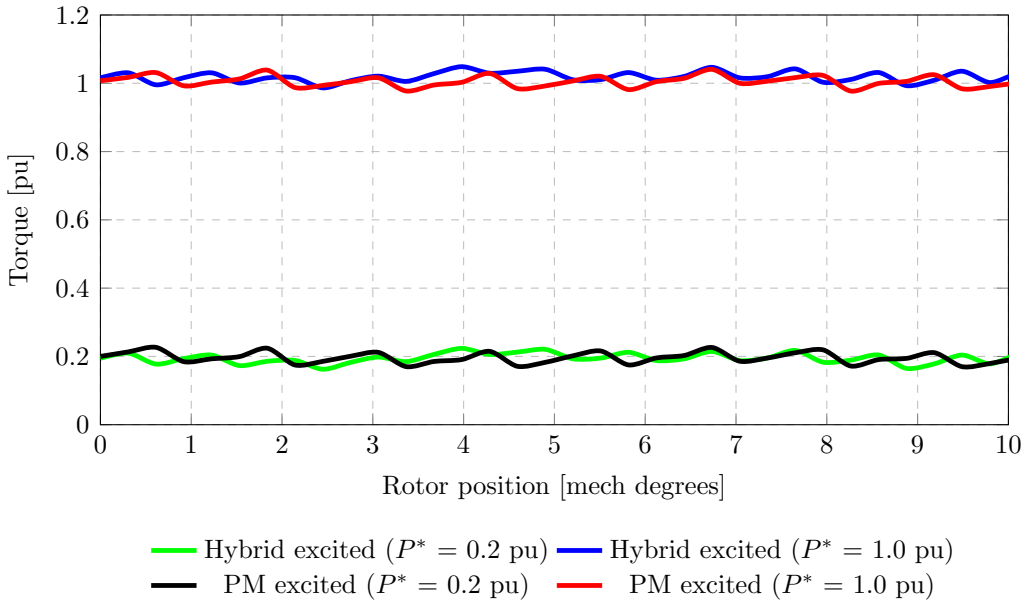

Figure 4.8: Torque versus rotor position with load a parameter for the PM and hybrid-excited generators.

Table 4.3 shows that the hybrid-excited generator's dq-reactances are on average nearly two times larger than the PM generator's dq-reactances. This is due to the added rotor field winding of the hybrid generator. It is shown that the cross-coupling reactance X_{dq} can be ignored in the analysis of both machines. An interesting result here is the per unit synchronous reactance of 0.55 pu of the hybrid-excited generator, which is, from Chapter 3, in the ideal range of values for synchronous reactance for grid-connected applications.

The flux linkages in Table 4.3 show that the d-axis field and PM-flux linkages of the hybrid generator add quite closely to those of the PM generator; this is expected due to the operating voltages being the same. Moreover, the analysis shows that the both machines' q-axis excitation-flux linkages can be ignored.

The efficiency of the PM generator is shown in Table 4.3 to be higher than that of the hybrid generator at both low and rated load conditions. This is due to the additional field-winding loss component in the hybrid generator, which is not present in the PM generator.

Finally, from Table 4.3, it can be seen that the conventional PM generator requires notably less iron and copper material when compared to the hybrid-excited generator. This reduction in iron mass and copper mass is attributed to the conventional PM generator not having DC-field windings. However, the hybrid-excited generator requires notably less PM material when compared to the conventional PM generator, which could result in an economic advantage when considering the high cost of PM material. Nevertheless, the hybrid-excited generator is approximately 24% heavier in total active mass than the PM generator, which could result in additional structural support being needed for the hybrid-excited generator.

4.6.2 Performance of Grid-tie Hybrid-Excited Generator

In this section, we focus on the performance of the proposed hybrid-excited generator in terms of grid code requirements. An example of a grid code power requirement for grid-connected renewable energy systems is shown in Fig. 4.9. According to [50], wind power systems and/or plants with rated power less than 100 kVA are required to operate at unity power factor across their operating range, which is indicated by the red dashed line in Fig. 4.9. Additionally, the performance of the grid-tied, hybrid-excited generator is determined according to the red operating dots of Fig. 4.9 at 0.2 pu and 1.0 pu active powers respectively. It should be noted that operating at the red operating dots is only required for wind power systems with rated powers greater than 100 kVA but less than 1 MVA. The results of the hybrid-excited generator are shown in Figs. 4.10 – 4.14.

The hybrid-excited generator's stator copper losses, field-winding copper losses and the core losses are shown in Fig. 4.10, whereas its efficiency is shown in Fig. 4.11. It is evident that the rotor field-winding copper losses increase significantly as the reactive power requirements increases at 1.0 pu power. Furthermore, it can be seen the generator's efficiency is at its highest when it is absorbing reactive power, $Q = -0.228$ pu. This is because the field-winding current, and hence the field-losses, required to achieve this operating power is at a relative minimum. Furthermore, it can be seen that the generator's efficiency at 0.2 pu power decreases sharply as the required reactive power increases. The sharp decrease in efficiency is due to relatively large core and field winding losses at 0.2 pu power.

The hybrid-excited generators per unit reactances are shown in Fig. 4.12. It can be

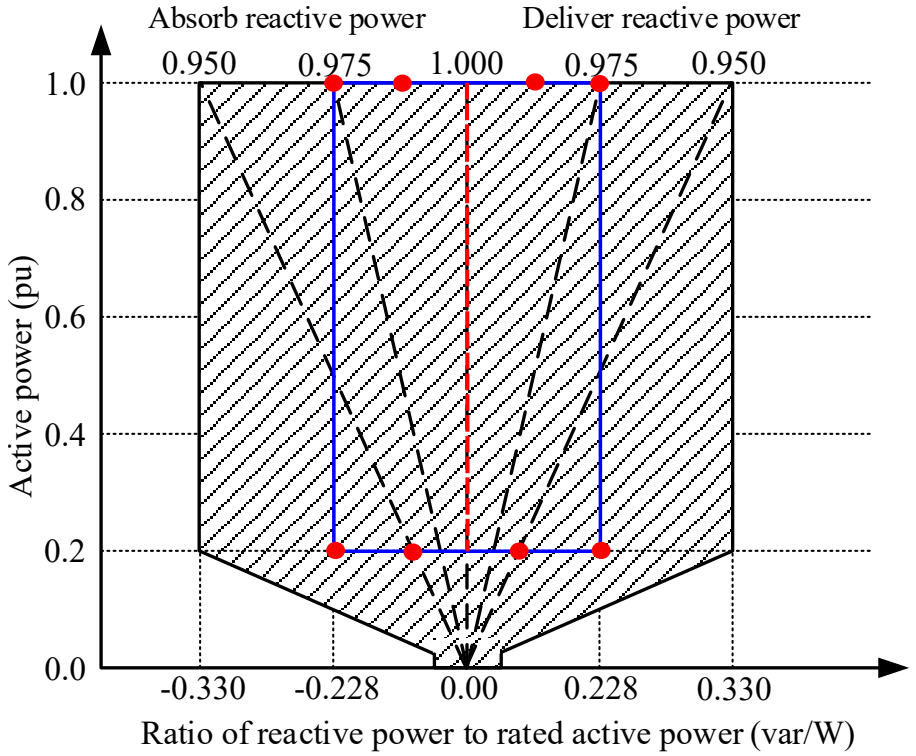

Figure 4.9: Example of grid-connected power versus reactive power requirement for wind turbine systems.

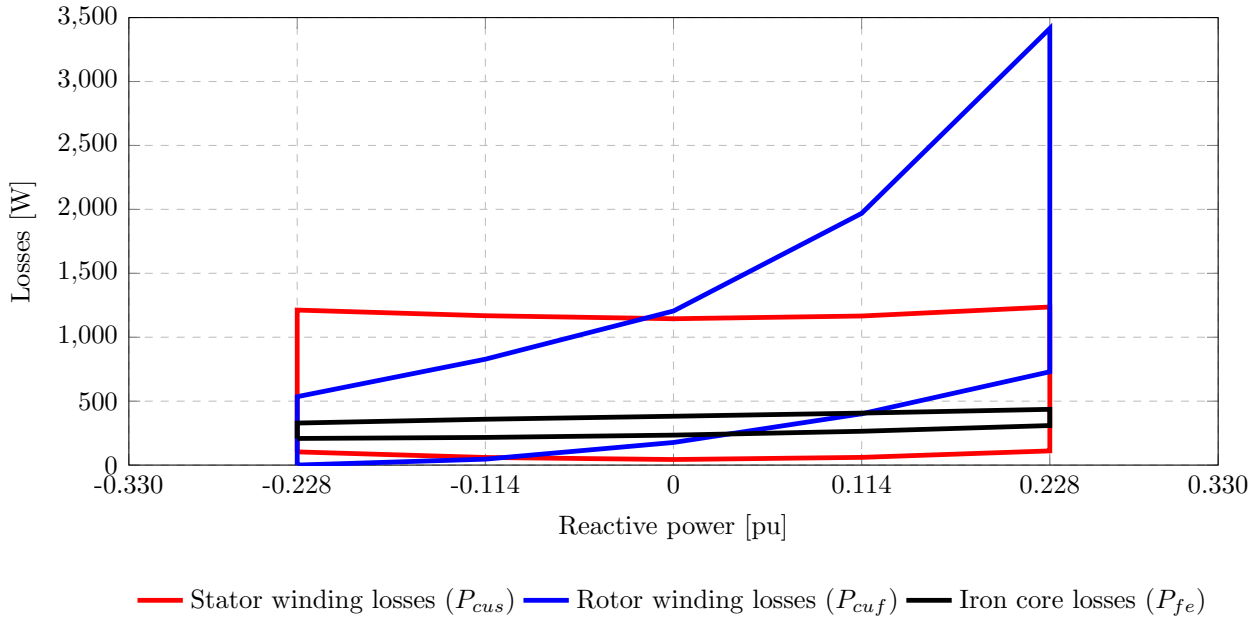

Figure 4.10: Generator stator winding (P_{cus}), field winding (P_{cuf}) and core losses (P_{fe}) versus reactive power requirement. The bottom curve is for P^* = 0.2 pu and the upper curve is for P^* = 1.0 pu.

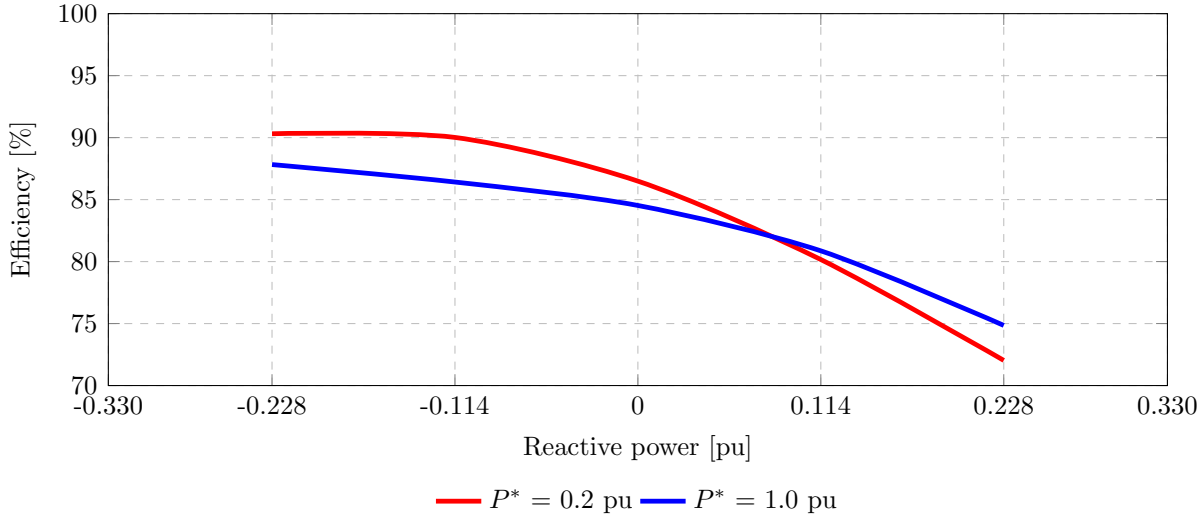

Figure 4.11: Hybrid-excited generator efficiency versus reactive power for P^* = 0.2 pu and for P^* = 1.0 pu.

seen that the generator's respective *d*- and *q*-axis reactances remain relatively constant for varying values of consuming and supplying reactive power at 0.2 pu power. This is because of the constant grid and terminal voltage and the relatively low values of field current at these conditions, which keeps the generator's saturation level constant versus loading. In contrast, it is evident that at 1.0 pu power, the hybrid-excited generators per unit *dq* reactances decrease versus reactive power loading. At 1.0 pu power, relatively large field currents are required to produce a particular reactive power response. Large field currents cause the iron to saturate, which results in a decrease in the hybrid-excited generator's *dq* inductances and reactances.

Finally, the induced voltages due to the PMs and the field windings of the hybrid-

excited generator are shown in Figs. 4.13 and 4.14. These voltages are calculated from (4.25) as

$$E_{dmf} = E_{df} + E_{dm} = \omega L_{df} I_f + \omega \lambda_{dm} \tag{4.26}$$

$$E_{qmf} = E_{qf} + E_{qm} = \omega L_{qf} I_f + \omega \lambda_{qm}. \tag{4.27}$$

Fig. 4.13 shows that the q-axis induced voltage E_{qmf} produced by the field windings and PMs can be considered negligible. Fig. 4.14 shows the respective field-current-induced and PM-induced voltages, the sum of which produces the E_{dmf} curve shown in Fig. 4.13. Fig. 4.14 also shows the field-winding current density versus reactive power requirement. It can be seen that the field current density (J_f) remains within the rated conditions when the generator is operating at unity power factor between 0.2 pu and 1.0 pu power. However, higher values of current density are required to supply positive reactive power at 1.0 pu versus. From Fig. 4.14, the hybrid-excited generator can reach the +0.228 pu

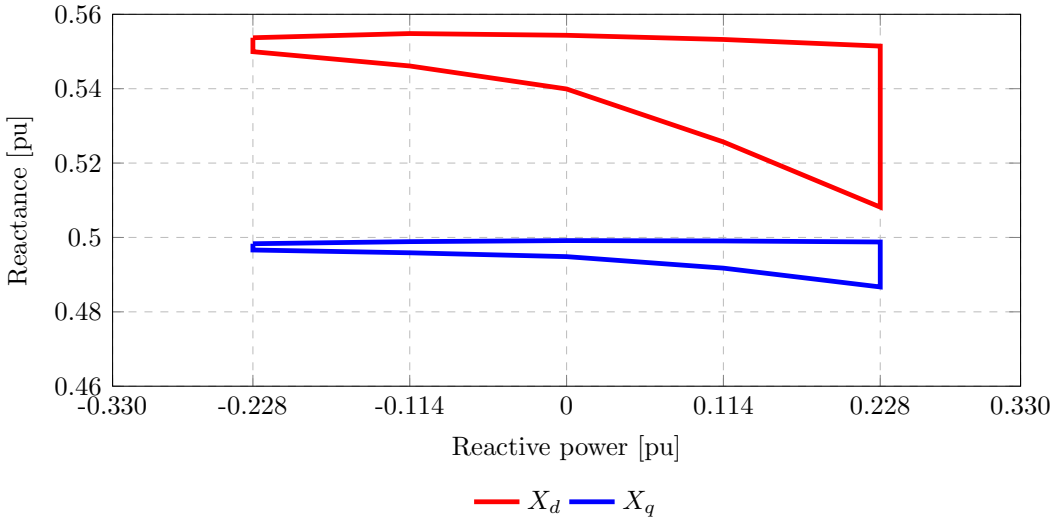

Figure 4.12: Per unit reactance X_d (red curve), X_q (blue curve) and X_{dq} (black curve) versus reactive power for $P^* = 0.2$ pu and for $P^* = 1.0$ pu. The upper curves are for $P^* = 0.2$ pu and the lower curves are for $P^* = 1.0$ pu.

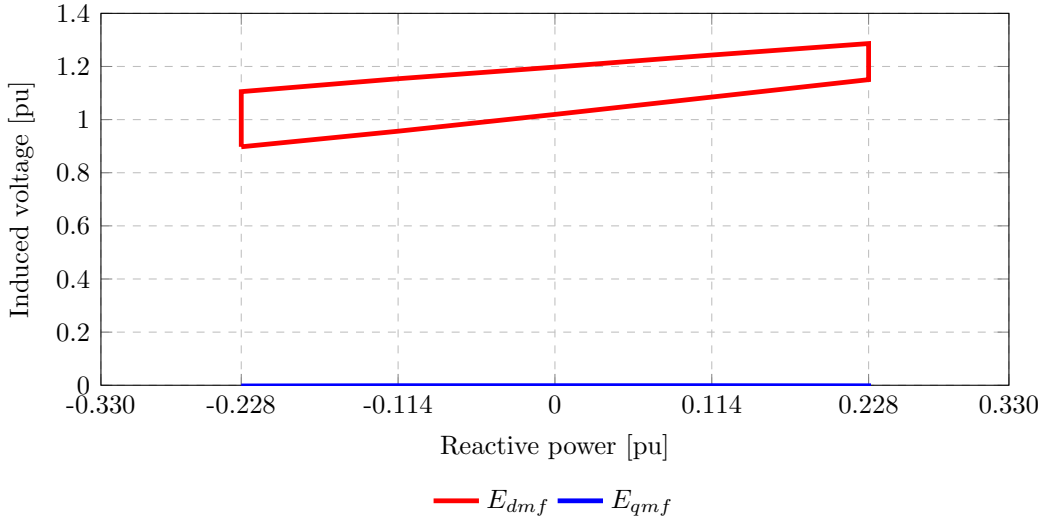

Figure 4.13: Generator per unit induced voltage E_{dmf} (red curve) and E_{qmf} (blue curve) versus reactive power requirement. The bottom curves are for $P^* = 0.2$ pu and the upper curves for $P^* = 1.0$ pu.

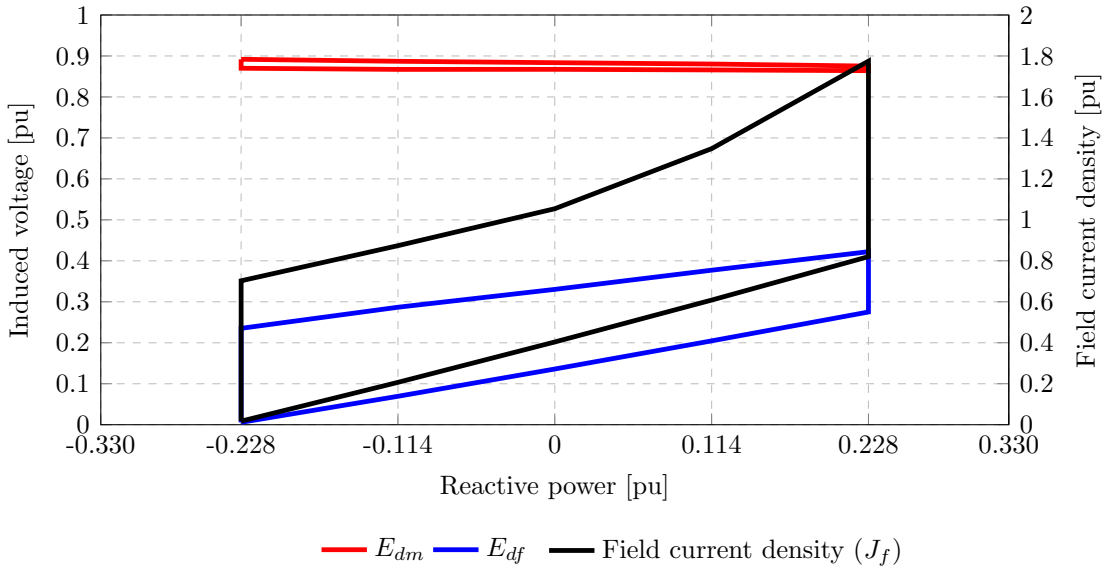

Figure 4.14: Generator per unit induced voltage E_{dm} (red curve), E_{df} (blue curve) and J_f (black curve) versus reactive power requirement. The bottom curves are for $P^* = 0.2$ pu and the upper curves for $P^* = 1.0$ pu. The base value for the field current density is $J_f = 6$ A/mm^2.

reactive power operating point at 0.5 pu active power while operating at 1.0 per unit (6 A/mm^2) field current density. This means that the hybrid-excited generator can operate as a synchronous condenser while still being capable of supplying active power to the grid.

4.7 Chapter Summary and Discussion

This Chapter proposes and investigates a parallel hybrid-excited method for directly grid-connected synchronous machines. The proposed method is shown to be applicable for use in synchronous machines with non-overlapping stator windings. However, the method has the following disadvantages: it limits the number of parallel circuits of the machine and limits the possible slot-pole combinations for non-overlap stator windings. However, these disadvantages become less of a problem as the number of poles of the machine increases. The proposed method of voltage variation allows the percentage voltage variation to vary from $\pm$ 10% to a maximum of $\pm$ 33% by changing the ratio of the number of wound field poles to the number of magnet poles. This voltage variation fits perfectly with what is required for fixed frequency, fixed voltage generators.

FE results obtained from an investigated 15 kW machine show an almost perfect linear variation of the line voltage versus field current. This proves the purely parallel, independent action of the proposed hybrid excited rotor's wound-field and magnet flux excitations. Accurate FE analysis shows that a grid-tied, 15 kW hybrid-excited SG is capable of reactive power compensation. The 15 kW hybrid-excited generator is capable of operating at unity power factor across its load range, which is the grid code requirement for 15 kW grid-connected generators. Additionally, with the proposed method, the hybrid-excited generator is capable of acting as a synchronous condenser by absorbing up to -0.228 per unit reactive power at 0.2 pu active power and supplying up to +0.228 reactive power at 0.5 pu.

Chapter 5

FE-Modelling and Analysis of PM Slip Couplers for Wind Turbine Applications

Chapters 3 and 4 focused on developing design methodologies for directly grid-connected synchronous generators. This Chapter focuses on developing fast and accurate modelling and solutions methods for slip-permanent magnetic couplers (S-PMCs) for wind turbine applications. In [55] and [78], various simplifications are made when modelling S-PMCs for wind turbine applications. However, this Chapter shows that these simplifying assumptions can result in a significant error when predicting the maximum torque of S-PMCs used in wind turbine applications and hence, jeopardise the stability of the wind turbine system during high wind speed conditions and during grid faults.

The solution method proposed in this Chapter incorporates the frozen permeability technique, enabling the user to quickly and accurately determine and evaluate the relevant modelling parameters and machine performance results over a wide slip range. Moreover, the proposed analysis method accurately predicts the zero-sequence (3^{rd} harmonic) and higher-order harmonic induced voltages and currents that are present in magnetic couplings. The method is verified by comparing its results to those obtained from a commercial transient FE (T-FE) package, and measurements of a 1000 Nm S-PMC prototype. The S-FE method solutions are verified over a wide slip range and are shown to be significantly less computationally time-intensive compared to the T-FE package, making it ideally suited for design optimisation purposes. It should be noted that the majority of the work in this Chapter has been presented as a conference paper by Ockhuis and Kamper (2021) [79].

5.1 The Role of Slip-Magnetic Couplers in Slip-Synchronous Drivetrains

Fig. 5.1 shows an example of a directly grid-connected SG-based WTS. It consists of a fixed-speed wind turbine coupled to the grid-connected SG using a gearbox and, in this case, two slip permanent magnetic couplings (S-PMCs) on both sides of the gearbox. Power transfer via the S-PMCs is through a slip-induction action as described in the next section. The S-PMCs provide the necessary stability and torsional damping resulting from wind and grid disturbances, which allows the SG of the WTS to be directly connected to the grid without an inverter [80]. The use of one S-PMC in the WTS is also sufficient, as in gearless direct drive systems, but two S-PMCs provide transient torque

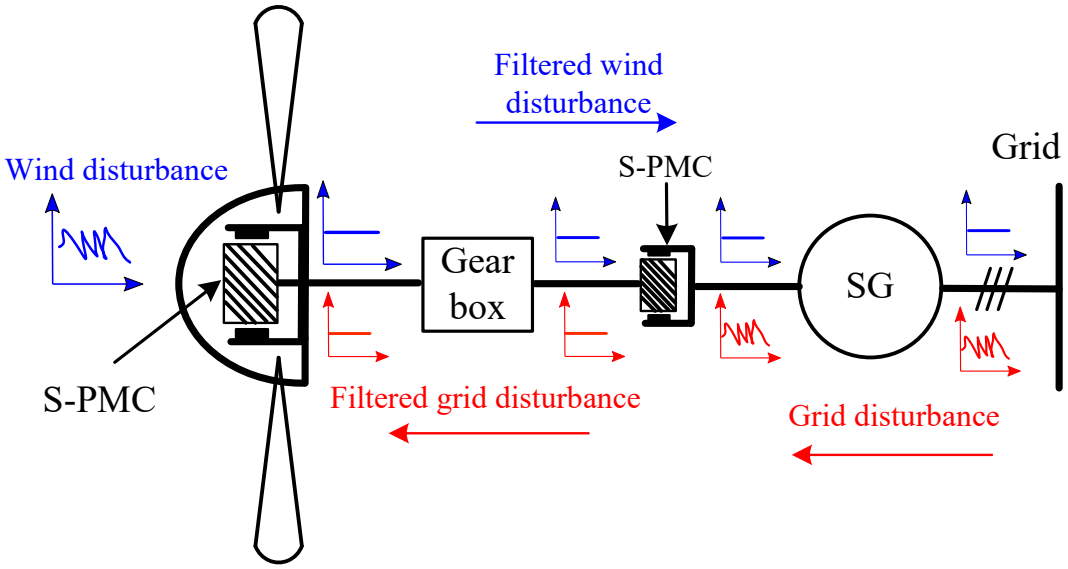

Figure 5.1: Simplified line diagram representation of a geared wind turbine system with two slip magnetic couplings, one integrated with the turbine (left) and one between the gearbox and generator (right).

protection to the gearbox from both sides of the WTS, as illustrated in Fig. 5.1.

The S-PMC used in WTS applications consists of two rotors separated by an air gap. One of the rotors is equipped with permanent magnets (PMs). The other rotor consists of an eddy-current conduction plate as in [81], or a slotted iron-cored rotor with individually short-circuited coils [82, 55], or an actively controlled wound-rotor as in [44]. The PM-rotor of the S-PMC and the SG-rotor can be integrated or shared to form one common rotor, as in the case of [47]. The iron-cored short-circuited-coil rotor is commonly connected to the shaft of the drivetrain gearbox or the shaft of the turbine. Torque is transferred by the S-PMCs in the WTS of Fig. 5.1 by electromagnetic induction due to the difference in speed between the rotating sections. This difference in speed is referred to as slip-speed.

In WTS applications, the maximum torque capability of the S-PMC must always be larger than that generated within the WTS. This ensures that the slip-speed does not become too large, typically during electrical braking, grid faults, or extreme wind conditions. If the generated torque in the WTS exceeds the maximum torque capabilities of the S-PMC, the tight mechanical coupling between the turbine and the drivetrain will be lost. This will result in a sharp increase in the generated loss in the S-PMC due to the large induced currents at the high slip speeds and frequencies. Hence, an accurate prediction of the maximum capable torque in the design and design optimisation of the S-PMC is critical.

5.2 Modelling

In this section, an analytic model of the S-PMC in Fig. 5.2a is derived. The considered S-PMC consists of 28 magnet poles, 30 slots and 30 individually short-circuited, non-overlap coils. An example of one such short-circuited coil is shown in Fig. 5.2c. In [78], it is shown that the 30 short-circuited coils of the S-PMC can be divided into ten balanced three-phase sets. Moreover, 15 adjacent coils can further be divided into five three-phase

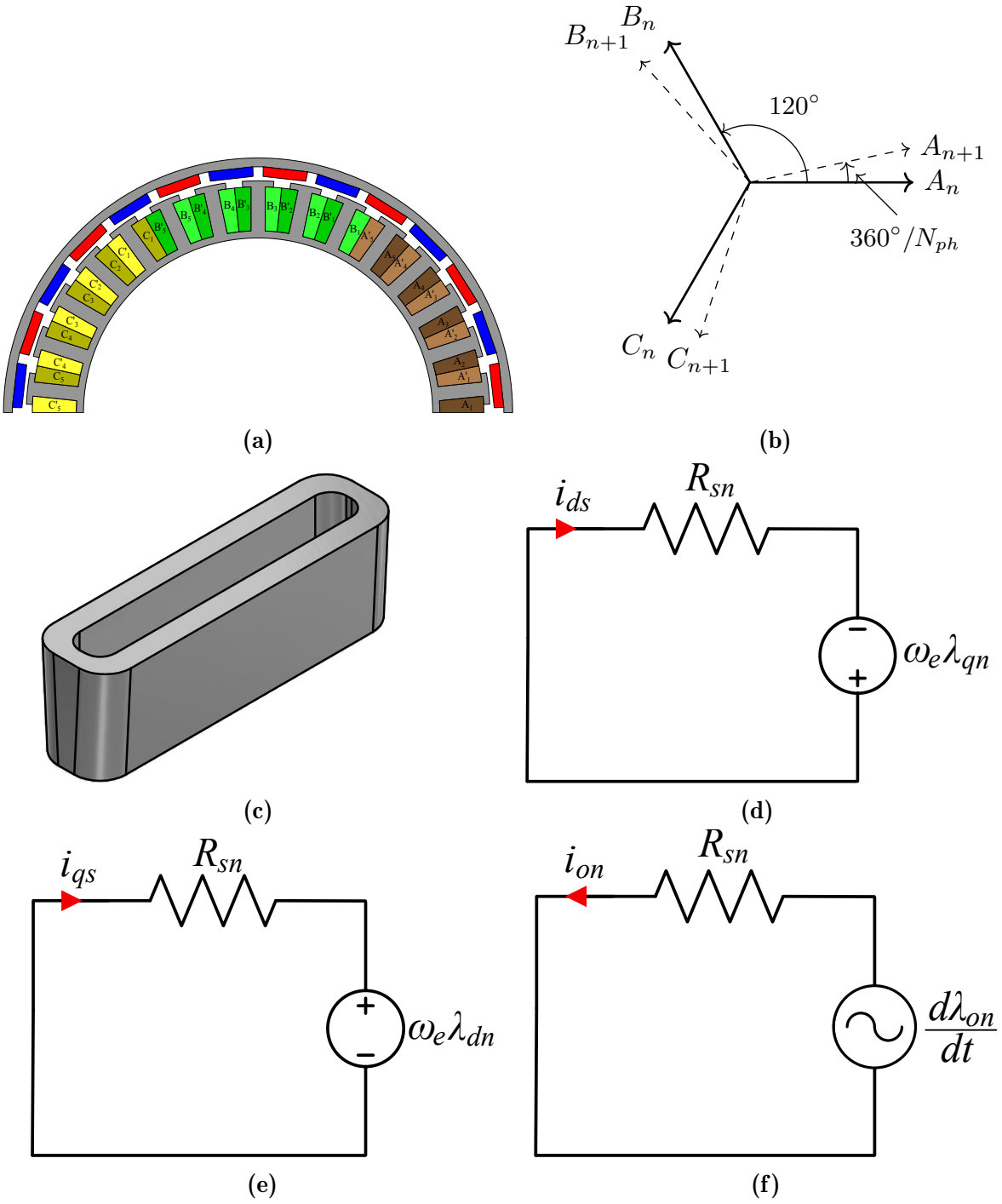

Figure 5.2: (a) FE model of a multi-phase slip coupler, (b) example of an individual short-circuited coil, e.g. $A_1 - A_1^{'}$, (c) vector diagram for the n^{th} three phase coil set, (d) to (f) direct (d)-, quadrature (q)- and zero-axis equivalent circuit representations for the n^{th} three-phase coil set.

coil sets to form a complete winding-pole section. Fig. 5.2b shows a phase-vector diagram of a generalized n-phase S-PMC.

5.2.1 Multi-Three-Phase DQ-Axis Modelling

If we first consider only one three-phase set, then from the $dq0$ voltage equations of a three-phase winding PM synchronous machine, we have

$$\begin{aligned} v_d &= R_s i_d + \frac{d\lambda_d}{dt} - \lambda_q \omega_e \\ v_q &= R_s i_q + \frac{d\lambda_q}{dt} + \lambda_d \omega_e \\ v_o &= R_s i_o + \frac{d\lambda_o}{dt}. \end{aligned} \tag{5.1}$$

If we consider average inductances with rotor position and average (steady-state) I_d and I_q currents (that we want to solve) and thus average λ_d and λ_q flux linkages, then for the considered S-PMC with its short-circuited stator coils, and from Figs 5.2d to 5.2f, (5.1) simplifies to

$$\begin{aligned} 0 &= R_{sn} I_{dn} - \lambda_{qn} \omega_e \qquad \text{(a)} \\ 0 &= R_{sn} I_{qn} + \lambda_{dn} \omega_e \qquad \text{(b)} \\ 0 &= R_{sn} i_{on} + \frac{d\lambda_{on}}{dt}, \qquad \text{(c)} \end{aligned} \tag{5.2}$$

where the subscript n denotes the set number of a particular three-phase coil set, where $n = 1, 2, ..., 5$. Each of the individually short-circuited coils have identical coil currents such that $I_{d1} = I_{d2} = ... = I_{d5} = I_d$ and $I_{q1} = I_{q2} = ... = I_{q5} = I_q$. Consequently, the total d-axis flux linkage for the first coil set, $n = 1$, can be written as

$$\begin{aligned} \lambda_{d1} =& [L_{d(1,1)} + L_{d(1,2)} + ... + L_{d(1,5)}] I_d \\ &+ [L_{dq(1,1)} + L_{dq(1,2)} + ... + L_{dq(1,5)}] I_q \\ &+ \lambda_{dm(1)} \\ =& L_{d1} I_d + M_{dq1} I_q + \lambda_{dm1}. \end{aligned} \tag{5.3}$$

Similarly, the total q-axis and the zero-axis flux linkages for the first coil set $n = 1$ can be written as

$$\begin{aligned} \lambda_{q1} =& [L_{q(1,1)} + L_{q(1,2)} + ... + L_{q(1,5)}] I_q \\ &+ [L_{qd(1,1)} + L_{qd(1,2)} + ... + L_{qd(1,5)}] I_d \\ &+ \lambda_{qm(1)} \\ =& L_{q1} I_q + M_{qd1} I_d + \lambda_{qm1}, \end{aligned} \tag{5.4}$$

and

$$\begin{aligned} \lambda_{o1} =& [L_{o(1,1)} + L_{o(1,2)} + ... + L_{o(1,5)}] i_o + \lambda_{om(1)} \\ =& L_{o1} i_o + \lambda_{om1}. \end{aligned} \tag{5.5}$$

The flux linkages of equation (5.2) can now be rewritten in general for any particular coil set as

$$\begin{aligned} \lambda_d &= L_d I_d + M_{dq} I_q + \lambda_{dm} \qquad \text{(a)} \\ \lambda_q &= L_q I_q + M_{qd} I_d + \lambda_{qm} \qquad \text{(b)} \\ \lambda_o &= L_o i_o + \lambda_{om}, \qquad \text{(c)} \end{aligned} \tag{5.6}$$

where L_d, L_q and L_o are the respective total $dq0$-axis self-inductances, and $M_{dq} = M_{qd}$ are the respective total dq-axis cross-coupling mutual-inductances. It should be noted

that 3-D effects such as the end-winding resistance and inductance are calculated and accounted for as per [75] and are included in R_{sn} and L_{dq0} in (5.2) and (5.6) respectively.

If we substitute λ_q and λ_d into (5.2a) and (5.2b) respectively, and re-write the resulting equations in matrix form, we obtain

$$\mathbf{I}_{dq} = \mathbf{Z}_{dq}^{-1}\mathbf{E}_{dq}, \tag{5.7}$$

where

$$\mathbf{E}_{dq} = \begin{bmatrix}\omega_e\lambda_{qm} & -\omega_e\lambda_{dm}\end{bmatrix}^T, \tag{5.8}$$

$$\mathbf{I}_{dq} = \begin{bmatrix}I_d & I_q\end{bmatrix}^T \tag{5.9}$$

and

$$\mathbf{Z}_{dq} = \begin{bmatrix}(R_s - \omega_e M_{qd}) & -\omega_e L_q \\ \omega_e L_d & (R_s + \omega_e M_{dq})\end{bmatrix}. \tag{5.10}$$

5.2.2 The Skin Effect

Also included in the values for R_{sn} and L_{dq0} is the so-called bar-skin effect. The skin effect is a phenomenon whereby the current distribution in a conductor, which carries an alternating current, varies with the frequency of the alternating current. That is to say, at relatively high frequencies, the electric current within a conductor distributes in a manner whereby the current density is largest near the surface of a conductor at the slot opening and decreases exponentially down the slot.

An increase in current density increases the effective resistance of a conductor when compared to its dc resistance [83]. An expression for this increase in the effective resistance of a rectangular conductor in a slot was developed by [83] and is given by

$$k_d = \varphi(\xi) + \frac{z^2 - 1}{3}\psi(\xi), \tag{5.11}$$

where

$$\varphi(\xi) = \xi\frac{\sinh 2\xi + \sin 2\xi}{\cosh 2\xi - \cos 2\xi} \quad \text{and} \quad \psi(\xi) = 2\xi\frac{\sinh 2\xi - \sin 2\xi}{\cosh 2\xi - \cos 2\xi} \quad \text{and} \quad \xi = h\sqrt{\frac{\omega\mu_o\gamma}{2}}, \tag{5.12}$$

where z refers to the amount of conductors arranged above each other and ξ is a dimensionless quantity referred to as the relative skin depth of the conductor. Furthermore, h is the hight of the conductor within a slot, ω is the frequency of the alternating current, μ_o is the permeability of free space and γ is the electrical conductivity of the conductor. For the considered S-PMC with its side-by-side double-layer winding, $m = 1$ such that the effective resistance of a conductor is then given by

$$R_{sn} = \frac{l\varphi(\xi)}{\gamma b h} \tag{5.13}$$

where l is the stack length and b is the width of the conductor in the slot.

5.3 Harmonic Analysis

Fig. 5.3 shows the theoretical PM- and coil-rotor MMF harmonics for a 28-pole, 30-slot S-PMC with a magnet pitch of $\sigma_m = 81\%$. From Fig. 5.3a, it can be seen that the higher-order rotor MMF harmonics aren't necessarily insignificant and will induce voltages and currents in the short-circuited coils of the S-PMC at various harmonic frequencies. Furthermore, Fig. 5.3b, shows the harmonic cancelling effect of such a multi-three-phase system as described in [78] and in Appendix B. The higher-order harmonics of the PM-rotor will alter the shape of the coil currents and cause them to become non-sinusoidal. To solve the harmonic currents of (5.7), the PM flux linkages of (5.8) and the impedances of (5.10) must be determined. To do this, the phase currents and flux linkages are expressed in terms of Fourier components as

$$s_{abc}(\alpha) = \begin{cases} s_a(\alpha) = \sum_{k=1}^{m} A_k \cos(k\alpha + \phi_k) \\ s_b(\alpha) = \sum_{k=1}^{m} A_k \cos(k\alpha + \phi_k - \frac{2\pi}{3}) \\ s_c(\alpha) = \sum_{k=1}^{m} A_k \cos(k\alpha + \phi_k + \frac{2\pi}{3}) \end{cases} \tag{5.14}$$

where $s_{abc}(\alpha)$ are the phase-domain FE variables, k represents the harmonic order, A_k is the amplitude of the k^{th} harmonic component, ϕ_k denotes the phase shift of a given signal and m indicates the highest-order harmonic component considered within a phase-domain signal. The Park transform can then be utilised on the respective harmonic components of $s_{abc}(\alpha)$ to obtain the respective dq-axis harmonic components in the harmonic rotor reference frames as

$$\begin{aligned} S_{d(k)}(\alpha) &= \frac{2}{3} A_k \cos(\phi_k) \\ S_{q(k)}(\alpha) &= -\frac{2}{3} A_k \sin(\phi_k) \end{aligned} \tag{5.15}$$

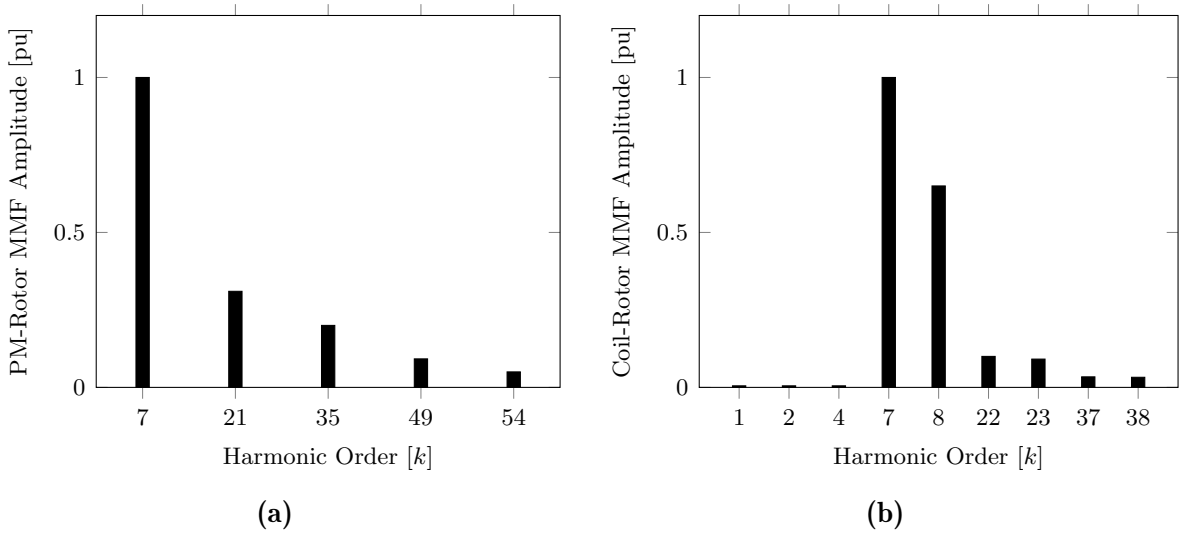

Figure 5.3: Per-unit (a) PM-rotor and (b) coil-rotor MMF harmonics for a 28-pole, 30-slot S-PMC with a magnet pitch of $\sigma_m = 81\%$ (per unit values are calculated with the working harmonic as the base value, where the working harmonic is $k = 1 \times 7$).

and the inverse as

$$\begin{bmatrix} s_{a(k)}(\alpha) \\ s_{b(k)}(\alpha) \\ s_{c(k)}(\alpha) \end{bmatrix} = \mathbf{K}_{\mathrm{p}}^{-1}(k\alpha) \begin{bmatrix} S_{d(k)} \\ S_{q(k)} \end{bmatrix}, \tag{5.16}$$

where $\mathbf{K}_{\mathrm{p}}^{-1}(k\alpha)$ is the inverse Park transformation matrix.

5.3.1 Zero-Sequence Analysis

We are particularly interested in the alternating zero-sequence (3^{rd} harmonic) current component of (5.1). By considering the zero-sequence components of (5.2c) and (5.6c),

$$\begin{aligned} \frac{d\lambda_o}{dt} &= L_o \frac{di_o}{dt} + \frac{\partial \lambda_{om}}{\partial \alpha}\frac{d\alpha}{dt} \\ &= L_o \frac{di_o}{dt} + k_o \omega_e \qquad \left[k_o = \frac{\partial \lambda_{om}}{\partial \alpha}\right], \end{aligned} \tag{5.17}$$

we see thus that an alternating voltage is induced in the zero-sequence winding by the varying zero-sequence PM flux linkage. By assuming only a 3^{rd} zero-sequence harmonic, which is a valid approximation as the higher-order zero-sequence harmonics are minimal, then the 3^{rd} harmonic zero-sequence harmonic flux linkage in phase a and the zero-sequence circuit due to the PMs can be expressed by the general form as

$$\lambda_{am(3)} = \lambda_{om(3)} = -\lambda_{m(3)} \cos(3\alpha + \phi_{(3)}). \tag{5.18}$$

The minus sign in (5.18) is normally the case for the 3^{rd} harmonic. The peak value of the flux linkage of (5.18) is determined by the Fourier transform method as previously described. Using (5.18), the 3^{rd} harmonic induced voltage in the zero-axis circuit is given from (5.17) by

$$e_{o(3)} = k_{o(3)}\omega_e = 3\omega_e \lambda_{m(3)} \sin(3\alpha), \tag{5.19}$$

where $\alpha = \omega_e t$. From (5.2c), (5.17) and (5.19) it follows that

$$3\omega_e \lambda_{m(3)} \sin(3\omega_e t) = R_s i_{o(3)} + L_{o(3)} \frac{di_{o(3)}}{dt}. \tag{5.20}$$

From (5.19), the peak zero-sequence harmonic voltage is given by

$$E_{o(3)} = 3\omega_e \lambda_{m(3)}, \tag{5.21}$$

and hence the peak zero-sequence harmonic current, according to (5.20), by

$$I_{o(3)} = \frac{E_{o(3)}}{\sqrt{R_s^2 + X_{o(3)}^2}}, \tag{5.22}$$

where $X_{o(3)} = 3\omega_e L_{o(3)}$. The latter inductance $L_{o(3)}$ can be determined from the frozen permeability method. The zero-sequence current can be expressed from (5.20) and (5.22) as

$$i_{o(3)}(t) = I_{o(3)} \sin(3\omega_e t - \theta_{o(3)}), \tag{5.23}$$

where $\theta_{o(3)}$ is the zero-sequence power factor angle given by

$$\theta_{o(3)} = \tan^{-1}\left(\frac{X_{o(3)}}{R_s}\right). \tag{5.24}$$

5.3.2 Developed Torque

It must be noted from the steady-state modelling of (5.2) that the dq-currents and flux linkages are DC quantities, while the zero-sequence current and flux linkages are AC quantities. The instantaneous power from the circuit equations of (5.2) is given for a three-phase winding by

$$p_{dq0} = \frac{3}{2}[\lambda_d \omega_e I_q - \lambda_q \omega_e I_d + 2k_{o(3)}\omega_e i_{o(3)}]. \tag{5.25}$$

Using (5.6) and (5.19), (5.25) becomes

$$\begin{aligned} p_{dq0} &= \frac{3}{2}\omega_e[\lambda_{dm} I_q - \lambda_{qm} I_d + (L_d - L_q) I_d I_q \\ &\quad + M_{dq}(I_q^2 - I_d^2) + 6\lambda_{m(3)} \sin(3\alpha) i_{o(3)}] \\ &= \omega_s[T_{pm} + T_r + T_m + \tau_{o(3)}] \\ &= \omega_s[T_d + \tau_{o(3)}], \end{aligned} \tag{5.26}$$

where ω_s is the synchronous output speed of the S-PMC. From the above, the slip-coupler torque can then be described by

$$\begin{aligned} T_{pm} &= \frac{3}{4}p[\lambda_{dm} I_q - \lambda_{qm} I_d] && (a) \\ T_{rl} &= \frac{3}{4}p[L_d - L_q] I_d I_q && (b) \\ T_m &= \frac{3}{4}p M_{dq}[I_q^2 - I_d^2] && (c) \\ \tau_{o(3)} &= \frac{9}{2}p\lambda_{m(3)} \sin(3\alpha) i_{o(3)}, && (d) \end{aligned} \tag{5.27}$$

where T_{pm} is the rotor PM-flux torque and T_{rl}, T_m, $\tau_{o(3)}$ are the respective reluctance, cross-magnetization and zero-sequence torque components. If we focus for a moment on the zero-sequence torque of (5.27d), by replacing the zero-sequence current of (5.27d) by (5.23) we get

$$\begin{aligned} \tau_{o(3)} &= \frac{9}{2}p\lambda_{m(3)} I_{o(3)} \sin(3\alpha) \sin(3\alpha - \theta_{o(3)}) \\ &= \frac{9}{4}p\lambda_{m(3)} I_{o(3)}[\cos(\theta_{o(3)}) - \cos(6\alpha - \theta_{o(3)})] \\ &= \frac{9}{4}p\lambda_{m(3)} I_{o(3)}[1 - \cos(6\alpha)] \quad [\text{assuming} \quad \theta_{o(3)} \approx 0] \\ &= T_{o(3)} - \tau_{a(3)}. \end{aligned} \tag{5.28}$$

This result shows that the zero-sequence induced voltage and current in the S-PMC generates a DC- and an alternating torque component. If the torque equations of (5.27a) - (5.27c) are calculated for each harmonic component k, the total generated torque of the S-PMC is calculated by

$$T_{net} = N\left[T_{o(3)} + \sum_{k=1}^{m} T_{d(k)}\right] \tag{5.29}$$

where $N = 5$ is the number of balanced three-phase sets for the S-PMC of Fig. 5.2a.

5.3.3 Conduction Losses and Efficiency

From the circuit equations of (5.2), the total conduction losses produced by the short-circuited coils for an N-three-phase S-PMC can be expressed as

$$\begin{aligned} P_{cu} &= N\left[\frac{3}{2}I_{o(3)}^2 R_s + \frac{3}{2}\sum_{k=1}^{m}\left(I_{d(k)}^2 R_s + I_{q(k)}^2 R_s\right)\right] \\ &= N\left[P_{cuo(3)} + \sum_{k=1}^{m} P_{cu(k)}\right]. \end{aligned} \tag{5.30}$$

As in classical induction machine theory, this conduction loss of (5.30) can also be expressed as

$$\begin{aligned} P_{cu} &= N\left[sP_{dqo}\right] \\ &= N\left[s\omega_s T_{o(3)} + s\omega_s \sum_{k=1}^{m} T_{d(k)}\right] \\ &= s\omega_s T_{net}. \end{aligned} \tag{5.31}$$

If we assume that the induced iron-core losses are negligible, which is a fair assumption considering the low rated slip speeds and hence low rated frequencies S-PMC's operate at (sub 5 Hz), the efficiency of the S-PMC can be written as

$$\begin{aligned} \eta &\approx \frac{\omega_s T_{net}}{\omega_s T_{net} + s\omega_s T_{net}} \\ &= \frac{1}{1+s}. \end{aligned} \tag{5.32}$$

From (5.32), we see that the efficiency of the S-PMC is inversely related to the value of slip. S-PMCs for wind turbine applications typically have rated slip values between 1% and 3%. For example, if an S-PMC was operating at 1% slip, it would have an efficiency of 99%. It is worth mentioning that (5.32) is very accurate even at maximum torque conditions since the core losses at these higher slip frequencies remain very low.

5.4 Finite Element Computation of Coil Currents

It should be noted that the coil currents, and hence the performance of the S-PMC, aren't known for a given slip value. Consequently, in this section, a solution method is proposed to verify the analytical derivations outlined in the previous sections whereby the $dq0$-axis inductances and coil currents of (5.6) are determined. To achieve this, a *Python*-based S-FE analysis method, which incorporates the frozen permeability method (FPM), is used.

In the FPM, the magnetic iron permeabilities of each S-FE mesh element is fixed or "frozen" (for a given rotor position) after each non-linear S-FE solution to preserve the information regarding the saturation of the machine at the specified load condition and rotor position. By freezing the magnetic iron permeabilities, the non-linear problem turns into a linear problem, and additional (fast) linear S-FE solutions can be used to determine the individual flux linkage components of $\boldsymbol{\lambda}_{dq0}$ as expressed in (5.6).

5.4.1 PM-Flux Linkages

To solve for the dq-PM flux linkages of (5.8), 2ν non-linear S-FE solutions are run at 2ν rotor positions for a given current $i_{abc}(\alpha)$, where the rotor positions are equally spaced

across a magnet pole pitch, and where ν is the number of harmonic components being solved [e.g. if only the 1^{st}, 3^{rd} and 5^{th} harmonics of Fig. 5.3 are considered, then $\nu = 3$]. The PM flux linkage values $\lambda_{abcm}(\alpha)$ at the 2ν positions are then obtained by the FPM with $i_{abc}(\alpha) = 0$ used in the linear S-FE solutions. With $\lambda_{abcm}(\alpha)$ known, the Fourier constants A_k and ϕ_k are determined using (5.14) and from that, the harmonic flux linkages $\lambda_{dm(k)}$ and $\lambda_{qm(k)}$ are determined using (5.15). Note that $\lambda_{m(3)}$ of (5.19) and (5.20) is already obtained from (5.14).

5.4.2 Inductances

The FPM is used to determine the $dq0$-inductances by setting the excitation due to the PMs to zero and executing linear FE solutions where the machine is excited with only $I_{d(k)}$, $I_{q(k)}$, or $i_{o(3)}$ currents respectively, where k represents the harmonic order of a particular current input. The total respective $dq0$ inductances for each harmonic order can then be determined by

$$\begin{aligned} L_{d(k)} &= \left.\frac{\lambda_{dd(k)}}{I_{d(k)}}\right|_{I_q=i_o=0} & M_{qd(k)} &= \left.\frac{\lambda_{qd(k)}}{I_{d(k)}}\right|_{I_q=i_o=0} \\ L_{q(k)} &= \left.\frac{\lambda_{qq(k)}}{I_{q(k)}}\right|_{I_d=i_o=0} & M_{dq(k)} &= \left.\frac{\lambda_{dq(k)}}{I_{q(k)}}\right|_{I_d=i_o=0} \\ L_{o(3)} &= \left.\frac{\lambda_{oo(3)}}{i_{o(3)}}\right|_{I_d=I_q=0} \end{aligned} \tag{5.33}$$

where $\lambda_{dd(k)}$, $\lambda_{qq(k)}$, and $\lambda_{oo(3)}$ are the respective flux linkages resulting from linear FE solutions where only k^{th}-order d-axis currents or q-axis currents or zero-axis currents respectively are used to excite the machine. Moreover, $\lambda_{qd(k)}$ is the q-axis cross-coupling flux linkage due to the k^{th}-order d-axis current. Similarly, $\lambda_{dq(k)}$ is the d-axis cross-coupling flux linkage due to the k^{th}-order q-axis current.

5.4.3 Solving Coil Currents

Since the coil currents of the slip coupler aren't known for a given slip (load) value, an iterative technique is required to solve the coil currents at a specific load condition. The iterative technique is outlined as follows:

1. The $dq0$ PM flux linkages are determined as outlined in Section IV-B. An initial set of $dq0$ inductances are then obtained by solving linear FE solutions with k^{th}-order current inputs as outlined in (5.33).

2. The dq voltage matrix $\mathbf{E}_{dq}$ of (5.8) and the dq impedance matrix $\mathbf{Z}_{dq}$ of (5.10) can now respectively be determined for each harmonic component, along with the zero-sequence reactance $X_{o(3)} = 3\omega_e L_{o(3)}$. Equation (5.7) can now be solved separately for each harmonic component in terms of the current matrix $\mathbf{I}_{dq(k)}$ of (5.9) and an updated set of dq harmonic currents are obtained.

3. With $\lambda_{m(3)}$ known from the first step, the peak value of the zero-sequence voltage $E_{o(3)}$ is determined from (5.21) and the peak value of the zero-sequence current is determined from (5.22). The zero-sequence power factor angle is determined from (5.24).

4. The updated $dq0$-harmonic currents are separately transformed into their respective abc-harmonic currents using (5.16) and are compared to the previous iteration's results. Steps 1) to 4) are iterated until each harmonic current component converges.

Fig. 5.4 shows the results of the RMS current $I_{rms(1)}$ of the fundamental harmonic component versus a convergence iterator Q for various slip (load) conditions. Fig. 5.4 reveals that the proposed S-FE method requires at least $Q = 4$ iterations for the currents to converge for the considered slip values, which indicates the proposed method's speed and effectiveness.

5.5 Simulation Results

In this section, the performance and the computed parameter results using the solution method proposed in the previous section are given for the 28-pole, 30-slot S-PMC of Fig. 5.2a. The dimensions and parameters of the considered S-PMC are given in Table 5.1. In the analysis, the highest-order harmonic selected was $m = 5$, then, according to Fig. 5.3, $\nu = 3$ and solutions at six-rotor positions are required to determine the harmonic components. The proposed method's results are compared and validated with the commercial transient-FE package *JMAG Designer*.

5.5.1 Performance Results

Table 5.2 provides the performance results of the considered S-PMC shown in Fig. 5.2a at rated conditions (slip = 3%). It can be seen that the q-axis current of the fundamental harmonic is the largest of the current components. Furthermore, it can be seen that the peak value of zero-sequence current $I_{o(3)}$ is comparable to that of the 5^{th} harmonic dq-currents. Also shown in Table 5.2 are the $dq0$-axis inductances as calculated from (5.33). It can be seen that the harmonic self-inductance are of comparable magnitude and that the harmonic mutual-inductances are of negligible magnitude.

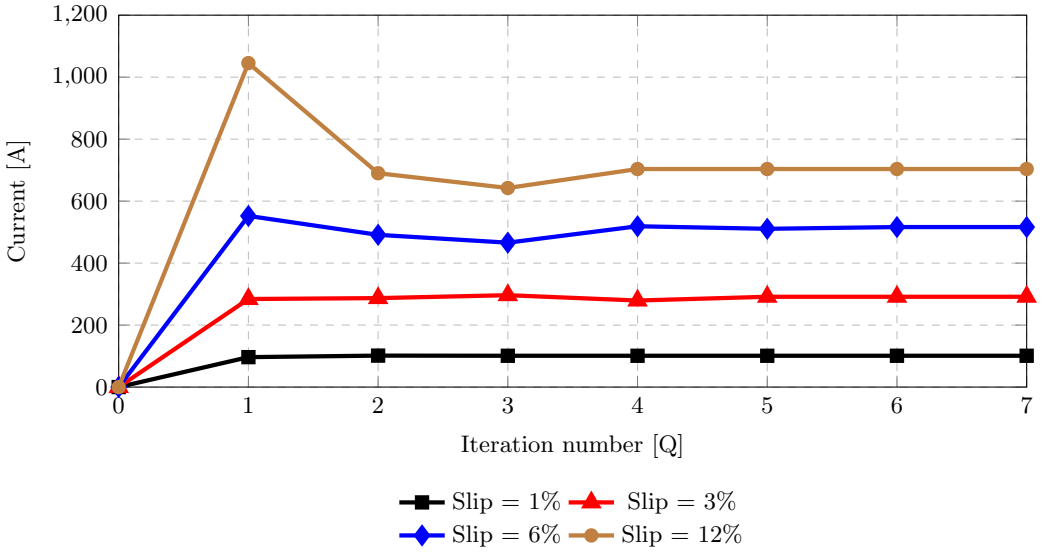

Figure 5.4: RMS current of the fundamental ($k = 1$) harmonic component versus iteration number for slip values: $s = 1\%$, 3%, 6% and 12%.

The S-PMC torque components of (5.27) are determined separately for the respective individual harmonic components and are given in Table 5.2. It can be seen that the PM-flux linkage torque of the fundamental component $T_{pm(1)}$ is the main contributor to the developed torque. In contrast, the zero-sequence and 5^{th} harmonic torque components are negligibly small. Furthermore, the reluctance T_{rl} and cross-magnetization T_m torque components are also negligible. However, this may not be true for other S-PMC topologies, or at all operating (slip) conditions.

5.5.2 Flux Linkages

Fig. 5.5 shows the S-FE-determined PM-flux linkages at rated slip conditions. From this, it is clear that a zero-sequence PM-flux linkage component is present. Additionally, there is a small contribution of the fundamental q-axis PM-flux linkage $\lambda_{qm(1)}$, however, the fundamental d-axis PM-flux linkage $\lambda_{dm(1)}$ is the dominant contributor to the PM-flux linkage. Also shown are the 5^{th} harmonic dq PM-flux linkages. It can be seen that the 5^{th} harmonic dq PM-flux linkages are relatively small and are of comparable magnitude.

Fig. 5.6 shows the S-FE calculated dq PM-flux linkages for the fundamental harmonic versus slip-percentage. It can be seen that the dq-axis PM-flux linkages $\lambda_{dm(1)}$ and $\lambda_{qm(1)}$

Table 5.1: Dimension and Parameter Values of the Slip Coupler of Fig. 5.2a.

Dimension	**Value**	**Parameter**	**Value**
Outer diameter	173.5 mm	Rated output speed	600 rpm
Inner diameter	118.9 mm	Rated slip	3%
Wound rotor yoke	2.99 mm	Number of poles	28
Tooth height	15 mm	Number of slots	30
Tooth width	4.86 mm	Magnet type	N48H
Coil height	14.8 mm	Coil resistance	60 uΩ
Magnet height	3.27 mm	Current density	3.71 A/mm^2
Magnet pitch	81%	Rated power	2.5 kW
Air gap	1.2 mm	Rated torque	40 Nm
Axial length	54.74 mm	Rated frequency	4.3 Hz

Table 5.2: Performance Parameter Values at Rated Conditions of the Slip Coupler of Fig. 5.2a.

1^{st} Harmonic		3^{rd} Harmonic		5^{th} Harmonic	
Parameter	Value	Parameter	Value	Parameter	Value
Current	A	Current	A	Current	A
$I_{d(1)}$	137.5	$I_{o(3)}$	-24.38	$I_{d(5)}$	-8.81
$I_{q(1)}$	422.7	——	——	$I_{q(5)}$	-28.6
Inductance	nH	Inductance	nH	Inductance	nH
$L_{d(1)}$	756			$L_{d(5)}$	706.2
$L_{q(1)}$	870	$L_{o(3)}$	778	$L_{q(5)}$	711.4
$M_{dq(1)}$	21			$M_{dq(5)}$	3.4
Torque	Nm	Torque	Nm	Torque	Nm
$T_{pm(1)}$	42.59			$T_{pm(5)}$	0.6
$T_{rl(1)}$	-0.568	$T_{o(3)}$	-0.28	$T_{rl(5)}$	0
$T_{m(1)}$	-0.36			$T_{m(5)}$	0

do not remain constant as the slip-percentage (loading) increases. Moreover, $\lambda_{dm(1)}$ decreases from no load (slip = 0%) to rated slip (slip = 3%) by approximately 10%. Furthermore, the magnitude of $\lambda_{qm(1)}$ is shown to increase (negatively) as the loading increases, from approximately 0% to 14% of $\lambda_{dm(1)}$, which is the main effect of iron saturation.

5.5.3 Current

Fig. 5.7 shows the S-FE predicted coil current and the respective coil current harmonics at slip = 1%. It is clear that the 3^{rd} harmonic and the 5^{th} harmonic components have a significant effect on the shape of the coil current and that the assumption that the coil currents are sinusoidal isn't valid for this S-PMC topology.

Fig. 5.8 shows the variation of the magnitude of the dq-axis currents versus slip-percentage. It can be seen that the q-axis current, $I_{q(1)}$, is initially significantly larger than the d-axis current. This is because, from equations (5.2) to (5.4), the d-axis PM-flux linkage $\lambda_{dm(1)}$ is much larger than $\lambda_{qm(1)}$. However, from Fig. 5.6, it can be seen that $\lambda_{qm(1)}$ increases rapidly and significantly versus slip-percentage. This results in a rapid increase in $I_{d(1)}$, which surpasses $I_{q(1)}$ for slip-percentages greater than 11%.

Furthermore, it can be seen that the magnitude of the zero-sequence current, I_o, is comparable to the d-axis current at small slip values. However, I_o becomes negligible as the slip-percentage increases compared to the dq-currents.

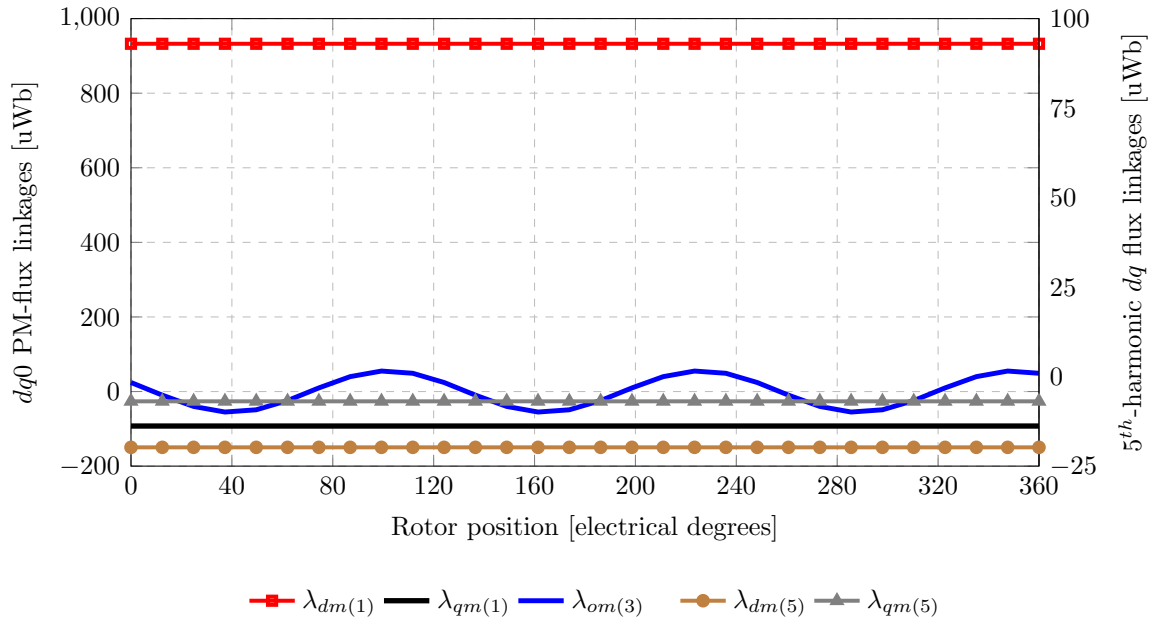

Figure 5.5: Static-FE-determined PM-flux linkage component results obtained from a linear FE solution where $I_{dq0(k)} = 0$ for the 28-pole, 30-slot S-PMC of Fig. 5.2a. The fundamental and zero-sequence harmonic flux linkages are on the primary y-axis and the 5^{th}-harmonic dq flux linkages are on the secondary y-axis.

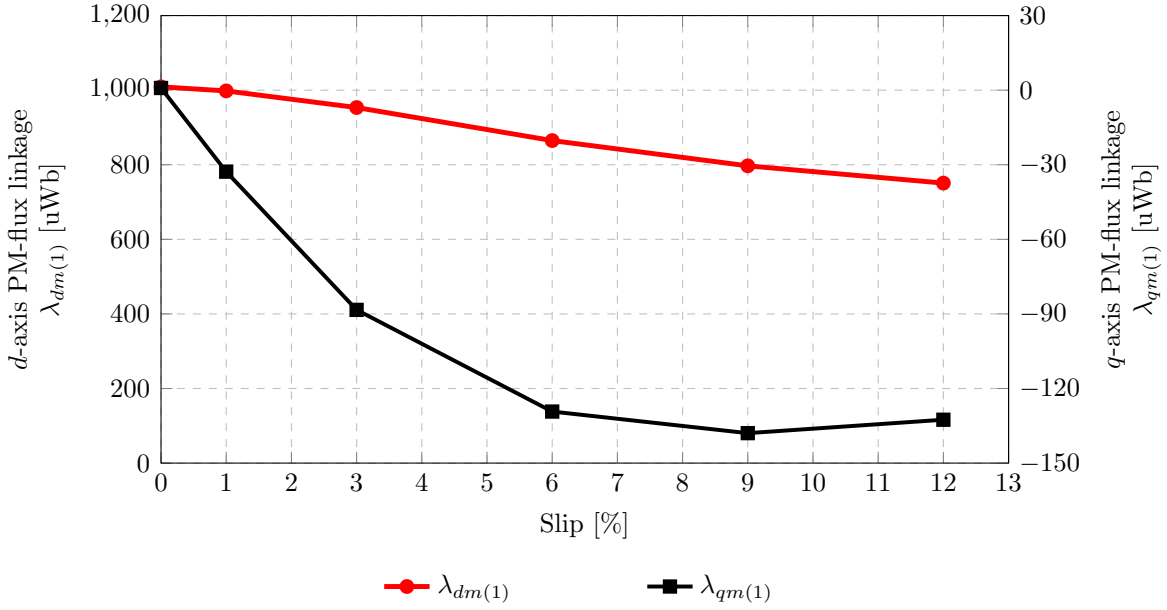

Figure 5.6: PM-flux linkages $\lambda_{dm(1)}$ and $\lambda_{qm(1)}$ versus slip percentage for the 28-pole, 30-slot S-PMC of Fig. 5.2a. Rated slip is at 3 %.

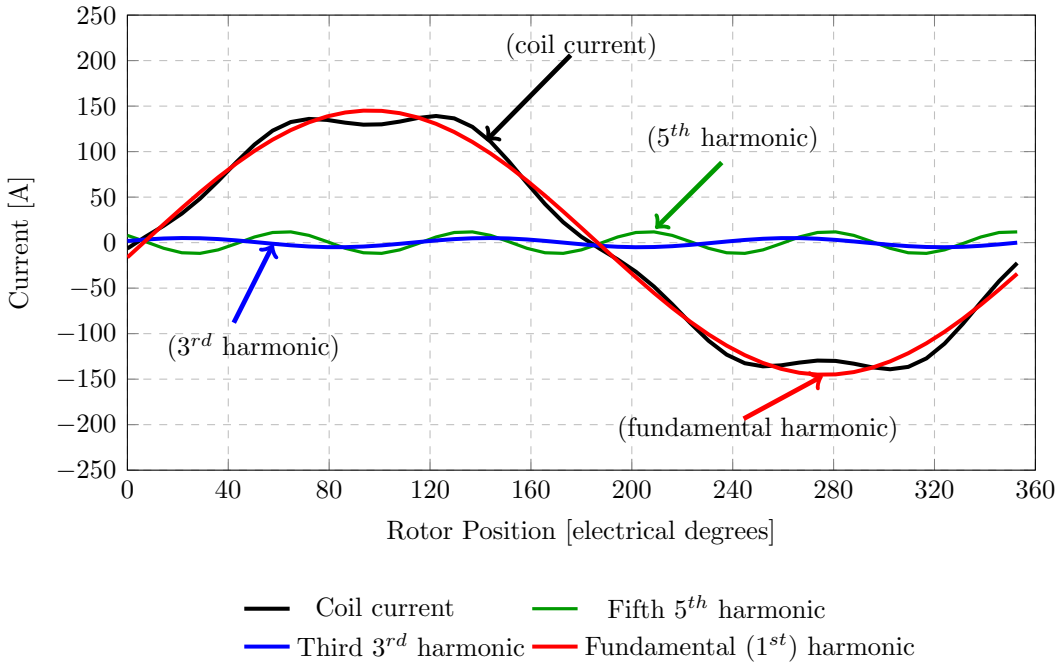

Figure 5.7: Static-FE predicted coil and coil current harmonics versus electrical rotor position at slip = 1% for the 28-pole, 30-slot S-PMC of Fig. 5.2a.

5.5.4 Inductance

Fig. 5.9 shows the variation of the average $dq0$-inductances versus slip-percentage as determined using (5.33). It can be seen that the $dq0$-inductances do not remain constant but instead decrease versus loading. Furthermore, it was found that the influence of the mutual inductances, M_{dq0}, versus slip-percentage can be considered negligible.

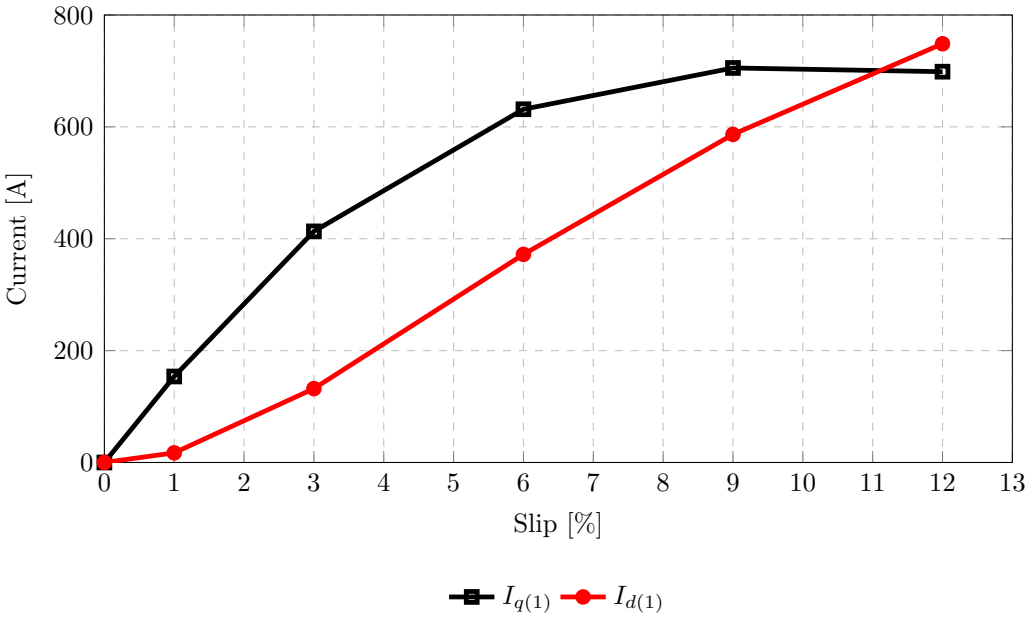

Figure 5.8: Magnitude of the *dq*-axis currents versus slip-percentage for the 28-pole, 30-slot S-PMC of Fig. 5.2a. Rated slip is at 3%.

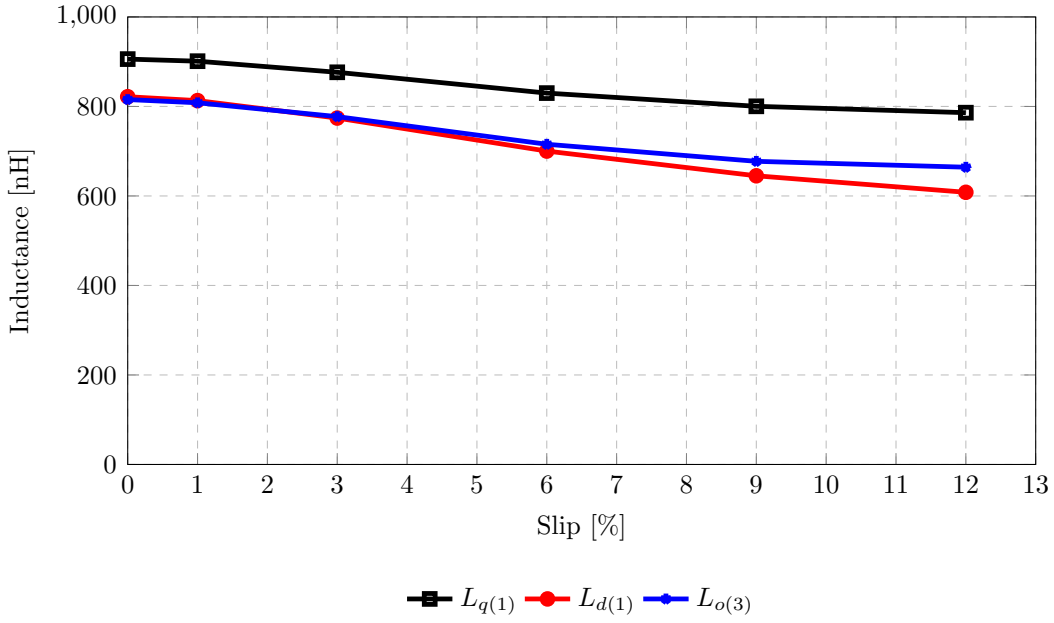

Figure 5.9: Variation of the respective *dq*0-axis inductance versus slip percentage for the 28-pole, 30-slot S-PMC of Fig. 5.2a. Rated slip is at 3%.

5.5.5 Verification using 2-D Transient-FE Solution Results

The results of the proposed S-FE method are validated by modelling and analysing the S-PMC of Fig. 5.2a using the commercial transient-FE (T-FE) package *JMAG Designer*. Fig. 5.10 shows the coil current versus rotor position at slip = 1% and at rated slip (3%) as determined by the T-FE program *JMAG Designer* and the S-FE solution method. It can be seen that a good agreement between the results is obtained.

Fig. 5.11 shows the results for current harmonic amplitude versus slip percentage for the S-FE and T-FE solutions. From this, it can be seen that a good agreement between

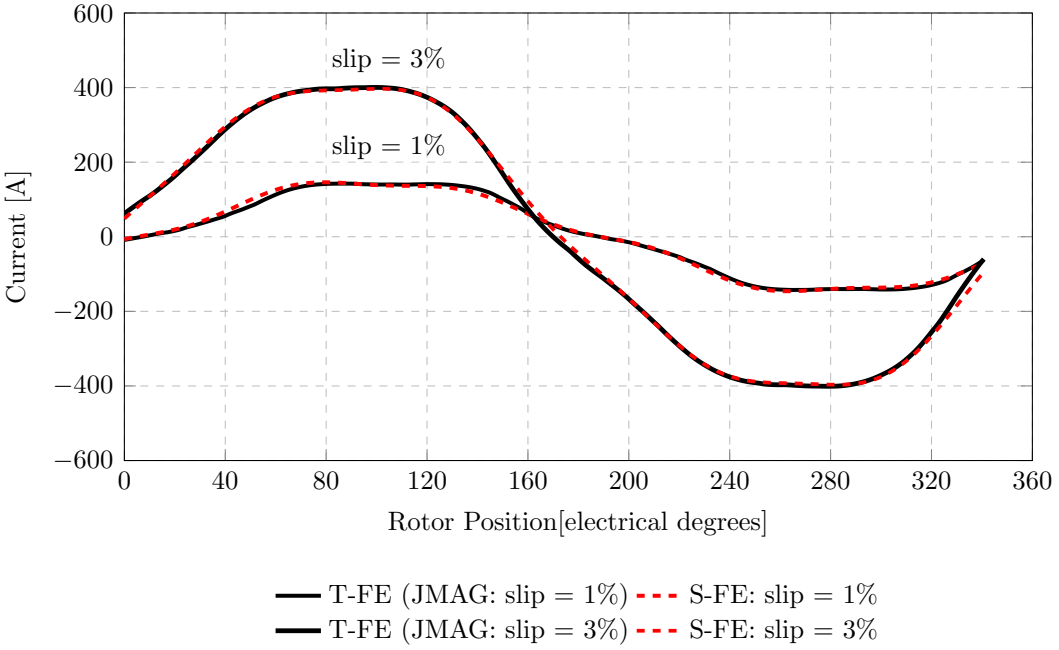

Figure 5.10: Transient- and static-FE comparison of coil current versus electrical rotor position for slip = 1% and 3% for the 28-pole, 30-slot S-PMC of Fig. 5.2a.

the results is achieved over a wide slip range, which validates the effectiveness of the proposed S-FE solution method.

Fig. 5.12 shows the results for the average value of the developed torque of the considered S-PMC versus slip-percentage, as determined by the T-FE solution and the proposed S-FE solution method. As can be seen, an excellent agreement between the results is achieved over a wide slip range. Also shown in Fig. 5.12 are the respective PM-torque (T_{pm}) and reluctance torque (T_{rl}) components as determined by the S-FE method using (5.27). It can be seen that the influence of reluctance torque on the developed torque increases as the slip-percentage increases. The influence of the respective zero-sequence and 5^{th}-harmonic torque components can be considered negligible across the versus slip-percentage range for the considered S-PMC.

5.6 Verification Using Measured Results of a 1000 Nm S-PMC Prototype

The results of the proposed S-FE method are further verified using measured results obtained from a 15 kW, 1000 Nm S-PMC prototype. A finite-element cross-section model of the 1000 Nm prototype S-PMC is shown in Fig. 5.13, and the main dimensions of the prototype S-PMC are given in Table 5.3. Figs. 5.14 and 5.15 show the respective PM-rotor and the iron-cored wound-rotor sections of the 1000 Nm S-PMC prototype. Furthermore, Fig. 5.16 shows the laboratory test-bench layout used to obtain the measured results of the prototype S-PMC. The S-PMC is driven by a 75 kW induction motor (IM) which is subjected to torque control using an *Allen-Bradly* Powerflex 700 variable-speed drive (VSD). The permanent magnet rotor of the S-PMC is locked on a steel frame such that it is unable to rotate. The S-PMC's wound-rotor's shaft is coupled to a torque sensor, which itself is coupled to the shaft of the IM.

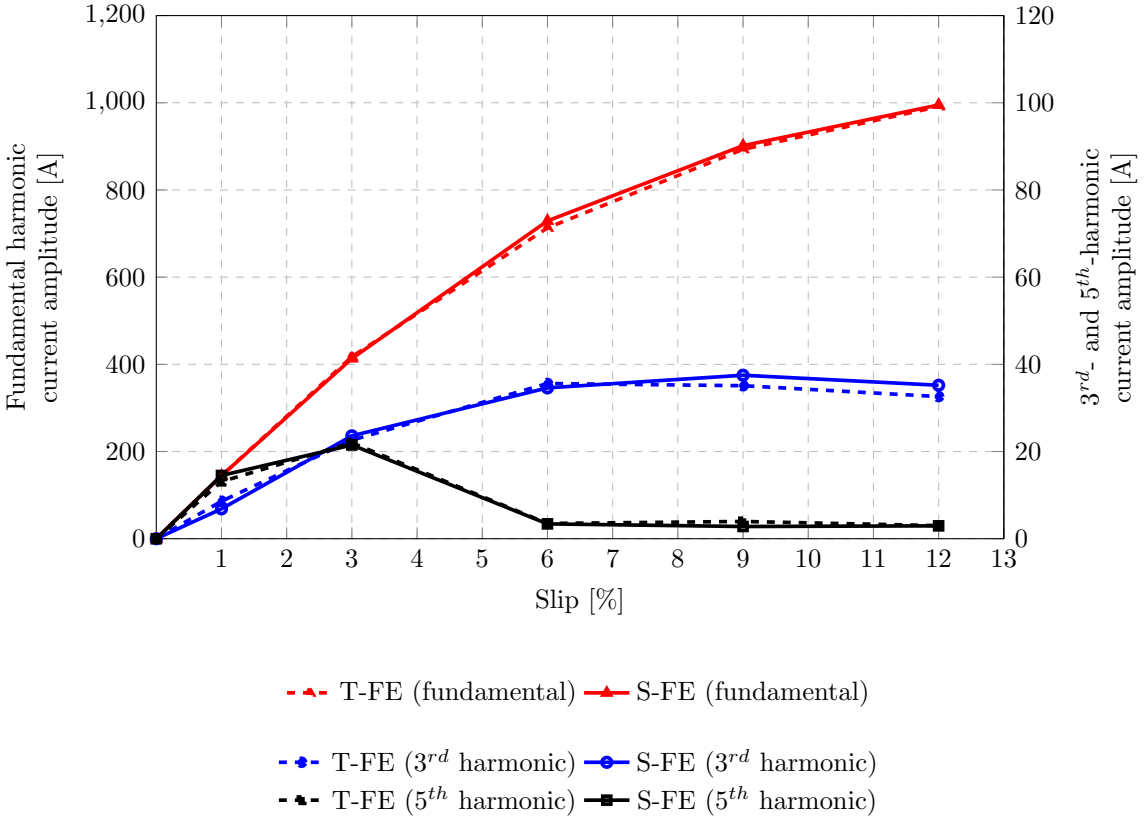

Figure 5.11: Transient- and static-FE current harmonic amplitudes versus slip percentage for the 28-pole, 30-slot S-PMC of Fig. 5.2a. The fundamental current harmonic amplitude is on the primary y-axis and the 3^{rd} and 5^{th} current harmonic amplitudes are on the secondary y-axis.

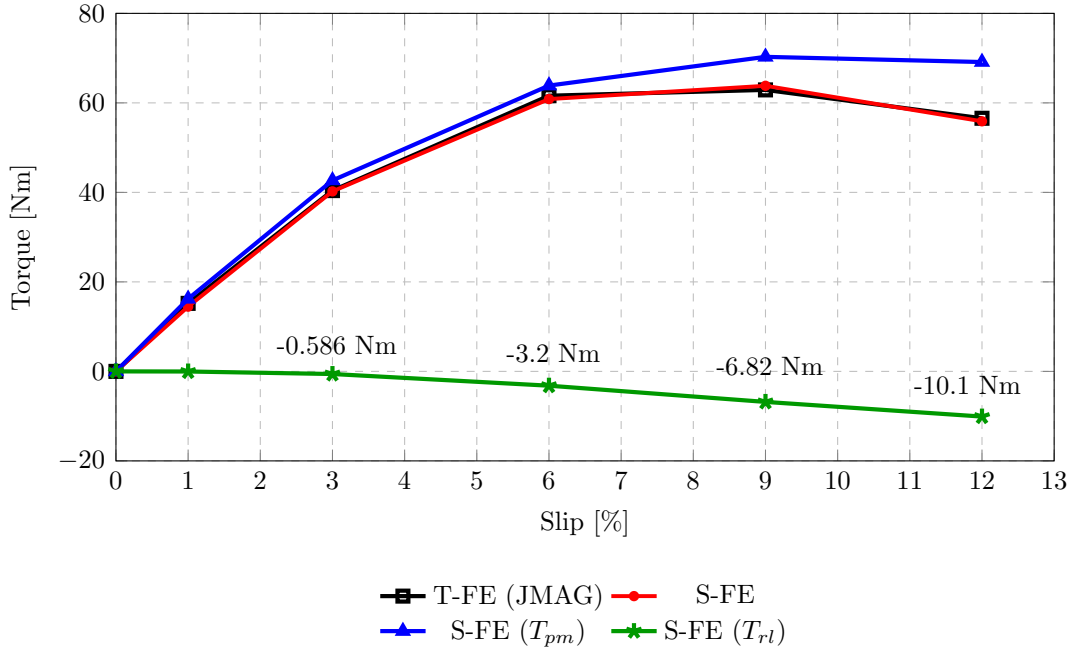

Figure 5.12: Torque comparison showing the average torque versus slip as determined by the transient-FE and the proposed static-FE solutions for the 28-pole, 30-slot S-PMC of Fig. 5.2a. Also shown are the S-FE determined PM-torque (T_{pm}) and reluctance torque (T_{rl}) components versus slip-percentage. Rated slip is at 3%.

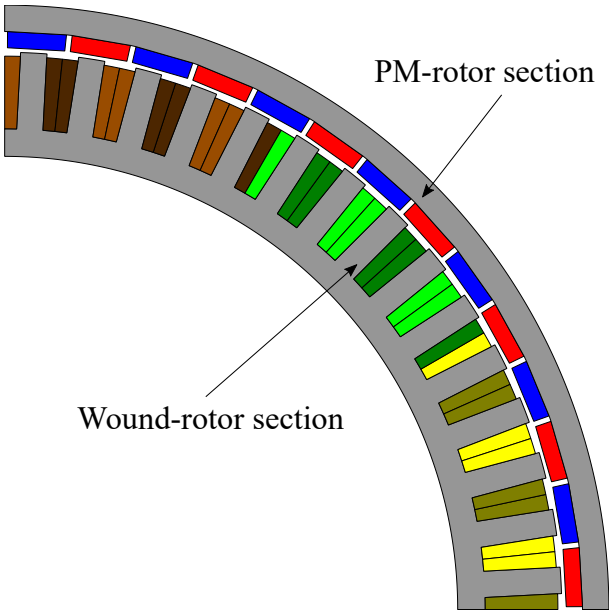

Figure 5.13: Finite-element cross-section model of the 15 kW, 1000 Nm S-PMC prototype. This S-PMC has in total 56 magnet poles and 60 slots with 60 individually short-circuited coils.

Table 5.3: Dimension and Parameter Values of the 1000 Nm Prototype Slip Coupler.

Dimension	**Value**	**Parameter**	**Value**
Outer diameter	632 mm	Rated output speed	150 rpm
Inner diameter	474 mm	Rated slip	3%
Wound rotor yoke	14.4 mm	Number of poles	56
Tooth height	40 mm	Number of slots	60
Tooth width	13.8 mm	Magnet grade	N48H
Coil height	38 mm	Lamination grade (steel)	M530-65A
Magnet height	8.5 mm	Aluminium grade (coils)	6061 T
Magnet pitch	87.1 %	Rated power	15 kW
Air gap	2 mm	Rated torque	1000 Nm
Axial length	90 mm	Rated efficiency	97 %

To ensure that an accurate and thermally consistent coil resistance value is used in the 2-D S-FE analysis, the prototype S-PMC is driven at rated conditions for 1 hour until a thermal equilibrium of the coils and the magnets is achieved. Temperature measurements were taken at various intervals using a *FLUKE* Thermal Imager temperature sensor. At thermal equilibrium, the temperature of the coils and the PMs were $T_{coil} = 70°$ C and $T_{pm} = 30°$ C respectively.

Fig. 5.17 shows the measured and proposed S-FE torque versus slip percentage results for the 1000 Nm prototype S-PMC. Also shown in Fig. 5.17 are the corresponding 2D-FE torque-speed results of the prototype S-PMC using the solution method proposed in [78]. It can be seen that a good agreement between the results of the measured torque and the torque predicted using the proposed S-FE method is achieved; however an error of approximately 12 % is incurred when using the method of [78], which assumes that a constant PM-flux linkage is maintained across the S-PMCs torque-speed range.

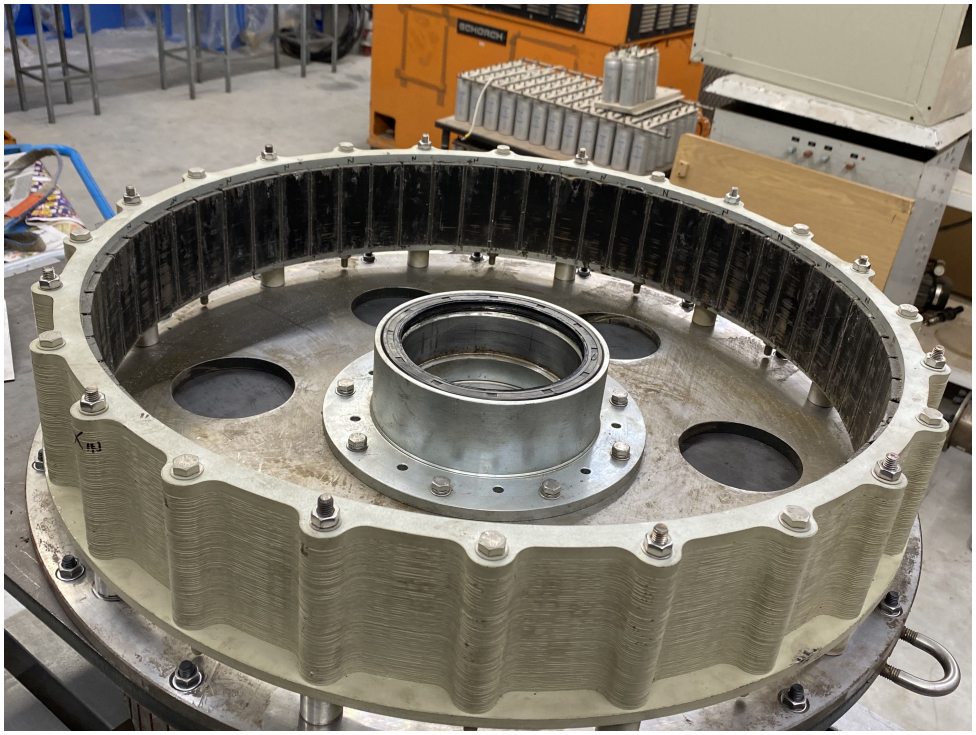

Figure 5.14: PM-rotor section of the built prototype 15 kW, 1000 Nm S-PMC shown in Fig. 5.13.

Figure 5.15: Wound-rotor section of the built prototype containing the short-circuited non-overlap aluminium coils of the 15 kW, 1000 Nm S-PMC shown in Fig. 5.13.

The small difference between the S-FE and measured results in Fig. 5.17 at low slip values is attributed to the inaccuracies in the coil temperature and torque sensor measurements. At low slip values, the S-PMC's coil resistance and thus performance is very dependent on the coil temperature. In contrast, at high slip values and frequencies, the performance of the S-PMC is dictated by the reactance of the coils. Furthermore,

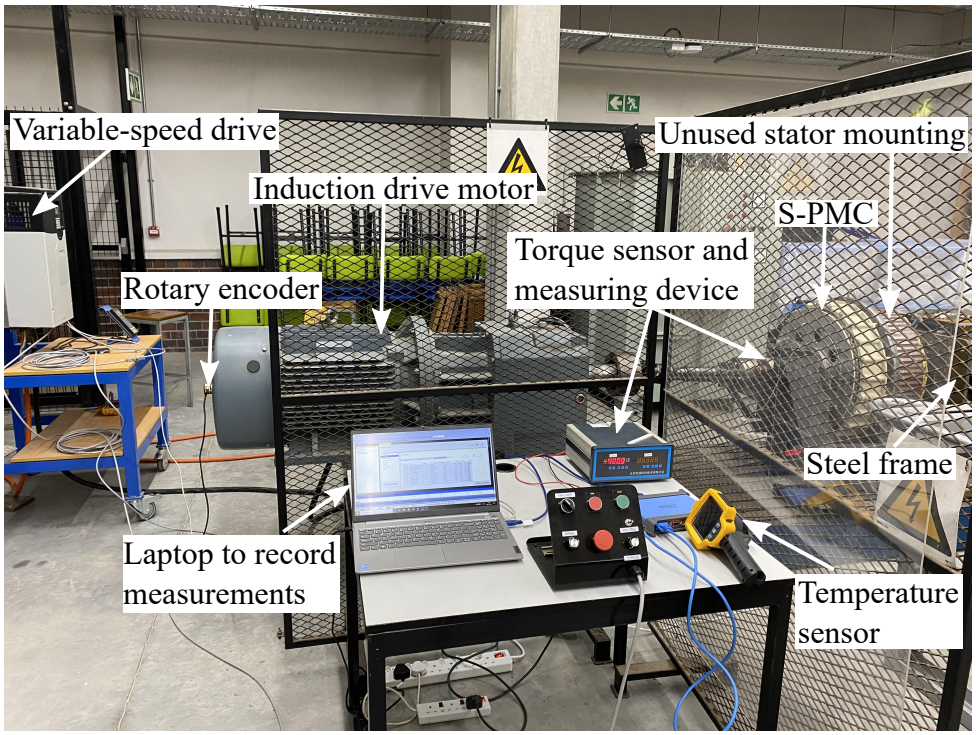

Figure 5.16: Test bench layout used to measure the performance of the S-PMC prototype.

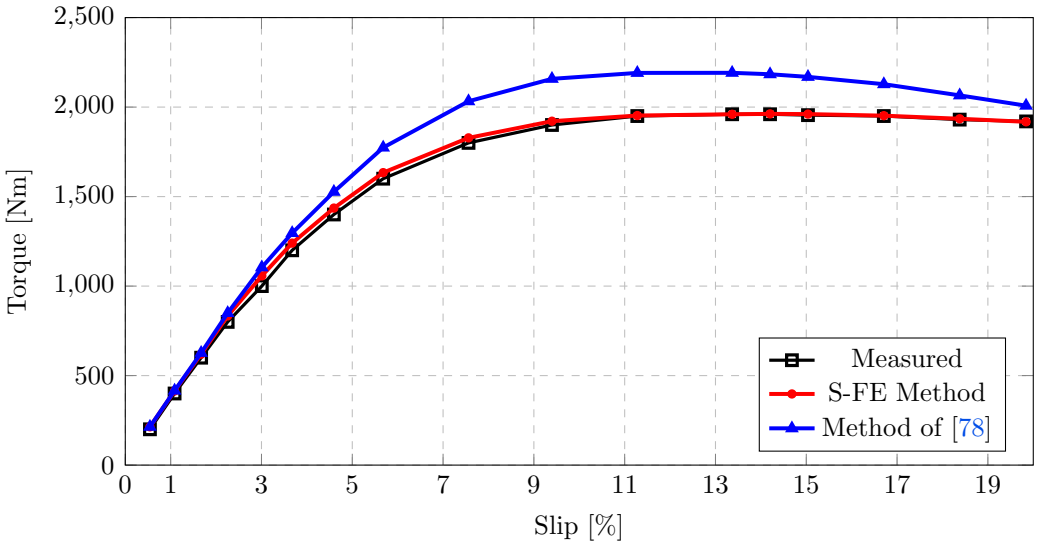

Figure 5.17: Torque versus slip comparison: measured results, proposed S-FE method, and the method of [78] for the prototype S-PMC shown in Fig. 5.13. Rated slip = 3 %.

it is evident from Fig. 5.17 that neglecting the core loss in (5.32) does not result in a significant error when predicting the torque of the S-PMC at very high slip values. At the very large 20% slip operating point, the operating frequency is only 14 Hz for the 1000 Nm coupler prototype. Thus, the induced core loss remains very small.

It took approximately 1 hour of continuous testing to obtain all the measurements shown in Fig. 5.17 (the total experiment thus took 2 hours to complete). Figs. 5.18a and 5.18b show temperature measurements of a short-circuited coil and of a magnet, respectively, immediately after all of the measurements of Fig. 5.17 were taken and the

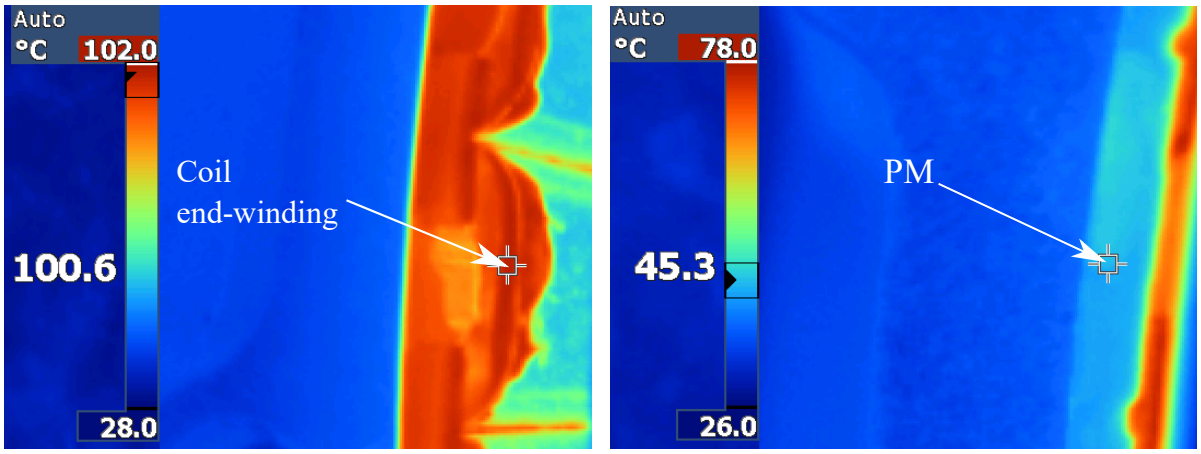

(a) (b)

Figure 5.18: Thermal camera images of the S-PMC prototype taken immediately after the measurements of Fig. 5.17, showing the temperature of (a) a coil-end of 100.6° C and (b) a permanent magnet of 45.3° C respectively after all of the measurements of Fig. 5.17 were taken.

S-PMC was brought to a standstill. Figs. 5.18a and 5.18b provide an indication of the change in temperature from the thermal equilibrium point at the beginning to the end of the experiment, and show that the N48H magnets and the aluminium coils of the S-PMC prototype do not overheat despite operating at various operating points significantly above rated conditions.

5.7 Discussion

Regarding Fig. 5.4, the average time taken for the proposed S-FE method to solve the S-PMC currents is approximately 100 seconds. The mesh used in the S-FE method consists of 12030 elements and 7001 nodes. This was done on an Intel(R) Core i7 CPU, with a clock speed of 3.40 GHz and 16 GB of RAM. In comparison, on the same computer and with a similar number of mesh elements (12988) and nodes (6928), the commercial T-FE program *JMAG* requires on average approximately 900 seconds to provide a convergent solution for the S-PMC currents. Hence, the proposed S-FE method is nine times faster than the T-FE solution, significantly reducing computation time, which is very important in design optimisation applications.

It should be noted that the proposed S-FE method presented in this paper considers the 5^{th} harmonic as the highest-order harmonic component present in the coil currents. However, the proposed method is suitable for predicting even higher-order harmonics. However, additional harmonics will result in longer simulation times. Furthermore, if certain higher-order harmonic currents are found to be negligible, the number of linear FE-solutions per iteration can be reduced, which will reduce the solution time of the proposed S-FE solution method.

Regarding Fig. 5.17, it is evident that a significant error is made when predicting the S-PMC's breakdown torque if the PM-flux linkages are assumed constant. This error would result in S-PMCs being "under"-designed incapable of generating the torque required to maintain stability during high wind speeds, grid faults or braking events [54].

Finally, S-PMCs typically operate at rated slip speeds of 1% to 3% above the synchronous speed of the SG in WTS applications. Furthermore, the efficiency of S-PMCs is inversely proportional to the slip percentage. Consequently, with WTS rarely operating at rated conditions, the S-PMC operates at near 100% efficiency in the WTS for extended periods during average wind speed conditions.

5.8 Chapter Summary

A 2-D static-FE modelling and performance solution method for iron-cored PM slip couplers (S-PMCs) is proposed and evaluated in this Chapter. Particular attention is given to the zero-sequence (3^{rd} harmonic) and 5^{th} harmonic parameters and the performance of the coupler over a wide slip-speed operating range.

It is found that the assumptions made in the literature regarding the influence of the dq-PM flux linkages on the machine performance can result in a significant error when predicting the maximum torque of the S-PMC.

The accuracy of the proposed 2-D static-FE solution method is theoretically verified over a wide operating range using 2-D transient-FE commercial package solutions of a theoretical 2.5 kW, 40 Nm S-PMC. The accuracy of the proposed solution method is further verified by measured results of a built 15 kW, 1000 Nm S-PMC prototype. Also, the proposed modelling and 2-D static-FE solution method is shown to be more accurate than previously proposed 2-D static-FE solution methods in the literature for these types of couplers.

Finally, an important advantage of the proposed S-FE solution method is that it provides insight into how the different modelling parameters of the S-PMC change versus slip speed. These modelling parameters can, for example, be incorporated into *MATLAB-SIMULINK* or into *DIGSILENT* to analyse the dynamic interaction of the WTS of Fig. 5.1 within an existing power system model.

Chapter 6

Measurements of a Prototype Hybrid-Excited Synchronous Generator

In this Chapter, the theoretical 15 kW hybrid-excited generator of Fig. 4.7b in Chapter 4 is built and its grid-connected performance is evaluated. The measured results of the built hybrid-excited generator serve as verification of the proposed hybrid-excited methodology. Practical tests are conducted in a laboratory to determine the prototype hybrid-excited SG's:

- synchronous reactance, X_s,
- grid-connected performance,
- grid-code compliance compatibility, and
- reactive power compensation capabilities.

6.1 Prototype Construction

Fig. 6.1a shows a finite-element cross-section model of the built 15 kW prototype hybrid-excited SG, and Fig. 6.1b shows sample laminations of the respective hybrid rotor and stator sections. Both stator and rotor laminations that form the iron cores are made of non-grain oriented M400-50A electrical steel. The hybrid rotor is constructed using

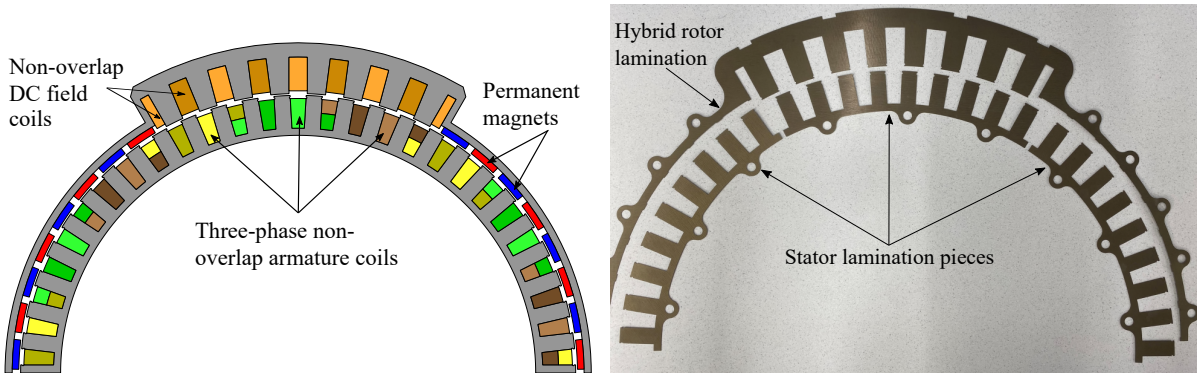

Figure 6.1: (a) Finite-element cross-section model of the 15 kW prototype SG, and (b) sample laminations of the hybrid rotor and stator sections of the prototype SG.

0.5 mm, half-section laminations, whereas the stator is constructed using six 0.5 mm lamination pieces that form one layer. Different stator layers are stacked in an "overlapping" configuration to improve the rigidity of the lamination stack. Figs. 6.2a and 6.2b show the fully constructed prototype stator and hybrid rotor sections respectively. In Fig 6.2b, the slip-rings that the rotor field windings are connected to are mounted to the rotor mounting plate. Table 6.1 gives the main parameters and dimensions of the built prototype SG.

The prototype SG is equipped with a three-phase, double-layer non-overlap stator winding. The stator winding is placed in 54 slots in a top-bottom configuration. The hybrid rotor is fitted with 32 permanent magnets and has 16 rotor teeth, each wound with 16 non-overlap DC-field coils in a side-by-side configuration. The DC-field coils on the hybrid rotor are energised using slip-rings and brushes. The carbon brushes are

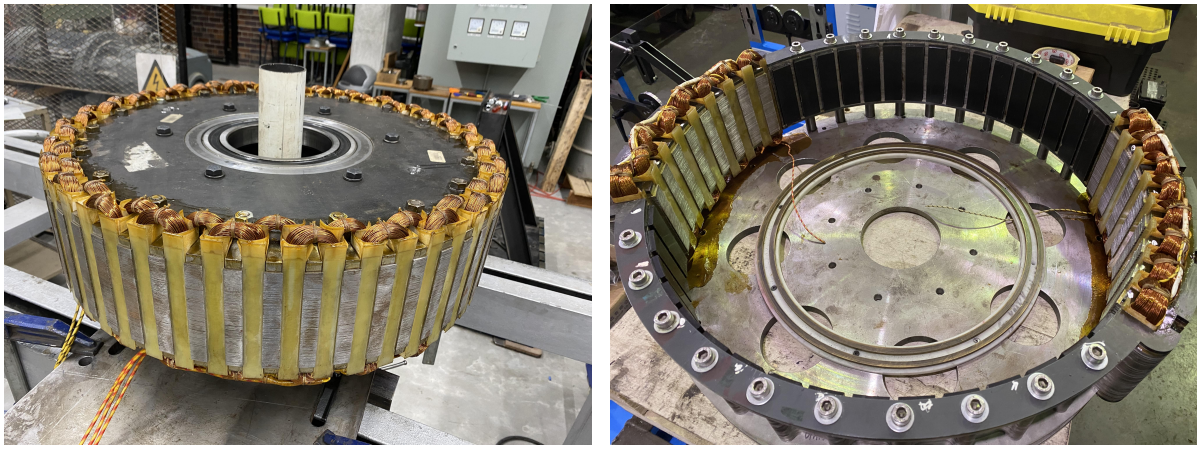

(a) **(b)**

Figure 6.2: Prototype SG construction: (a) wound stator unit and (b) hybrid rotor unit with PMs, DC-field windings and slip-ring mounting.

Table 6.1
Parameter and Dimension Values of the Built Prototype Hybrid-Excited Generator

Parameter	**Value**	**Dimension**	**Value**
Rated power	15 kW	Wound rotor outer diameter	750 mm
Rated voltage	400 V	Wound rotor yoke height	21 mm
Rated frequency	50 Hz	Wound rotor tooth height	42.3 mm
Rated speed	125 rpm	Wound rotor tooth width	21.4 mm
Rated stator current	21 A	PM rotor width	8.0 mm
Magnet poles	32	PM height	7.37 mm
Wound field poles	16	PM pitch	33 mm
Stator slots and coils	54	Airgap height	2.05 mm
Stator current density	6.0 A/mm^2	Stator tooth width	17.15 mm
Number of phases	3	Stator tooth height	36.28 mm
Stator series turns per phase	468 turns	Stator yoke height	8.0 mm
Stator winding resistance	0.9 Ω/phase	Lamination thickness	0.5 mm
Rotor current density	6.0 A/mm^2	Stack length	114 mm
Field circuit resistance	17 Ω	Stator inner diameter	530.8 mm

fitted inside insulated brush holders that are mounted to the stationary stator's end-plate.

As mentioned in previous Chapters, the slip-magnetic coupler (S-PMC) unit is an essential component within a slip-synchronous (SS) drivetrain. In testing the prototype SG, the S-PMC unit that was analysed and tested in Chapter 5 is mounted to the front of the prototype SG on a common mounting plate. Fig 6.3a shows the prototype stator and the assembled hybrid rotor, and the PM-rotor of the S-PMC, whereas Fig 6.3b shows the fully assembled S-PMC and SG units which are referred to as a slip synchronous permanent magnet generator (SS-PMG).

6.2 Laboratory Testing Setup

Fig. 6.4 shows a line diagram representation of the laboratory setup used to obtain the measured results of the SS-PMG. Figs. 6.5 and 6.6 show the laboratory testbench drivetrain that was used to conduct the experimental tests on the prototype SG. A 4-pole 75 kW induction machine (IM) that is equipped with a gearbox with a 15.1:1 gearing ratio serves as the prime mover in the experiment. The IM is controlled using an Allen-Bradly Powerflex 755 variable-speed drive (VSD). The input torque supplied to the SS-PMG by the IM is measured using a 5000 Nm STKC M&E Technologe torque sensor. A three-phase rectifier and a filter capacitor are used to rectify the AC grid voltage to supply the DC voltage and current required by the rotor field windings. A variable voltage transformer is connected between the three-phase rectifier and the grid connection point to allow the voltage across the field coils to be controlled. The SS-PMG's generated voltage, line currents and power are respectively measured using two PicoScope 4444 high-resolution differential PC oscilloscopes, and set of analog voltmeters and ammeters are used for verification. From Fig. 6.4, a set of synchronisation lights in conjunction with the PicoScopes are used to monitor and connect the SS-PMG to the grid once the SS-PMG's respective frequency, voltage magnitude and phase angle are within the required specification for grid connection.

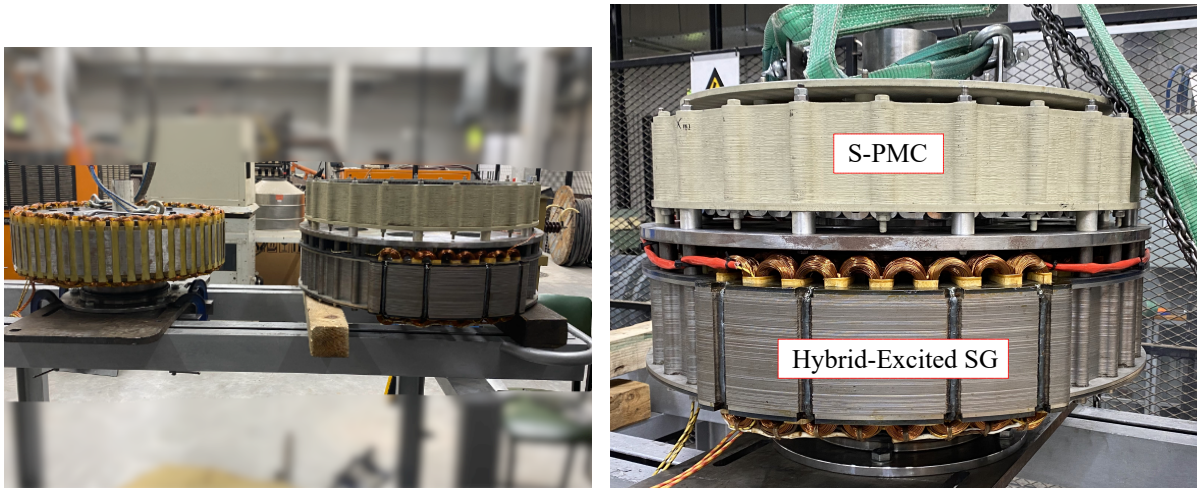

(a) **(b)**

Figure 6.3: Prototype SS-PMG construction: (a) SG stator and common PM-rotor sections and (b) the fully assembled SS-PMG.

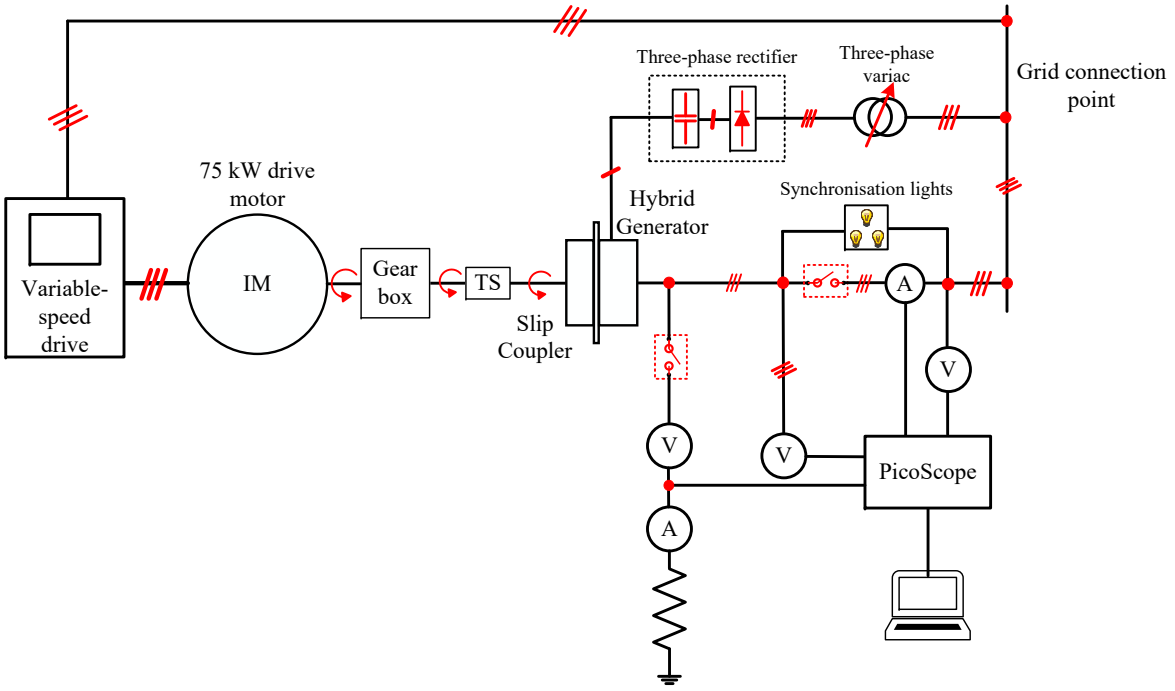

Figure 6.4: Line diagram representation of the laboratory setup used for testing the prototype SG.

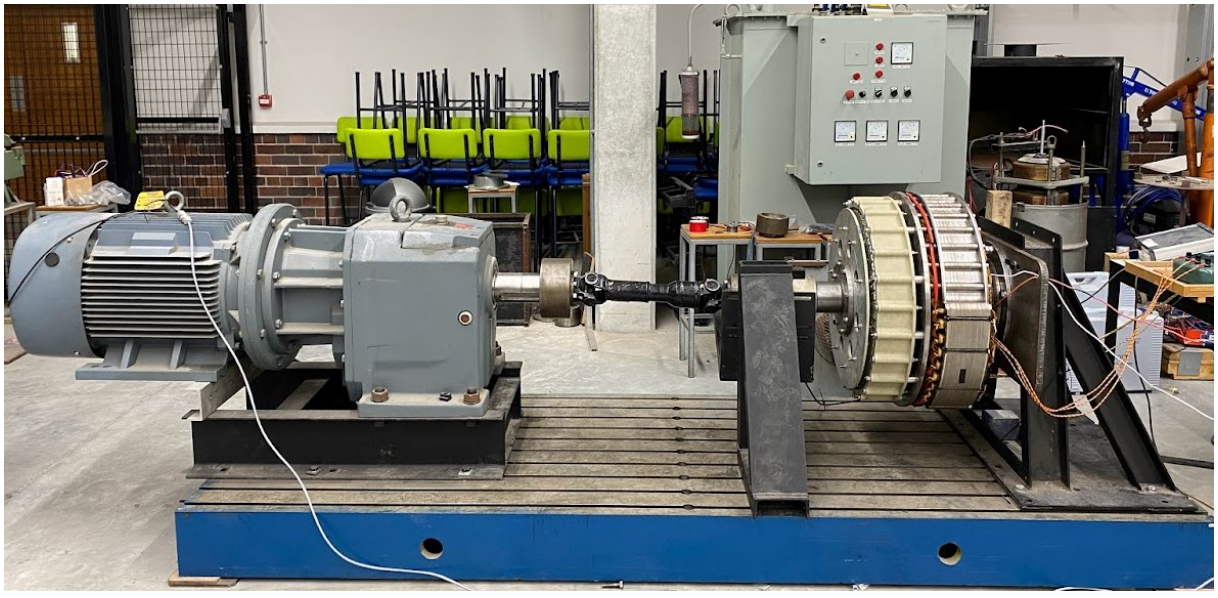

Figure 6.5: Prototype 15 kW SS-PMG on the testbench connected to an induction drive motor by means of a torque sensor (for the torque sensor, see Fig. 6.6).

6.3 Synchronous Machine Open- and Short-Circuit Measurements

This section presents the results of an open-circuit and short-circuit test with field current as a parameter. The respective open- and short circuit measurements are used to determine the per phase inductance and hence reactance of the prototype SG.

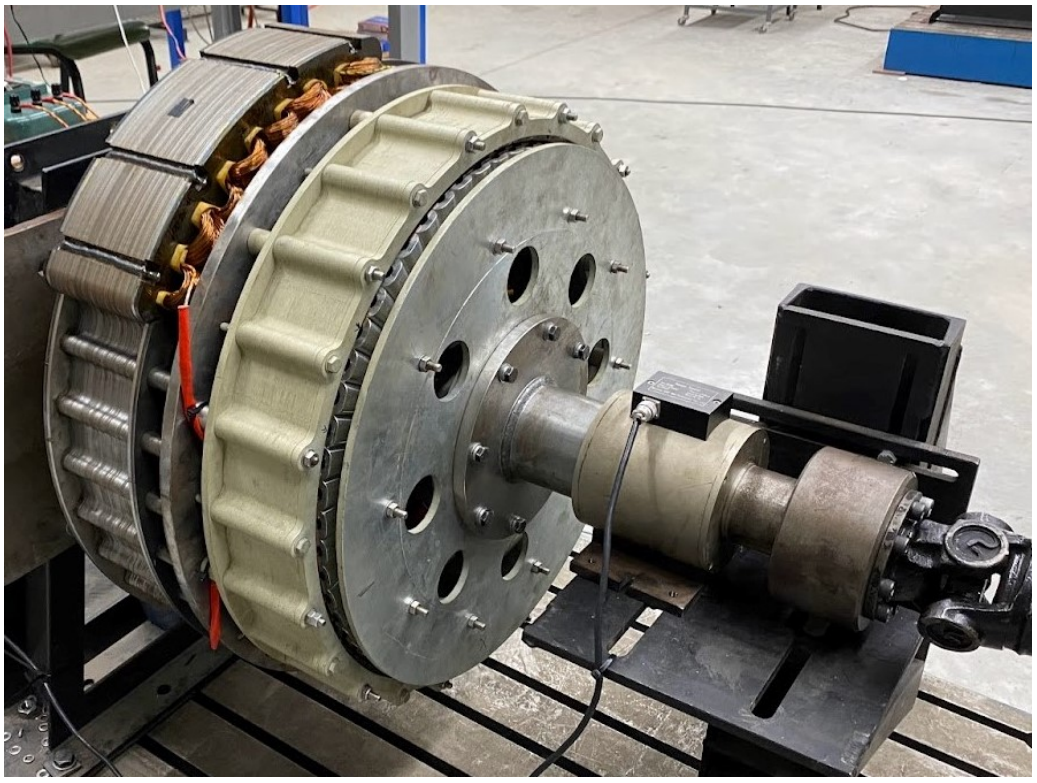

Figure 6.6: Prototype 15 kW SS-PMG on the testbench connected to a 5000 Nm torque sensor.

6.3.1 Open-Circuit Test

Fig. 6.7a shows the measured and FE-predicted open-circuit line voltage waveforms with field current as a parameter at rated speed for the prototype hybrid-excited SG. Furthermore, Fig. 6.7b shows the RMS value of the open-circuit line voltage versus frequency with field current as a parameter. It is worth noting how sinusoidal the open-circuit voltage waveforms are, especially with zero field current applied to the field windings. Moreover, from Fig. 6.7b the prototype SG achieves rated line voltage (400 V) at rated speed (125 rpm or 50 Hz) with 5 A_{dc} field current. Additionally from Fig. 6.7b, it is evident that increasing the field current from 5 A_{dc} to 10 A_{dc} results in a 14% boost in the RMS open-circuit voltage, whereas decreasing the field current from 5 A_{dc} to 0 A_{dc} results in a 17% reduction in the open-circuit voltage.

6.3.2 Short-Circuit Test

In the short-circuit test, an external three-phase resistor bank with a resistance value of $R_{ext} = 4\ \Omega$/phase is added to the generator's terminals to increase the the frequency at which the machine's rated current occurs. Figs. 6.8a and 6.8b show the measured and FE-predicted short-circuit current versus frequency with no field current, $I_f = 0$ A. Similarly, Figs. 6.9a and 6.9b show the measured and FE-predicted short-circuit current versus frequency with a field current of $I_f = 5$ A.

From Figs. 6.8a and 6.9a it is evident that there is a good agreement between the respective measured and FE-predicted results for the short-circuit current. However, from Figs. 6.8b and 6.9b, it is evident that a good agreement between the respective measured and FE predicted results for the per phase inductance is only achieved near the rated frequency of 50 Hz. The discrepancy between the respective measured and FE

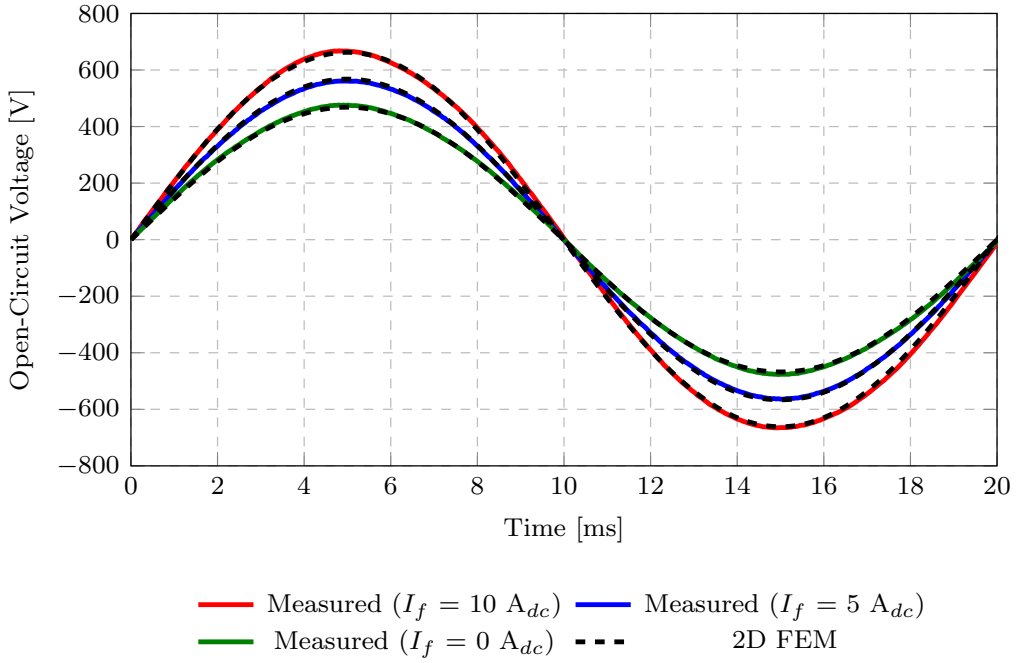

(a)

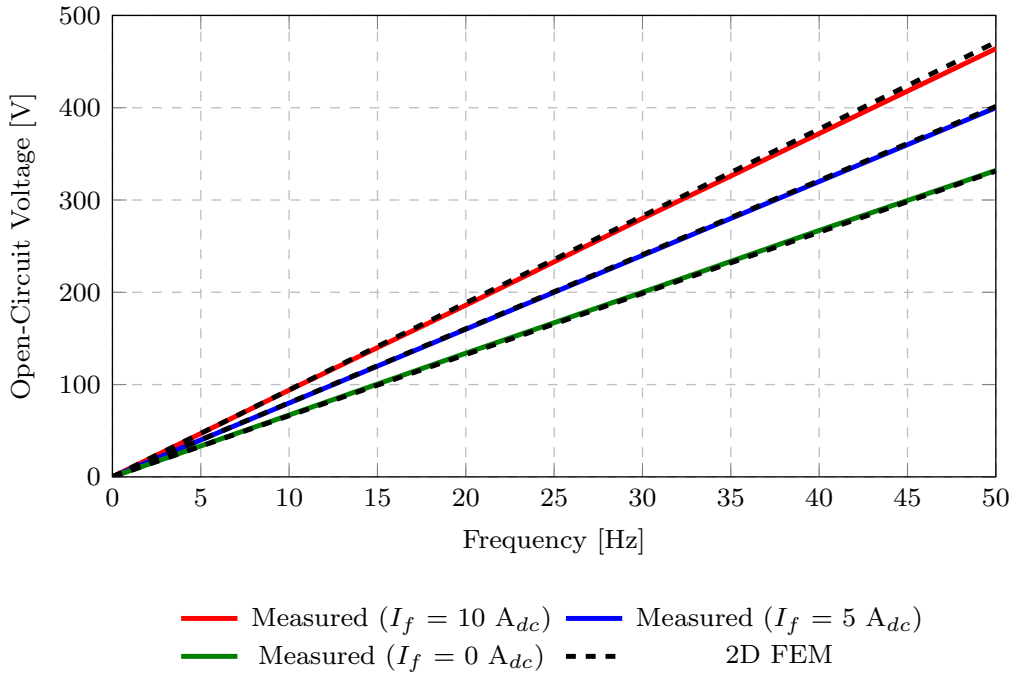

(b)

Figure 6.7: Measured and FE-predicted open-circuit line voltage with field-current as a parameter of the prototype SG: (a) at rated speed versus time, and (b) versus frequency.

predicted results in both Figs. 6.8b and 6.9b is due to inaccuracies in the measured current at those low frequencies, similar findings have also been reported in [45]. Nevertheless, from Fig. 6.9b, it is evident that with rated field current, the per phase inductance of the prototype SG is approximately 19 mH. Thus, the per-phase synchronous reactance of the

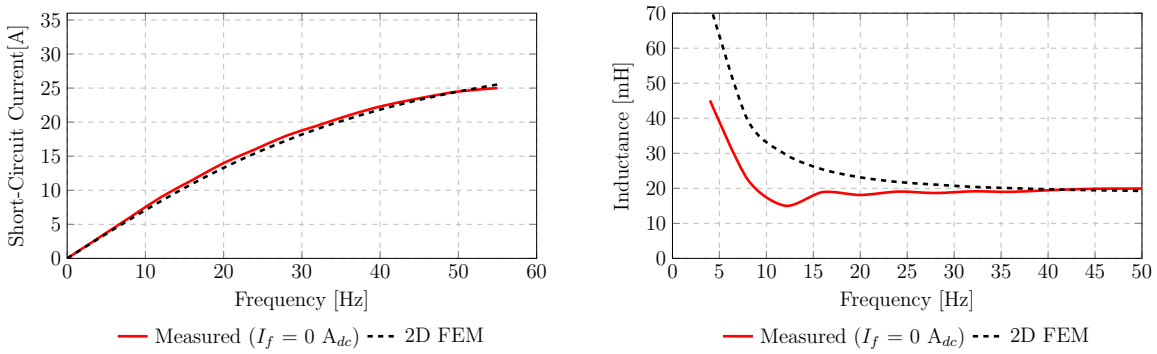

(a) **(b)**

Figure 6.8: Prototype SG measured and FE predicted: (a) short-circuit current and (b) per phase inductance versus frequency with field current, $I_f = 0$ A.

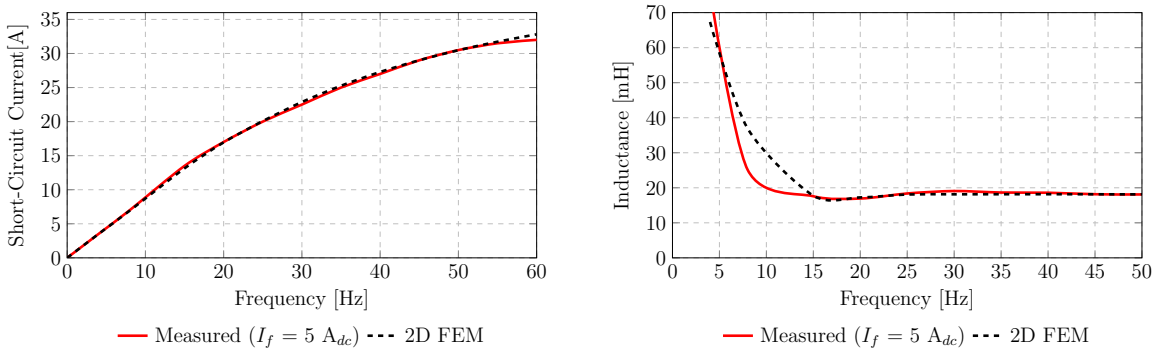

(a) **(b)**

Figure 6.9: Measured and FE-predicted short-circuit test results of the prototype SG: (a) short-circuit current and (b) per phase inductance versus frequency with field current, $I_f = 5$ A.

prototype SG is approximately $X_s = 6\ \Omega$/phase or 0.56 per unit, which is similar to the FE-predicted synchronous reactance value in Table 4.3 in Chapter 4.

6.4 Grid-Connected Tests

According to [50], renewable power plants (RPPs) with a rated power of greater than 13.8 kVA but less than 100 kVA are categorised as "Category A2" RPPs. The grid-code requirements for Category A2 RPPs are summarised as follows:

1) Category A RPPs must be designed to be capable of continuous operation within the voltage range of -15% to +10% around the nominal voltage at the point of connection (POC) [50].

2) Unless otherwise specified by the Network Service Provider or the System Operator, RPPs of category A1 (power ratings sub 13.8 kVA) and A2 shall operate at unity power factor as measured at the POC [50].

It was shown in Chapter 3 that a grid-connected PMSG unit within a slip synchronous drivetrain is capable of continued operation despite changes in grid voltage. Consequently

in this section, the focus is on the second grid-code requirement where the prototype SG's grid-connected performance with respect to operating at unity power factor is evaluated. In addition, the prototype SG's reactive power compensation capabilities are evaluated in this section.

6.4.1 Performance Evaluation at Unity Power Factor

Figs. 6.10a and 6.10b show the electrical output power and line current versus per unit load torque of the prototype SG. During the experiment, the required field current to maintain a unity power factor at each operating point is obtained using the solution method outlined by equations (4.13) to (4.22) in Chapter 4. The required field current and reactive power versus load torque of the prototype SS-PMG are shown in Figs. 6.10c and 6.10d respectively. Additionally in Fig. 6.10d, measured power factor (PF) values at selected load torque conditions are indicated by red dots. From Figs. 6.10a to 6.10d, it is evident that a good correlation between the measured results and the results of the 2D-FE solution method of Chapter 4 for this type of hybrid-excited SG is achieved.

From Fig. 6.10d, it is evident that the prototype SS-PMG is able to operate approximately at unity power across its load range. The small differences between the

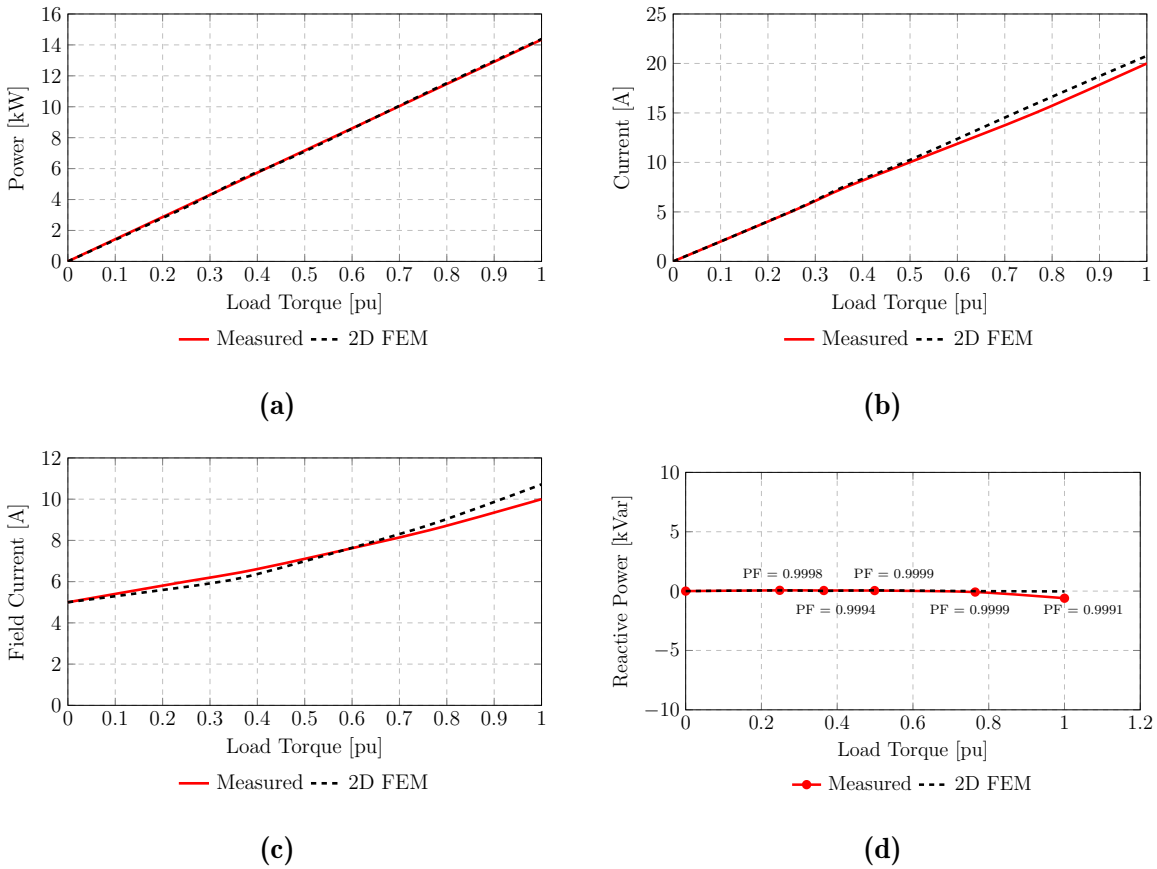

Figure 6.10: Grid-connected measured and FE-predicted results of the prototype SG: (a) active power, (b) line current, (c) field current, and (d) reactive power versus generator load at approximately unity power factor operating conditions. In (d), power factor (PF) values at selected measured operating points are indicated with red dots.

FE and the measured results in Fig. 6.10d are attributed to errors in the reactive power measurements. However, in Fig. 6.10d, it is evident that a small amount of reactive power is being absorbed from the grid at 1 per unit loading, which causes the power factor to noticeably deviate from unity. The deviation from unity power factor can be explained from Fig. 6.10c. In Fig. 6.10c, it can be seen that the FE-predicted field current required to achieve unity power factor at 1 per unit loading is slightly more than the maximum field current that could be supplied during the experiment, i.e., 10 A_{dc}. Consequently, at 1 per unit loading, the prototype SS-PMG is slightly under-magnetised. Nevertheless, the 2D FEM results suggest that the built prototype hybrid-excited SG would be capable of operating at unity power if the requisite field current was supplied.

Fig. 6.11a shows the FE predicted efficiencies of the S-PMC unit and the prototype SG respectively. From Fig. 6.11a, it is evident that a good agreement between the measured results and the predicted FE results is achieved. The prototype SG's relatively low efficiency is attributed to the large field winding resistance and the additional losses incurred by the slip-rings and brushes. Fig. 6.11b shows the FE predicted stator copper losses, rotor copper losses and iron core losses, respectively. From Fig. 6.11b, it is evident that at rated conditions, the rotor copper losses account for approximately 57% of the total losses of the prototype SG.

6.4.2 Reactive Power Compensation

Figs 6.12a, 6.12b, and 6.12c show the measured per phase voltage and the line current at unity, leading and lagging power factors respectively. In Figs 6.12a, 6.12b, and 6.12c, the electrical power output of the generator was kept near 0.5 per unit and the field current was varied from 3.8 A to 10 A. From Fig. 6.12a, it can be seen that a field current of 7.3 A is required to achieve unity power factor. Moreover, from Fig. 6.12c, a field current of 3.8 A is required to absorb -0.23 per unit reactive power from the grid whereas a field current of 10 A is required to supply +0.19 per unit reactive power to the grid. Figs. 6.12b, and 6.12c are included merely to demonstrate the reactive power compensating capabilities of the prototype SG since reactive power compensation is not required for RPPs of Category A2. According to [50], reactive power compensation is only a requirement for RPPs with a power rating greater than 100 kVA.

6.5 Chapter Summary

In this Chapter, a prototype 15 kW SS-PMG is practically evaluated. Various open- and short-circuit tests with field current as a parameter are conducted to determine the prototype SG's per phase inductance and thus per phase reactance. Furthermore, the prototype SG's grid-connected performance is evaluated. The 15 kW prototype SG can operate at unity power factor by suitably varying the rotor field across its load range. Consequently, the built prototype SG is grid code compliant. Although not a grid code requirement, the prototype SG's reactive power compensation capabilities are also shown. The prototype SG can supply a maximum of +0.19 per unit of reactive power to the grid at 0.5 per unit active power, which demonstrates the prototype SG's grid support capabilities. The measured results in this Chapter serve to verify the proposed hybrid-excited method and solution method for grid-tied hybrid-excited SGs developed in Chapter 4.

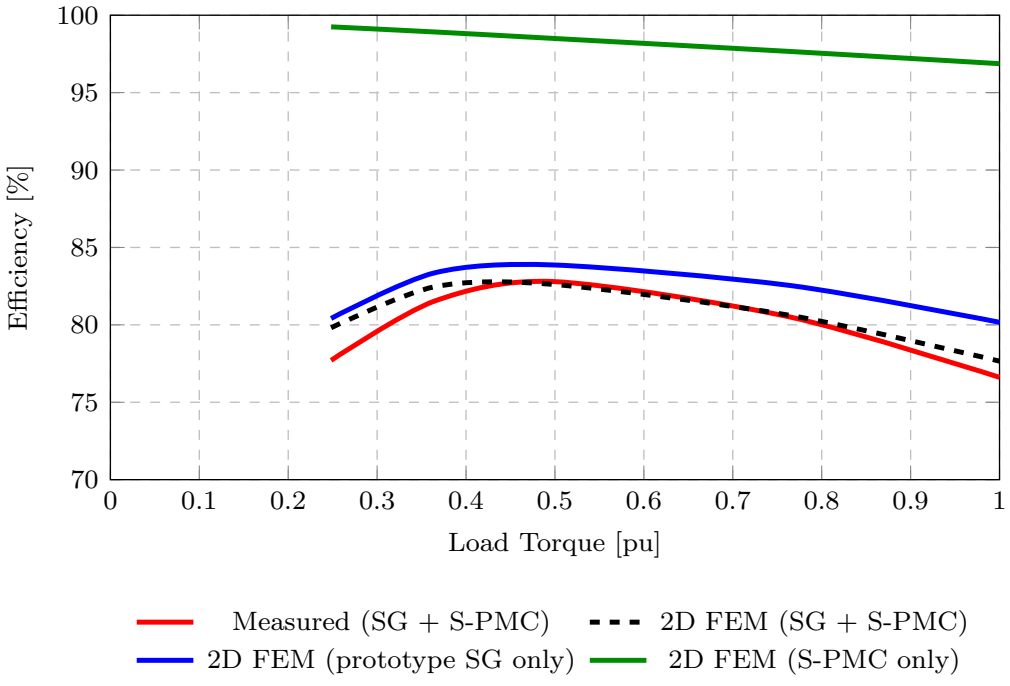

(a)

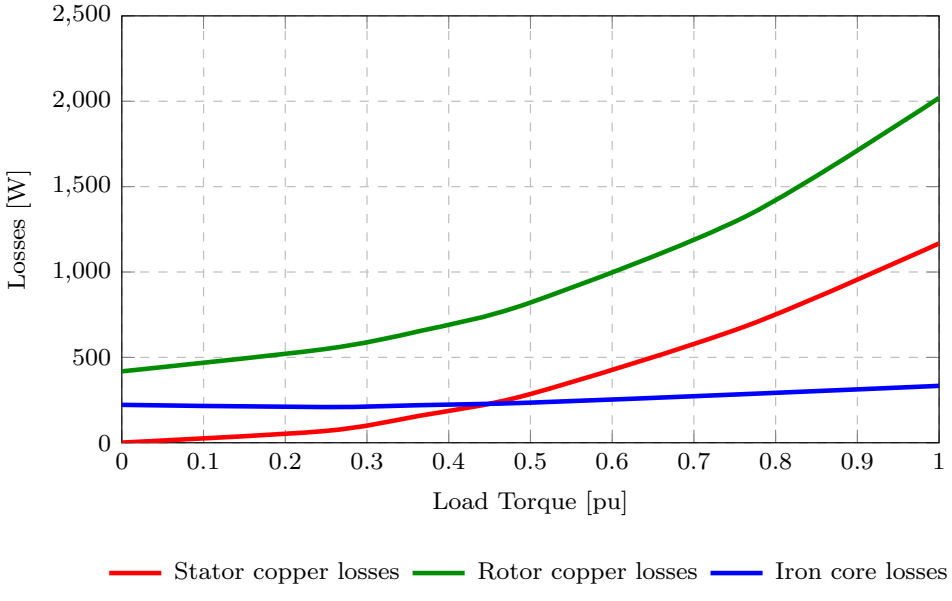

(b)

Figure 6.11: Grid-connected measured and FE-predicted results of the prototype SG: (a) measured efficiency versus loading, and (b) FE-predicted losses of the prototype SG.

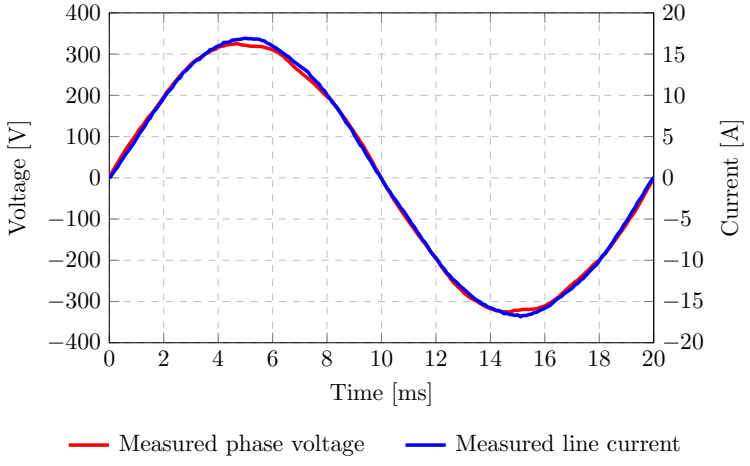

(a)

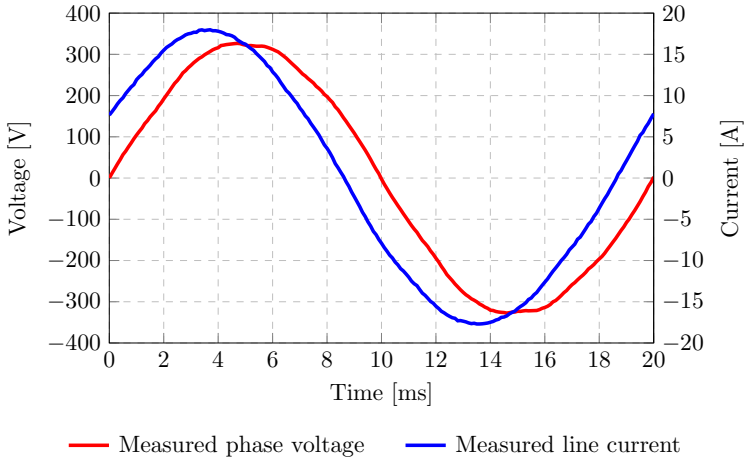

(b)

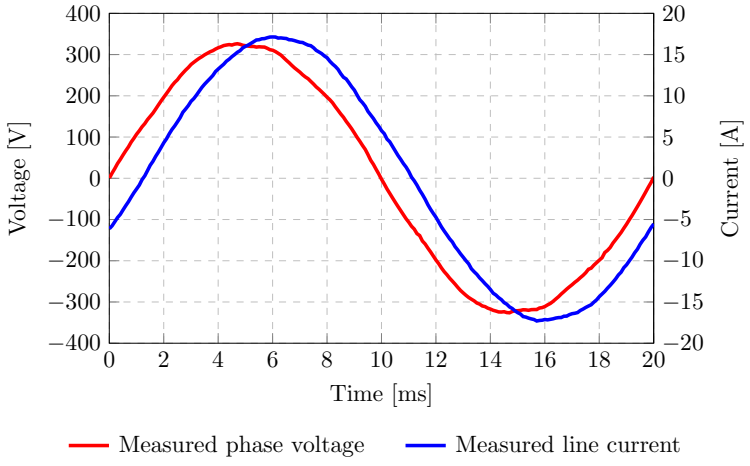

(c)

Figure 6.12: Prototype SG measured phase voltage and line current at 0.5 per unit power: (a) unity power factor with field current = 7.3 A, (b) lagging power factor with field current = 3.8 A and Q = -0.23 pu Var, and (c) leading power factor with field current = 10 A and Q = +0.194 pu Var. Voltage is shown on the primary y-axis and current is shown on the secondary y-axis.

Chapter 7

Design and Evaluation of 3-MW Geared Slip Synchronous Wind Turbine Drivetrains

In this Chapter, the modelling and analysis frameworks developed in Chapters 3 to 5 are used to design and evaluate two slip-magnetic couplers (S-PMCs) for two geared drivetrain topologies. In the analysis, a medium-speed 3 MW hybrid-excited generator is used for both drivetrain topologies, however, the focus of this Chapter is to compare (i) a medium-speed and (ii) a low-speed S-PMC in terms of its cost-per-kW contribution to the SS-drivetrain. The two geared SS drivetrains are then compared against one another in terms of their respective drivetrain active mass and active cost, where "active" refers to the drivetrain components responsible for converting the aerodynamic torque from the turbine blades to electrical power output. Finally, the cost and drivetrain mass of the two considered geared SS-drivetrains are compared with a conventional, converter-tied drivetrain reported in the literature.

7.1 Modern Wind Turbine Systems

Table 7.1 provides information on some of the commercially available wind turbine (WT) drivetrains from world-leading manufacturers. From Table 7.1, it can be deduced that the doubly-fed induction generator (DFIG) with a partially-rated converter (PRC) and a high-speed (three-stage) gearbox is the preferred drivetrain for applications below 6 MW [84]. Moreover, the permanent magnet synchronous generator (PMSG), equipped with a full-rated converter (FRC), is the preferred drivetrain for higher power applications, particularly offshore installations [84]. This section provides a summary of the advantages and disadvantages, as reported in the literature, of the WTSs given in Table 7.1.

7.1.1 DFIG Wind Turbine Systems

The prominence and market dominance of the DFIG-based wind turbine system (WTS) is attributed to its market maturity, which has led to cost-competitive, and low-complexity drivetrain configurations [93]. DFIG-drivetrains operate at high rotational speeds and low input torque ranges, allowing for smaller, low-pole-number and hence less complex generator designs. Moreover, DFIG-based drivetrains don't require expensive permanent magnet material and only need a partially-rated converter, unlike the full-rated converters

required by synchronous-generator based WTS. As a result, the DFIG-based wind turbine drivetrain is comparatively lighter and less expensive than lower-speed PMSG-based WT drivetrains [93].

However, DFIG-based WTSs are reported to be less reliable than equivalent PMSG-based WTSs [93, 94]. It is further argued that DFIG-based WTSs aren't suited to offshore applications due to the higher risk of unplanned (and thus more expensive) operation and maintenance (O&M) costs that stem from using high-speed gearboxes, slip-rings, and brushes [94, 93, 95, 96, 97, 98, 99, 100]. Nevertheless, the DFIG-PRC concept is expected to remain the preferred choice for onshore WT installations for the foreseeable future. This is partly because of its technological maturity and because the O&M costs for onshore WTSs are significantly less than for offshore WTSs [94]. Furthermore, it is argued that the relatively high O&M expenses incurred by DFIG WTSs are offset by its cost-effective and straightforward drivetrain configuration, which results in a competitive cost-of-energy-production when compared to PMSG-FRC drivetrains for onshore applications [99, 100, 101, 102, 103].

7.1.2 Direct-Drive Wind Turbine Systems

From Table 7.1, the direct-drive permanent magnet synchronous generator (DD-PMSG) with a full-rated power converter is the preferred drivetrain for multi-MW and offshore installations. Various studies have found that DD-PMSG WT-drivetrains are more reliable than DFIG-based and geared PMSG WTSs because they do not have field windings requiring slip-rings and brushes or a gearbox. The omission of the gearbox, slip-rings and brushes inherently increases the reliability of DD-PMSG drivetrains and lowers its O&M costs [93, 94]. Furthermore, DD-PMSG drivetrains are consistently reported to have lower values for cost-of-energy-production compared to geared drivetrains in offshore applications [99, 100, 101, 102, 103].

However, there are concerns regarding the reliability of the full-rated converter (FRC), particularly in direct-drive PMSG WTS [94]. Additionally, there are concerns regarding the volume and mass of direct-drive PMSGs. Direct-drive PMSGs operate at low rotational speeds and thus require a large diameter and volume compared to high- and medium-speed drivetrains with the same power rating. Consequently, large multi-MW direct-drive WTSs need more electromagnetic material when compared to geared PMSG drivetrains as the amount of PM material required is proportional to the size of the machine and inversely proportional to its speed [84, 103, 104]. Nevertheless, it is argued that

Table 7.1: Commercially Available Wind Turbine Drivetrains from World-Leading Manufacturers

Manufacturer		Capacity	Generator type	Converter	Gearbox	Reference
General Electric	Onshore	2 MW, 3 MW	DFIG	Partially-rated	High-speed	[85]
	Offshore	6 MW, 12 MW, 13 MW, 14 MW	DD-PMSG	Full-rated	-	[86]
Goldwind	Onshore	1.1 MW, 3 MW, 5 MW, 6 MW	DD-PMSG	Full-rated	-	[87]
	Offshore	6.45 MW, 8 MW	DD-PMSG	Full-rated	-	[88]
Vestas	Onshore	2 MW	DFIG	Partially-rated	High-speed	[89]
		3 MW, 4 MW	PMSG	Full-rated	High-speed	
	Offshore	9.5 MW, 10 MW, 15 MW	PMSG	Full-rated	Medium-speed	[90]
Siemens Gamesa	Onshore	2.1 MW, 3.4 MW, 6.6 MW	DFIG	Partially-rated	High-speed	[91]
	Offshore	6 MW, 7 MW, 8 MW	DD-PMSG	Full-rated	-	[92]

DFIG - doubly-fed induction generator
PMSG - permanent magnet synchronous generator
DD-PMSG - direct-drive permanent magnet synchronous generator

the inherently high reliability of DD-PMSG drivetrains offsets the costs associated with the increased mass, which would explain the preference for using the direct-drive concept for offshore and particularly high-power (+10 MW) applications [99, 100, 103].

7.1.3 Geared Permanent Magnet Wind Turbine Systems

Geared high- and medium-speed drivetrains concepts allow the size and mass of the generating unit to be reduced for a given power rating. For geared-PMSG wind turbine concepts, reducing mass and required PM material is a significant advantage over direct-drive wind turbine concepts. Furthermore, geared PMSG-FRC drivetrains are reported to have higher values for availability and lower O&M costs when compared to DFIG WTSs of the same power rating [94]. The increased availability makes the geared PMSG-FRC concept the preferred geared concept for offshore applications [93, 94, 99, 100].

However, the reliability of the FRC, in conjunction with the prolonged downtimes of gearboxes, remains a significant point of concern. In [94], the gearbox is noted as being the leading cause of downtime for three-stage (high-speed) geared PMSG-FRC drivetrains. However, for two-stage (medium-speed) geared PMSG-FRC drivetrains, the FRC converter contributes the most to downtime, followed by the gearbox and then the generator.

7.2 Geared Slip-Synchronous Wind Turbine Drivetrains

From Chapter 2, it is evident that much of the prevailing literature regarding SS-WTSs has focused on direct-drive drivetrains. Moreover, one of the main concerns regarding SS-WT technology is the added mass and cost associated with the S-PMC unit in the SS-drivetrain. Thus, from Chapter 2 and from the general concerns regarding the size, mass and cost of direct-drive WTSs, an argument can be made for considering geared SS-WTSs. The reason for this is that the S-PMC unit only transfers torque within the drivetrain; hence its size, weight and material costs scale with rated torque and not necessarily rated power. The inclusion of a drivetrain gearbox would allow for higher drivetrain speeds and lower input torque ranges, which would reduce the overall size and mass of the S-PMC.

Figs. 7.1a and 7.1b show two geared SS-WTSs where the S-PMC unit is either on the high-speed side of the geared SS-WTS or it is on the low-speed side of the geared SS-WTS. In this and the following sections, we compare the two geared drivetrains shown in Figs. 7.1a and 7.1b to a theoretical converter-tied geared WTS shown in Fig. 7.1c.

7.2.1 Multi-MW Hybrid-Excited SG Design Methodology

Fig. 7.2 shows a cross-section model of the 3-MW, medium-speed hybrid-excited generator considered in this section. The hybrid-excited generating unit is designed according to the constraints listed in Table 7.2 and the design and analysis methodologies outlined in Chapter 4. Thus, the hybrid-excited generator is grid code compliant according to the requirements of a 3-MW wind turbine system (See Appendix A). The same 3-MW medium-speed hybrid-excited generator is used for both geared SS-drivetrains of Figs. 7.1a and 7.1b. It should be noted that the hybrid-excited synchronous generator has not been

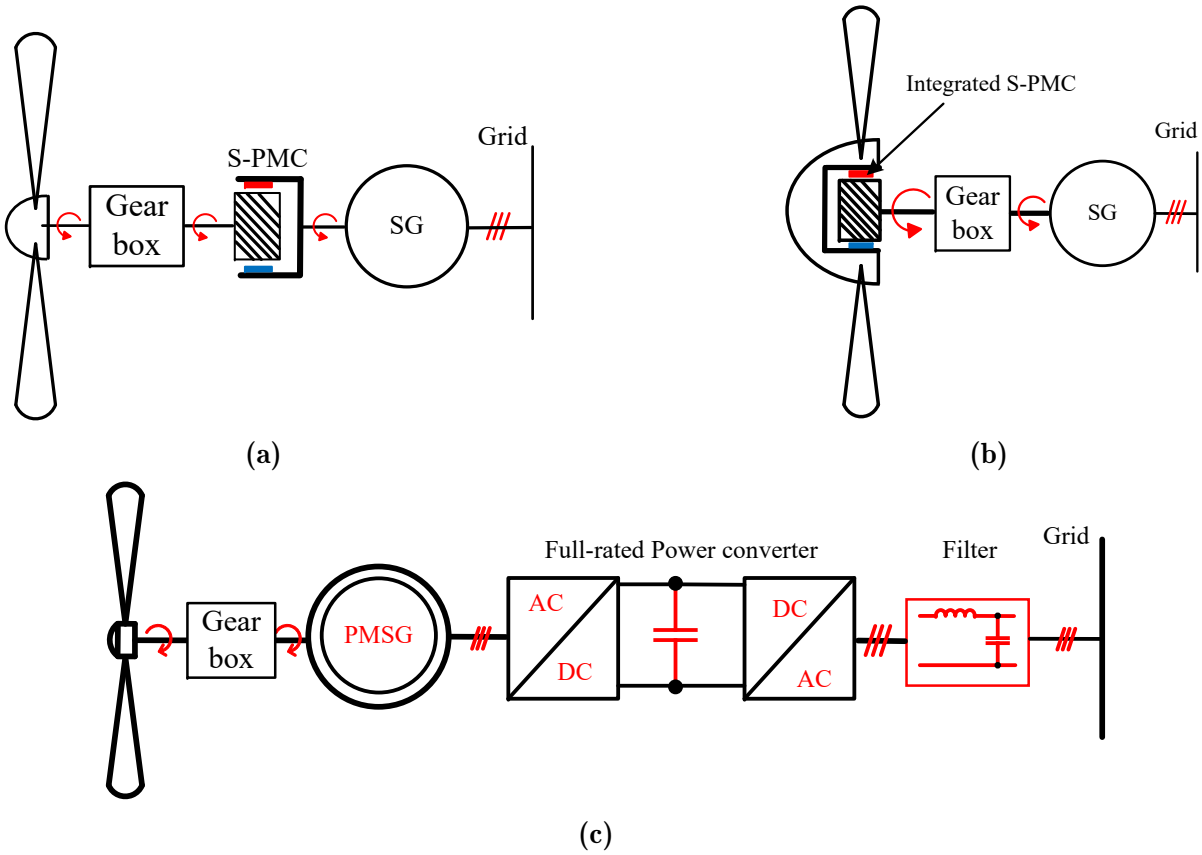

Figure 7.1: Line diagram representations of (a) a geared SS-drivetrain with the a medium-speed slip-coupler, (b) a SS-drivetrain with a direct-drive slip-coupler, and (c) a geared, converter-tied PMSG wind turbine system.

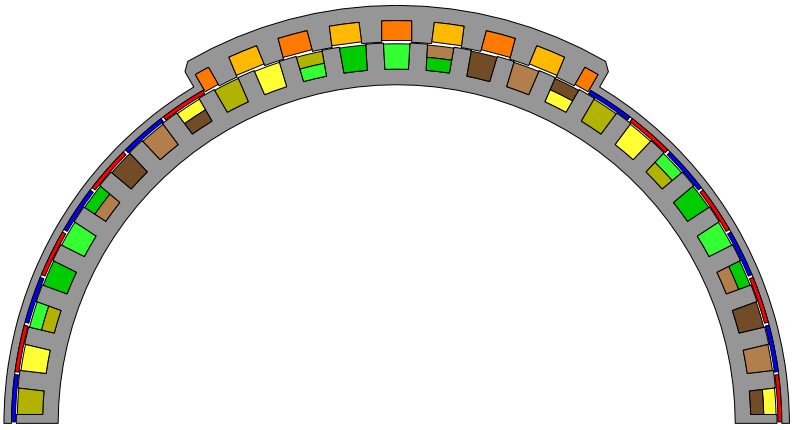

Figure 7.2: Finite-element cross section model of a medium-speed, 3-MW hybrid-excited synchronous generator.

optimised and is used merely to provide an indication of the mass and the cost of a 3-MW medium-speed hybrid-excited generator within an SS-WT drivetrain.

7.2.2 Multi-MW S-PMC Design Methodology

Unlike the hybrid-excited generator, there is a large degree of flexibility in selecting the pole-slot combination of slip-magnetic couplers (S-PMCs). This is because the electromagnetic frequency of the S-PMC is not dependent on the grid's electrical frequency.

Table 7.2: Design Constraints of the Considered 3-MW Medium-Speed, Grid-Tied Hybrid-Excited Generator of Fig. 7.2.

Parameter	Unit	Value
Rated Power, P_s	[MW]	3.0
Grid line voltage, V_L	[V]	6 600
Grid frequency, f_s	[Hz]	50
Copper fill factor f_{cu}	[-]	0.45
Stator current density, J_s	[A/mm^2]	$\leq$ 6.0
Rotor current density, J_r	[A/mm^2]	$\leq$ 6.0
Magnetic sheer stress, σ_m	[kN/m^2]	$\leq$ 25
Short-circuit current, I_{ss}	[pu]	$2.0 \leq I_{ss} \leq 4.5$

However, it is advisable to keep the slip frequency as low as possible to mitigate the effects of the bar-skin effect. An initial rated slip frequency of between 0.5 Hz and 1.5 Hz is selected for the considered S-PMCs. As with the hybrid-excited SG, the design constraints placed on the short-circuited coil current density J_{ss} and magnetic sheer stress σ_{ms} of the considered S-PMC are limited to those as given in Table 7.2, i.e., $J_{ss} = 6$ A/mm^2 and $\sigma_{ms} \leq 25$ kN/m^2 respectively. In the following section, the initial MS and LS S-PMCs designs are unoptimised but are designed to be capable of achieving a maximum torque value of $T_{max} \approx 2$ pu.

7.3 Case Study: SS-Drivetrain Cost Comparison

Table 7.3 gives the main design specifications and cost indicators of the respective geared drivetrain concepts of Fig. 7.1, and Table 7.4 gives additional machine dimensions for the hybrid-excited generator of Fig. 7.2 and the converter-tied PMSG of Fig. 7.1c which can be found in [101]. The full set of design specifications for the MS- and LS S-PMCs are given in the following sections. In the analysis, the cost of the respective active materials are chosen based on commonly referenced values in the literature [101, 105, 106, 107, 108, 109] and are given here as:

- PM-material cost [109] = \$192/kg,
- Laminated electrical steel cost = \$4.2/kg,

Table 7.3: Comparison of Selected Dimensions and Performance Indicators of the 3-MW Geared Drivetrains of Fig. 7.1.

	SS-drivetrain (Fig. 7.1a)		SS-drivetrain (Fig. 7.1b)		Converter-tied drivetrain (Fig. 7.1c [101])
	S-PMC	Hybrid SG	S-PMC	Hybrid SG	PMSG
Rated speed [mm]	125	125	19.5	125	90
Number of poles	112	48	392	48	112
Number of slots	120	54	420	54	336
Air gap radius [mm]	1 604	1 503	2 974	1 503	1 800
Air gap clearance [mm]	3.43	3.5	6.3	3.5	3.6
Axial length [mm]	1 040	905	2 350	905	400
*Active material cost (\$)	184 750	361 492	1 042 806	361 492	201 226
Gearbox cost (\$)	362 318		362 318		362 318
*Converter cost (\$74.5/kW)	—		—		223 500
Drivetrain cost-per-kW (\$/kW)	302.8		588.9		262.3

* Includes the structural costs associated with the unit's mass [105].

Table 7.4: Machine Dimensions of the Generating Units of the Hybrid-Excited Generator of Figs. 7.2 and the Converter-Tied PMSG of Fig. 7.1c respectfully.

Dimension [mm]	Hybrid Generator (Fig. 7.2)	PMSG of Fig. 7.1c [101]
PM-rotor yoke thickness	30	40
PM height	15.5	15
PM width	123.3	82
Stator slot depth	100	80
Stator tooth width	90	19
Rotor slot depth	77.55	—
Rotor tooth width	80	—
Stator yoke thickness	62.1	40

- Copper cost = \$9.4/kg,
- Aluminium cost = \$4.2/kg.
- Structural cost [105] = \$15/kg.

In the comparison, the cost-per-kilowatt (\$/kW) of a modern power electronic converter, as shown in Fig. 7.1c, is selected as the average value in the range of values considered in the literature, namely: \$40/kW to \$79/kW. However, an additional cost of \$15/kW is added to the cost of the converter to account for the converters mass. The mass of the power converter is obtained from [110]. The total cost of the considered medium-speed gearbox is obtained from equations as found in [111, 112], which are rewritten here as

$$\text{Cost}_{gearbox} = 16.45 \cdot (\text{machine rating})^{1.249}. \tag{7.1}$$

From the costs given in Table 7.3, it can be seen that the geared SS-drivetrain with the medium-speed (MS) S-PMC of Fig. 7.1a is approximately 16% more expensive on a cost-per-kW basis than a comparable geared, converter-tied drivetrain. In contrast, the SS-drivetrain with the low-speed (LS) S-PMC of Fig. 7.1a is 2.2 time more expensive than the converter-tied drivetrain. For the SS-drivetrain with the MS S-PMC, the main difference in the cost stems from the hybrid-excited generator being approximately 1.8 times more expensive than the converter-tied PMSG. However, the cost of the medium-speed S-PMC is notably less costly than the power converter, which reduces the overall cost of the SS-drivetrain. In contrast to the medium-speed S-PMC, the low-speed S-PMC of Fig. 7.1b is considerably more expensive than the converter-tied drivetrain. The disparity in cost is attributed to the increase in the volumetric dimensions and hence the PM-material and mass required by the direct-drive S-PMC unit.

7.4 S-PMC Design Optimisation

From the preceding section, it is evident that the mass and cost of the S-PMC units in both geared SS-drivetrains must be minimised to reduce the overall cost of the SS-drivetrain. To achieve these objectives, in this section, we use a multi-objective design optimisation algorithm to minimise the active mass and thus the cost of the S-PMC units for the medium-speed and low-speed S-PMCs.

7.4.1 Multi-Objective Design Optimisation

The need to minimise both the active mass and the active cost of the S-PMC can be described by a multi-objective minimisation function given by

$$\min_{\mathbf{X}} \mathbf{F(X)} = \min_{\mathbf{X}} \begin{bmatrix} M_{\text{act}}(\mathbf{X}) \\ M_{\text{PM}}(\mathbf{X}) \end{bmatrix}, \tag{7.2}$$

where the active mass M_{act} is the sum of the masses of the required electrical steel (M_{fe}), aluminium (M_{coil}) and PM material (M_{PM}) respectively. The multi-objective function of (7.2) is subject to a set of performance constraints $\mathbf{C}$ given by

$$\mathbf{C} = \begin{bmatrix} T_s \\ T_b \\ J_s \\ \eta \end{bmatrix} = \begin{bmatrix} P_s = 3.0 \\ T_b \geq 2.0 \\ J_s \leq 6.0 \\ \eta = 99.0 \end{bmatrix} \begin{bmatrix} \text{MW} \\ \text{pu} \\ \text{A/mm}^2 \\ \% \end{bmatrix}. \tag{7.3}$$

In (7.2), $\mathbf{X}$ is a dimensional vector with the design dimension variables of the considered machine. In (7.3), P_s, T_b, J_s, and η represent the machine's rated power, maximum torque, rated current density and rated efficiency respectively.

The population-based, non-gradient sorting genetic algorithm II (NSGA-II) is used for design optimisation. The NSGA-II optimisation algorithm is used because it generates a set of so-called Pareto-optimal solutions and places these solutions on a visually insightful Pareto-optimal front that illustrates the tradeoffs between the set of optimal solutions. Fig. 7.3 shows a representation of a Pareto-optimal front, which shows the set of Pareto-optimal and dominated solutions, respectively. A particular solution $\mathbf{x}^*$ is said to be Pareto-optimal if there exists no other solution $\mathbf{x}$ within the set of possible solutions that dominates $\mathbf{x}^*$ for each of the optimisation objectives. Thus, each Pareto-optimal solution $\mathbf{x}^*$ is a solution to the multi-objective function $\mathbf{F(X)}$ that adheres to the set of constraints $\mathbf{C}$.

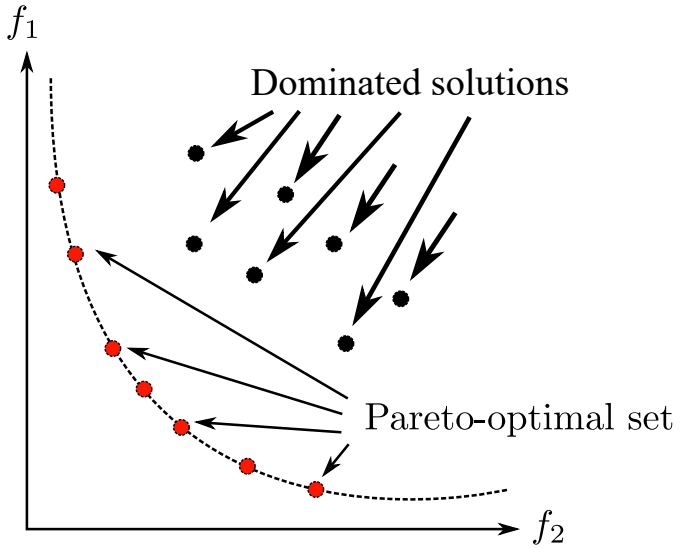

Figure 7.3: Representation of Pareto-optimal solutions located on a Pareto-front.

7.4.2 S-PMC Design Optimisation Strategy

In the design optimisation, the *Visualdoc* optimisation suite is used with the 2D python-based, static finite element (S-FE) software *SEMFEM* in conjunction with the analytical modelling equations outlined in Chapter 5. Only the fundamental and third-order harmonic flux linkages (and hence currents) are considered in the S-FE solutions to decrease the computational burden in the design optimisation process. Consequently, only a single non-linear and a single linear solution are required per FE iteration. Fig. 7.4 shows a flow diagram representation of the S-PMC design optimisation procedure.

In the design optimisation procedure, an initial set of input values **[X]** that describes the machine dimensions is imported into a two-dimensional (2D) static finite element (S-FE) program. Given **[X]**, fast, computationally efficient non-linear and linear S-FE solutions are performed to determine the machine's performance at a given operating condition. A subsequent set of machine performance indicators **[Y]** is then exported to a design optimisation suite. The optimisation suite compares **[Y]** against a pre-determined set of design objectives and constraints, **C** . If the design objectives aren't met, the optimisation suite then modifies **[X]** and exports it back to the S-FE program. This process is repeated until the design objectives are achieved, after which the corresponding set of optimal input values $[\mathbf{X_{opt}}]$ is exported to a computationally intensive but accurate transient FE (T-FE) program. Given $[\mathbf{X_{opt}}]$, the T-FE program produces a set of performance solutions $[\mathbf{Y_{opt}}]$, which are compared against the S-FE solutions to verify the optimisation results.

Both the medium-speed S-PMC of Fig. 7.1a and the low-speed S-PMC of Fig. 7.1b are optimised subject to a set of design constraints as given in Table 7.5. From Table 7.5, a maximum torque of $T_b \geq 2.0$ pu is selected to ensure sufficient braking torque and thus protection during periods of high wind speeds and grid faults. A rated slip value of $s = 1.0\%$ is selected to maximise the rated drivetrain efficiency at rated loads such that the S-PMC's efficiency is comparable to that of a commercially available wind turbine power converter [110]. Furthermore, the rated current density of both S-PMCs is limited to $J_{ss} \leq 6.0$ A/mm^2 so that air-cooling of the machine would be sufficient. In both machines, the

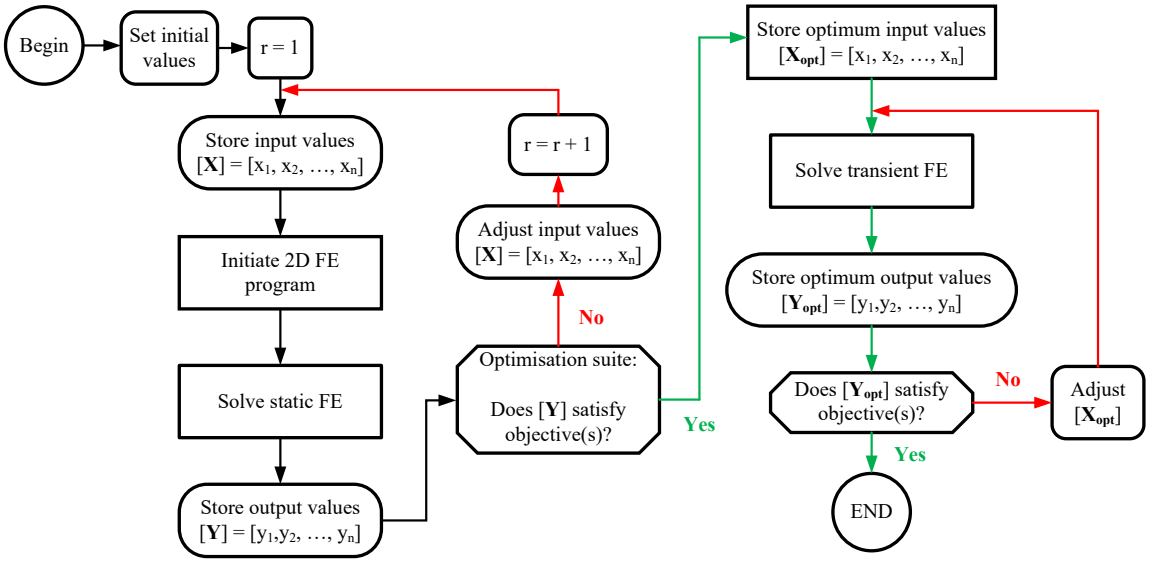

Figure 7.4: Flow diagram of the S-PMC design optimisation procedure.

Table 7.5: Design Constraints of the Considered S-PMCs.

Parameter	Unit	MS S-PMC	LS S-PMC
Rated speed, n_s	[rpm]	125	20
Rated torque, T_s	[kNm]	229.18	1432.4
Rated slip, s	[%]	1.0	1.0
Maximum torque, T_b	[pu]	≥ 2.0	≥ 2.0
Current density, J_s	[A/mm^2]	≤ 6	≤ 6
PM-pole number, N_m	[-]	112	392
Stator slot number, N_s	[-]	120	420
Outer Diameter, D_o	[mm]	≤ 4000	≤ 7000
Stack length, L_{st}	[mm]	≤ 1600	≤ 3000

airgap mechanical height or clearance g_m is defined as a function of the airgap diameter (D_g) such that

$$g_m = 0.0011 \times D_g \qquad [\text{mm}]. \tag{7.4}$$

Fig. 7.5 gives the dimension variable parameters that are used in $\mathbf{X}$ for the considered S-PMCs, where

$$\mathbf{X} = \begin{bmatrix} x1 \\ x2 \\ x3 \\ x4 \\ x5 \\ x6 \\ x7 \\ x8 \\ x9 \end{bmatrix} = \begin{bmatrix} d_o \\ l_{st} \\ w_{ry} \\ w_{pm} \\ h_{pm} \\ h_c \\ t_w \\ h_t \\ w_{sy} \end{bmatrix} = \begin{bmatrix} \text{PM-rotor outer diameter} \\ \text{Axial length} \\ \text{PM-rotor yoke thickness} \\ \text{PM width} \\ \text{PM height} \\ \text{Coil height} \\ \text{Tooth width} \\ \text{Tooth height} \\ \text{Slip-rotor yoke thickness} \end{bmatrix}. \tag{7.5}$$

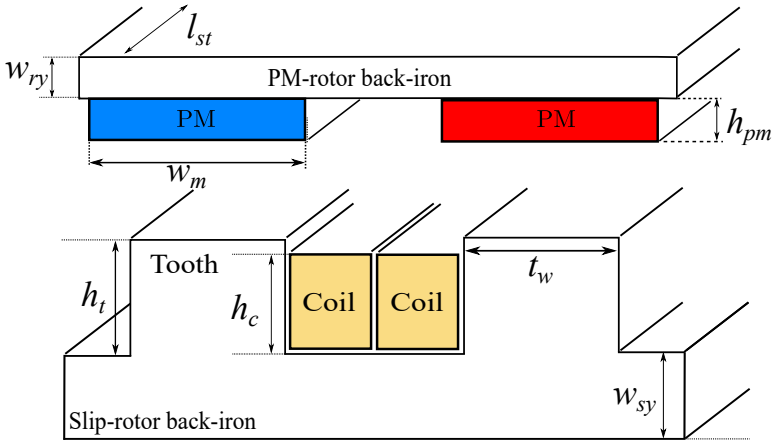

Figure 7.5: Representation of the S-PMC dimension variables used in $\mathbf{X}$ in the design optimisation.

7.4.3 Optimisation Results

Figs. 7.6a and 7.6b shows the respective Pareto front solutions for the considered medium-speed and low-speed S-PMCs. The respective Pareto-optimal solutions, as selected from the Pareto front of Fig. 7.6, for the respective medium- and low-speed S-PMCs are given in Table 7.6. Additionally, Figs. 7.7a and 7.7b shows cross-sectional finite-element models of the selected Pareto-optimal selected medium-speed and low-speed S-PMCs respectively.

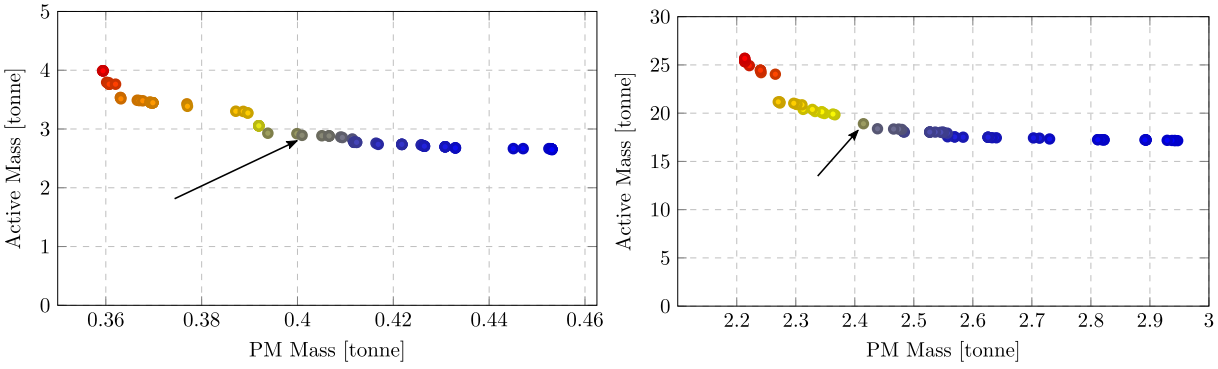

(a) **(b)**

Figure 7.6: Pareto-front solutions of (a) the 3-MW medium-speed (MS) S-PMC (b) the 3-MW low-speed (LS) S-PMC.

Table 7.6: Comparison of Results for the Starting and Optimised S-PMCs.

	MS S-PMC		LS S-PMC	
Variables **[X]** [mm]	Initial Machine	**Optimised Machine**	Initial Machine	**Optimised Machine**
Outer diameter	3 266	**3 465**	6 000	**6 978**
Axial length	1 040	**523.5**	2 350	**1 534**
Airgap clearance	3.43	**3.58**	6.3	**7.32**
PM-rotor yoke thickness	18.0	**17.53**	13.0	**10.98**
PM height	8.0	**10.45**	10.0	**11.89**
PM width	72.47	**63.1**	43.1	**45.4**
Coil height	22.0	**29.27**	60.97	**63.92**
Tooth width	27.0	**33.67**	15.0	**20.15**
Tooth height	25.0	**32.28**	67.0	**67.3**
Slip-rotor yoke width	18.0	**14.88**	13.0	**10.02**
F[X] [kg]	Initial Machine	**Optimised Machine**	Initial Machine	**Optimised Machine**
Active Mass	4 687	**2 895**	25 266	**18 904**
PM Mass	502.87	**403.1**	2 955	**2 415**
Active material cost [$]	184 750	**131 513**	1 042 806	**818 432**
Drivetrain cost-per-kW [$/kW]	302.8	**285.1**	588.9	**514.1**

From Table 7.6, it is evident that the NSGA-II algorithm seeks to increase the PM-rotor outer diameter and decrease the axial length of both the medium-speed and low-speed S-PMC units to satisfy the optimisation objectives. The selected Pareto-optimal solutions for the medium-speed and the low-speed S-PMC units yield solutions that reduce the S-PMC active material cost by $\approx 29\%$ and $\approx 21.5\%$, respectively. This reduction in active material cost results in a $\approx 5.8\%$ and $\approx 12.7\%$ reduction in the drivetrain cost-per-kW values for the medium-speed and low-speed S-PMC respectively.

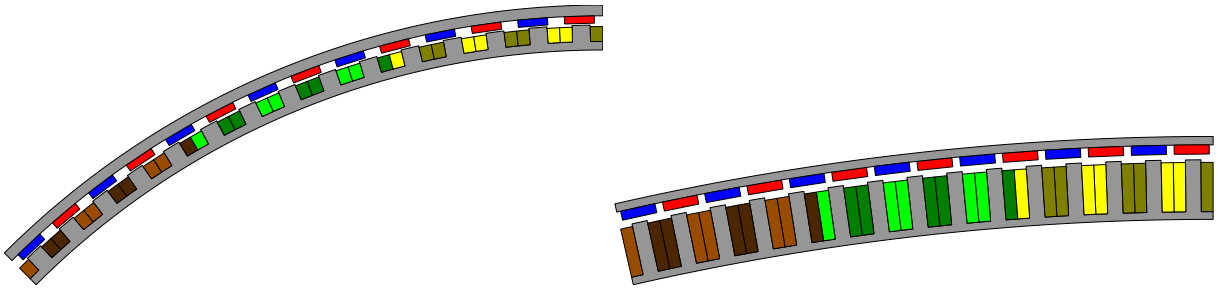

(a) (b)

Figure 7.7: Selected Pareto-optimal solutions of (a) the 3-MW medium-speed (MS) S-PMC (b) the 3-MW low-speed (LS) S-PMC.

Nevertheless, despite lowering the active material cost, the medium-speed SS-drivetrain is still $\approx$ 8.7% more costly than the converter-tied drivetrain of Fig. 7.1c. Moreover, the low-speed SS-drivetrain is $\approx$ 2 times more costly than the converter-tied drivetrain of Fig. 7.1c. The cost-per-kW of the respective S-PMCs could further be reduced by increasing the PM-rotor outer diameter and reducing the axial length, which would reduce required PM material. However, larger diameters may result in structural and transportation challenges.

7.5 Chapter Summary

Two geared SS-WT drivetrains are compared on a drivetrain cost-per-kW basis in this Chapter. One of the geared SS-WT drivetrains consists of a medium-speed (MS) S-PMC located on the high-speed side of the drivetrain gearbox, whereas the other drivetrain consists of a S-PMC located on the low-speed (LS) side of the gearbox. Both MS and LS S-PMC were optimised according to the same design optimisation criteria.

It is found that the medium-speed S-PMC is significantly less costly than the low-speed S-PMC. This is because the mass and cost of a S-PMC scales in proportion with the drivetrain rated torque and not necessarily with the rated power. Using the same design optimisation criteria, the capital expenditure for an optimised low-speed S-PMC is nearly 5 times that of a power converter of the same power rating. In contrast, the capital expenditure for an optimised medium-speed S-PMC is comparable to that of a power converter of the same power rating. Consequently, the findings in this Chapter suggest that a geared SS-WTSs with medium- to high-speed S-PMCs should be preferred over an SS-WTS with a low-speed S-PMC from an economic point of view. However, a design optimisation of the hybrid-excited generator of Fig. 7.2 is required and will be critical to further reduce the overall cost of the SS-WTS.

Chapter 8

Dynamic Modelling and Stability Analysis of Geared Slip-Synchronous Wind Turbine Systems

Most of the research literature about slip synchronous wind turbine systems (WTSs) has focused on direct-drive drivetrain topologies (without a gearbox). This chapter explores the potential of geared slip synchronous wind turbine drivetrains. As a first step, we derive an analytical transfer function model of a 1.5 MW geared slip-synchronous wind turbine system (SS-WTS). From the transfer function model, the dynamic stability of a geared SS-WTS is investigated when subjected to low-voltage ride-through (LVRT) conditions. Additionally, this Chapter explores and illustrates the potential for SS-WTSs to provide grid services in the form of direct frequency support and short-circuit current contribution. It should be noted that the work of this Chapter has been published as a journal contribution in Ockhuis and Kamper (2021) [80].

8.1 Gearbox Reliability

Wind turbine (WT) gearboxes are expected to last for approximately 20 years. However, a study by [95] found that gearboxes in offshore wind turbines might have to be replaced as early as 6.5 years. Furthermore, many studies conclude that the drivetrain gearbox contributes to the most prolonged periods of downtime [96, 113, 114, 115, 93]. According to the National Renewable Energy Laboratory (NREL), the high-speed side gearbox-bearing failure accounts for nearly half of the reported gearbox failures (48%) [116]. A study conducted by [97] found that high mean wind speeds, above the rated range, impose higher risks of failure in WT gearboxes. A study by [98] found that during grid loss transient events, the high-speed shaft of the gearbox undergoes a combined torsional and bending deformation. The unfavourable loading following a grid fault induces roller slip in the bearings, which is cited as a potential bearing failure initiator [98].

In [57], it is concluded that the S-PMC unit within a direct-drive WTS is capable of damping the drivetrain torque pulsations induced from gusty wind conditions. For geared SS-WTSs, it is crucial that the S-PMC is capable of damping the severe torque oscillations stemming from a grid fault. During a grid fault or a LVRT event, the generator experiences a sudden change in voltage at its terminals and, depending on the severity of the change in voltage, the generator will undergo a transient in its electromagnetic torque. This transient torque can result in significant stress being placed on the mechanical drivetrain

components of the wind turbine. As such, the feasibility of a geared SS-WTS largely depends on whether the S-PMC can provide sufficient damping to the drivetrain during these grid fault conditions.

8.2 Dynamic Stability of Direct Grid-Connected PMSG WTS

In this section, a mathematical model of a direct grid-connected SS-WTS is developed. The section starts by deriving a classical simplified transfer function of a conventional grid-tied PMSG, followed by the derivation of a transfer function of the SS-WTS to illustrate the importance of the S-PMC for direct grid-connected PMSGs.

8.2.1 Direct Grid-Connected PMSG

Figure 8.1a shows a line diagram model of a geared WTS with a direct grid-connected PMSG. Following classical analysis, the developed power (P_s) and torque (T_s) of the PMSG can be expressed respectively as

$$P_s = \frac{E_s V_s}{X_s}\sin(\delta) \quad \text{and} \quad T_s = \frac{E_s V_s}{\omega_{sm} X_s}\sin(\delta), \tag{8.1}$$

where E_s and V_s are the back-electromotive force (back-emf) voltage and line-voltage respectively, and X_s is the synchronous reactance of the PMSG. Additionally, in (8.1), ω_{sm} is the synchronous angular velocity and δ is the power angle between E_s and V_s. If we assume $V_s \approx E_s = \sqrt{2}\pi f_s N_{ph}\phi_p$, and with $X_s = 2\pi f_s L_s$, then at low loads (small values of δ) the developed torque can further be approximated as

$$T_s \approx \frac{3pN_s^2\phi_p^2}{4L_s}\delta = K_s\delta \tag{8.2}$$

where p is the number of poles, N_{ph} is the SG's effective number of turns in series per-phase, ϕ_p is the flux per pole of the PMSG, and L_s is the per-phase inductance. The drivetrain dynamics of the direct grid-connected PMSG can be described as

$$T_t^{'} - T_s = J_t^{'}\frac{d\omega_t^{'}}{d_t} \quad \text{and} \quad \omega_t^{'} - \omega_{sm} = \frac{d\delta_m}{d_t}, \tag{8.3}$$

where $\omega_t^{'}$ is the angular velocity of the wind turbine reflected across the gearbox (GB) and $\omega_{sm} = \frac{4\pi f_s}{p}$ is the synchronous angular velocity of the direct grid-connected PMSG, with f_s being the frequency of the grid. Furthermore, $J_t^{'} = J_t/\text{GB}^2$ is the inertia of the turbine reflected across the gearbox plus the rotational inertia of the PMSG, whereas $T_t^{'} = T_t/\text{GB}$ is the turbine torque reflected across the gearbox. Additionally, $\delta_m = \frac{2}{p}\delta$ is the mechanical power angle.

From Equations (8.1)–(8.3), a simplified block diagram model of the direct grid-connected PMSG was derived and is shown in Figure 8.1b, where the input to the block model is the turbine torque, T_t, and the output is the developed PMSG torque, T_s. It can be shown from classical textbook analysis that a second-order transfer function model that describes the torque dynamics of the system can be derived as

$$\frac{T_s(s)}{T_t^{'}(s)} = \frac{\frac{K_s}{J_t^{'}}}{s^2 + \frac{K_s}{J_t^{'}}}. \tag{8.4}$$

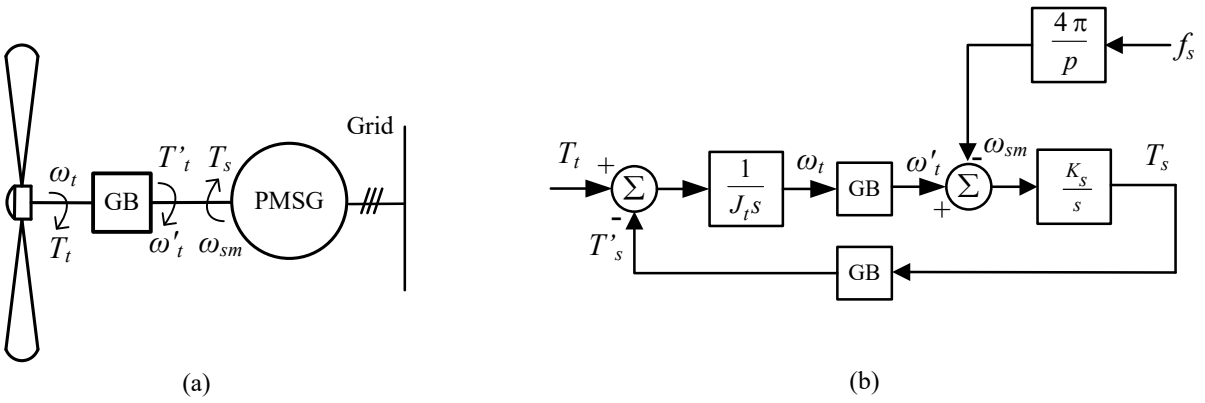

Figure 8.1: Simplified (**a**) line diagram representation model and (**b**) block diagram model of a direct grid-connected, geared PMSG WTS.

From (8.4), it can be seen that the second-order transfer function of the direct grid-connected PMSG WTS has poles that lie on the imaginary axis of the s-plain. This means that a step-change in $T_t^{'}(s)$ will result in an undamped and oscillatory PMSG torque (output) response T_s, which will continue to oscillate indefinitely. Consequently, the direct grid-connected PMSG is treated as an unstable system.

8.2.2 Direct Grid-Connected SS-PMSG

The same modelling procedure used to model the direct-grid connected PMSG was used to model the direct grid-connected SS-PMSG. A simplified line diagram of the SS-PMSG is shown in Figure 8.2a. Here it can be seen that the S-PMC is placed between the gearbox and the PMSG. The resulting block diagram transfer-function model of the SS-PMSG WTS is shown in Figure 8.2b.

The S-PMC in an SS-WTS is a magnetic coupling consisting of two rotating sections. One of the sections contains PMs, and the other section consists of individually short-circuited coils. The S-PMC transfers the torque of the geared turbine to the generator using electromagnetic induction due to the relative difference in speed between the two rotating sections. The difference in speed between the rotating sections is referred to as slip (ς), which is defined as

$$\varsigma = \frac{\omega_t^{'} - \omega_m}{\omega_m}. \tag{8.5}$$

With reference to Figure 8.2b, the slip speed is given as $\omega_{sl} = \omega_t^{'} - \omega_m = \varsigma\omega_m$. Moreover, the efficiency of the S-PMC is given by

$$\eta = \frac{\omega_m}{\omega_t^{'}} = \frac{1}{1+\varsigma}. \tag{8.6}$$

Concerning (8.6), the S-PMC's efficiency is inversely proportional to slip. When considering that WTSs rarely operate at rated conditions, the S-PMC operates at near 100% efficiency for extended periods at average power conditions.

Due to the linear nature of the torque developed by the S-PMC (T_r) and the slip speed (ω_{sl}), as shown in Chapter 5 in Fig. 5.17, the S-PMC can be modelled as a gain of which the value is determined by

$$G_c = \frac{T_r}{\omega_{sl}}. \tag{8.7}$$

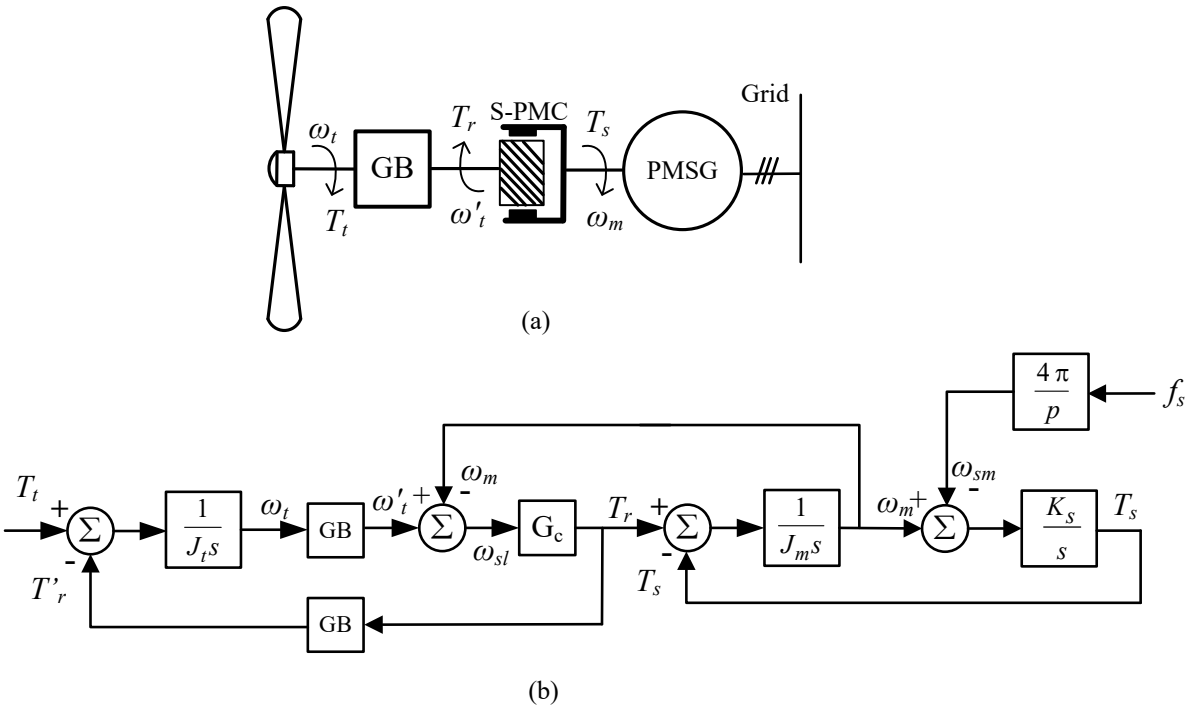

Figure 8.2: Simplified (**a**) line diagram representation model and (**b**) block diagram model of a geared SS-PMSG WTS.

It should be noted that (8.7) is typically only valid in the slip range of $\varsigma < 2$ pu.

The dynamics of the direct grid-connected SS-PMSG of Figure 8.2 is given as

$$T_t' - T_r = J_t' \frac{d\omega_t'}{dt}, \tag{8.8}$$

whereas the dynamics of the S-PMC's PM rotor and the rotor of the PMSG are given by

$$T_r - T_s = J_m \frac{d\omega_m}{dt}, \tag{8.9}$$

where J_m is the inertia of the PMSG plus S-PMC respectively.

From the block diagram model of Figure 8.2b, a transfer function model of the SS-PMSG WTS can be derived as

$$\frac{T_s(s)}{T_t'(s)} = \frac{K_s G_c}{J_m J_t' s^3 + G_c J_m s^2 + K_s J_t' s + G_c K_s}. \tag{8.10}$$

Since the coefficients of the third-order transfer function of (8.10) are all positive, the transfer function will only have negative roots (poles) in the s-plain, which means that the direct grid-connected SS-PMSG system is inherently stable.

8.3 Modelling

In this section, a more sophisticated analytical model of the SS-WTS and the grid is developed. The developed model is used in the following section to simulate the dynamic response and stability of the direct grid-connected SS-WTS during various disturbances resulting from the grid.

8.3.1 Grid Model

To evaluate the on-grid dynamics of the SS-WTS, a more sophisticated model of the grid and PMSG is required. The grid is modelled as a large synchronous generator (SG) equipped with load frequency control. The grid supplies a balanced set of three-phase voltages, v_{abc} and a variable grid frequency, f_s. The grid frequency is governed by the swing equation, which is given in classical texts as

$$P_{m(pu)} - P_{e(pu)} - D(\omega_{pu} - \omega_{syn}) = \frac{2H}{\omega_{syn}}\omega\frac{d\omega}{dt}, \tag{8.11}$$

where $P_{m(pu)}$ is the mechanical power supplied by the SG's prime mover and $P_{e(pu)}$ is the electrical output power of the generator, both in per unit (pu). The angular velocity of the SG's rotor is given by ω, and ω_{syn} is the synchronous angular velocity. The inertia constant of the grid is given by H, and D is a torque-damping term. It was shown in [117] that after a disturbance, (8.11) can be written in terms of a small-signal model as

$$\Delta P_m - \Delta P_e + \Delta P_s - D\Delta\omega = 2H\frac{\Delta\omega}{dt}. \tag{8.12}$$

In (8.12), the term ΔP_s is included to represent the additional supply power of the grid-connected SS-WTS. In the grid model considered here, the mechanical output power of the generator is controlled by a simple turbine-governor controller, which is described by

$$\Delta P_{m(pu)} = \Delta P_{ref(pu)} - \frac{1}{R}\Delta f, \tag{8.13}$$

where Δf is the change in frequency, $\Delta P_{ref(pu)}$ is a change in the reference power setting, and R is a regulating constant. Figure 8.3 shows a block diagram representation of Equations (8.11)–(8.13), where T_G, T_{RH}, and T_{CH} are the respective governor, re-heat, and steam-flow time constants of the turbine driving the SG's prime mover.

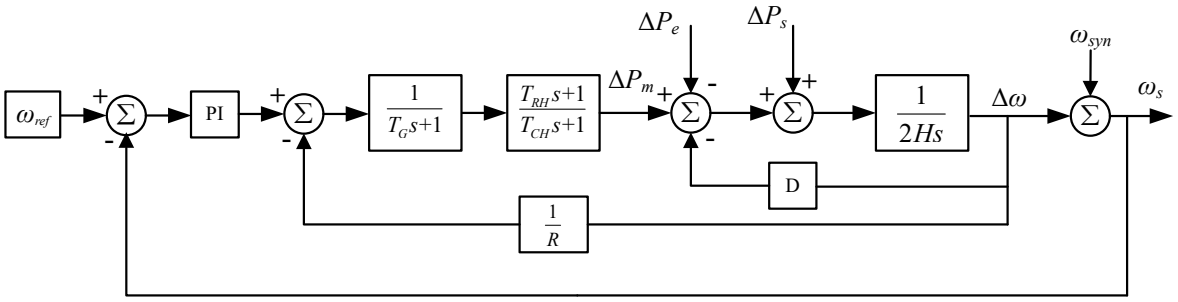

Figure 8.3: Block diagram model of a power system grid with load frequency control.

8.3.2 SS-WTS Model

The PMSG model of (8.2) is replaced with a dq reference frame dynamic model of the generator without damper windings, described by

$$\begin{aligned} v_{ds} &= -R_s i_{ds} - L_{ds}\frac{di_{ds}}{dt} + \omega_e L_{qs} i_{qs}, \\ v_{qs} &= -R_s i_{qs} - L_{qs}\frac{di_{qs}}{dt} - \omega_s L_{ds} i_{ds} + \omega_e \lambda_{ms}, \end{aligned} \tag{8.14}$$

where v_{dq} are the terminal voltages of the direct grid-connected PMSG and i_{dq} are the dq-axis currents. The per-phase inductances are given by L_{ds} and L_{qs} respectively, and the per-phase armature winding resistance is given as R_s. The flux linkage due to the permanent magnets is given by λ_{ms}, and ω_e is the electrical angular speed.

The respective electromagnetic torque, power, and reactive power of the PMSG are given by

$$T_s = \frac{3}{4}p[(L_{qs} - L_{ds})i_{ds}i_{qs} + \lambda_{ms}i_{qs}], \tag{8.15}$$

$$P_s = \frac{3}{2}(v_{ds}i_{ds} + v_{qs}i_{qs}) \quad \text{and} \quad Q_s = \frac{3}{2}(v_{qs}i_{ds} - v_{ds}i_{qs}). \tag{8.16}$$

The block diagram model of the direct grid-connected SS-WTS of Figure 8.2b is replaced by the block diagram model shown in Figure 8.4. The grid is modelled as a voltage source that produces a balanced set of three-phase voltages, v_{abc}, which are transformed into the dq reference frame using the Park transformation. The resulting dq voltages, v_{dq}, are used in conjunction with (8.14) and (8.15) to produce the torque and current response of the SS-WTS.

8.3.3 PMSG under Short-Circuit Conditions

It can be shown from classical texts that the dq currents of (8.14) and torque of (8.15) during a short circuit can be approximated as

$$\begin{aligned} i_{dss}(t) &\approx \frac{-E_q}{x_{ds}} - E_q\left(\frac{1}{x''_d} - \frac{1}{x'_d}\right)e^{\frac{-t}{T''_d}} - \frac{E_q}{x''_d}e^{\frac{-t}{T_a}}\cos(\omega_e t), \\ i_{qss}(t) &\approx \frac{-E_q}{x_{qs}}e^{\frac{-t}{T_a}}(\sin\omega_e t), \end{aligned} \tag{8.17}$$

and

$$\begin{aligned} T_{ss}(t) \approx \frac{3p}{4\omega_e}\Bigg\{ & E_q^2 e^{\frac{-t}{T_a}}\left[\frac{1}{x_{ds}} + \left(\frac{1}{x'_d} - \frac{1}{x_{ds}}\right)e^{\frac{-t}{T'_d}} + \left(\frac{1}{x''_d} - \frac{1}{x'_d}\right)e^{\frac{-t}{T''_d}}\right]\sin\omega_e t \\ & + \frac{E_q^2}{2}e^{\frac{-2t}{T_a}}\left(\frac{1}{x''_d} - \frac{1}{x''_q}\right)\sin 2\omega_e t\Bigg\}. \end{aligned} \tag{8.18}$$

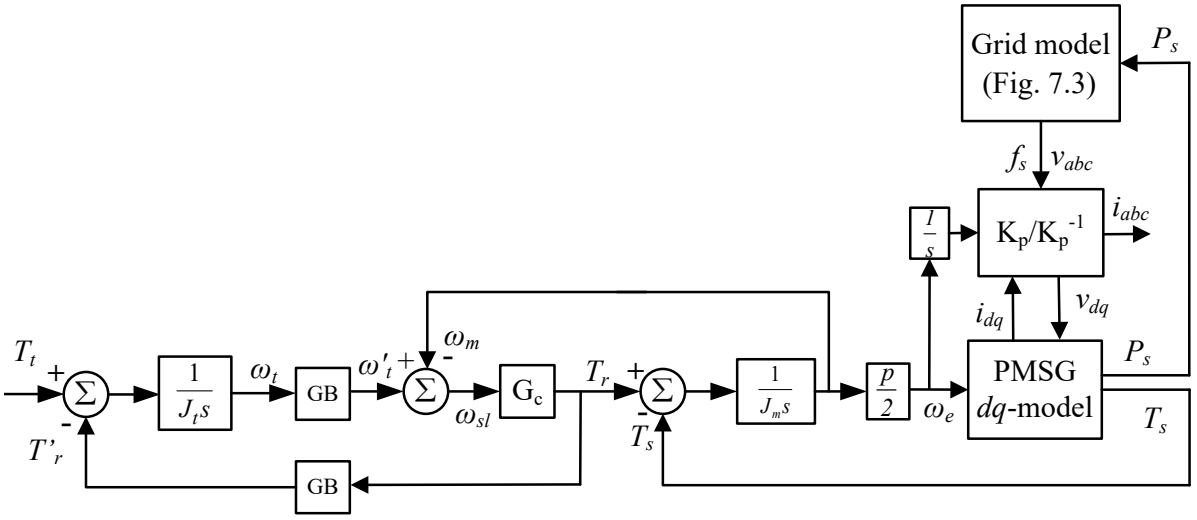

Figure 8.4: Block diagram model of a geared, direct grid-connected SS-PMSG WTS.

In (8.17) and (8.18), $x_{ds} = \omega_e L_{ds}$ and $x_{qs} = \omega_e L_{qs}$ are the dq-axis synchronous reactances, $x_d^{'}$ is the transient reactance, and $x_{dq}^{''}$ are the dq subtransient reactances respectively. Moreover, $E_q = \omega_e \lambda_{ms}$ is the open-circuit back-emf of the PMSG, and the symbol T denotes the respective time constants associated with the short-circuit condition.

When considering that PM machines do not have field windings, the transient reactance, $x_d^{'}$, and the associated transient time constant, $T_d^{'}$, are not defined. However, as shown in [118], the transient parameters are represented by setting $x_d^{'} = x_{ds}$ and $T_d^{'} = T_d^{''}$, where $T_d^{''}$ is the subtransient time constant. Furthermore, segmenting the PM poles of a synchronous machine is typically done to reduce induced eddy currents in the PM material, thereby reducing the overall losses. It is shown in [118] that, as the number of segments per PM pole increases, $x_d^{''} \approx x_{ds}$ and, as a result, the middle term in (8.17) for the d-axis short-circuit current, and the two exponential terms in the square brackets in (8.18) are zero. Finally, the PMSG considered here is equipped with a round rotor with surface-mounted PMs, such that $x_{ds} = x_{qs} \approx x_{dq}^{''}$ and, as a result, the double-frequency term in (8.18) is zero. Consequently, the torque appearing at the short circuit is approximately

$$T_{ss}(t) \approx \frac{3p}{4\omega_e}\left[\frac{E_q^2}{x_{ds}} e^{\frac{-t}{T_a}} \sin(\omega_e t)\right], \tag{8.19}$$

where T_a is the armature (stator) transient time constant, defined as

$$T_a = \frac{2}{R_s\left(\frac{1}{L_{qs}} + \frac{1}{L_{ds}}\right)}. \tag{8.20}$$

Equation (8.19) shows that the short-circuit torque for a direct grid-connected PMSG is a sinusoidal function with a large amplitude that is inversely proportional to x_{ds} and swings from positive to negative. This sudden and large torque reversal indicates that a high degree of sheering stress will be placed on the rotor shaft and gear teeth of the drivetrain gearbox. Hence, this has the potential to damage the drivetrain gearbox if T_{ss} is not dampened sufficiently.

8.3.4 Torque-Damping Effect of the S-PMC and PMSG

Short-circuit and LVRT conditions are some of the most severe grid-fault conditions a WTS must endure. Furthermore, the gearbox is one of the most expensive drivetrain components and is responsible for the most extended periods of downtime. In this section, the block diagram model of Figure 8.4, is used to derive a transfer function representation of the grid-connected SS-WTS to investigate its ability to dampen drivetrain torque pulsations induced by the grid.

Figure 8.5 shows a section of the block diagram of Figure 8.4 where, in this case, we are interested in the relationship between the generator torque, T_s, and the torque of the S-PMC, T_r. In Figure 8.5, the input is T_s and the output is T_r. The relationship between T_s and T_r gives an indication of the S-PMC's ability to filter the torque transients produced by the PMSG, which ultimately penetrate the drivetrain gearbox. From Figure 8.5, a classical transfer function model can be derived as

$$\frac{T_r(s)}{T_s(s)} \approx \frac{\frac{G_c}{J_m}}{s + \frac{G_c}{J_m}}. \tag{8.21}$$

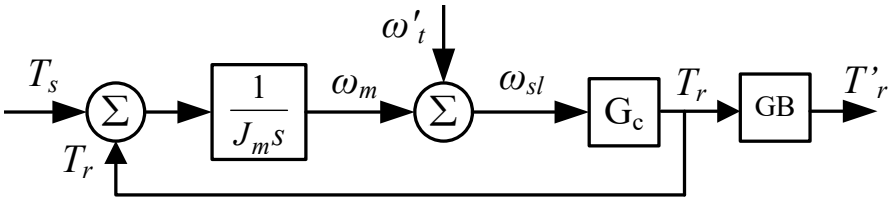

Figure 8.5: Block diagram model illustratrating the relationship between the torque of the PMSG and the torque of the S-PMC in an SS-WTS (see Figure 8.4).

Equation (8.21) shows that the relationship between T_s and T_r is that of a low-pass filter with a cut-off frequency of

$$f_c \approx \frac{G_c}{2\pi J_m}. \tag{8.22}$$

Furthermore, (8.22) indicates that the filtering response of the SS-WTS depends on the ratio of the gain of the S-PMC G_c, and the inertia of the PMSG, J_m. Moreover, from (8.19), we see that the frequency of the short-circuit torque of a surface-mount PMSG (assuming segmented magnet poles) is that of the grid frequency, f_s. Consequently, the magnitude of the short-circuit torque response produced by the PMSG will be attenuated by a factor of

$$A_f = 20 \log \left(\frac{f_c}{f_s} \right) \quad \text{dB}. \tag{8.23}$$

Equations (8.7), (8.22) and (8.23) can thus be used to design an S-PMC for a given PMSG to dampen the magnitude of torque transients resulting from the PMSG during an LVRT event.

8.4 Simulation Results

In this section, the dynamic stability models developed in the previous sections were transferred to MATLAB/Simulink to investigate the dynamic behaviour of the direct grid-connected SS-WTS. The simulation was conducted on a 1.5 MW power level, and Table 8.1 gives the simulation parameters used in the investigation. During the simulation, the considered SS-WTS was operating under a 0.5 per-unit torque input. Furthermore, the dq synchronous reactance, x_{dq}, in Table 8.1 is the reactance of the PMSG plus an additional series-line reactance (SLR), as is recommended in [51] to reduce the sensitivity of the PMSG to variations in grid voltage.

8.4.1 LVRT Dynamic Response

Figure 8.6 shows an example of a severe low-voltage ride-through (LVRT) condition for wind turbines. For this LVRT condition, Figure 8.7 shows the torque response of the PMSG (T_s) and that of the S-PMC (T_r) during the time period $t = 1.98$ to 2.22 s. With reference to (8.22), Table 8.1, and Figure 8.8, which shows the transfer function frequency response, $T_r(s)/T_s(s)$, of the considered SS-WTS, it is clear that the ratio of the S-PMC gain and the inertia of the PMSG has the effect of attenuating the 50 Hz torque transient of the generator by the attenuation factor of (8.23).

Figure 8.9 shows the three-phase short-circuit current response of the PMSG. It can be seen that, during the period $t = 1.98$ to 2.24 s, the SS-WTS produces a substantial steady-state, peak short-circuit current response of approximately 2.5 per unit. The relatively

Table 8.1: SS-WTS and grid simulation parameters.

SS-WTS Parameter	Value	Grid Parameter	Value
Rated power (P_{rated})	1.5 MW	Rated frequency	50 Hz
Synchronous speed (n_s)	1500 rpm	Line voltage (1.0 pu)	690 V
Pole number (p)	4	Governor time constant (T_G)	0.1 s
S-PMC gain (G_c)	6085	Steam flow time constant (T_{CH})	0.2 s
Turbine inertia (J_t)	6×10^6 kg·m^2	Re-heat time constant (T_{RH})	7 s
Generator inertia (J_m)	144 kg·m^2	Grid inertia constant (H)	10 s
Gear ratio (GB)	83	Damping coefficient (D)	1
Synchronous reactance (x_{dq})	0.5 pu	Proportional gain (P)	10
Stator resistance (R_s)	0.035 pu	Integral gain (I)	2
Percentage rated slip (ς)	1 %	Regulating constant (R)	0.05

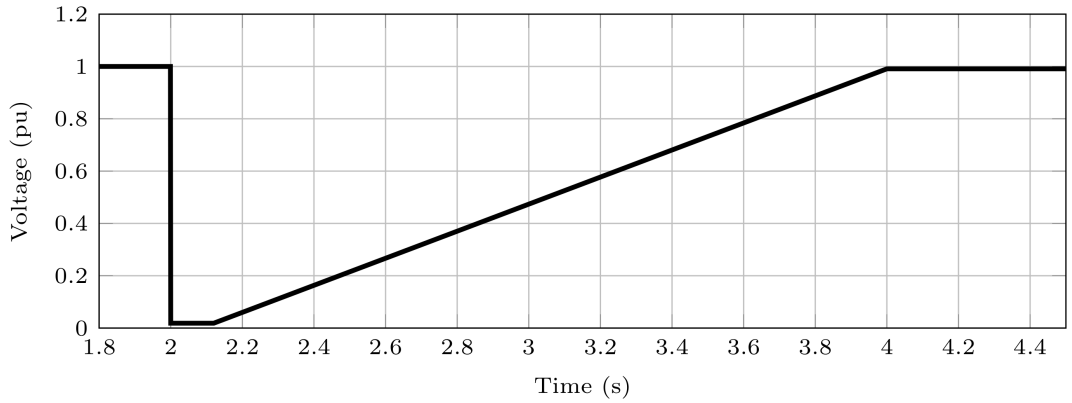

Figure 8.6: LVRT condition for wind turbine systems.

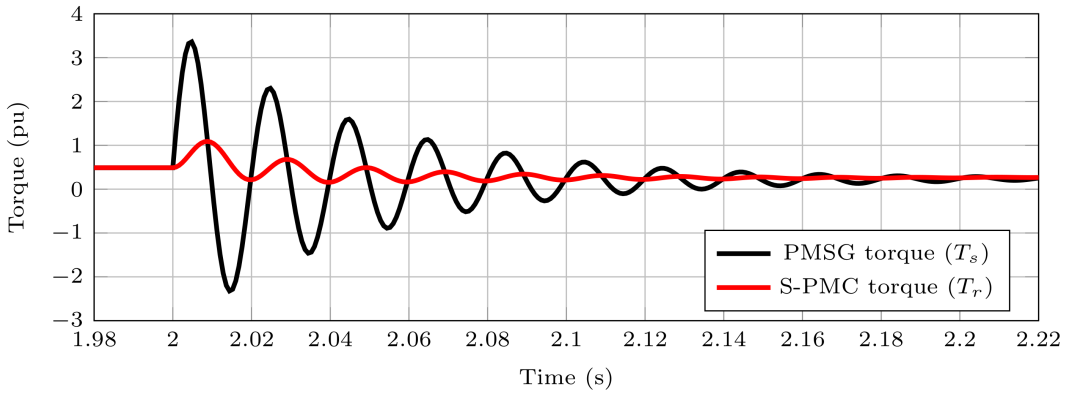

Figure 8.7: Short-circuit torque responses of the PSMG and the S-PMC during the time period $t = 1.98$ s to $t = 2.22$ s of the LVRT event in Figure 8.6.

large synchronous reactance (of the PMSG plus the SLR) results in the short-circuit current being sufficient to trip the grid protection relays while being low enough to avoid potential demagnetisation of the PMs.

Figure 8.10 shows the power angle response of the SS-WTS during the LVRT event. It can be seen that the power angle remains far below 90°, which illustrates the stability of the direct grid-connected SS-WTS during the LVRT event of Figure 8.6.

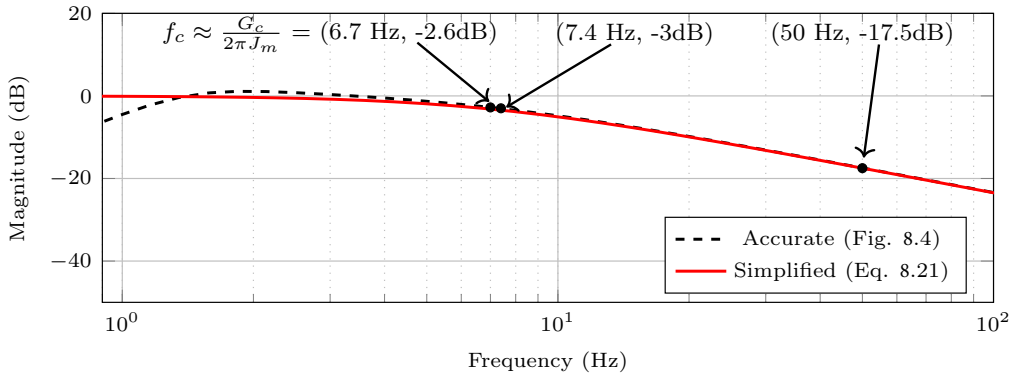

Figure 8.8: Frequency bode plot of the SS-WTS, where the bode plot as determined by Matlab/SIMULINK (Accurate) is given by the dashed line and the simplified transfer function of (8.21) is given by the solid line.

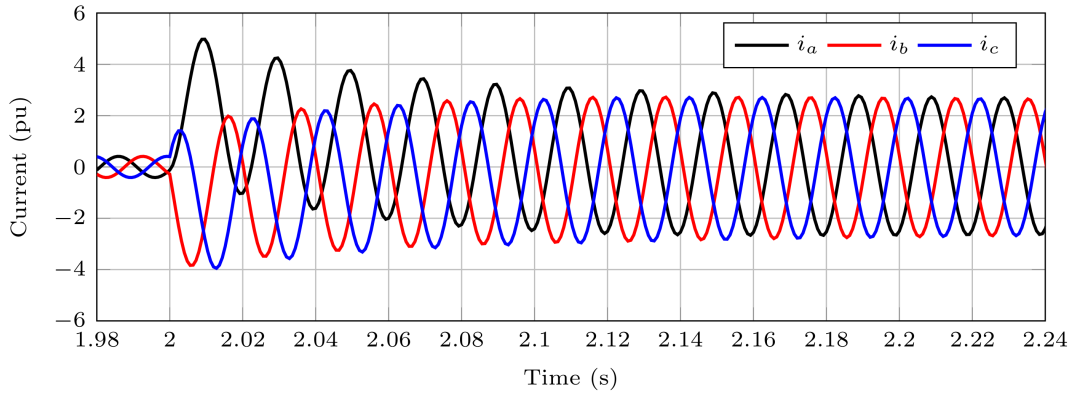

Figure 8.9: Short-circuit current response during the time period $t = 0.98$ s to $t = 2.24$ s of the LVRT event of Figure 8.6.

8.4.2 Inertial Response

Figure 8.11 shows the grid frequency response for a 5% loss of generating capacity (ΔP_e, see Figure 8.3) with and without the direct grid-connected SS-WTS. It can be seen that having the SS-WTS connected to the grid helps reduce the rate of change of frequency (RoCoF), as well as to reduce the frequency nadir. This inherent primary frequency response of the direct grid-connected PMSG allows transmission system operators more flexibility when bringing slower-acting regulating and contingency reserves online.

8.5 Discussion

In this section, some of the design compromises regarding S-PMC gain versus efficiency and drivetrain speed versus cutoff frequency are discussed. Furthermore, the passive reactive power compensation of the SS-WTS is addressed.

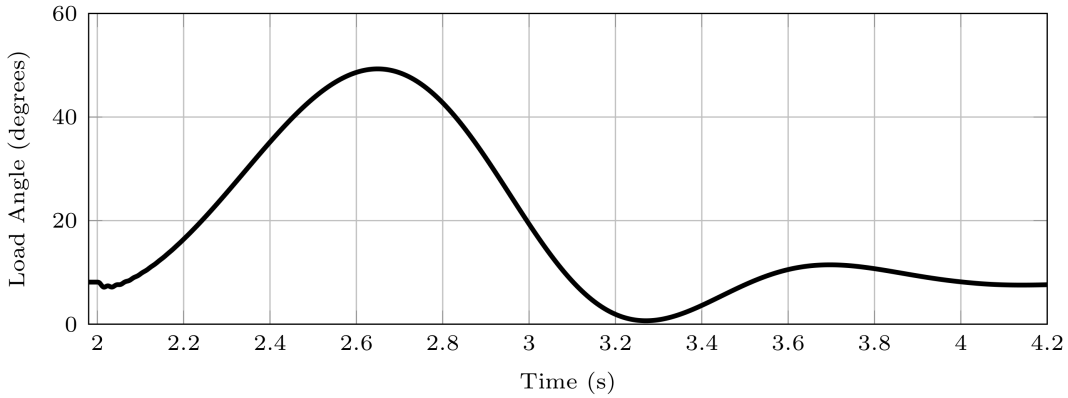

Figure 8.10: Load angle versus time during the LVRT event of Figure 8.6.

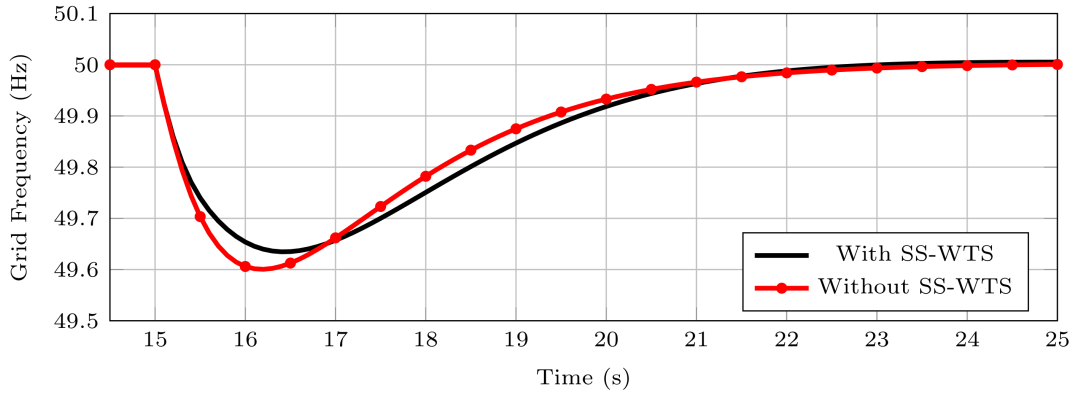

Figure 8.11: Grid frequency variation for a 5% loss of generating capacity (ΔP_e) with and without a SS-WTS connected to the grid.

8.5.1 Slip versus Damping

The S-PMC is shown to effectively attenuate the large torque transients resulting from an LVRT event, a feature that is critical for extending the life cycle of a drivetrain gearbox. Moreover, (8.22) and consequently (8.23) indicate that increasing the selected rated slip value results in a greater degree of drivetrain damping at the cost of a lowered efficiency, as expressed in (8.6). Figure 8.12 shows bode diagram plots of the considered SS-WTS for three values of rated slip and the corresponding S-PMC gain. It can be seen that increasing the rated slip to $\varsigma = 3\%$ or $\varsigma = 5\%$ (thus reducing the gain) has the effect of further attenuating the magnitude of the 50 Hz short-circuit torque. Additionally, Figure 8.12 shows that the frequency response for rated slip values of 3% and 5% has a narrower frequency passband (f_b) range, of 2.8 Hz $< f_b <$ 4.2 Hz, when compared to the case where $\varsigma = 1\%$, where the frequency passband range is 1 Hz $< f_b <$ 7.4 Hz. There is thus a design trade-off between the value of rated slip and acceptable efficiency when it comes to attenuating both lower- and higher-order drivetrain frequencies. However, when considering that a WTS rarely operates at rated conditions, one may opt for larger rated slip values to narrow the passband frequencies and further dampen the 50 Hz transient torque of the PMSG.

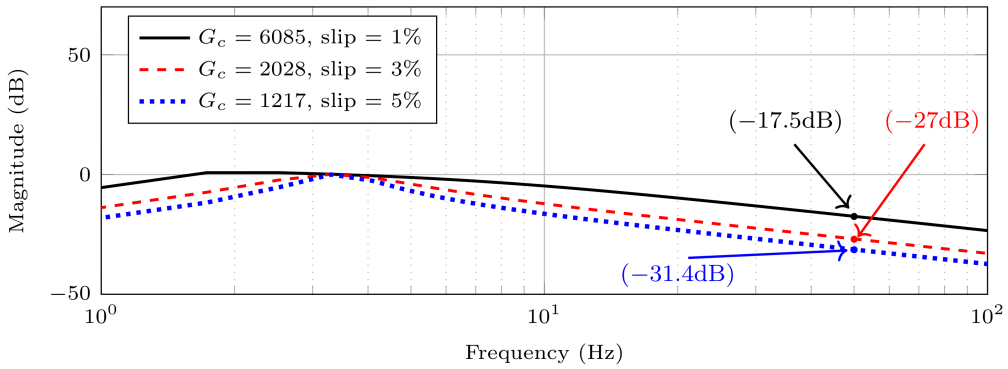

Figure 8.12: Frequency response with rated slip (and corresponding gain) a parameter. The inertia (J_m) of the PMSG remained the same in the comparison.

8.5.2 Drivetrain Speed versus Damping

The SS-WTS considered in this paper consists of a high-speed (HS) drivetrain categorised as having a generator speed range of between 600 rpm and 2000 rpm. Medium-speed (MS) drivetrains are categorised as having a speed range between 40 rpm and 600 rpm. Table 8.2 compares the HS-WTS drivetrain considered here with two MS-WTS drivetrains with two different drivetrain speeds. The aspect ratio (X) of the generators for the considered drivetrains is defined as

$$X = \frac{L}{D}\,, \tag{8.24}$$

where L is the axial length of the PM-rotor and D is the air-gap diameter. The aspect ratio of the respective machines was used to determine suitable values for D and L, based on dimensions found in [119, 120] for large-scale, geared PMSGs. The PM rotor was treated as a solid cylinder of which the inertia (J_m) and volume (V_r) respectively were determined by

$$J_m = \frac{1}{32}\pi\rho L D^4 \quad \text{and} \quad V_r = \frac{\pi}{4}D^2 L, \tag{8.25}$$

where $\rho = 7700$ kg·m^{-3} is the density of the rotor steel.

Considering the results in Table 8.2, low values for the cut-off frequency, f_c, are preferred, as they result in greater attenuation of the 50 Hz short-circuit torque of the PMSG. It can be seen that the S-PMC gain (G_c) increases more rapidly than the respective increase in rotor inertia as the rated WTS drivetrain speed decreases. Consequently, MS drivetrains have to operate at higher-rated slip values (compared to HS drivetrains) to provide a comparable degree of attenuation to the short-circuit torque response of the

Table 8.2: Comparison between the considered high-speed (HS) SS-WTS and two medium-speed (MS) SS-WTS drivetrains.

	HS (1500 rpm)	**MS (200 rpm)**	**MS (40 rpm)**
Aspect ratio (X)	1.14	0.31	0.23
Volume (m^3)	0.3	1.7	4.95
S-PMC gain ($G_c, \varsigma = 1\%$)	6085	342,025	8,546,506
Inertia (kg·m^2)	144	5911	85,724
Cut-off frequency, f_c (Hz)	6.7	9.2	15.9
Attenuation, A_f (dB)	−17.5	−14.7	−9.95

PMSG. However, the choice of drivetrain speed has to be considered within the holistic design of the considered system, where factors such as cooling, overall efficiency, and system cost need to be considered.

8.6 Chapter Summary

In this Chapter, the potential of direct grid-connected SS-WTS to provide essential grid services and withstand the subsequent mechanical loading was investigated. A transfer function model of a 1.5 MW, geared, direct grid-connected SS-WTS was derived and implemented in MATLAB/Simulink.

It was found that the S-PMC in the SS-WTS is capable of effectively damping the magnitude of the extreme short-circuit torque transients generated by the PMSG, a feature that is vital in extending the life cycle of the drivetrain components, specifically the drivetrain gearbox. Furthermore, the degree of damping is directly proportional to the selected rated slip (or inversely proportional to S-PMC gain, G_c); however, there is a trade-off between rated slip and the efficiency of the S-PMC.

Furthermore, it was found that higher-speed drivetrains provide a greater degree of damping (lower cut-off frequency, f_c) than lower-speed drivetrains. This is because the S-PMC gain increases more rapidly than the rotor inertia of the generator as the drivetrain speed decreases.

The SS-WTS can increase the short-circuit strength of the grid while maintaining stability. The inherent ability of the SS-WTS to provide primary frequency response to the grid in the event of a loss of generating capacity was also demonstrated.

Chapter 9

Conclusions, Contributions and Recommendations

This Chapter concludes the study by summarising the key research findings in relation to the research aims and objectives as set out in Chapter 1. In this dissertation, various aspects regarding the modelling, design and analysis of slip-magnetic couplers (S-PMCs) and grid-tied synchronous generators (SGs) have been investigated and proposed. The conclusions in this Chapter are divided into three categories, namely:

- Conclusions from the design and analysis of grid-tied synchronous generators,
- conclusions from the design and analysis of slip-magnetic couplers for wind turbine applications, and
- conclusions regarding the influence of the S-PMC on the cost and on the dynamics of the SS-WTS.

9.1 On the Design of Grid-Tied Synchronous Generators

In this study, two of the main challenges and shortcomings in the literature regarding the design of PM grid-tied synchronous generators for SS-WTSs have been addressed, namely (i) the PM generators designed for SS-WTSs in the literature are extremely sensitive to changes in grid voltage due to their low synchronous reactance values and (ii) the designed PM generators aren't grid code compliant as they are not capable of variable-flux operation.

(i) In this study, it is found that the optimal values of synchronous reactance range from 0.3 to 0.5 per unit (pu). A synchronous reactance of 0.3 pu is low enough to provide a significant short-circuit current response during a grid fault. However, the generator's performance, in terms of its efficiency, is still susceptible to grid voltage variations, especially at low loads. A synchronous reactance of 0.5 pu results in the highest generator efficiency at low grid voltage conditions and low operating loads. The generator's reactive power is also less sensitive to grid voltage variations at high and low load conditions. However, the generator's short-circuit current capabilities are reduced with a synchronous reactance of 0.5 pu; there is thus a tradeoff between the generator's performance and its ability to provide large amounts of short-circuit current.

(ii) The PMSG's hitherto designed in the literature for SS-WT applications have not been grid code compliant. This is because the PMSGs designed in the literature have no means of variable-flux operation and thus cannot adhere to the grid-code requirements regarding power factor and reactive power control. In [58], a series hybrid-excited SG (HESG) is designed that theoretically has the potential to be grid-code compliant. However, this generator concept was never practically verified.

In this study, a novel parallel hybrid-excitation method for grid-tied SGs is proposed and investigated. Accurate finite-element analysis shows that the proposed hybrid-excitation method allows for a theoretical generator induced voltage variation from 10% to a maximum of 33%. FE results from a theoretical 15 kW parallel HESG show that using the proposed hybrid-excitation method, the generator has variable flux capabilities that allow the generator to operate at unit power across its load range, which is the grid code requirement for generators of this power rating.

The proposed hybrid-excitation method and the FE results are verified with measured results of a built 15 kW hybrid-excited synchronous generator. The built hybrid-excited generator is found to have a synchronous reactance value of 0.56 pu, which is in the ideal range of values for overall grid-connected performance. Measured results of the built 15 kW prototype generator show that it can operate at unity power factor across its load range and is thus grid code complaint. To the best of the author's knowledge the measured results presented in Chapter 6 are the first verification of a grid code complaint, grid-tied synchronous generator for SS-WT applications. Additionally, the reactive power compensation capabilities of the built 15 kW prototype hybrid-excited generator are shown. The prototype generator can supply a maximum of +0.19 per unit reactive power to the grid while operating at 0.5 per unit active power. This result indicates that the parallel hybrid-excited generator can operate as a synchronous condenser and can provide valuable grid services in terms of reactive power support.

Although the 15 kW prototype parallel HESG requires less PM material than a comparable conventional PMSG, the 15 kW parallel HESG is 24% heavier. The main difference in mass is due to the field-winding section on the hybrid-rotor. The 15 kW parallel HESG is also notably less efficient than the 15 kW conventional PMSG. However, the reduced efficiency should be considered with respect to the parallel HESG being grid code compliant, when the conventional PMSG is not. The additional costs associated with the increased mass of the parallel HESG could potentially be offset by the additional revenue generated from the increase in inertia, and the additional grid supporting services provided by the parallel HESG [30].

9.2 On the Modelling and Design of Slip-Magnetic Couplers for Wind Turbine Applications

The S-PMC is a vital component within the SS-drivetrain. The S-PMC is required to dampen the turbulent aerodynamic torque of the wind turbine blades and transfer this dampened torque to the grid-connected generator. Furthermore, the S-PMC is responsible for providing the necessary stability to the SS-WTS drivetrain during

periods of high wind speed, braking events and grid fault conditions. As such, the maximum torque capability of the S-PMC must be larger than that generated within the WTS.

Traditionally, the simplifying assumptions made during the modelling and analysis of S-PMCs can result in an incorrect overestimation of the maximum (breakdown) torque capabilities of S-PMCs. In Chapter 5, using the frozen permeability technique, it was found that the value of PM-flux does not remain constant with an increase in load conditions, as is commonly assumed in the literature. Instead, the PM-flux value decreases with load, resulting in a predicted maximum torque value of $\approx 10\%$ lower than expected if the PM-flux is assumed constant versus load. The S-PMCs considered in this dissertation are equipped with individually short-circuited coils. As such, all the PM-rotor harmonics, which include the zero-sequence (3^{rd} order) harmonics, are present in the short-circuit currents that flow in these coils. In Chapter 5, it is concluded that these higher-order harmonics have a negligible effect on the torque performance of the considered S-PMC. However, this may not necessarily be the case for all S-PMC topologies.

9.3 The Influence of the S-PMC unit on the Cost and Dynamics of a SS-WTS

In Chapter 7, two geared, 3 MW slip synchronous wind turbine drivetrains are designed and benchmarked against a comparable converter-tied wind turbine drivetrain found in the literature. It was found that the mass and cost of the S-PMC unit scales with rated torque and not necessarily with rated power. This contrasts with power converters, whose cost scales with rated power. Consequently, high-speed S-PMCs (low rated torque) have a significantly lower active mass and are less costly than direct-drive (high rated torque) S-PMCs for a given set of design constraints. A design-optimised medium-speed (125 rpm) S-PMC unit has a cost-per-kW ($/kW) value of 43.84, whereas a design-optimised direct-drive (20 rpm) S-PMC has a cost-per-kW value of 272.8. From the study conducted in Chapter 7, it concluded that medium- to high-speed S-PMCs should be used instead of low-speed, direct-drive S-PMCs for utility-scale SS-WTSs. A similar conclusion is found in Chapter 8, which is discussed below.

In Chapter 8, it was found that the S-PMC unit in a geared SS-WTS is capable of effectively damping and attenuating the magnitude of torque transients following a low-voltage ride-through event. The S-PMC thus has the potential to extend the lifetime of the drivetrain gearbox in an SS-WTS. Additionally, it was found that the degree of attenuation is directly proportional to the selected rated slip and is a function of the S-PMC's gain (G_c) and the inertia of the grid-tied generator. The degree of damping provided by the S-PMC and the generator's inertia is described by a so-called attenuation factor, A_f. S-PMCs in high-speed drivetrains provide a greater degree of damping compared to lower-speed drivetrains.

9.4 Contributions

Based on the results and outcomes of the preceding Chapters in this dissertation and the conclusions above, the following aspects of this study are considered by the author as original and hence a contribution to the body of knowledge regarding the design of grid-tied SS-WTS:

1) The impedance matching design and analysis methodologies developed in Chapter 3 are considered a contribution to the design of grid-tied wind turbine systems. The analysis shows that the optimal values for the generator's induced voltage (E_a = 1.05 pu) and synchronous reactance (X_s = 0.5 pu) yield the best electromagnetic performance.

2) The hybrid-excited design and analysis methodologies developed in Chapter 4 for grid-tied synchronous generators are considered unique. Moreover, the method used to determine the generator's performance for a given operating point using the frozen permeability method in conjunction with interpolating polynomials is considered novel.

4) To the best of the author's knowledge, the 15 kW hybrid-excited generator is the first synchronous generator of its kind to be practically built. Moreover, the measured grid-connected results of the built 15 kW hybrid-excited generator prototype are the first verification of the grid code compliance for directly grid-connected SGs for SS-WT applications.

4) The harmonic model and coil-current solution technique for slip-magnetic couplers are considered contributions. Using the frozen permeability technique in conjunction with finite element analysis, it was shown that the traditional assumptions used when modelling S-PMCs are inaccurate and can result in a significant error when predicting the maximum torque of S-PMCs.

5) The attenuation factor A_f, which describes the relationship between the S-PMC's gain and the grid-tied generator's inertia, was for the first time derived in Chapter 8. The attenuation factor describes the degree of damping provided to the SS-drivetrain in terms of the S-PMC's rated slip and the generator's inertia. The attenuation factor can be used to inform engineers during the S-PMC design process.

9.5 Recommendations and Future Work

Despite the work presented in this dissertation, there remains a large scope for additional research regarding the design and feasibility of grid code compliant synchronous generators for SS-WTS applications. To that end, recommendations for future work are listed below:

- This dissertation primarily focused on developing the modelling, design and analysis aspects for grid-tied and grid compliant synchronous generators for SS-WTSs. Consequently, a compressive design optimisation methodology of the developed hybrid-excited SG could not be conducted and is thus left for future consideration.

- A detailed investigation which compares the electromagnetic performance of the parallel hybrid-excited generator proposed in this dissertation, the series hybrid-excitation generator proposed in [58] and a conventional wound rotor synchronous

generator at utility-scale power ratings should be considered. This investigation would provide valuable insight regarding which variable-flux generator topology is best suited for SS-WTSs.

- From the outcomes of Chapters 7 and 8, it is concluded that the study of SS-WT technology should now focus on geared drivetrains rather than direct-drive drivetrains. However, a more comprehensive study that compares direct-drive, medium-speed and low-speed SS-WT drivetrains on a techno-economic basis is still required.

Appendices

Appendix A

Grid-Code Requirements

Modern wind turbine systems (WTSs) are required to operate as traditional grid-tied synchronous generators. Previously, these WTSs could disconnect from the grid following a disturbance in the network. Nowadays, modern WTSs and wind farms are expected to contribute to the grid's stability in response to a fault by providing ancillary grid services according to a grid code. Grid codes specify the requirements of WTSs regarding frequency regulation, active power regulation, reactive power support, and low-voltage ride-through (LVRT) capabilities [121, 122]. The grid-code requirements for renewable power plants (RPPs) are relatively similar across the world [121]. However, this section provides a summary of the most important grid connection codes as stated in [50].

A.0.1 Frequency Support

The continued proliferation of RPPs into existing electrical networks has made it mandatory for these RPPs to behave as traditional grid-tied SGs regarding grid-frequency control. Fig. A.1 shows the active power curtailment requirements that RPPs must adhere to stabilise the grid frequency should it deviate from its nominal value, which in the case of Fig. A.1 is 50 Hz. If the system frequency exceeds 50.5 Hz, the RPPs must reduce their active power as a function of the change in frequency, as shown in Figure A.1. If, however, the system frequency exceeds 51.5 Hz for longer than 4 seconds, the RPPs must be disconnected from the grid [50].

A.0.2 Reactive Power Control

Fig. A.2 shows the reactive power requirements for RPPs when the voltage at the point of coupling (POC) is at its nominal value (U = 1.0 pu) [50]. RPPs with a rated capacity between 100 kVA and 1.0 MVA are required to supply reactive power (available from 0.2 pu and 1.0 pu rated power) at power factor (PF) values ranging from -0.95 (lagging) and 0.95 (leading).

RPPs with a rated capacity between 1.0 MVA and 20 MVA are required to supply reactive power (available from 0.05 pu and 1.0 pu rated power) at power factor (PF) values ranging from -0.975 (lagging) and 0.975 (leading). The respective minimum and maximum values of reactive power required are $Q_{\min}$ = -0.228 and $Q_{\max}$ = 0.228. Furthermore, RPPs are not required to perform any reactive power control when operating below 5% of its rated active power (MW). However, RPPs are required to operate within the reactive power range of ± 5% of its rated power as indicated by the Area A, B, C and D [50].

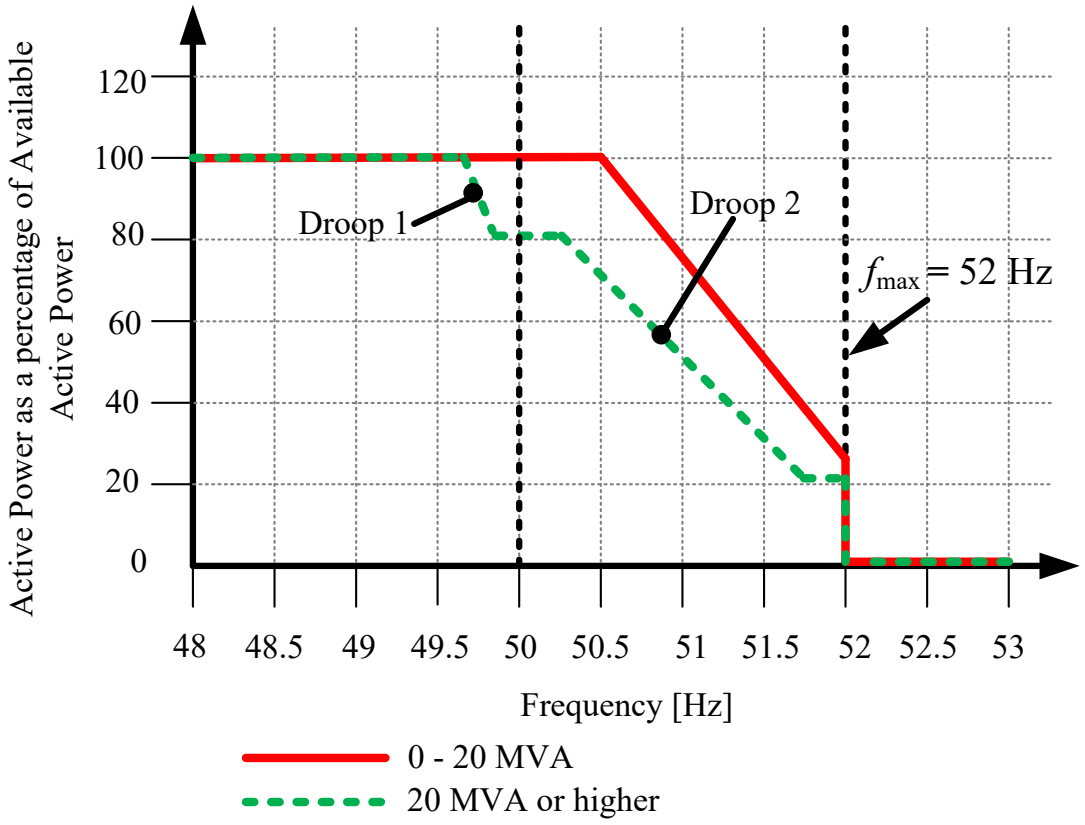

Figure A.1: Frequency response for renewable power plants in South Africa [50].

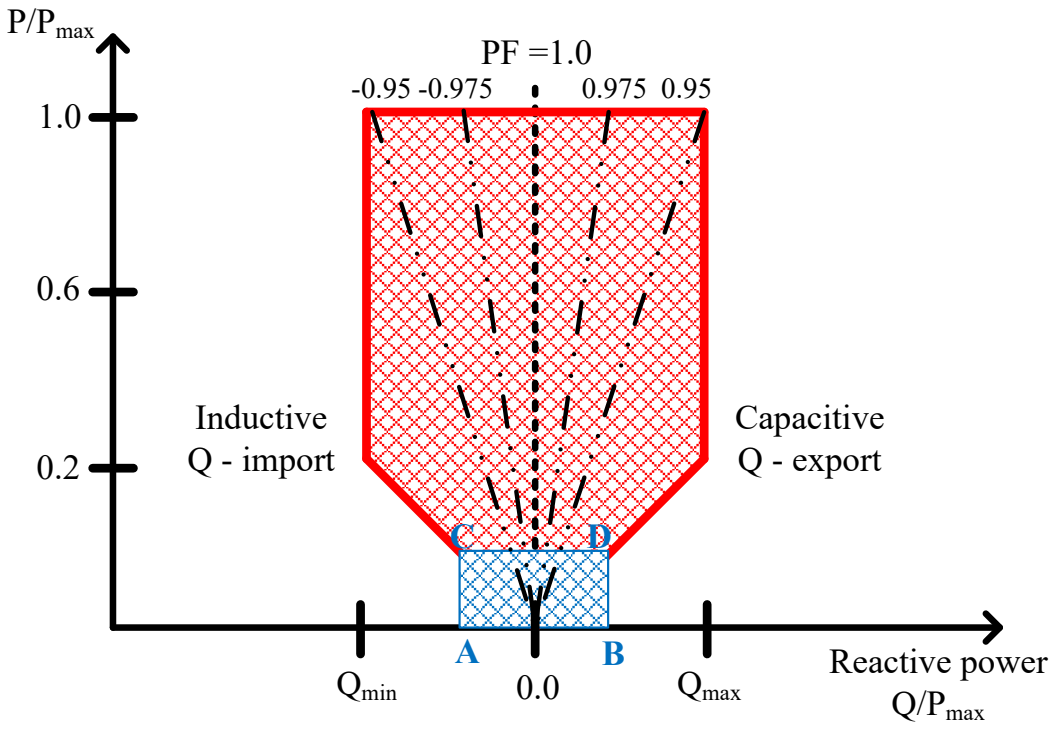

Figure A.2: Reactive power requirements for renewable power plants in South Africa when U = 1.0 pu. [50].

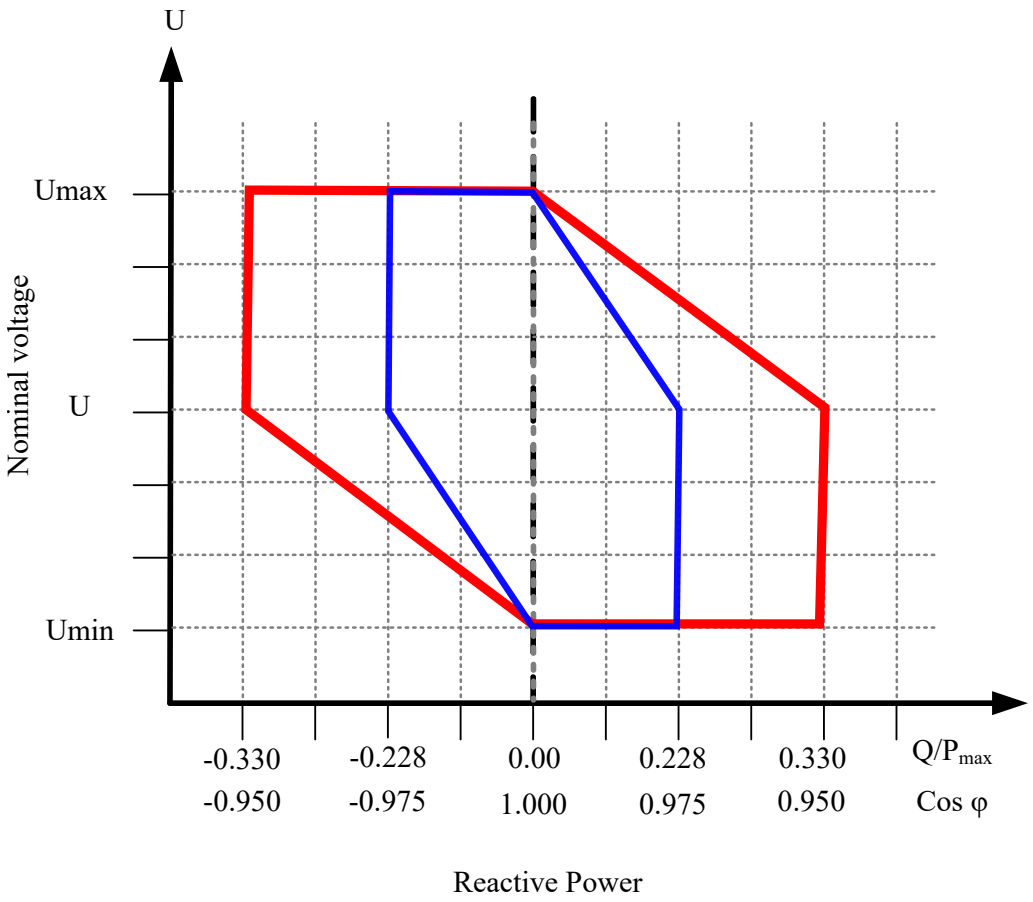

Figure A.3: Reactive power requirements for renewable power plants in South Africa when U $\neq$ 1.0 pu. [50].

RPPs with a rated capacity larger than 20 MVA are required to supply rated power (available from 0.05 pu and 1.0 pu rated power) at power factor (PF) values ranging from -0.95 (lagging) and 0.95 (leading). The respective minimum and maximum values of reactive power required are Q_{min} = -0.330 and Q_{max} = 0.330. Furthermore, these RPPs are required to operate within the reactive power range of $\pm$ 5% of its rated power as indicated by the Area A, B, C and D [50].

Fig. A.3 illustrates the reactive power requirements for RPPs with a rated capacity larger than 1 MVA when the voltage at the POC is not 1.0 pu (U $\neq$ 1.0 pu). Under these circumstances, the RPP is only required to supply maximum reactive power (Q_{max}) when the voltage at the POC is at its minimum (U_{min}). Moreover, the RPP is only required to absorb maximum reactive power (Q_{min}) when the voltage at the POC is at its maximum (U_{max}).

A.0.3 Voltage Ride Through Capability

Fig. A.4 shows the voltage ride-through requirements of medium-to-large scale RPPs (power ratings between 100 kVA - 20 MVA). According to Fig. A.4, RPPs must stay connected to the network and uphold normal production while in Area A. In Area B, the RPP must remain connected to the network and provide maximum voltage support by supplying a controlled amount of reactive current to help stabilise the grid [50]. The reactive power supply has priority in area B, while the active power supply has secondary importance. RPPs are allowed to disconnect from the network while in Area C. In Area

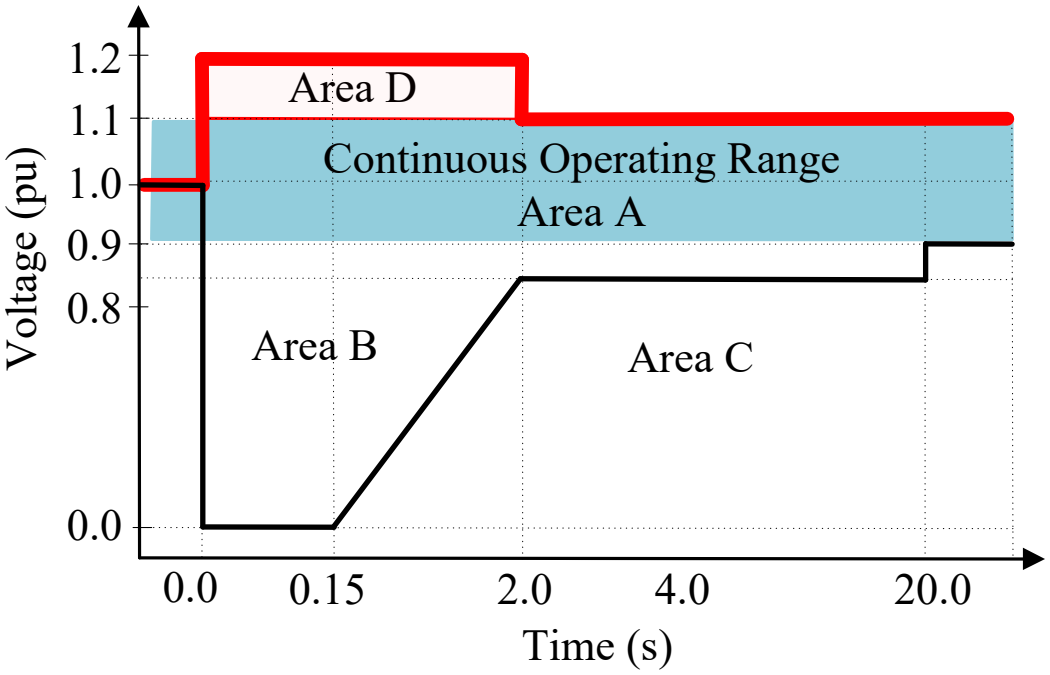

Figure A.4: Voltage Ride Through Capabilities for RPPs utilizing synchronous machines with a rated capacity of 100 kVA - 20 MVA and larger [50].

D, the RPP must stay connected to the network and provide maximum voltage support by absorbing a controlled amount of reactive current to help stabilise the grid.

Appendix B

Analytical Modelling and Optimisation of PM Slip Couplers

The work presented in this Appendix is derived from the work of [123] and [78] and adds to their work by deriving a set of analytical modelling equations that describes the harmonic content of the S-PMC's permanent magnet (PM) rotor and wound-rotor sections.

B.1 PM-Rotor Harmonic Model

The S-PMC PMs are modelled as current-carrying coils wrapped around a material with a specific permeability. The fictitious current flowing within these coils generates a magneto-motive force (MMF) that is proportional to the magnet height (h_m) and the coercivity of the magnet material (H_c) and is given by

$$I_m = H_c h_m. \tag{B.1}$$

Fig. B.1 shown the MMF waveform generated by all of the fictitious magents-currents of (B.1). The MMF waveform of Fig. B.1 can analytically be expressed as

$$F_{mn}(\theta) = \sum_{n_m=1,3,5,\ldots,n}^{n} \frac{2pI_m k_{pmn}}{n_m \pi} \cos\left[n_m(\omega_{slm}t + \theta)\right] \tag{B.2}$$

- p $= \frac{N_m}{M_s}$ is number of poles per machine section,
- N_m is the total number of PM poles,

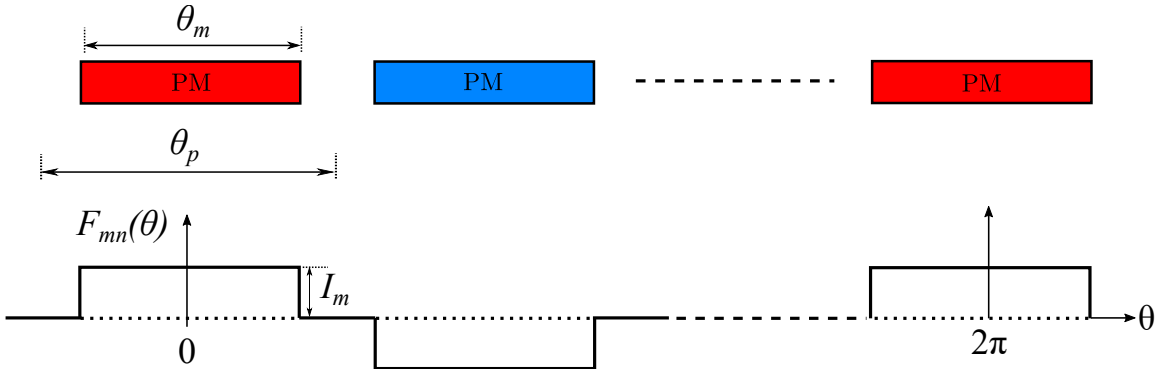

Figure B.1: MMF waveform generated by all magnet coils [123].

- M_s $= \gcd(0.5N_m,\, N_s)$ is the number of machine sections,
- N_s is the total number of slip-rotor slots,
- n_m $= \frac{(1+2k)p}{2}$ is the magnet harmonic-order number, where $k = 1,\, 2,\, 3,\, 4,\, ...$,
- k_{pmn} $= \sin\left(\frac{n_m\theta_m}{2}\right)$ is the n_m^{th} order magnet coil pitch factor, where
- θ_m $=$ is the pitch of a permanent magnet pole and,
- ω_{slm} is the PM-rotor slip-angular velocity.

From (B.2), an expression for the airgap flux density B_m can be written as

$$B_{mn}(\theta) = \frac{\mu_o F_{mn}(\theta)}{g_m k_c} = \sum_{n_m=1,3,5,\ldots,n}^{n} \frac{2\mu_o p I_m k_{pmn}}{g_m n_m \pi k_c} \cos\left[n_m(\omega_{slm}t + \theta)\right] \tag{B.3}$$

B.2 Slip-Rotor Harmonic Model

The MMF generated by double-layer, non-overlap short-circuited coils is analytically derived in [78] and is repeated here for completeness. Fig. B.2 shows the MMF waveform generated by a single short-circuited coil. The MMF waveform of Fig. B.2 can analytically be expressed as

$$F_c(\theta) = \frac{2k_{wn_s}\vec{\boldsymbol{i}}}{|n_s|\,\pi}\cos(n_s\theta) \tag{B.4}$$

where:

- k_{wn_s} $=$ is the n_s^{th} order winding factor,
- $\vec{\boldsymbol{i}}$ is a vector representing a balanced set of three-phase coil currents, and
- n_s $= 3\tau k - 1$, where $\tau = \frac{W_s}{M_s}$ represents the S-PMC's periodicity, and where $k \in \mathbb{Z}$.

From [78] and from Fig. 5.2b in Chapter 5, we can group three short-circuited coils that are 120° out of phase to generate a time-varying three-phase MMF that can analytically be expressed as

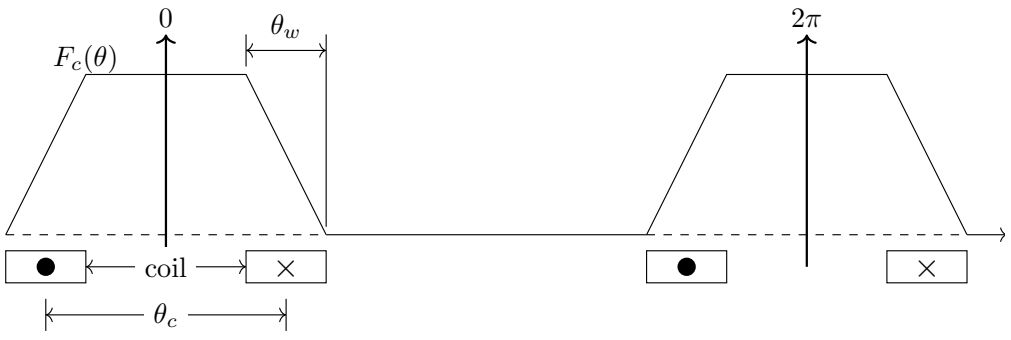

Figure B.2: MMF waveform of a short-circuited non-overlap coil [78].

$$F_s(t,\theta) = F_1(t,\theta) + F_2(t,\theta) + F_3(t,\theta), \tag{B.5}$$

where,

$$\begin{bmatrix} F_1(t,\theta) \\ F_2(t,\theta) \\ F_3(t,\theta) \end{bmatrix} = \begin{bmatrix} F_{max} \cdot \cos(\omega_e t - \theta n_s) \\ F_{max} \cdot \cos(\omega_e t - \theta n_s - (\theta_t + n_s\theta_s)) \\ F_{max} \cdot \cos(\omega_e t - \theta n_s - 2 \cdot (\theta_t + n_s\theta_s)) \end{bmatrix}. \tag{B.6}$$

In (B.6),

- $F_{max} = \frac{3 \cdot I \cdot k_{wsn}}{|n_s|\pi}$ and I are the amplitudes of the MMF waveform and coil-currents respectively,
- $\theta_t = \frac{p \cdot \pi}{N_s}$ is the phase angle between the currents of adjacent coils, and
- $\theta_s = \frac{2\pi}{S}$ is the electrical slot pitch angle where S is the number of slip-rotor slots per machine section M_s.

Equations (B.4) - (B.6) can be used to analytically describe the MMF waveform for any arbitrary number of m three-phase coil sets as

$$\frac{3Ik_{wsn}}{|n_s|\,\pi} \sum_{q=0,1,\ldots,(m-1)}^{m-1} \cos\left[\omega_e t - n_s\theta - q \cdot (\theta_t + n_s\theta_s)\right]. \tag{B.7}$$

It can be shown that for an odd number multiple of three-phase coil sets, (B.7) simplifies to

$$F_{sj} = \frac{3 \cdot m}{|n_s|\,\pi} k_{wsn} I \cos(w_e t + \nu_s \theta), \tag{B.8}$$

where only ν_s MMF harmonic numbers are present and the remaining harmonic orders are cancelled out. In (B.8), the MMF harmonic numbers that remain present can be analytically determined by

$$\nu_s = \frac{2\pi x - \theta_t}{\theta_s}, \quad \text{for} \quad x \in \mathbb{Z}. \tag{B.9}$$

B.2.1 Case Study

Fig. B.3 shows the winding harmonics for two S-PMCs both equipped with double-layer non-overlap windings (in the side-by-side configuration). The S-PMC in Fig. B.3a has 56 magnet poles and 60-slots, which has a base winding of $p = 14$ poles and $S = 15$ slots. Consequently, from Chapter 5, this base winding has $m = \frac{15}{3} = 5$ three phase coils sets. Similarly, the results in Fig. B.3b represents an S-PMC with 40 magnet poles and 48-slots, which thus has a base winding of $p = 10$ poles and $S = 12$ slots and subsequently has $m = \frac{12}{3} = 4$ three-phase coil sets per machine section.

From Fig. B.3, it is can be seen that the 56-pole, 60-slot machine, which has a base-winding that has an odd number of three-phase sets ($m = 5$), generates no sub-harmonics and that the relationship of (B.9) accurately predicts the MMF harmonics that are and aren't present for such multi-three-phase system. In contrast, the 40-pole, 48-slot machine, which has a base-winding that has an even number of three-phase sets ($m = 4$), generates a sub-harmonic at $\nu_s = 1$.

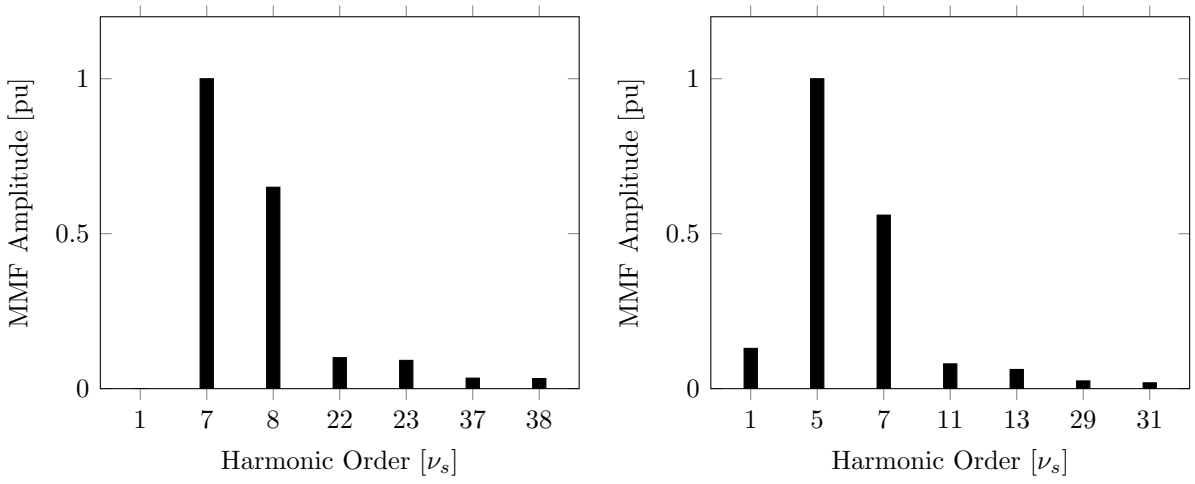

Figure B.3: Per unit MMF harmonics for (a) a 56-pole, 60-slot side-by-side non-overlap winding with a working harmonic of $\nu_s = 7$ and (b) a 40-pole, 48-slot side-by-side non-overlap winding with a working harmonic of $\nu_s = 5$.

Bibliography

[1] United Nations. (2015) Paris Agreement. [Online]. Available: https://unfccc.int/sites/default/files/english_paris_agreement.pdf

[2] The United Nations Framework Convention on Climate Change. (2021) The Paris Agreement. [Online]. Available: https://www.un.org/en/climatechange/paris-agreement

[3] J. Lee and F. Zhao, "Global Wind Report 2021," 2021. [Online]. Available: https://gwec.net/global-wind-report-2021/

[4] International Renewable Energy Agency, *Renewable Energy and Climate Pledges:*, 2020.

[5] REN21, *Renewables 2021 Global Status Report*, 2021.

[6] International Energy Agency. (2020) Renewables 2020. IEA , Paris. [Online]. Available: https://www.iea.org/reports/renewables-2020

[7] Australian Energy Market Operator. (2018, July) System strength requirements methodology and system strength requirements and fault level shortfalls. [Online]. Available: https://www.aemo.com.au/-/media/files/electricity/nem/security_and_reliability/system-security-market-frameworks-review/2018/system_strength_requirements_methodology_published.pdf?la=en&hash=9748847CDF423A9C8829BD1932D7D2A4

[8] IEEE/NERC Task Force on Short-Circuit and System Performance Impact of Inverter Based Generation. (2018, 07) Impact of inverter based generation on bulk power system dynamics and short-circuit performance. [Online]. Available: https://globalpst.org/wp-content/uploads/FINAL-2021_Presentation_PES-NERC_TF_IBR_Impacts_Rev5.0_042621.pdf

[9] "Fault current contributions from wind plants," in *2015 68th Annual Conference for Protective Relay Engineers*, 2015, pp. 137–227.

[10] Gu, Huajie and Yan, Ruifeng and Saha, Tapan, "Review of system strength and inertia requirements for the national electricity market of Australia," *CSEE Journal of Power and Energy Systems*, vol. 5, no. 3, pp. 295–305, 2019.

[11] North American Electric Reliability Corperation, "Short-Cirucit Modeling and System Strength," NERC, Tech. Rep., February 2018.

[12] B. Mountain and S. Percy, "Inerta and system strength in the National Energy Market: A report prepared for the Australian Institute," Victoria Energy Policy Center (VEPC), Melbourne, Tech. Rep., 2021.

[13] Andreas Ulbig and Theodor S. Borsche and Göran Andersson, "Impact of Low Rotational Inertia on Power System Stability and Operation," *IFAC Proceedings Volumes*, vol. 47, no. 3, pp. 7290–7297, 2014, 19th IFAC World Congress.

[14] M. Paolone, T. Gaunt, X. Guillaud, M. Liserre, S. Meliopoulos, A. Monti, T. Van Cutsem, V. Vittal, and C. Vournas, "Fundamentals of power systems modelling in the presence of converter-interfaced generation," *Electric Power Systems Research*, vol. 189, p. 106811, 2020. [Online]. Available: https://www.sciencedirect.com/science/article/pii/S037877962030482X

[15] WU, Z., GAO, W., GAO, T. et al., "state-of-the-art review on frequency response of wind power plants in power systems," *J. Mod. Power Syst. Clean Energy*, vol. 6, p. 1–16, 2018.

[16] L. Ruttledge and D. Flynn, "System-wide inertial response from fixed speed and variable speed wind turbines," in *IEEE Power and Energy Society General Meeting*, July 2011, pp. 1–7.

[17] E. Muljadi, V. Gevorgian, M. Singh, and S. Santoso, "Understanding inertial and frequency response of wind power plants," in *2012 IEEE Power Electronics and Machines in Wind Applications*, 2012, pp. 1–8.

[18] Gloe, Arne and Jauch, Clemens and Craciun, Bogdan and Winkelmann, Jörg, "Continuous provision of synthetic inertia with wind turbines: implications for the wind turbine and for the grid," *IET Renewable Power Generation*, vol. 13, no. 5, pp. 668–675, 2019.

[19] Haddadi, Aboutaleb and Farantatos, Evangelos and Kocar, Ilhan and Karaagac, Ulas, "Impact of Inverter Based Resources on System Protection," *Energies*, vol. 14, no. 4, 2021. [Online]. Available: https://www.mdpi.com/1996-1073/14/4/1050

[20] Kou, Gefei and Chen, Le and VanSant, Philip and Velez-Cedeno, Francisco and Liu, Yilu, "Fault Characteristics of Distributed Solar Generation," *IEEE Transactions on Power Delivery*, vol. 35, no. 2, pp. 1062–1064, 2020.

[21] Kauffmann, Thomas and Karaagac, Ulas and Kocar, Ilhan and Jensen, Simon and Farantatos, Evangelos and Haddadi, Aboutaleb and Mahseredjian, Jean, "Short-Circuit Model for Type-IV Wind Turbine Generators With Decoupled Sequence Control," *IEEE Transactions on Power Delivery*, vol. 34, no. 5, pp. 1998–2007, 2019.

[22] Erlich, Istvàn and Neumann, Tobias and Shewarega, Fekadu and Schegner, Peter and Meyer, Jö rg, "Wind turbine negative sequence current control and its effect on power system protection," in *2013 IEEE Power Energy Society General Meeting*, 2013, pp. 1–5.

[23] Nagpal, Mukesh and Henville, Charles, "Impact of Power-Electronic Sources on Transmission Line Ground Fault Protection," *IEEE Transactions on Power Delivery*, vol. 33, no. 1, pp. 62–70, 2018.

[24] The Australian Energy Market Operator, "Draft 2020 Integrated System Plan For the National Electricity Market," AEMO, Tech. Rep., 2019.

[Online]. Available: https://www.aemo.com.au/-/media/Files/Electricity/NEM/Planning_and_Forecasting/ISP/2019/Draft-2020-Integrated-System-Plan.pdf

[25] Cigre Working Group B4.62, "Connection of wind farms to weak AC networks," TGS, CIGRE WG B4-62, Tech. Rep., 2017.

[26] Zhou, Jenny Z. and Ding, Hui and Fan, Shengtao and Zhang, Yi and Gole, Aniruddha M., "Impact of Short-Circuit Ratio and Phase-Locked-Loop Parameters on the Small-Signal Behavior of a VSC-HVDC Converter," *IEEE Transactions on Power Delivery*, vol. 29, no. 5, pp. 2287–2296, 2014.

[27] Liyanarachchi, Lakna and Hosseinzadeh, Nasser and Mahmud, Apel and Gargoom, Ameen, "Challenges in Power System Strength Assessment with Inverter-Based Resources," in *2021 3rd International Conference on SmartPower Internet Energy Systems (SPIES)*, 2021, pp. 158–163.

[28] Operator, Australian Energy Market, "Black System South Australia 28 September 2016," 2017.

[29] National Grid Electricity System Operator, "Technical Report on the Events of 9 August 2019-UK," Electricity System Operator, Tech. Rep., 2019.

[30] Y. S. Denholm, Paul and T. Mai, "An Introduction to Grid Services: Concepts, Technical Requirements, and Provision from Wind," National Renewable Energy Laboratory, Golden, CO, Tech. Rep., 2019. [Online]. Available: https://www.nrel.gov/docs/fy19osti/72578.pdf

[31] J. Leslie, "Stability pathfinder," 4 November 2020. [Online]. Available: https://www.waterpowermagazine.com/features/featurestability-pathfinder-8345488

[32] ETEnergyWorld, "India to have 70,000 MW of hydropower capacity by 2030: Official," online, May 2020. [Online]. Available: https://energy.economictimes.indiatimes.com/news/power/india-to-have-70000-mw-of-hydropower-capacity-by-2030-official/75859241

[33] General Electric, "GE Renewable Energy Signs Agreement with Walcha Energy to Accelerate 500MW Pumped Hydro Storage Project in Australia," online, 4 August 2020. [Online]. Available: https://www.ge.com/news/press-releases/ge-renewable-energy-signs-agreement-walcha-energy-accelerate-500mw-pumped-hydro

[34] J. Liston, "Typical Synchronous Condenser Installations," *General Electric Company Review*, vol. 14, pp. 234–241, 1911.

[35] P. E. Marken, A. C. Depoian, J. Skliutas, and M. Verrier, "Modern synchronous condenser performance considerations," in *2011 IEEE Power and Energy Society General Meeting*, 2011, pp. 1–5.

[36] H. T. Nguyen, G. Yang, A. H. Nielsen, and P. H. Jensen, "Combination of synchronous condenser and synthetic inertia for frequency stability enhancement in low-inertia systems," *IEEE Transactions on Sustainable Energy*, vol. 10, no. 3, pp. 997–1005, 2019.

[37] A. Wade, "Power moves: Synchronous condensers make a comeback," online, 2021. [Online]. Available: https://www.theengineer.co.uk/power-moves-synchronous-condensers-make-a-comeback/

[38] G. Advisory, "Economic life for electranet synchronous condensers," 2019.

[39] J. Esch, "High-power wind energy conversion systems: State-of-the-art and emerging technologies," *Proceedings of the IEEE*, vol. 103, no. 5, pp. 736–739, 2015.

[40] X. Yin, "An up to date review of continuously variable speed wind turbines with mechatronic variable transmissions," *International Journal of Energy Research*, vol. 42, no. 4, pp. 1442–1454, 2018.

[41] E. Taherian-Fard, R. Sahebi, T. Niknam, A. Izadian, and M. Shasadeghi, "Wind turbine drivetrain technologies," *IEEE Transactions on Industry Applications*, vol. 56, no. 2, pp. 1729–1741, 2020.

[42] F. Wang, J. Chen, B. Xu, and K. A. Stelson, "Improving the reliability and energy production of large wind turbine with a digital hydrostatic drivetrain," *Applied Energy*, vol. 251, p. 113309, 2019.

[43] B. Mohanty and K. A. Stelson, "Experimental validation of a hydrostatic transmission for community wind turbines," *Energies*, vol. 15, no. 1, 2022.

[44] R. You, J. Chai, X. Sun, and Y. Lin, "Variable speed wind turbine based on electromagnetic coupler and its experimental measurement," in *2014 IEEE PES General Meeting | Conference Exposition*, 2014, pp. 1–5.

[45] J. H. J. Potgieter, "Optimal Topology and Critical Evaluation of Slip Synchronous Permanent Magnet Wind Generator," Ph.D. dissertation, Stellenbosch University, 2014.

[46] Potgieter, Johannes H.J. and Kamper, Maarten J., "Design of new concept permanent magnet induction wind generator," in *2010 IEEE Energy Conversion Congress and Exposition*, 2010, pp. 2403–2408.

[47] J. H. J. Potgieter and M. J. Kamper, "Design of new concept direct grid-connected slip-synchronous permanent-magnet wind generator," *IEEE Transactions on Industry Applications*, vol. 48, no. 3, pp. 913–922, 2012.

[48] U. Hoffmann, P. Bouwer, and M. Kamper, "Direct grid connection of a slip-permanent magnet wind turbine generator," in *2011 IEEE Energy Conversion Congress and Exposition*, 2011, pp. 2373–2380.

[49] Ockhuis, Dillan K. and Kamper, Maarten J., "Grid Connection Power Converter and Speed Controller for Slip-Synchronous Wind Generators," in *2019 IEEE Energy Conversion Congress and Exposition (ECCE)*, 2019, pp. 6741–6748.

[50] NERSA, "Grid Connection Code for Renewable Power Plants (RPPs) connected to the Electricity Transmission System (TS) or Distribution System (DS) in South Africa," National Energy Regulator of South Africa, Tech. Rep. Version 2.9, July 2016.

[51] J. H. J. Potgieter and M. J. Kamper, "Design optimization of directly grid-connected pm machines for wind energy applications," *IEEE Transactions on Industry Applications*, vol. 51, no. 4, pp. 2949–2958, 2015.

[52] ——, "Torque and voltage quality in design optimization of low-cost non-overlap single layer winding permanent magnet wind generator," *IEEE Transactions on Industrial Electronics*, vol. 59, no. 5, pp. 2147–2156, 2012.

[53] ——, "Design specifications and optimisation of a directly grid-connected pm wind generator," in *2013 IEEE Energy Conversion Congress and Exposition*, 2013, pp. 882–889.

[54] ——, "Design considerations in the implementation of an electromagnetic brake for a 15 kw pm wind generator," in *Southern African Universities Power Engineering Conference*, 2013.

[55] ——, "Optimum design and comparison of slip permanent-magnet couplings with wind energy as case study application," *IEEE Transactions on Industry Applications*, vol. 50, no. 5, pp. 3223–3234, 2014.

[56] Z. Mouton and M. J. Kamper, "Modeling and optimal design of an eddy current coupling for slip-synchronous permanent magnet wind generators," *IEEE Transactions on Industrial Electronics*, vol. 61, no. 7, pp. 3367–3376, 2014.

[57] J. H. J. Potgieter and M. J. Kamper, "Modeling and stability analysis of a direct-drive direct-grid slip–synchronous permanent-magnet wind generator," *IEEE Transactions on Industry Applications*, vol. 50, no. 3, pp. 1738–1747, 2014.

[58] L. L. Amuhaya and M. J. Kamper, "Design and optimisation of variable-flux synchronous generators over the grid-code range using analytical and pso methods," in *2017 International Conference on the Domestic Use of Energy (DUE)*, 2017, pp. 160–166.

[59] Amuhaya, L. L. and Kamper, M. J., "Design analysis of a hybrid-PM synchronous generator for wind energy applications," in *2015 International Conference on the Domestic Use of Energy (DUE)*, 2015, pp. 163–167.

[60] L. L. Amuhaya and M. J. Kamper, "Design and optimisation of grid compliant variable-flux pm synchronous generator for wind turbine applications," in *2015 IEEE Energy Conversion Congress and Exposition (ECCE)*, 2015, pp. 829–836.

[61] ——, "Effect of rotor field winding mmf on performance of grid-compliant hybrid-pm slip synchronous wind generator," in *2016 IEEE PES PowerAfrica*, 2016, pp. 254–258.

[62] H. Hua and Z. Q. Zhu, "Comparative study of series and parallel hybrid excited machines," *IEEE Transactions on Energy Conversion*, vol. 35, no. 3, pp. 1705–1714, 2020.

[63] L. Amuhaya and M. J. Kamper, "Design by optimisation of a buried pm variable-flux wind generator for grid connection," in *2017 International Conference on Optimization of Electrical and Electronic Equipment (OPTIM) 2017 Intl Aegean Conference on Electrical Machines and Power Electronics (ACEMP)*, 2017, pp. 305–310.

[64] J. N. Stander, M. J. Kamper, and G. Venter, "Analytic modelling and optimization of slip synchronous permanent magnet wind turbine generator topologies," *Wind Energy*, vol. 18, no. 7, pp. 1221–1238, 2015.

[65] D. Ockhuis, M. J. Kamper, and A. T. Loubser, "Impedance matching of direct grid-connected renewable energy synchronous generators," in *2020 International SAUPEC/RobMech/PRASA Conference*, 2020, pp. 1–6.

[66] Hlioui, Sami and Amara, Yacine and Hoang, Emmanuel and Lecrivain, Michel and Gabsi, Mohamed, "Overview of hybrid excitation synchronous machines technology," in *2013 International Conference on Electrical Engineering and Software Applications*, 2013, pp. 1–10.

[67] D. K. Ockhuis, M. J. Kamper, and A. T. Loubser, "Hybrid excitation method for higher pole number grid-tie synchronous generators," in *2020 IEEE Energy Conversion Congress and Exposition (ECCE)*, 2020, pp. 1439–1446.

[68] D. Fodorean, A. Djerdir, I.-A. Viorel, and A. Miraoui, "A double excited synchronous machine for direct drive application—design and prototype tests," *IEEE Transactions on Energy Conversion*, vol. 22, no. 3, pp. 656–665, 2007.

[69] K. Kamiev, J. Nerg, J. Pyrhönen, V. Zaboin, and J. Tapia, "Feasibility of an armature-reaction-compensated permanent-magnet synchronous generator in island operation," *IEEE Transactions on Industrial Electronics*, vol. 61, no. 9, pp. 5075–5085, 2014.

[70] K. Yamazaki, K. Nishioka, K. Shima, T. Fukami, and K. Shirai, "Estimation of assist effects by additional permanent magnets in salient-pole synchronous generators," *IEEE Transactions on Industrial Electronics*, vol. 59, no. 6, pp. 2515–2523, 2012.

[71] M. Ployard, F. Gillon, A. Ammar, D. Laloy, and L. Vido, "Hybrid excitation topologies of synchronous generator for direct drive wind turbine," in *2016 IEEE Energy Conversion Congress and Exposition (ECCE)*, 2016, pp. 1–7.

[72] Xiaogang Luo and Lipo, T.A., "A synchronous/permanent magnet hybrid ac machine," *IEEE Transactions on Energy Conversion*, vol. 15, no. 2, pp. 203–210, 2000.

[73] K. Yamazaki, K. Nishioka, K. Shima, T. Fukami, and K. Shirai, "Estimation of assist effects by additional permanent magnets in salient-pole synchronous generators," *IEEE Transactions on Industrial Electronics*, vol. 59, no. 6, pp. 2515–2523, 2012.

[74] K. Kamiev, A. Parviainen, and J. Pyrhönen, "Hybrid excitation synchronous generators for small hydropower plants," in *2016 XXII International Conference on Electrical Machines (ICEM)*, 2016, pp. 2529–2535.

[75] J. H. J. Potgieter and M. J. Kamper, "Calculation methods and effects of end-winding inductance and permanent-magnet end flux on performance prediction of nonoverlap winding permanent-magnet machines," *IEEE Transactions on Industry Applications*, vol. 50, no. 4, pp. 2458–2466, 2014.

[76] Jürgens, J. and Brune, A. and Ponick, B., "Electromagnetic design and analysis of a salient-pole synchronous machine with tooth-coil windings for use as a wheel hub motor in an electric vehicle," in *2014 International Conference on Electrical Machines (ICEM)*, 2014, pp. 744–750.

[77] Garner, Karen S. and Kamper, Maarten J., "Reducing mmf harmonics and core loss effect of non-overlap winding wound rotor synchronous machine (wrsm)," in *2017 IEEE Energy Conversion Congress and Exposition (ECCE)*, 2017, pp. 1850–1856.

[78] P. J. J. van Wyk and M. J. Kamper, "Simplified analysis of nonoverlap short-circuited coil winding slip permanent magnet couplers," *IEEE Transactions on Industry Applications*, vol. 52, no. 6, pp. 4740–4751, 2016.

[79] D. K. Ockhuis and M. J. Kamper, "Static-fe harmonic analysis of PM slip couplers," in *2021 International Aegean Conference on Electrical Machines and Power Electronics (ACEMP) and 2021 International Conference on Optimization of Electrical and Electronic Equipment (OPTIM)*, 2021, pp. 398–404.

[80] D.K. Ockhuis and M. Kamper, "Potential of slip synchronous wind turbine systems: Grid support and mechanical load mitigation," *Energies*, 2021.

[81] A. S. Erasmus and M. J. Kamper, "Computationally efficient analysis of double pm-rotor radial-flux eddy current couplers," *IEEE Transactions on Industry Applications*, vol. 53, no. 4, pp. 3519–3527, 2017.

[82] P. J. J. van Wyk and M. J. Kamper, "Simplified analysis technique for double layer non-overlap multiphase slip permanent magnet couplings in wind energy applications," in *2015 IEEE International Electric Machines Drives Conference (IEMDC)*, 2015, pp. 1317–1323.

[83] J. Lammeraner and M. Stafl, "Eddy currents." 1964.

[84] Nejad, A. R. *et al*, "Wind turbine drivetrains: state-of-the-art technologies and future development trends," *Wind Energy Science Discussions*, vol. 2021, pp. 1–35, 2021. [Online]. Available: https://wes.copernicus.org/preprints/wes-2021-63/

[85] General Electric. [Online]. Available: https://www.ge.com/renewableenergy/wind-energy/onshore-wind/(accessedon13December˜2021)

[86] ——. [Online]. Available: https://www.ge.com/renewableenergy/wind-energy/offshore-wind/

[87] Goldwind. [Online]. Available: https://www.goldwind.com/en/windpower/

[88] Goldwind. [Online]. Available: https://www.goldwind.com/en/windpower/product-gw6s/

[89] Vestas, "Product portfolio." [Online]. Available: https://www.vestas.com/en/products/overview

[90] ——, "Offshore solutions." [Online]. Available: https://www.vestas.com/en/products/offshore/offshore-solutions

[91] Siemens Gamesa, "Onshore wind power portfolio." [Online]. Available: https://www.siemensgamesa.com/en-int/products-and-services/onshore

[92] ——. Offshore wind power portfolio. [Online]. Available: https://www.siemensgamesa.com/en-int/products-and-services/offshore

[93] F. Harzendorf, R. Schelenz, and G. Jacobs, "Reducing cost uncertainty in the drivetrain design decision with a focus on the operational phase," *Wind Energy Science*, vol. 6, no. 2, pp. 571–584, 2021. [Online]. Available: https://wes.copernicus.org/articles/6/571/2021/

[94] J. Carroll, A. McDonald, I. Dinwoodie, D. McMillan, M. Revie, and I. Lazakis, "Availability, operation and maintenance costs of offshore wind turbines with different drive train configurations," *Wind Energy*, vol. 20, no. 2, pp. 361–378, 2017.

[95] Carroll, James and McDonald, Alasdair and McMillan, David, "Failure rate, repair time and unscheduled o&m cost analysis of offshore wind turbines," *Wind Energy*, vol. 19, no. 6, pp. 1107–1119, 2016.

[96] Alexios Koltsidopoulos Papatzimos and Tariq Dawood and Philipp R. Thies, "Data Insights from an Offshore Wind Turbine Gearbox Replacement," *Journal of Physics: Conference Series*, vol. 1104, p. 012003, oct 2018. [Online]. Available: https://doi.org/10.1088/1742-6596/1104/1/012003

[97] Qiu, Yingning and Chen, Lang and Feng, Yanhui and Xu, Yili, "An approach of quantifying gear fatigue life for wind turbine gearboxes using supervisory control and data acquisition data," *Energies*, vol. 10, no. 8, p. 1084, 2017.

[98] J. Helsen, Y. Guo, J. Keller, and P. Guillaume, "Experimental investigation of bearing slip in a wind turbine gearbox during a transient grid loss event," *Wind Energy*, vol. 19, no. 12, pp. 2255–2269, 2016.

[99] J. Carroll, A. McDonald, D. McMillan, T. Stehly, C. Mone, and B. Maples, "Improved cost energy comparison of permanent magnet generators for large offshore wind turbines," *European Wind Energy Association 2014 Annual Conference*, 2014.

[100] ——, "Cost of energy for offshore wind turbines with different drive train types," *EWEA 2015 Annual Event*, 2015.

[101] H. Polinder, F. van der Pijl, G.-J. de Vilder, and P. Tavner, "Comparison of direct-drive and geared generator concepts for wind turbines," *IEEE Transactions on Energy Conversion*, vol. 21, no. 3, pp. 725–733, 2006.

[102] Y.-S. Xue, L. Han, H. Li, and L.-D. Xie, "Optimal design and comparison of different pm synchronous generator systems for wind turbines," in *2008 International Conference on Electrical Machines and Systems*, 2008, pp. 2448–2453.

[103] S. Alshibani, V. G. Agelidis, and R. Dutta, "Lifetime cost assessment of permanent magnet synchronous generators for mw level wind turbines," *IEEE Transactions on Sustainable Energy*, vol. 5, no. 1, pp. 10–17, 2014.

[104] A. Bensalah, M. Benhamida, G. Barakat, and Y. Amara, "Large wind turbine generators: State-of-the-art review," in *2018 XIII International Conference on Electrical Machines (ICEM)*, 2018, pp. 2205–2211.

[105] S. Schmidt and A. Vath, "Comparison of existing medium-speed drive train concepts with a differential gearbox approach," *European Wind Energy Conference and Exhibition 2012, EWEC 2012*, vol. 1, pp. 179–186, 01 2012.

[106] N. A. Bhuiyan and A. McDonald, "Optimisation and comparison of generators with different magnet materials for a 6mw offshore direct drive wind turbine," in *8th IET International Conference on Power Electronics, Machines and Drives (PEMD 2016)*, 2016, pp. 1–6.

[107] J. Chen, F. Wang, and K. A. Stelson, "A mathematical approach to minimizing the cost of energy for large utility wind turbines," *Applied Energy*, vol. 228, no. C, pp. 1413–1422, 2018. [Online]. Available: https://ideas.repec.org/a/eee/appene/v228y2018icp1413-1422.html

[108] I. Boldea, L. Tutelea, and F. Blaabjerg, "High power wind generator designs with less or no pms: An overview," in *2014 17th International Conference on Electrical Machines and Systems (ICEMS)*, 2014, pp. 1–14.

[109] T. Economics. (2022) Market price of neodymium. Accessed on: 18 January 2022 (09h11 AM). [Online]. Available: https://tradingeconomics.com/commodity/neodymium

[110] ABB. ABB wind turbine converters ACS880, 800 kW to 8 MW. [Online]. Available: https://search.abb.com/library/Download.aspx?DocumentID=3AUA0000231755&LanguageCode=en&DocumentPartId=&Action=Launch

[111] S. Tegen, M. Hand, B. Maples, E. Lantz P. Schwabe, and A. Smith, " 2010 Cost of Wind Energy Review," National Renewable Energy Laboratory, Tech. Rep., 2012.

[112] T. Stehly and P. Duffy, " 2020 Cost of Wind Energy Review," National Renewable Energy Laboratory, Tech. Rep., 2021.

[113] F. Spinato, P. J. Tavner, G. J. W. V. Bussel, and E. Koutoulakos, "Reliability of wind turbine subassemblies," *IET Renewable Power Generation*, vol. 3, no. 4, pp. 387–401, 2009.

[114] "The wind energy operation and maintenance report," Wind Energy Update, 2016.

[115] Reder, Maik Dennis and Gonzalez, Elena and Melero, Julio J, "Wind turbine failures-tackling current problems in failure data analysis," in *Journal of Physics: Conference Series*, vol. 753, no. 7. IOP Publishing, 2016, p. 072027.

[116] S. S, K. J, C. N, and G. C, "Gearbox reliability collaborative update (Presentation)," National Renewable Energy Laboratory (NREL), Golden, CO, Technical Report NREL/PR-5000-60141, 2013.

[117] M. Saeedian, B. Pournazarian, S. S. Seyedalipour, B. Eskandari, and E. Pouresmaeil, "Emulating rotational inertia of synchronous machines by a new control technique in grid-interactive converters," *Sustainability*, vol. 12, p. 5346, 2020.

[118] K. W. Klontz, T. J. E. Miller, M. I. McGilp, H. Karmaker, and P. Zhong, "Short-circuit analysis of permanent-magnet generators," *IEEE Transactions on Industry Applications*, vol. 47, no. 4, pp. 1670–1680, 2011.

[119] H. Polinder, F. van der Pijl, G.-J. de Vilder, and P. Tavner, "Comparison of direct-drive and geared generator concepts for wind turbines," *IEEE Transactions on Energy Conversion*, vol. 21, no. 3, pp. 725–733, 2006.

[120] Y.-S. Xue, L. Han, H. Li, and L.-D. Xie, "Optimal design and comparison of different pm synchronous generator systems for wind turbines," in *2008 International Conference on Electrical Machines and Systems*, 2008, pp. 2448–2453.

[121] Yuan-Kang Wu and Shih-Ming Chang and Paras Mandal, "Grid-Connected Wind Power Plants: A Survey on the Integration Requirements in Modern Grid Codes," *IEEE Transactions on Industry Applications*, vol. 55, pp. 5584–5593, 2019.

[122] Luo, Xing and Wang, Jihong and Wojcik, Jacek D. and Wang, Jianguo and Li, Decai and Draganescu, Mihai and Li, Yaowang and Miao, Shihong, "Review of Voltage and Frequency Grid Code Specifications for Electrical Energy Storage Applications," *Energies*, vol. 11, no. 5, 2018. [Online]. Available: https://www.mdpi.com/1996-1073/11/5/1070

[123] A. J. Rix, "Non-Overlap Winding Radial Flux Permanent Magnet Hub Drives for Electrical Vehicles," Ph.D. dissertation, Stellenbosch University, 2011.